Windblown Sand Modelling and Mitigation for Civil Structures


Doctoral Dissertation
Doctoral Program in Civil and Environmental Engineering (31.th cycle)

Windblown Sand Modelling and Mitigation for Civil Structures

Lorenzo Raffaele

* * * * * *

Supervisors
Prof. L.Bruno, Supervisor
Prof. L.Preziosi, Co-supervisor

Doctoral Examination Committee:
Prof. M.P., Repetto, Università degli studi di Genova
Prof. J., van Beeck, von Karman Institute for Fluid Dynamics
Prof. E.F., University of ...
Prof. G.H., University of ...
Prof. I.J., University of ...

Politecnico di Torino
November 07, 2018

I hereby declare that, the contents and organisation of this dissertation constitute my own original work and does not compromise in any way the rights of third parties, including those relating to the security of personal data.

. . . . . .

Lorenzo Raffaele

Turin, November 07, 2018

Summary

This PhD thesis deals with the modelling of windblown sand action on civil structures and infrastructures, and the performance assessment of sand mitigation measures. The engineering interest about windblown sand is dictated by the harmful interactions that sand has with a number of structures and infrastructures in arid environments, such as pipelines, industrial facilities, towns, single buildings, farms, roads, and railways. In particular, this represents an emerging issue especially in relation to the design of railway infrastructures crossing deserts. Several failure cases have recently occurred in China and Middle East countries. For example, the Lanzhou-Xinjiang line and the Dammam-Riyadh line have recently suffered derailments, service suspension and loss of capacity due to windblown sand. Other lines are currently in the design, testing and commissioning stages worldwide. However, the design-and-building process suffers significant delays, due to the windblown sand accumulation along the alignment and the retrofitting of the designed railways through sand mitigation measures.

Despite the development of ad-hoc studies for specific projects, systematic and comprehensive problem setting and solving is still missing in the scientific and technical engineering literature. Existing modelling frameworks are limited to the assessment of sand drift far from any built structure. They have been introduced in the past for geomorphology applications. However, these frameworks are purely deterministic despite the inborn variability of the phenomenon. Moreover, albeit with a few remarkable exceptions, the rigorous design and performance assessment of sand mitigation measures are still based on trial and error approach.

This PhD thesis aims at contributing to the proper quantification of windblown sand action on civil structures and infrastructures, and the performance assessment of different kinds of sand mitigation measures. The proposed modelling framework requires a multidisciplinary approach, by making use of notions from mathematics and statistics, physics, geomorphology to structural engineering. The proposed modelling framework is conceived on the basis of the wind engineering analysis chain. Incoming windblown sand is defined in analogy to incoming undisturbed wind. It depends on the environmental characteristics of the construction site, such as the wind field and the sand granulometry. The local windblown sand action is then quantified by taking into account both aerodynamics and morphodynamics of

the affected structure by defining sedimentation coefficients, in analogy to force coefficients for the wind action. Finally, the performance level of the affected structure and the adopted sand mitigation measures can be assessed via a reliability analysis.

The thesis develops according to the above objectives through the following chapters.

The introduction to the study is presented in **Chapter 1**.

Chapter 2 is devoted to the state-of-art and includes a phenomenological analysis of the physical processes, a review concerning the existing semi-empirical models to assess windblown sand transport, a critical review of existing sand mitigation measures for railways, and existing design codes and best practices.

The modelling framework and the study outline are conceptually introduced and justified in **Chapter 3**.

Chapter 4 is devoted to the probabilistic modelling of incoming windblown sand upwind built structures. The outlined probabilistic approach is then applied to different test cases around Arabian Peninsula.

Chapter 5 is devoted to the probabilistic modelling of windblown sand action on structures. First, a phenomenological analysis of windblown sand processes around built structures is provided. The so-called windblown sand limit states are defined in analogy to the common practice in structural engineering. Then, the modelling framework to assess windblown sand action is outlined. Finally, the proposed modelling framework is applied to a case study in order to demonstrate its technical feasibility of the approach and assess the performances of two alternative design solutions against windblown sand.

Finally, conclusions and research perspectives are discussed in **Chapter 6**.

Acknowledgements

First, I would like to express my greatest and sincere gratitude to my supervisors. I thank Luca Bruno for the enthusiasm for research he gave me, and for his dedication and the care throughout the PhD. Then, I thank Luigi Preziosi for the continuing mathematical support, and for opening my eyes to the marvellous world of multiphase flows.
I wish also to thank all the people with whom I had the luck to collaborate with and from whom I learnt a lot. In particular, Franco Pellerey, Giles Wiggs, Walter Ceretto, and Davide Fransos.
Finally, I would like to thank all my PhD colleagues involved in the SMaRT project (Marko Horvat, Andrea Lo Giudice, Ciaran Nash, Roberto Nuca), and the department colleagues (Fiammetta Venuti and Emiliano Matta).

Among key institutions, I thank Windblown Sand Modelling and Mitigation (WSMM) joint research, development & consulting group involving Politecnico di Torino (DAD, DISMA) and the Optiflow Company (France) for the priceless opportunity to be part of a wonderful multidisciplinary group.
I also thank the Research Support and Technology Transfer Department (TRIN) supporting the project "Proof of Concept 2016" (POC) co-funded by Compagnia di San Paolo and WSMM. A unique opportunity for young researchers to be part of technology transfer activities for the development of patented technologies.
Part of the study has been developed as sideground of the "Sand Mitigation around Railway Tracks" (SMaRT) project in the framework of the Horizon 2020 European Research Program, Marie Skłodowska-Curie Actions, Innovative Training Networks (ITN), European Industrial Doctorate (EID), call H2020-MSCA-ITN-2016. Grant agreement no. 721798.

Contents

List of Tables

List of Figures

Chapter 1

Introduction

The design of civil structures and infrastructures needs to face environmental actions. Among them, wind action, snow action, and their interaction have gained wide attention in structural design. Wind action on structures and its effects have been extensively investigated from the pioneering studies of Davenport [64] and the seminal and influential book of Simiu and Scanlan [278]. Snow loads on structures have been defined on the basis of nation and international research project, such as the European Snow Load Research Project [66]. Codes and standards often do not address the interaction between wind and snow and complex civil structures, while it has been investigated in a number of scientific studies in the form of snow drift (e.g. [219, 352]) and ice accretion (e.g. [65]). National and international standards and guidelines now regulate wind action (e.g. [83]), snow action (e.g. [82]), snow drift effects on simple roofs (e.g. [82]), design criteria against windblown snow for roads and highways [289], and atmospheric icing of structures [132]. Climate change has a strong impact on environmental conditions (e.g. [58, 106]). As a result, environmental actions needs to be updated in order to properly design new structures and grant the reliability of the existing ones. From this perspective, research activity is recently addressing such issue for both wind action [282] and snow loads [59]. Furthermore, the modern trend in civil and structural engineering pushes the worldwide conception and design of increasingly large-scale structures and infrastructures. Accordingly, such projects are more and more frequently confronted with new challenges.

In this framework, windblown sand effects on civil structures and infrastructures represent an emerging but increasingly significant engineering issue for design and construction in desert and coastal zones. Windblown sand transport results from sand erosion and translates into sand accumulation around any kind of human-built obstacle. In general, windblown sand interacts with a number of civil structures and infrastructures, such as industrial facilities and pipelines (e.g. [2]), farms (e.g. [315]), towns and buildings (e.g. [256, 26]), roads and highways (e.g. [248, 72]),

and railways (e.g. [344, 346, 46]). Railway infrastructures are particularly sensitive to windblown sand because of their extension and their technical complexity, resulting from components in civil works, railway equipment, rolling stock and signalling technologies. The number of desert railways has considerably increased in the last years. Railways crossing regions affected by windblown sand are particularly located in the desert belt at the northern horse latitudes, ranging from China, through Middle East and North Africa. Windblown sand effects can lead to several incremental costs in infrastructure management, e.g. loss of capacity and increased maintenance costs [339], but also to disastrous events, such as train derailment [47]. As such, the demand for the design of windblown sand mitigation solutions has grown in the last decade and it is expected to further increase in the next years. However, several failure cases have recently occurred (e.g. [200]).

More in general, the design and performance assessment of sand exposed structures and infrastructures actually remain at their infancy and in the realm of the qualitative empiricism. Indeed, both the definition of windblown sand action and a modelling framework for its quantification are still missing in both scientific and technical literature. In order to help bridge these gaps, this thesis aims at: (i) providing a solid review of existing methods from other disciplines to quantify windblown sand transport and a categorization of the existing sand mitigation measures; (ii) defining windblown sand environmental action and outlining a limit state approach for its effects on civil structures, by analogy to the common practice in structural engineering; (iii) conceiving a probabilistic modelling framework capable of quantifying windblown sand action on civil structures/infrastructures and assessing the performance of sand mitigation measures.

Chapter 2

State of the Art

Part of the work described in this chapter has been previously published by the author and co-workers in international peer-reviewed journals [244, 243, 242, 33, 241].

Existing studies dealing with windblown sand modelling and mitigation for civil structures are in general very recent and, as a consequence, scarce. The increasing *research interest* in windblown sand modelling mitigation is here testified by the growing number of published studies in the last years. In particular, Fig. 2.1 (a) plots the trend of the published studies cited in [33] versus the year of publication. Multidisciplinarity in windblown sand mitigation is testified by the graph in Fig. 2.1(b), showing the distribution of the cited peer-reviewed studies among the addressed research fields. Given the high fragmentation in research fields, scientific affiliations have been reduced to three main research area, i.e. engineering disciplines, environmental sciences, and applied mathematics and physics. Studies classified in environmental sciences come from geology, ecology, geography. Engineering disciplines comprehend structural, mechanical, geotechnical, and transport engineering. It is worth stressing that several cited studies cross over more than one research area. Finally, the *industrial interest* is testified by the growing number of patents versus filing year shown in Fig. 2.1(c). Patents landscaping has been performed by means of the patent database Orbit©. The patents taken into account are classified by the International Patent Classification (IPC) codes E01F 7/02 "Snow fences or similar devices, e.g. devices affording protection against sand drifts or side-wind effects" and E04H 17/00 "Fencing, e.g. fences, enclosures, corrals".

The aim of this chapter is to provide a solid basis to the work contained in the next chapters. The present chapter is organized into the following sections:

- Phenomenology;
- Modelling;
- Windblown Sand Mitigation Measures;

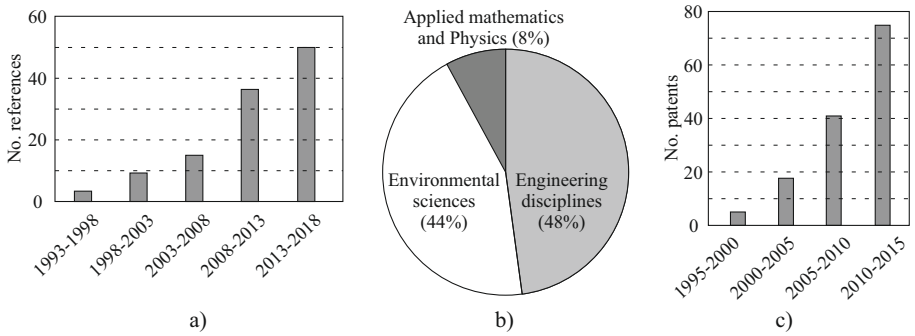

Figure 2.1: Cited references versus year of publication (a), classification of cited references according to macro research areas (b), increasing trend of filed patents versus filing year (c).

- Design codes and best practices.

2.1 Phenomenology

Windblown sand is a *multiphase flow* resulting from the interaction of two physical subsystems, i.e. the wind and the sand. Windblown sand involves different aeolian processes, i.e. sand erosion, transport, and deposition, that in turn trigger the mechanical processes causing sand avalanching. A phenomenological similarity can be drawn with other multiphase flows, such as windblown snow, and, at least in terms of transport, with wind driven rain (see Fig. 2.2). Under in-equilibrium steady state conditions, erosion and deposition processes are balanced. As a result, the sandy surface does not evolve in time. Conversely, non-equilibrium unsteady state conditions, i.e. when erosion and deposition do not balance, lead to the evolution of the sandy surface resulting in sand scouring or accumulation. In turn, windblown sand induced sedimentation/erosion and progressive accumulation/scouring give rise to sand avalanching. In general, non-equilibrium conditions are caused from the presence of any kind of obstacle, such as rocks and clumps of vegetation, but also human built structures and infrastructures. As a result, such non-equilibrium scenarios are the most interesting cases from the engineering point of view.

The worldwide *geographical location* of the regions potentially susceptible to windblown sand is shown in Fig. 2.3. Such regions are coastal zones with well developed dune systems [186] and arid and desert regions with active sand sources, i.e. desert areas covered with sand with little or no vegetation [92]. Windblown sand-prone zones take up about one fifteenth of the Earth's land surface. These

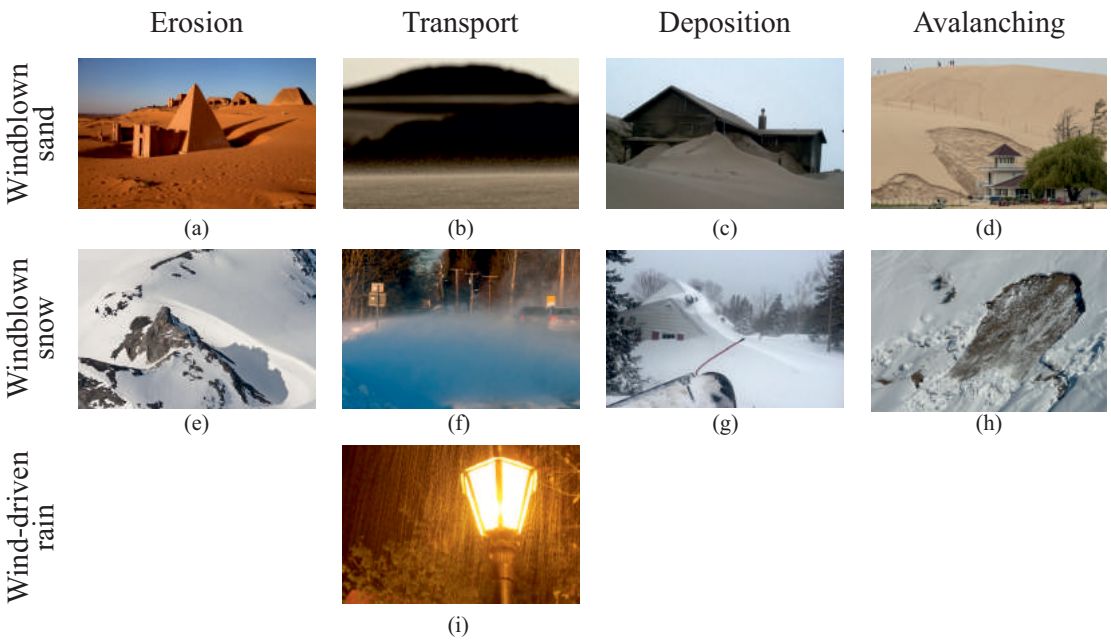

Figure 2.2: Processes and phenomenological similarities. Erosion around a Meroe Pyramid in Sudan (a, explicit publishing permission from the owner of the photo: Boris Kester, www.traveladventures.org), sand transport (b, explicit publishing permission from the owner of the photo: Nik Barte, www.nikbarte.it), sand accumulation in the lee of a house in Waldport, Oregon (c, explicit publishing permission from the owner of the photo: Jason Durrett), sand avalanching from a migrating dune at the Silver Lake, Michigan (d, explicit publishing permission from the owner of the photo: Andraya Croft), snow erosion around a peat hag (e, publishing permission under Creative Commons Attribution-Share Alike 2.0 Generic license, owner of the photo: Walter Baxter), snow transport in New York (f, publishing permission under Creative Commons Attribution-Share Alike 3.0 Unported license, owner of the photo: Daniel Case), snow accumulation in the lee of a house (g, photo credit: Amazonaws.com), snow avalanching (h, publishing permission under Creative Commons Zero license), wind driven rain (i, publishing permission under Creative Commons Zero license).

zones are increasingly hosting human activities, such as transport, industrial, mineral, and residential ones. The hazards induced by windblown sand in drylands and along coastal zones are reviewed in the field of Earth sciences by [206] and [273], respectively.

The *effects of windblown sand* are highly bound to the scale and the nature of the structure it interacts with. Windblown sand can act at the scale of a single built structure [118] (Fig. 2.4c,e), at the urban scale [204] (Fig. 2.4b,d), and/or at the

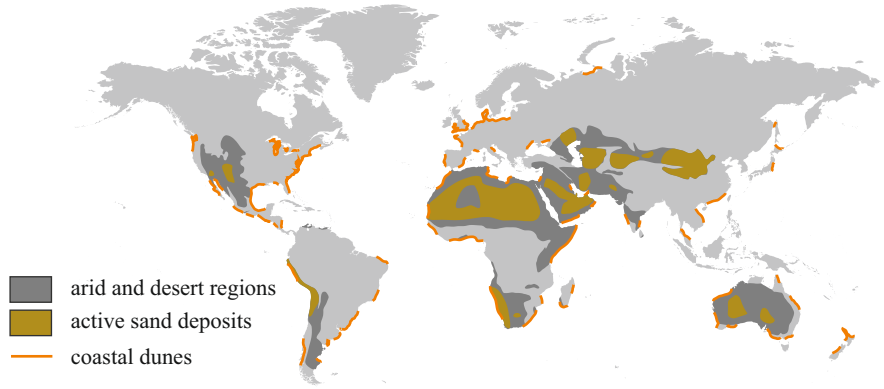

Figure 2.3: Geographical location of the regions potentially susceptible to windblown sand. Coastal dunes redrawn from [186], active sand deposits redrawn from [92].

infrastructure scale [33] (Fig. 2.4g-j). The geographical location of some remarkable documented case of windblown sand attacking built structures is reported in Fig. 2.4(a). Among coastal sites, it is worth mentioning severe windblown sand affecting each year Bayshore district in Waldport, Oregon [273], moving dunes at Silver Lake shore in Michigan [226], the Shoyna village in Russia half buried in sand, windblown sand affecting the North Sea costs in northern Europe [296] (Fig. 2.4b,c). Among desert sites, it is worth mentioning the towns of Nouakchott in Mauritania (Fig. 2.4d), In-Salah in Algeria [28] (Fig. 2.4e), Shiquanhe in Tibet [344], and Dunhuang in China [169], but also archaeological sites, e.g. the Kharga Oasis monuments in Egypt [262], the Meroe Pyramids in Sudan, the Mogao Grottoes in China [169].
Railways crossing deserts or arid environments shall be designed by devoting particular attention to windblown sand environmental action. Their interaction with windblown sand is of particular engineering interest because of both their extension and technical complexity. Indeed, windblown sand translates into several effects given their components in civil works, track superstructure, rolling stock and signalling technologies. New ultra-long transnational railway megaprojects are currently being planned. Fig. 2.4(f) depicts railways currently in service, in construction and future proposed in Middle East and North Africa (MENA) region. In general, sand action on railway infrastructures leads to incremental costs in infrastructure management, e.g. service suspension, loss of capacity and increased maintenance costs [339], but also to destructive failures, such as train derailment [97, 63, 47]. Among other civil infrastructures, windblown sand particularly affects roads and highways [248] (Fig. 2.4e), pipelines and refineries [147] (Fig. 2.4h), industrial facilities [2], and airports [126] (Fig. 2.4i).

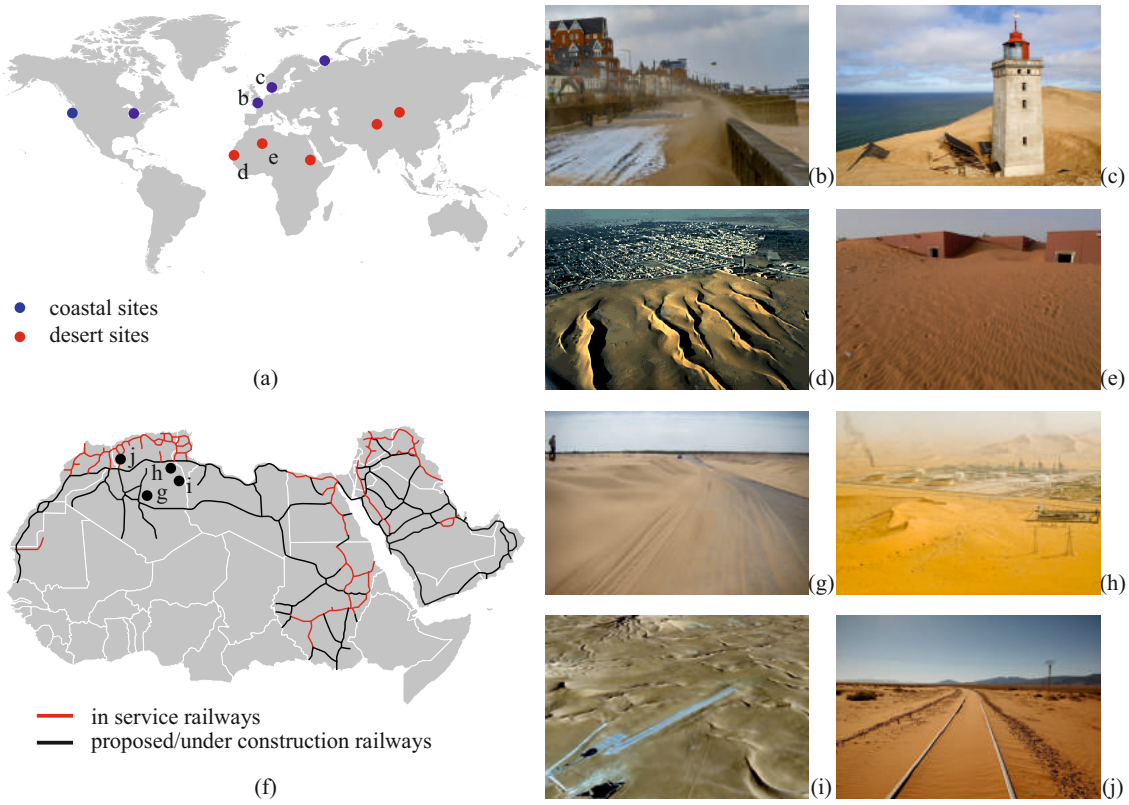

Figure 2.4: Examples of civil structures affected by windblown sand (a): Cleethorpes, UK (b, explicit publishing permission from the owner of the photo: Duncan Young [224]), Rubjerg Knude lighthouse, Denmark (c, explicit publishing permission from the owner of the photo: Andreas Lembke), Nouakchott, capital of Mauritania (d, Landsat 1565-10032-6, 1974), In-Salah, Algeria (e, from Panoramio). Examples of civil infrastructures affected by windblown sand in MENA region (f): road (g, explicit publishing permission from the owner of the photo: Nouar Boulghobra [29]), oil refinery (h, publishing permission under Creative Commons Attribution License from Stefano F, www.flickr.com/photos/stefof), airport runway (i, from Google Earth), railway (j).

The *physics of windblown sand* transport comprehend different modes of motion. They mainly depends on the grains diameter d and include creep ($d > 0.5$ mm), saltation ($0.5 > d > 0.07$ mm) and suspension ($d < 0.07$ mm) [11, 270] (see Fig. 2.5a). Dust particles ($d < 0.07$ mm) are entrained by the wind into the upper part of the atmospheric boundary layer resulting in short-term and long-term suspension [e.g. 236, 109]. Very fine particles ($d < 0.02$ mm) remain suspended for characteristic times of the order of the day and are transported up to thousand of kilometers. Slightly coarser particles ($0.02 < d < 0.07$ mm) remain suspended for

characteristic times of the order of the hour and are transported up to hundreds of kilometers. Sand particles ($0.07 < d < 2$ mm) follows saltation and creep modes of motion. Saltating particles bounce over the sandy surface following a ballistic trajectory. A single particle can hop from several millimeters to several meters with a flight time of the order of $0.1 - 0.2$ s. The saltation layer characteristic height is of the order of $0.1 - 1$ m. Heavy sand particles cannot be lifted by the wind. As a result, they roll on the sandy surface because of both the wind and the impact of other saltating finer particles. Among all of modes of motion, saltation is recognized as the mechanism which mainly contributes to the overall transported sand mass [153]. Indeed, it mainly contributes to the formation and evolution of sand seas and aeolian sand dunes [270].

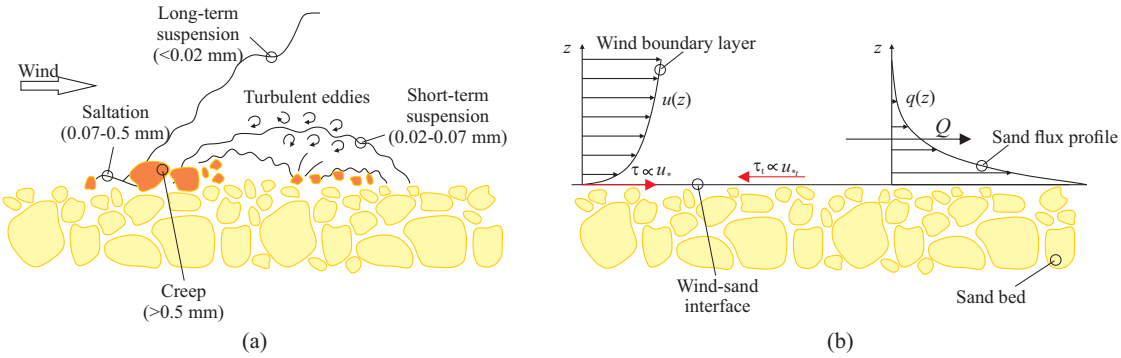

Figure 2.5: Windblown sand transport modes of motion (a, redrawn from [236]), sand transport rate modelling (b).

2.2 Modelling

The first attempt to model windblown sand saltation is dated back to the pioneering work of Bagnold [10] and still holds to date. The windblown sand saltation flux q results from the shear stress τ induced by the wind over the sand bed (see Fig. 2.5b). τ is proportional to the rate of change of a wind velocity $u(z)$ in the vertical direction ($\tau \propto \partial u/\partial z$) and is usually expressed in term of wind shear velocity $u_* = \sqrt{\tau/\rho}$. If the shear stress acting on the sand bed exceeds a certain threshold ($u_* > u_{*t}$), sand grains are entrained into the lower part of atmospheric boundary layer, grain bouncing is triggered and saltation occurs. The resulting sand flux $q(z)$ [kg m^{-2} s^{-1}] is defined by the product of the sand grain velocity $v(z)$ and the sand concentration $\varphi(z)$, whose distribution follows a decreasing exponential function in vertical direction [350].
In the following, the fundamental quantities to model windblown sand transport are reviewed.

2.2.1 Threshold shear velocity

The threshold shear velocity u_{*t} is usually defined as the minimum value of the wind shear stress above which saltation occurs. Since the seminal studies of Bagnold [11], two threshold shear velocities have been recognized: the fluid or static threshold, defined as the minimum wind speed for initiation of sediment transport without antecedent transport, and the dynamic or impact threshold, i.e. the minimum wind speed for sustaining sediment transport with the presence of transport. Most studies proposing transport laws in steady saturated flow refer to the impact threshold [153]. Hence, fundamental studies [e.g. 5, 225, 151] recently proposed models of the impact threshold in light of a few number of experimental measures, e.g. [12, 51, 246, 162]. However, the impact threshold shear velocity is approximated for application purposes as equal about 80% of the fluid threshold one [e.g. 12, 237, 351, 153]. From here on out, we address to the fluid threshold shear velocity as "threshold shear velocity" u_{*t} for the sake of compactness.

Systematic *experimental measurements* of u_{*t} versus the grain diameter were carried out by [12], [51], [354], [90], [136] amongst others. These measurements constitute the consolidated literature data base. They are reported in Fig. 2.6(a) versus the equivalent particle diameter $d_{eq} = d\rho_p/\rho_s$ [53, 153], where ρ_s is the density of the quartz sand, in order to account for the effect of different densities ρ_p. A significant scatter among data can be observed notably at low values of the particle diameter. However, two general trends can be observed, divided by a local minimum at about 75-100μm [153].

A number of *deterministic models* of the threshold shear velocity have been proposed in literature so far. They can be categorized in two classes with respect to both modelling scale and goal. *Microscopic models* discuss the equilibrium of the moments of the forces acting on the single particle resting on a bed of other particles [270]. They aim at pointing out the physical phenomena underlying each force and at modelling it. In a general framework, entraining aerodynamic forces (drag and lift ones) induce saltation, while stabilizing forces (gravitational and the interparticle ones) counteract them [110, 271]. On one hand, the effective gravitational force including buoyancy, and the drag force correspond to well known phenomena and their modelling is widely accepted, see e.g. [110] and the cited reviews. On the other hand, the same does not hold for the other forces: the resultant lift force results form the Saffman one [260] and the lift induced by vortical structures; the overall interparticle force results from several kinds of forces, including van der Waals forces, water adsorption forces and electrostatic forces. Although interparticle forces are expected to scale with the soil particle size [e.g. 271], their modelling for aspherical and rough sand and dust remains poorly understood [153]. In particular, such forces depend upon a number of parameters such as surface cleanliness, surface roughness at micro/nano meter scale, air and grain humidity, mineralogy and surface contaminants affecting hydrophilicity [202]. Semi-empirical

macroscopic models aim at approximating the threshold shear velocity trend versus the particle diameter. Some of them are compared to the experimental data in Fig. 2.6(a). Because of the above modelling difficulties, they do not analytically include the contribution of lift and interparticle forces while they explicitly retain the gravitational and drag ones. Any other contribution is accounted for in a semi empirical approach by introducing one or more free parameter(s), and the value of the latter obtained by fitting experimental data. The pioneering model by Bagnold [11] involves a single dimensionless constant A_B, resulting independent from the grain diameter or, in other terms, from Reynolds number. Then, it gives rise to a monotonic increasing trend of $u_{*t}(d)$. The model by Iversen & White [135] defines the same parameter $A(\mathrm{Re}_{*t})$ as a piece-wise empirical function of the friction Reynolds number Re_{*t} to mimic the effects of lift and interparticle forces: the resulting $u_{*t}(d)$ law is no longer monotonic and qualitatively reflect the trend of the experimental data. The model by Shao & Lu [271] is more compact than the previous one. It neglects the Re_{*t} dependency, and at the same time generalizes the Bagnold one by introducing a novel correction term to account for the interparticle forces. A second dimensional constant free parameter γ [N/m] is included in the correction term. More recently, McKenna Neumann [192] has considered the effect of soil moisture on the interparticle cohesive force by defining $\gamma(\Delta P, d)$ as a function of the capillary-suction pressure deficit and of the grain diameter. Other laws of u_{*t} have been proposed for natural surfaces: they account for the effects of soil texture, soil moisture, salt concentration, surface crust, vegetation and/or pebbles on the surface. Interested readers can refer to [270, 317]. The analytical structure of the most common semi-empirical macroscopic models is summarized in Table 2.1 where ρ_a is the air density and g is the gravity acceleration.

Table 2.1: Most common semi-empirical macroscopic deterministic models for threshold shear velocity.

Reference	u_{*t}	A	γ
Bagnold (1941) [11]	$A\sqrt{\frac{\rho_p-\rho_a}{\rho_a}gd}$	0.100	-
Iversen & White (1982) [135]	$A\sqrt{\frac{\rho_p-\rho_a}{\rho_a}gd}$	$Cf(Re_{*t})g(d)$	-
Shao & Lu (2000) [271]	$A\sqrt{\frac{\rho_p-\rho_a}{\rho_a}gd+\frac{\gamma}{\rho_a d}}$	0.111	2.9×10^{-4}
McKenna Neumann (2003) [192]	$A\sqrt{\frac{\rho_p-\rho_a}{\rho_a}gd+\frac{\gamma}{\rho_a d}}$	$Cf(Re_{*t})$	$f(\Delta P, d)$

Although the deterministic approach largely prevails in aeolian literature, the view that the threshold velocity should be regarded as a statistical phenomenon may be dated back to the pioneering studies by Chepil [51]. The *probabilistic modelling approach* is motivated by the scatter of the experimental data at low values

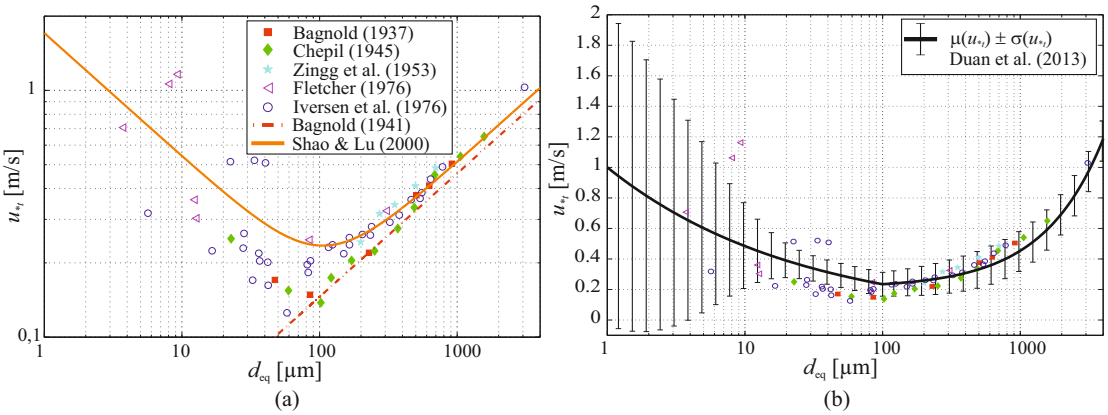

Figure 2.6: Threshold shear velocity: experimental data (symbols) compared with semi-empirical deterministic models (a, redrawn after [153]) and the probabilistic model by [75] (b).

of d even for a common nominal setup condition (Fig. 2.6a), and by the difficulties experienced by the deterministic approach, i.e. the challenge of parametrizing threshold variability and relating this variability to its different sources.
The randomness of *bed grain geometry* and of the *turbulent wind flow* have been early recognized as sources of threshold variability in the experimental studies of Niclkling [214] and Williams [323, 322], respectively. In particular, the wind tunnel tests by [214] first showed that measured fluid and impact thresholds could not be reproduced, presumably because it is impossible to replicate grain positioning between each test. In fact, most sediment is composed of a range of grain sizes and shapes. Thus, for a given surface, variability is expected due to the positioning of sediment grains. Since the positioning of grains affects their susceptibility to entrainment, the fluid or impact threshold for a given surface is not easily described by a single value [215]. Values of u_{*t} were found to span an unexpectedly wide range for each grain fraction during the wind tunnel tests by [323, 322]. Such a variability was conjectured to be due to the effects of turbulent flow regimes changing in space and time. They obtained approximations of the probability density function for u_{*t} required for future stochastic treatment of the threshold condition. More recently, both the randomness of bed grain geometry and of the turbulent wind flow have been included in the probabilistic models proposed by Wu [327], and Zhen-shan [349]. Conceptually, both studies agree that the initial movement of sand grains should be regarded as a random phenomenon and probabilistic models of entrainment could provide better understanding of it. Technically, both probabilistic models are microscopic ones, limited to ideal spherical particles, and do not consider random interparticle forces. However, the studies differ in their results and conclusions: [349] propose a probabilistic reading of the conventional threshold

friction velocity, while [327] separately derive the probability of entrainment in the rolling and lifting mode, and call into question the consistency embedded in the conventional definition of the critical shear stress for incipient motion, following the remarks by other authors (see the review by [191]).
The randomness of the *interparticle forces* and their effects of the threshold variability have been first recognized by Zimon [353]. He suggested to treat cohesive forces acting upon dust particles as random variables (r.v.s). He argued from experimental data that their probability distribution can be approximated by a lognormal one. Following Zimon's findings, Shao [270] has recently assumed that also the threshold shear velocity of dust particles is a log-normally distributed r.v. It is worth pointing out that such an assumption looks questionable from an analytical point of view even by assuming that the cohesive force is the sole random variable among the grain acting forces. In fact, u_{*t} does not result from a simple rescaling of the cohesive force. The smaller the grain size, the bigger the role of the interparticle forces, the higher the expected effect of the their uncertainties on the threshold shear velocity. Having this qualitative dependency in mind, Shao [270] conjectured that the obtained results do not hold for sand-sized particles, for which threshold shear velocity can be still defined as a deterministic quantity. It is worth pointing out that the discontinuous switch from a probabilistic model for dust to a deterministic one for sand seems questionable having in mind that the diameter is a continuous quantity and the relative effects of interparticle forces are expected to be continuously decreasing with it.
Even more recently, the effects of the random nature of the *soil surface microstructure* and of the *irregular shape of the particles* have been included in a probabilistic model for threshold shear velocity by Duan [75]. The proposed microscopic model describes the moments induced by gravitational, electrostatic, cohesion, and drag forces as functions of four microscopic r.v.s. The threshold shear velocity is then expressed as a function of these random quantities, some of them independent, some dependent. Its probability density function is then evaluated through a statistical estimation of the distributions of the predictors. Subsequently, the mean value and standard deviation of the threshold shear velocity are fitted as functions of d. The obtained results (Fig. 2.6b) are not not entirely convincing. First, the standard deviation $\sigma(u_{*t})$ is monotonically increasing for $d \geq 100$ μm and asymptotically tends to 0.132, while the scatter of experimental data clearly decreases for increasing d. Second, the mean $\mu(u_{*t})$ is a linear function of d for $d > 100$ μm, while its deterministic counterpart, i.e. the nominal values obtained by semi-empirical macroscopic models, is not. In our opinion, such critical features can be ascribed to both modelling and technical difficulties. Among the former ones, the challenging task in writing a microscopic model inclusive of all the r.v.s affecting the sand grain acting forces. Among the latter ones, the difficulties in obtaining probability distribution for each microscopic r.v. from measurements and in handling mutually dependent r.v.s.

2.2.2 Sand transport rate

The sand transport rate Q [kg m−1 s^{-1}] is a bulk metrics derived from q by its integration in the vertical direction, i.e. $Q = \int_0^\infty q(z)dz$. Since this physical quantity represents a straightforward measure to estimate wind erosion, sand transport, and deposition, a number of semi-empirical models to predict sand transport rate (Q-models) have been formulated [e.g. 144, 221, 161, 153].

Dong [71] classified sand transport models into four categories defined by their basic form. *Bagnold type* equations [e.g. 11, 354] relate sand transport rate to the cube of shear velocity u_*^3 but do not explicitly consider the excess of shear velocity compared to a threshold value u_{*t}. This results in unrealistic sand transport rates when u_* is less than u_{*t}. *Modified Bagnold type* equations [e.g. 144, 221, 161, 153] relate sand transport rate to the cube of an effective shear velocity that is defined as a function of both the shear velocity and the threshold value. *O'Brien-Rindlaub type* and *modified O'Brien-Rindlaub type* equations [e.g. 218, 71] relate transport rate to wind speed instead of shear velocity. These first three categories usually take into account the particle size directly through the sand grain diameter, d. The remaining models may be categorized as *complex*. These include physical models that account for additional phenomena in the saltation process such as inertial effects [189] or hysteresis [152]. These models include multiple empirical fitting parameters usually related to quantities other than simply sand grain diameter.

Because of their ease of use and their sound physical basis, *modified Bagnold type* models are widespread in the literature and popularly employed in the practice, see for example the field studies by [94], [9], [15], [272], [274], [338] and [171]. The most common models are summarized in Table 2.2 and plotted in Fig. 2.7. However, *modified Bagnold type* models lead to significant variability in their prediction, despite belonging to the same conceptual form [see e.g. 264, 275, 274, 272]. These discrepancies follow from differences in the structure of models and can be related to the way the grain diameter, the shear velocity and the threshold shear velocity are treated in the model. Indeed, the effect of d on Q remains an open issue and needs further investigation [71, 305]. For example, whilst some models explicitly account for changes in d [e.g. 161], others do not [e.g. 144], and still others account for the effect of d by introducing other related variables, such as the particle terminal velocity in the model of [221]. Furthermore, the dependence of Q from u_* and u_{*t} remains unclear [see e.g. 185].

2.2.3 Drift Potential

The amount of incoming windblown sand is defined as the mass per unit time and per unit length, and usually called *incoming sand drift*. The sand drift depends on both the wind velocity and the sand characteristics. The modelling framework to sand drift evaluation has been first introduced by Fryberger & Dean [94]. Their

Table 2.2: Most common sand transport rate models

Reference	Q	C
Bagnold (1936) [10]	$C\sqrt{\frac{d}{d_r}}\frac{\rho_a}{g}u_*^3$	$1.5 \div 2.8$
Kawamura (1951) [144]	$C\frac{\rho_a}{g}u_*^3\left(1-\frac{u_{*t}^2}{u_*^2}\right)\left(1+\frac{u_{*t}}{u_*}\right)$	2.78
Owen (1964) [221]	$C\frac{\rho_a}{g}u_*^3\left(1-\frac{u_{*t}^2}{u_*^2}\right)$	$0.25+\frac{v_t}{3u_*}$
Lettau & Lettau (1978) [161]	$C\sqrt{\frac{d}{d_r}}\frac{\rho_a}{g}u_*^3\left(1-\frac{u_{*t}}{u_*}\right)$	6.7
Kok et al. (2012) [153]	$C\frac{\rho_a}{g}u_{*t}u_*^2\left(1-\frac{u_{*t}^2}{u_*^2}\right)$	5

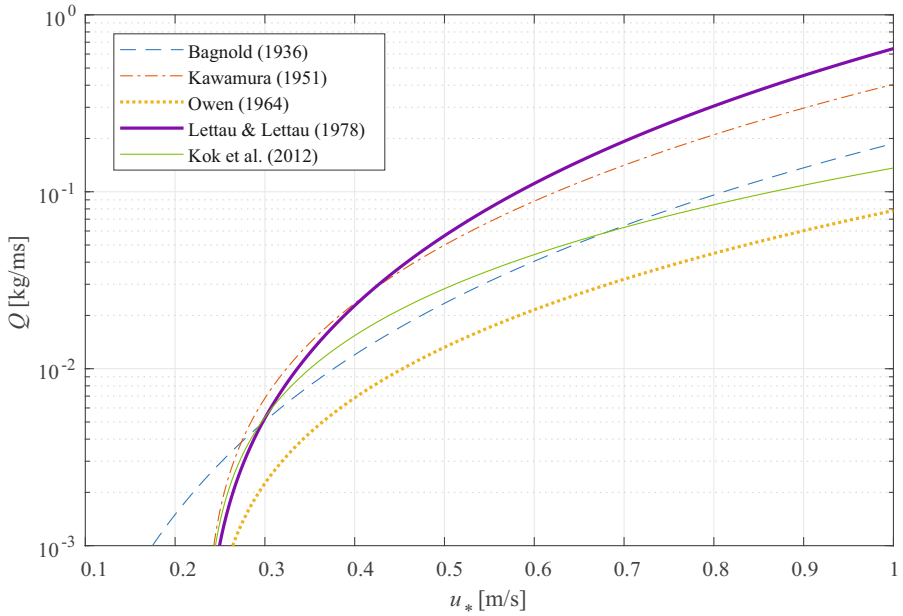

Figure 2.7: Sand transport rate models comparison.

seminal work still grounds the current scientific and technical literature in several application fields, such as highway engineering [72], railway engineering [346, 47, 330], fundamental research [e.g. 9, 15], geomorphology [e.g. 306, 27, 148, 337], paleo sedimentology [e.g. 338], climatology [e.g. 27], coastal management [e.g. 255]. In the framework of Fryberger & Dean, the so-called Drift Potential (DP) is defined for each wind direction, while the Resultant Drift Potential (RDP) and the Resultant Drift Direction (RDD) stand for the magnitude and direction of the vector sum of DP over the directions, respectively. These quantities are called "potential" because they provide a measure of sand-moving capacity of the wind blowing over

an ideal sand bed, neglecting the local covering of the ground surface [237]. Fryberger & Dean obtain DP per reference time (usually 1 year) by cumulating the sand transport rate Q over the wind speed recording time, and rescaling it on the reference time. For a given wind direction, DP is expressed as:

$$DP = \frac{T}{\Delta t}\frac{1}{n}\sum_{i=1}^{n} Q_{i,\Delta t}\ \Delta t, \tag{2.1}$$

where, n is the number of $Q_{i,\Delta t}$ instances taken into account used to average the value of DP over an arbitrary time period ($T_r = n\Delta t$). $Q_{i,\Delta t}$ is the i-th value of sand transport rate, evaluated by means of one of the Q semi-empirical models over the wind sampling time Δt (e.g. 10 min), and a $T/\Delta t$ is a factor used to normalize DP to a time scale of an arbitrary reference time. DP [kg m^{-1} T^{-1}] defined in such a way is giving an averaged amount of sand mass accumulated over the unit length of cross-wind direction and over the reference time T. $T = 1$ year is usually adopted in the field of sand mitigation. DP and RDP are graphically represented by a so-called sand rose, as shown in Fig. 2.8. Each arm of the sand rose represents DP from a given direction towards the center circle. The sand drift directional variability can be expressed by the ratio $|RDP| \,/\, \sum |DP|$. The lower the ratio, the higher the directional variability. In particular $|RDP| \,/\, \sum |DP|$ close to 1 identify unimodal winds while lower ratios identifies bimodal and complex regimes.

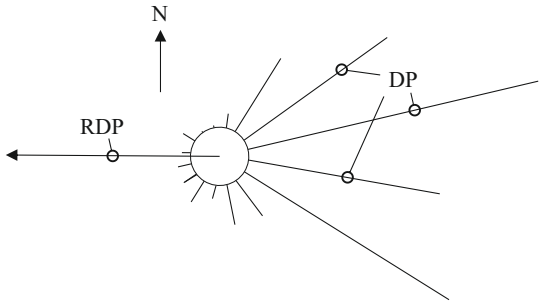

Figure 2.8: Sand rose of Drift Potentials and Resultant Drift Potential (redrawn from [94]).

2.2.4 Windblown sand around obstacles

Topographic obstacles such as natural obstacles, e.g. clumps of vegetation, boulders, hills, and built obstacles, i.e. structures and infrastructures, give rise to zones of acceleration and deceleration of the wind flow and zones of increased turbulence [237]. In turn, they induce sand erosion and/or accumulation around them depending on whether $u_* > u_{*t}$ or $u_* \leq u_{*t}$, respectively. Such zones are initially

under non-equilibrium conditions, i.e. sand erosion and/or accumulation progressively increase. Once equilibrium conditions are reached, the sand surface does not evolve anymore and the accumulated and/or eroded sand remain fixed. Fig. 2.9

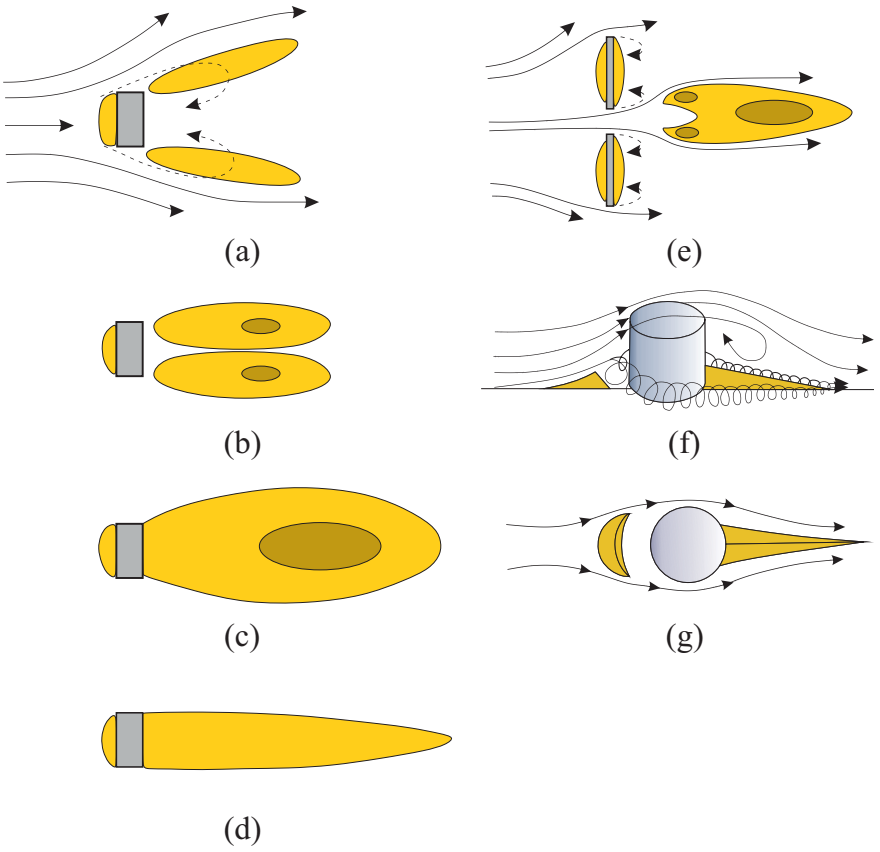

Figure 2.9: Windblown sand sedimentation around an obstacle (a-d, redrawn from [181]), around a gap (e, redrawn from [180]), around a wall mounted cylinder (f,g, redrawn from [237]).

shows some early schematic examples from the literature of sand erosion/deposition pattern around some simplified obstacle. In particular, Fig. 2.9(a-d) shows successive time-steps of the sand morphodynamics in the wake of an isolated obstacle, Fig. 2.9(e) shows the sand pattern downwind a gap between two obstacles, and Fig. 2.9(f,g) schematically shows the three-dimensional wind flow and sand accumulation around a wall mounted cylinder, symbolizing a generic pointwise obstacle.

The prediction of windblown sand erosion and deposition around any kind of obstacle cannot be achieved in analytical terms because of the multiple simultaneous physical phenomena involved. As a result, physical or computational testing

are required in order to study both the wind flow and sand morphodynamics simultaneously. Full-scale tests have mainly been performed around natural obstacles (e.g. [121, 309]). Beside in-situ tests, the published literature include a number of wind tunnel tests with drifting sand on natural obstacles (e.g. [74, 196, 194, 329, 188]), and artificial obstacles (e.g. [348, 181, 163, 179, 314]). Computational simulations mainly split into cellular automaton models and Computational Fluid Dynamics (CDF) simulations coupled with sediment transport models. The former are simpler and computationally less expensive. In general, they do not model neither the sand flux nor the wind profile, even if recently an effort has been made in order to include them [e.g. 345]. The latter shall solve the full governing equation of the multiphase wind+sand flow, i.e. couple the Navier-Stokes equations for the turbulent wind with proper models for the windblown sand processes [e.g. 235], in order to correctly simulate both aerodynamics and morphodynamics around any obstacle. However, each approach implies specific issues:

- *in-situ full scale tests* are subject to uncontrolled environmental setup conditions [174] and to very long term measurement times;
- *wind tunnel tests* are often subject to:
  - aerodynamic scaling effects and similarity issues [320]. The aerodynamic scaling issues are particularly critical for porous obstacles [170]. In the aeolian and geomorphology literature, free flow blockage, end-tip aerodynamic effects and model aspect ratio are often incorrectly neglected. For example, [328] tested an embankment of cross-section equal to 0.19 m^2 into a wind tunnel test section of 1.44 m^2. It results in a blockage ratio equal to 13%. Furthermore, the average aspect ratio S/L, i.e span S over chord L, is about 1.33. Similarly, [310] tested a transverse dune of aspect ratio $S/L = 1.28$. Such values of the aspect ratio significantly affect the wind flow in the wake of the dune due to the edge effect caused by the interaction between the boundary layers surrounding the dune surface and the side walls of the wind tunnel, as proved by [31].
  - sand scaling effects. Zhang et al. [348] tested a 3 cm high fence with circular holes of 1.4 mm uniformly distributed over the surface, i.e. a geometrical scaling of about 1:100. However, the diameter of the tested sand is still in full scale and equal to $d = 0.2 \div 0.3$ mm. This affects of course the sand morphodynamics around the obstacle. It is worth highlighting that the scaling of the grains would imply the adoption of dust instead of sand, and therefore the rising of strong interparticle forces that would inevitably affect the sand morphodynamics.
- *computational simulations* are still at their infancy in this specific domain [281], and modelling and numerical issues must be handled with caution.

Indeed, the erosion/sedimentation processes modify the surface of the computational domain demanding the adoption of an adaptive mesh. This further increases the computational cost.

2.3 Windblown Sand Mitigation Measures

Effective, durable, robust and sustainable *design solutions* are mandatory in order to mitigate windblown sand effects. Given the particular sensitivity of railways to windblown sand induced effects, design solution have been mostly developed in the railway infrastructure domain. As a result, in the following we focus on design solutions for railways. Nevertheless, some of the reviewed solutions can be easily transposed to the domain of civil structures. Design solutions adopted along railways are commonly named Sand Mitigation Measures (SMMs). In the reviewed literature, there is a number of SMMs proposed in the past, notably in the last decade. Their rationale collection is needed in order to orient railway owners, designers, general contractors and railway operators among the available technical solutions.

2.3.1 Historical review of desert railways

Past railways across deserts

Historically, the first railways along deserts have been built by colonial countries. The British military railway was built at the end of the 19th century (1897-1899) from Wadi Halfa to Abu Hamed over the Nubian desert (Sudan [324, 325]). The French railway form Mecheria to Ain Sefra in Algeria was opened in 1887 [18] across the norther part of the Kenadsa desert, and then extended to Beni Ounif in 1903, and to Colomb-Bechar in 1906 [325], in the framework of the never finished Trans-Saharan Railway project (1870-1941, [119]). The best example of a German railway is the line from Aus to Lüderitz (1906) over the Namib desert (Namibia, [68]). The Hejaz Railway was built from Damascus to Medina, through the arid Hejaz region of Saudi Arabia and was a part of the Ottoman railway network built from 1900 to 1908 with German advice and support [213]. At the present time, most of the mentioned lines are partially or totally decommissioned, and their remains buried by accumulated windblown sand or encroaching dunes. An example of the Grasplatz railway station along the Aus to Lüderitz railway before and after the sand hazardous effect can be seen in Fig. 2.10.

From the reviewed literature, the first SMMs for railways have been empirically tested along the Kundian-Mianwali section of the Sher Shah-Attock line in the arid Punjab province of Pakistan (probably built in 1891, surely in service in 1910, [245]). The 550 km long Dammam-Riyadh line is the first pioneering modern railway whose design systematically addressed the windblown sand challenges

(a) (b)

Figure 2.10: Grasplatz railway station along the Aus to Lüderitz railway before (a) and after (b) sand dune encroaching (permission to reuse under a Creative Commons Attribution License; owner of the photo: [68]).

(Kingdom of Saudi Arabia, 1947-1950, today in service). The team of American designers guided by J.H. Gildea tackled the problem of *"Combating the engineering obstacles of locating track on sands that drift constantly like snow. It was, in fact, this similarity to snow that provided an important key to solving the difficulty. As strong prevailing north-west winds, known in Arabia as chamals, kept the sand in continual movement, engineers employed plows and spreader, previously successful in snow operations, to level and clear the wavelike dunes. Fences, comparable to snow fences, were erected along the right of way. Heavy coatings of crude oil were applied and the heavy crust thus created not only held the sand firm beneath it but provided a surface over which the blowing sand would not hold"* [120]. It is worth pointing out that engineers were applying technology known from the snow mitigation, even though sand and snow have dramatically different physical properties and the first influential book on the physics of windblown sand had been published 10 years before [11]. In other words, at early stages of the development, sand mitigation measures were suffering the scarce transfer of knowledge from base and specialist research fields (e.g. Aeolian Geomorphology, Fluid and Porous Mechanics, Wind Engineering) to the Civil and Transportation Engineering design practice.

In 1956, 40 km of the Batou-Lanzhou railway was constructed in the south of the Tengger Desert, China [207]. The railway was massively buried by mobile dunes since its construction. In the following years, a procedure for establishing an artificial ecosystem on mobile dunes was started by application of straw checkerboards over the mobile sand source [173]. This technique has been widely used in China along a number of railway lines (for the full list of the railway lines, interested readers are referred to [239]). All the mentioned historical lines can be seen in Fig. 2.11.

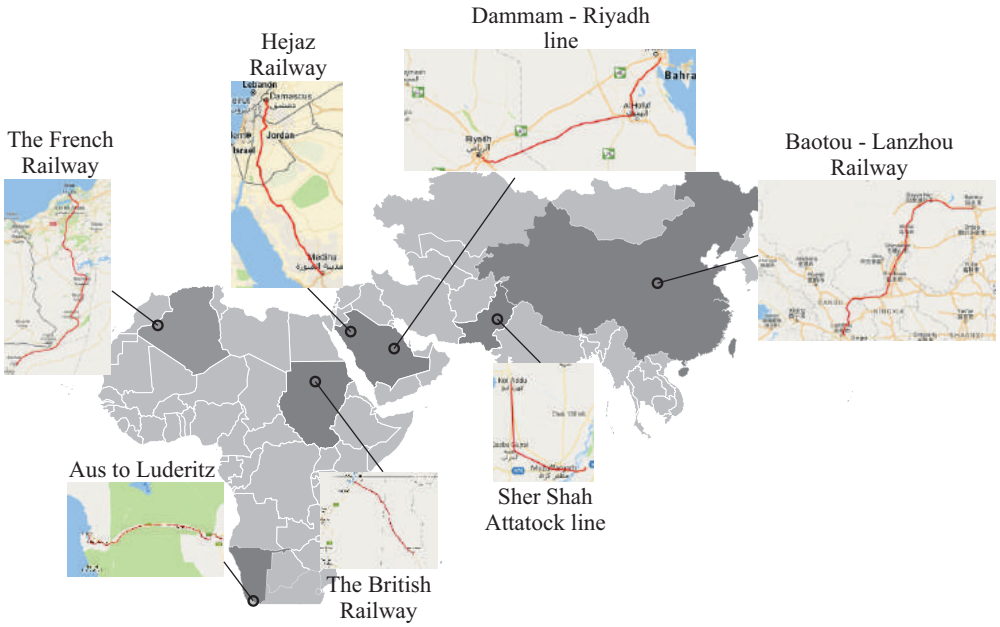

Figure 2.11: Historical railways in the desert.

Present railways across deserts

At the present time, most of the in-service railway lines crossing deserts and arid regions are located in north-western China with a total length of about 10.000 km [165, 166, 46]. For example, the Lanzhou-Xinjiang line across the Gobi desert (1904 km, completed in 1990, [47]), the Xining-Lhasa line along the Tibet plateau (1956 km, completed in 2006), the Linhai-Ceke line across the Ulanbuhe, Yamaleike, and the Badain Jaran Deserts (707 km, completed in 2009). Despite the tremendous effort of the Chinese scientific community in the past 15 years, China has the greatest windblown sand disaster distribution along its railway network [47]. The Linhai-Ceke line seems to be one of the most vulnerable ones: in the first year of operation, over 10.000 workers were mobilized and CNY 71 million was spent on windblown sand-induced maintenance; service was suspended for two months in the spring of 2010; in the first 36 days after passenger service was introduced in November 2010, sand storms buried the track for 27 days and caused 51 service disruptions. Sand storms have reduced effective speed on eight sections of track between Suhongtu to Swan Lake to 25 km/h [208].

A report of sand hazards from India was given in a detailed survey of railways in the desert and semi desert areas of Rajasthan by [211]. An overall length of about 1250 km is prone to windblown sand in the Jodhpur and Bikaner Divisions of the NW Railway. The survey includes the list of windblown sand induced accidents per year (1 to 2 derailments, 3 to 7 days of service disruptions) and manpower lost

on sand removal activities (about 1480 man-day per year).

Apart from Far East, most of the in-service desert railways are located in the Middle East - North Africa (MENA) region. The cited Dammam-Riyadh line in KSA has recently suffered a service suspension due to a windblown sand-induced train derailment [97]. The precise mapping of the in-service railway lines along sandy areas is available for the Iranian railway Network: an overall length of 416 km [342] is exposed to windblown sand, with severe operational difficulties in the Bafgh-Mashhad line along the Lout desert. At the present time, two other main lines are in the testing and commissioning stage in the Arabic peninsula. The North-South Railway is a 2400 km long railway project in Kingdom of Saudi Arabia (KSA) [1]. The so-called phase 1 of the Etihad Rail network is a 266 km long line from Shah and Habshan to Ruwais in the United Arab Emirates. In the same time, the 450 km long Haramain High Speed railway between Medina and Mecca is under construction. Despite the ad-hoc dedicated studies during the design phase [231], the construction advancement is suffering significant delays, also due to the windblown sand accumulation along the line under construction and the retrofitting of the designed SMM [e.g. 140, 107].
On the other side, some desert trains in Africa are converted into touristic attractions thanks to windblown sand (e.g. the Oriental Desert Express in Oujda-Bouarfa, Morocco or the Desert Express in Windhoek-Swakopmund, Namibia).

Future railways across deserts

In the short and mid term, the railway lines in desert and arid regions are expected to rapidly grow, particularly in the MENA region. The Arab Countries are conceiving, evaluating and building a large railway network at different scales. The Arab Network Railway (ANR, preliminary study by the consortium Italferr-Dar El Omran, 2009-2012) is a 30.000 km long, high-speed/high-capacity railway network conceived to connect all the Arab League Countries across Middle East and North Africa. It is worth pointing out that the length of such a single project is more than twice the overall European high-speed railway network currently in operation and under construction. The Gulf Railway (GR) is a 2.217 km long project proposed to connect six Arab Gulf Co-operation Council (GCC) member states. In this framework, national railway networks are currently under design and/or construction, e.g. the Oman, UAE and KSA ones. The corresponding investments are significant. For instance, the Middle East Countries have allocated about USD 260 billion to build 40.000 km of railway tracks up to 2030 [198]. The map of the mentioned railways currently in service, in construction and future proposed is shown in Fig. 2.12.

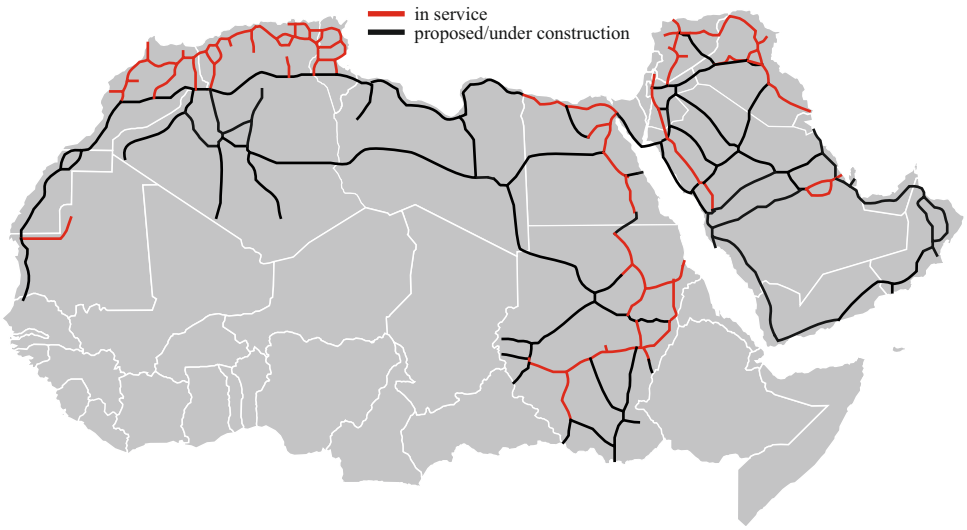

Figure 2.12: Map of currently in service, under construction, and proposed railways in MENA region. Data collected and map drawn by the authors [33]

2.3.2 SMM categorization criteria in the literature

Historically, the first SMMs categorization attempt has been made by Rahim [245]. In his pioneering survey, Rahim proposes an early categorization of "*methods adopted from time to time to deal with the evil* [windblown sand Ed.]". Rahim's classification is driven by two ordering criteria: space-extent and time-length. The first criterion allows distinguishing between: i. country-wide measures (i.e. "*to eradicate the evil from the country as a whole by a coordinated effort between various department like Forest, Irrigation, Road and Railways*"); and ii. narrow-strip measures (i.e. "*arresting the onslaught of the sand dunes on to the railway track [...] in the narrow strip of the land belonging to the railway*"). The first group, also called "*reclamation of the sand drifts*" analogous to "*solutions against desertification*" in the current language, is no further articulated by Rahim. Conversely, the time-length criterion is further applied to the narrow-strip SMMs, so that permanent, semi-permanent and temporary SMMs are sorted by decreasing initial cost and increasing maintenance frequency and related costs. The Rahim's time-length categorization has been somewhat recently revised by [339], who refers to short-term and long-term approaches to the windblown sand challenges. A different kind of categorization is objective-based. Kerr & Nigra [146, 147] firstly applied this approach to SMMs adopted for oil-field operations, and selected four objectives: i. Destruction or stabilization of sand dunes; ii. Diversion of wind-blown sand; iii. Direct and permanent stoppage or impounding of sand before the object to be protected; iv. Rendition of deliberate aid to sand movement so as to avoid

deposition over the object. Analogously, Watson [316] adopted four other objectives: i. Enhancement of the deposition of entrained sand; ii. Enhancement of the transportation of sand; iii. Reduction of the sand supply; iv. Deflection of the moving sand. Cheng and Xue [46] have recently proposed an objective-driven classification with reference to the SMMs employed along the Qinghai-Tibet railway: i. Sand-resistance engineering measure; ii. Sand-stabilization engineering measure; iii. Sand-guidance engineering measure. Finally, it is worth citing the somewhat hybrid categorization proposed by Stipho [285], resulting in three categories: i. Protection management; ii. Stabilization management; iii. Land management.

In our opinion, each criterion has its pros and cons. The space-extent and time-length based categorizations are technically sound, because they lie in the design dimensions, but they fail in guaranteeing the categorization uniqueness: a single kind of SMM (e.g. straw checkerboard) can belong to both country-wide measures and narrow-strip ones, while the time-length of a SMM (e.g. a sand trapping ditch) strongly depends on its capacity (e.g. its size). The objective-based categorization are directly informative once the design goals are fixed, but once more, it does not guarantee the categorization uniqueness: the same SMM (e.g. a porous fence) can be adopted to reach multiple objectives [e.g. enhancement of the deposition of entrained sand, reduction of the sand supply, deflection of the moving sand in 316]. Furthermore, such a categorization is not directly defining the SMM spatial location.

2.3.3 SMM categorization: a new proposal

In the following, we propose a new categorization of the SMMs for railways with the goal of partially contributing in overcoming the previously mentioned shortcomings. The categorization criterion follows the SMM location with respect to the sand course. An innovative Source-Path-Receiver (SPR) scheme results (see Fig. 2.13):

1. *Source* SMMs are directly located over the sand source (dunes or loose sand sheets), whatever the spacing between the sand source and the infrastructure is. They are almost independent from the type of infrastructure.

2. *Path* SMMs are located along the windblown sand path ranging from the sand source to the infrastructure. They depend on the overall geometry of the infrastructure, e.g. point-wise or line-like infrastructure components.

3. *Receiver* SMMs are directly located on the infrastructure (e.g. the railroad or its shoulder). As a result, they strongly depend on the type of the infrastructure.

SPR categorization can be complemented by the recognized SMM working principles from the reviewed literature: i. Sand-modifying, where the mitigation is

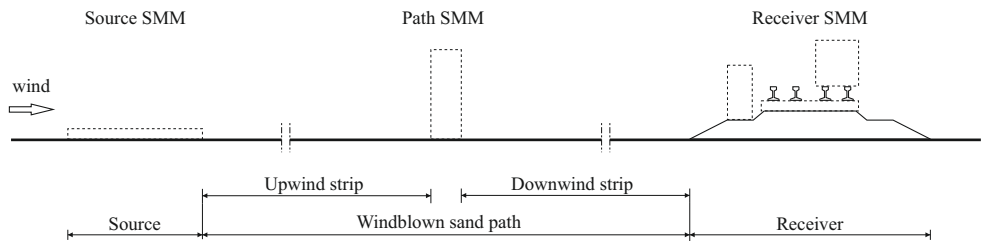

Figure 2.13: Conceptual scheme of the Source, Path and Receiver SMM classification.

achieved by modifying the properties of sand; ii. Aerodynamic, where the mitigation is carried out by changing the local wind flow; iii. Sand-resistant, where the mitigation is achieved by improving the material properties of the infrastructure component to be protected. Such major differences in the working principles results from the multidisciplinarity in windblown sand mitigation. In this overview, the focus is put on the aerodynamic-based SMMs.

It is worth pointing out that SPR categorization is consistent with a complementary criterion based on the windblown sand moving processes. The windblown sand movement is described by the three main processes: Erosion, Transport, and Sedimentation [ETS, e.g. 235]. Sand-modifying and Aerodynamic SMMs aim at controlling, promoting and/or preventing such processes. Table 2.3 shows the correlation between SPR classification and ETS processes.

Table 2.3: Correlation between types of mitigation measure and sand moving processes.

	1. Source	2. Path	3. Receiver
Erosion	Prevented		Promoted
Transport		Controlled	Controlled
Sedimentation		Promoted	

The working principle of source SMMs is mainly based on preventing sand source Erosion. Path SMMs aim at controlling sand Transport by driving the wind flow and/or at promoting sand Sedimentation around them along the windblown sand path. Receiver SMMs are applied to control the Transport of windblown sand by deflecting it from the infrastructure, and/or by promoting the Erosion of the sedimented sand.

Source and Path SMMs are mainly addressed to mitigate massive sand erosion and transport upwind the infrastructure. However, even if such SMMs exhibit high

sand trapping performance, it is not likely that they completely trap the whole incoming windblown sand. Receiver SMMs definitely cope with sand crossing Source and Path SMMs. Aerodynamic receiver SMMs are addressed to avoid the local sedimentation on the railway body of small amount of of sand filtered by Source and Path SMMs. Sand-resistant receiver SMMs are ad-hoc modified track superstructure components characterized by increased sand resistance, i.e. increased lifetime.

Bearing in mind the above, the proposed classification also offers a new rationale to the combined use of complementary SMMs, as recently proposed by other authors [e.g. in 46, 331, 48, 49]. It is, however, worth to be stressed that the proposed SPR categorization does not necessarily cover any potential sand mitigation strategy that can be imagined. Fig. 2.14 shows the synoptic scheme of the proposed categorization, and anticipates the sub-categories reviewed in the following.

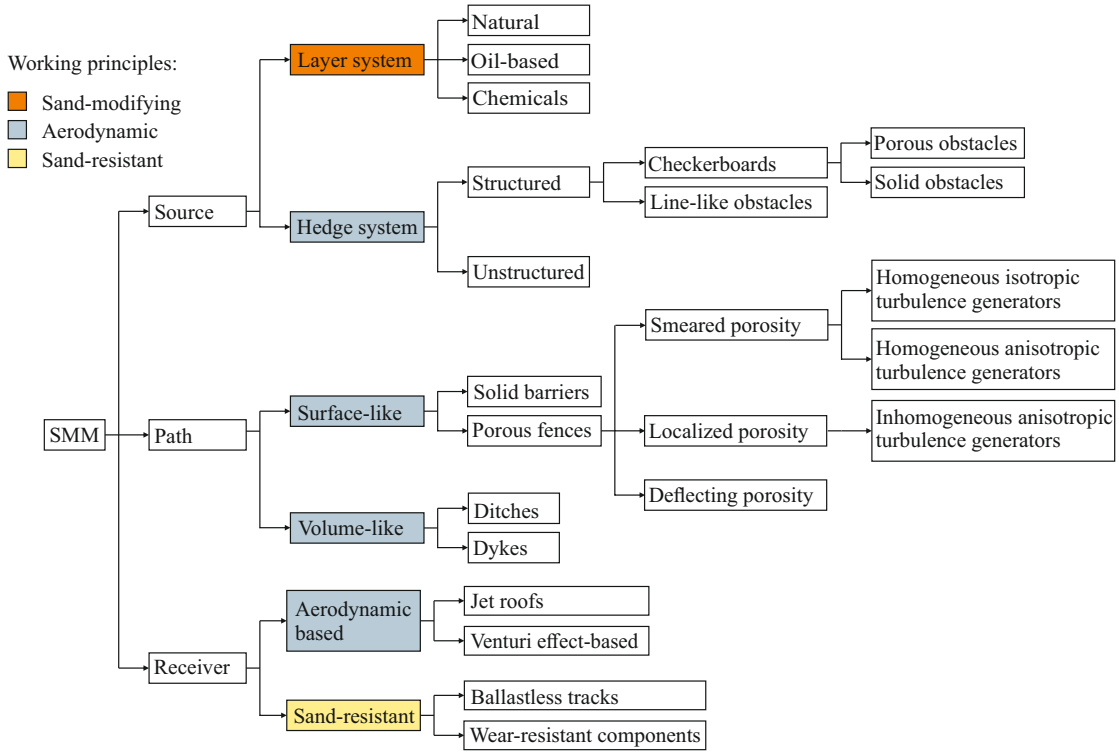

Figure 2.14: Scheme of the proposed SMM categorization.

2.3.4 Source SMM

Source SMMs aim at reducing incoming windblown sand flux by: i. reducing erosion from localized sand sources (e.g. sand dunes) and/or smeared sources (e.g. loose sand sheets); ii. stopping mobile dunes, such as marching (e.g. barchans

dunes) or unstable dunes, (e.g. transverse dunes evolving in barchanoid chains). Such measures have been mainly developed and applied in International [177] and National [e.g. 284, 315, 19, 261] Country-wide systematic actions against desertification. In this perspective, the ten-kilometres-wide green belts are by far wider than the railway corridor, and its objectives are beyond the funding capabilities and the scope of the railway promoters. At a smaller scale, such measures have been also applied in tens-of-meter-wide areas to control small dune fields, single dunes or loose sand sheet in the infrastructure corridor [e.g. 2, 169, 46]. In the following, desertification literature is referenced regarding the technique categorization, while engineering bibliographic references are given for infrastructure applications. The approach usually involves short-term, temporary stabilization of the sand surface, followed by progressive, long-term, permanent stabilization by means of vegetational covering. Source SMMs can be further divided into Layer systems [21, also called mulching techniques], and Hedge systems [142], on the basis of their working principle.

Layer system

The idea behind the *layer system* derives from the nature, where it was observed that the sand layer is prone to crusting. Fig. 2.15(a) shows a naturally crusted surface of sand. The crusting phenomenon relies on increasing of cohesive forces between sand grains, consequently increasing the erosion threshold u_{*t} by cementing the sand surface. In such a way, the incoming sand flux is reduced according to the equations in Table 2.2. The moisture content of dry sand is approximately $0.2 - 0.6\%$ depending on the moisture of the surrounding atmosphere. When a sand layer is wet, moisture is retained by sand as a surface film. Thus, cohesion results from tensile forces between water molecules and sand grains. A content of moisture above 4% fully inhibits sand grain movement, at least under the incoming wind speed tested in wind tunnel experiments by [20, 138]. Salt in low concentrations can significantly raise the erosion threshold, even without increased content of moisture. Salt and other cementing agents act as cement at points of grain contacts. The cementing effect can be achieved by artificially increasing the moisture content or other cementing agents like salt, clay skins, fungal hyphae, algae and lichens [237]. According to the material used, layer SMMs can be divided into: i. natural material layers, such as soil, salty water, biological crust; ii. oil-based layers, such as asphalt (e.g. [316, 8], see Fig. 2.15b), high gravity waxy oil, crude oil (e.g. applied for industrial facilities and pipelines, [2]); iii. layers made of chemical products (e.g. applied for line-like transport infrastructures, [292, 277]).

Besides the growth of erosion resistance they induce, materials applied in layer SMMs should satisfy other industrial criteria, such as durability, rain water solubility, cost, environmental effects and in-situ availability being the most important ones. In the example of asphalt-latex mixture used as a layer SMM shown in Fig.

2.15(b), the mixture is laid using a pressure injection technique which achieves penetration up to 28 mm. The penetration depth is an important parameter in order to avoid the destruction of the layer due to dune movement. For a thicknesses lower than 10 mm, dune movement causes the collapse of the treated surface making the SMM ineffective [316].

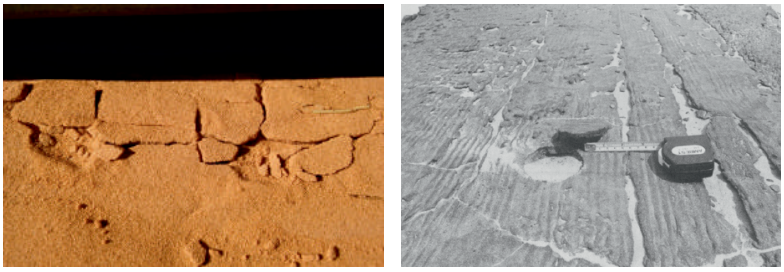

(a) (b)

Figure 2.15: Layer system. Natural sand crusting (a), asphalt-latex mixture layer (b, reprinted from [316], with the permission to reuse under a Creative Commons Attribution License).

Hedge system

The *hedge system* involves discontinuous, closely spaced obstacles placed on the ground to increase its aerodynamic roughness (z_0), and to locally reduce in turn the shear stress at the wind-sand interface. Indeed, a decrease in wind shear stress leads to a reduction of the sand transport rate (see Table 2.2). Obstacles could be arranged in a regular or irregular pattern, resulting in two hedge sub-categories: Structured hedge system, and Unstructured hedge system, respectively.
Structured hedge solutions can be in turn divided into pointwise obstacles and checkerboard systems. Some examples of pointwise obstacles as an SMM are reported in [104, 103]. The checkerboard solution (Fig. 2.16a-c) is the most widely adopted structured hedge system, since the early field tests along the Baotou-Lanzhou railway in the 1950s [173]. Small obstacles are usually manually arranged in an orthogonal and equally spaced alignments, resulting in square cells. About half of the obstacle is buried in the sand, while the other half is above the ground level and exposed to the wind. An SMM example similar to the checkerboard system is shown in Fig. 2.16(d). A structured array of line-like obstacles is arranged orthogonally to the prevailing wind direction. As a result, it is only effective along the orthogonal direction. Several materials are used depending on the in-situ availability, and according to this criterion structured hedge system can be further divided in:

1. porous obstacles, built from straw (Fig. 2.16a, [239]), reed [72], polyethylene-net (Fig. 2.16b, [46]), and coconut leaves (Fig. 2.16d, [168]);

2. solid obstacles, e.g. stones (Fig. 2.16c, [346]).

(a) (b) (c) (d)

Figure 2.16: Structured Hedge system: straw checkerboard (a, reprinted from [112], with the permission to reuse under a Creative Commons Attribution License), polyethylene-net checkerboard (b, reprinted from [346] with the permission from Elsevier), stones checkerboard (c, reprinted from [346] with the permission from Elsevier), array of line-like obstacles (d, reprinted from [168] with the permission to reuse under a Creative Commons Attribution License).

The checkerboard system aerodynamic working principle is qualitatively shown in Fig. 2.17. Generally speaking, the flow regime inside a cavity (i.e. the checkerboard cell mostly depends on the aspect ratio ($AR = w/h$, [220]). As a result, three characteristic flow regimes are defined [23]: i.) Skimming flow ($AR \leqslant 1.5$), where only a single vortex appears inside of a cavity; ii.) Wake interference flow ($1.5 \leqslant AR \leqslant 2.5$), where the main vortex is significantly shifted downwind and a stable secondary counter rotating vortex appears; iii.) Isolated flow ($AR \geqslant 2.5$), where the flow is qualitatively similar to the flow around an isolated obstacle, i.e. a large vortex appears downwind an obstacle before the flow reattachment point, and recirculates again in front of a downwind obstacle. In real world applications along railways, the cell side length usually varies from 1 to 3 m, and the exposed height is from 10 to 30 cm respectively, resulting in an $AR \approx 10$. Hence, the flow inside the cell should correspond to the isolated flow regime. Fig. 2.17(a) shows the conjectured flow regime for an array of cells bounded by solid obstacles. Recirculating vortices drain energy from the incoming wind flow, by reducing the mean wind velocity. The reduction of wind velocity near the ground can be accounted for via the increase of the aerodynamic roughness to about 0.015 m, i.e. about 1000 time greater than the one of a flat sandy surface. The sand level evolution inside a cell is qualitatively given in Fig. 2.17(b). The arrow crossing the sand levels depicts the trend of the sedimentation process. Fig. 2.17(b) is complemented by Fig. 2.17(c-e), where some real world examples of the sand level inside cells are shown. The two vortices inside the initially empty cell promote sand sedimentation close to the inner side of the obstacles (see Fig. 2.17c). At equilibrium between erosion and

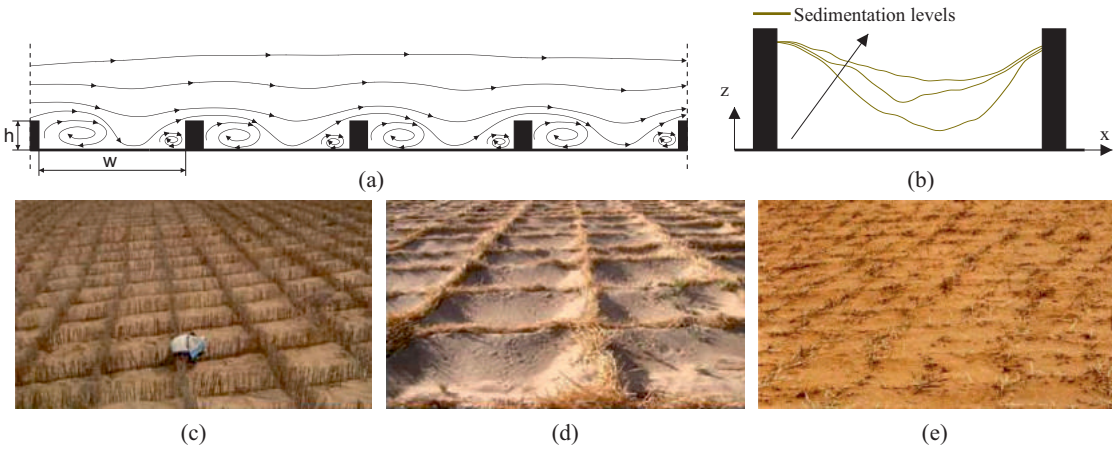

Figure 2.17: Checkerboard Hedge system: isolated flow regime inside cells (a, cells geometry scale: $Dz \approx 2Dx$), corresponding qualitative sedimentation levels in a cell (b, redrawn from [167], sand sedimentation levels scale: $Dz \approx 6Dx$), initial unstable condition of empty cells (c, reprinted from [112], with the permission to reuse under a Creative Commons Attribution License), stable concave surface (d, reprinted from [112], with the permission to reuse under a Creative Commons Attribution License), stable flat surface (e, reprinted from [240] with the permission from Elsevier).

sedimentation, two different stable conditions result in the cell, differently reducing wind velocities [240]: i. a concave sand surface with a ratio of the cell length and sand-free height ranging between 1:10 and 1:8 (see Fig. 2.17d). In this configuration, the SMM is working properly and is preventing further erosion. ii. A flat sand surface at the top of the exposed part (see Fig. 2.17e). When the checkerboard is completely buried by sand, it is unable to further promote sand sedimentation and it becomes a sand source in turn. As a result, manual sand removal maintenance is required. Alternatively, vegetation growth may be promoted inside the cells, once the sand inhibits most of the cell volume. Since the evaporation rate is inversely proportional to the aerodynamic roughness [62], the adoption of checkerboards allows for an increment in sand bed moisture retaining and in turn to the promotion of vegetation growth. Despite the number of scientific studies devoted to the topic of the sand sedimentation around checkerboard system (for a recent review, see [167]), the critical values of the full set of parameters inducing the transition from the favorable (i) to the unfavorable equilibrium condition (ii) are still not clearly defined.

Unstructured hedge solutions are often employed in the form of gravels spread on the sandy surface (Fig. 2.18a). However, attention should be paid regarding both the gravels size and the covering ratio since they can be buried by sand leading

(a) (b) (c)

Figure 2.18: Unstructured Hedge system: gravel surface (a, reprinted from [169] with the permission from Elsevier), large roughness elements (b, reprinted from [105] , with the permission from Elsevier), trees planted over dunes near a railway (c).

to an increment in the sand source [169]. Irregular vegetation pattern could be also ascribed to this subcategory. [105] attempts to mimic a natural vegetation pattern by arranging large-size roughness elements, such as straw bales (Fig. 2.18b). Since they do not require water for their maintenance, they could be preferred to plant-based SMMs where it is not available. Permanent stabilization of sand is possible with an artificial vegetation layer upwind the infrastructure planned to be protected. However, attempts of vegetative stabilization should consider the inter-relationships between several physical and biological habitation factors, most important one being the quantity of available water. A vegetation system around a single oasis takes the form of shelterbelts. For more details, the interested readers are referred to the recent in situ observation at the Minqin oasis, Badai Jaran Desert and Tengger Desert (in Gansu Province, [183]). A vegetation system along line-like infrastructures takes the form of upwind and downwind vegetation belts. To our best knowledge, this vegetation solution has been adopted, in the recent past, along the Jing-Tong Railway [311] and the Tarim Desert Highway crossing the Taklamakan Desert [72]. An example is shown in Fig. 2.18(c).

2.3.5 Path SMM

The goal of Path SMMs is the promotion of sand sedimentation, achieved by controlling windblown sand transport, i.e. by driving the local wind flow in turn. The wind flow is modified by reducing the longitudinal component of its velocity and/or by promoting the wind flow recirculation. Due to the amount and variety of Path SMMs proposed in the literature, we further divide them into two subcategories, according to a geometric criterion:

1. Above-ground Surface-like SMMs, i.e. solid barriers and porous fences (Fig. 2.19a,b);

2. Volume-like SMMs, i.e. ditches, dikes and ridges (Fig. 2.19c,d,e).

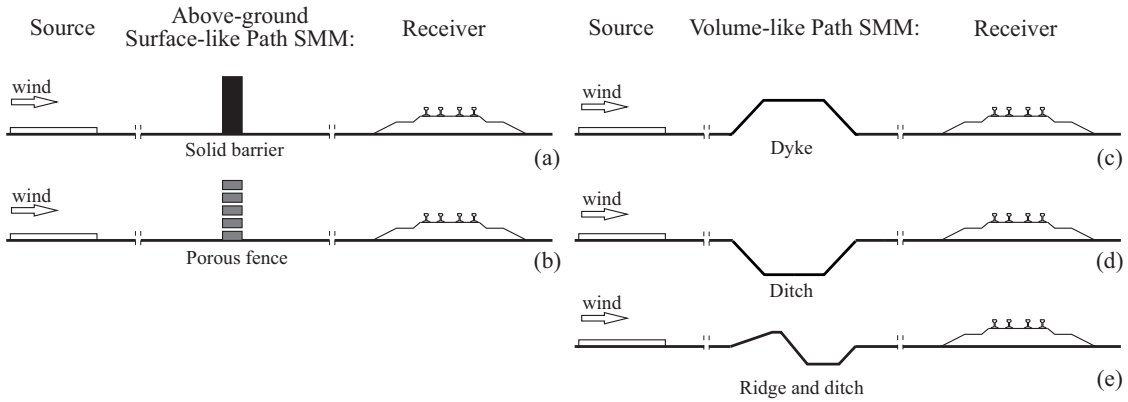

Figure 2.19: Path SMMs: surface-like (a,b), volume-like (c,d,e).

It is worth stressing that such a classification is also compliant with the sedimentation mechanism they induce. Surface-like SMMs promote sedimentation along the upwind and/or downwind strips (see Fig. 2.13), while volume-like SMMs allow sand sedimentation also over and/or inside them. Whatever the geometry of Path SMMs is, they can be arranged in two main configurations, as shown in Fig. 2.20. Both the configurations tend to preserve the angle of attack $\alpha = 90^o$ between the direction of the prevailing wind and the SMM longitudinal axis. In the case of skewed wind with respect to the railway longitudinal axis, ($\theta \neq 90^o$, as shown in Fig. 2.20b), the SMM modules are slanted and their tips overlapped alongwind.

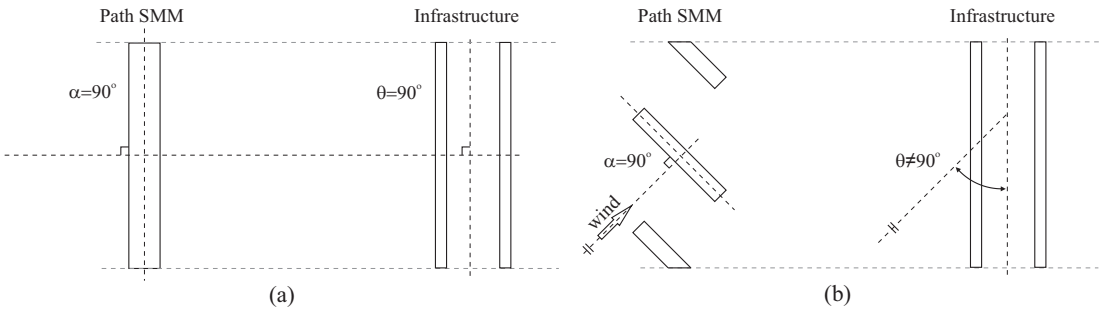

Figure 2.20: Path SMM arrangement configurations: wind direction orthogonal to the longitudinal railway axis (a), skewed wind direction (b).

Since the current state of the art does not allow a comparative and comprehensive quantitative assessments of every Path SMM, qualitative schemes representing the morphodynamics of sand accumulation are provided in the following subsections.

Surface-like

The optical porosity β is the degree of permeability of a surface-like SMM, i.e. the percentage ratio of the open area to the total area [158]. It is commonly considered the most important parameter controlling the performances of straight vertical surface-like SMMs of a given height and for a given incoming wind. Based on that, surface-like SMMs can be further divided into two main categories:

1. Porous fences, if $\beta > 0$;
2. Solid barriers, if $\beta = 0$.

Porous fences have been widely investigated in the scientific literature since the early aerodynamic studies at the beginning of the 20th century [e.g. 17], and the pioneering applications to control windblown snow [e.g. 88] and sand [e.g. 197]. The research activity about fences has been recently reviewed with respect to both wind loads [101], aerodynamics [123], and induced morphodynamics [163, 314]. Conversely, to our best knowledge, scientific studies on solid barriers are surprisingly scarce, and usually limited to the aerodynamics [e.g. 13, 108, 160] and sand morphodynamics [e.g. 127, 57] of Straight Vertical Walls (SVWs). In the following, straight vertical surface-like SMMs are reviewed first, and solid SVWs are viewed as a limit term of reference to porous fences. Secondly, solid barriers with shapes other than straight vertical plane are scrutinized.

Fig. 2.21 collects results from a number of experimental studies in order to describe the evolution of both the wind pattern and the sand sedimentation process versus the porosity ratio. The wind pattern around null porosity SVW barriers (Fig. 2.21a, [13]) is characterized by a large reversed flow region in the wake of the barrier (R_d) and by a stable clockwise vortex upwind the barrier (R_u) below the stagnation point. R_u reduces the wind shear stress close to the ground and promotes upwind sand sedimentation in turn (Fig. 2.21b, [127]), acting as a sand trapping vortex. As a result, the larger the upwind vortex, the higher the upwind sand accumulation potential, i.e. the maximum amount of trapped sand volume (see [36] for further details). An increment of the porosity (Fig. 2.21c, [70]) induces the shrinking of the stable clockwise vortex R_u. The watershed value $\beta_0 \approx 5 - 10\%$ is defined as the one at which R_u vanishes. Given the non-null porosity, sand sedimentation occurs on both sides of the fence with a downwind steep slope (Fig. 2.21d, [127]). However, most of the sedimentation still occurs upwind the fence. A further increment of the porosity induces the growth of R_d (Fig. 2.21e, [334]). This occurs in the interval $\beta_0 < \beta < \beta_c$, where β_c is defined as the porosity value at which the reversed flow region in the wake of the barrier R_d vanishes, too. Most of the sedimentation occurs downwind the fence and the downwind slope is more shallow (Fig. 2.21f, [127]). For values of β greater than the critical value $\beta_c \approx 20 - 40\%$ ([163], and related references), the flow is dominated by the bleed flow through the fence openings (Fig. 2.21g, [334]). Sand sedimentation is no longer induced by the

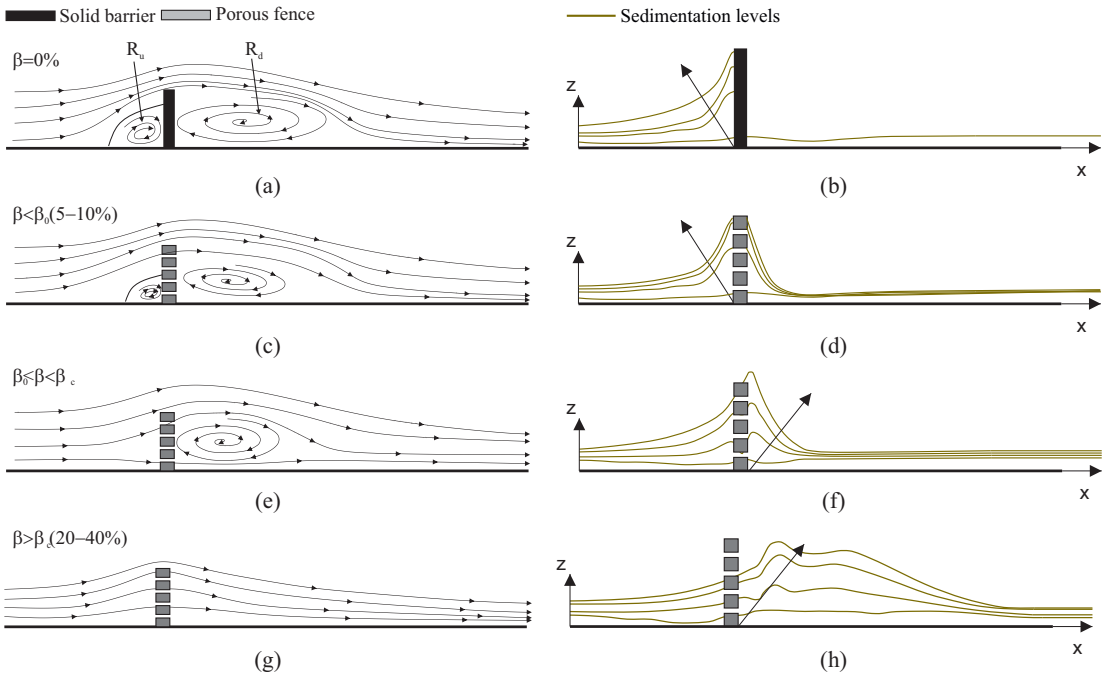

Figure 2.21: Wind flow mean streamlines and related sedimentation levels around: (a,b) solid SVW barriers (redrawn from [13, 127]), (c,d) very low porosity fences ($\beta < \beta_0$, redrawn from [70, 127]), (e,f) low porosity fences ($\beta_0 < \beta < \beta_c$, redrawn from [334, 127]), (g,h) high porosity fences ($\beta > \beta_c$, redrawn from [334, 127]). Sand sedimentation levels scale: $Dz = 5Dx$.

reversed flow downwind the fence, but simply by the velocity defect in its wake (Fig. 2.21h, [127]). The porosity $\beta_{opt} \approx 40 - 50\%$ is widely established as optimal value in terms of sand trapping overall efficiency [266, 25], defined as the maximum volume of accumulated sand per fence unit length, irrespectively of where sedimentation occur. Fences with β higher than 50% are rarely used, because of their low sand trapping efficiency [127].

The variability of the values of β_0, β_c and β_{opt} testify that the porosity ratio, i.e. a macroscopic feature, cannot summarize all the relevant parameters that drive the aerodynamic and sand morphodynamics of porous fences. Besides the porosity ratio, sand sedimentation depends on a number of other parameters. Some of them are not directly related to the SMM (e.g. environmental and experimental setup, related incoming wind conditions, measurement uncertainties), while others are related to SMM microscopic features, such as size, shape, distribution and orientation of openings and solid elements [163]. Based on that, we propose to schematically divide porous fences into three subcategories: i.) Fences with smeared porosity; ii.) Fences with localized porosity; iii.) Fences with deflecting porosity.

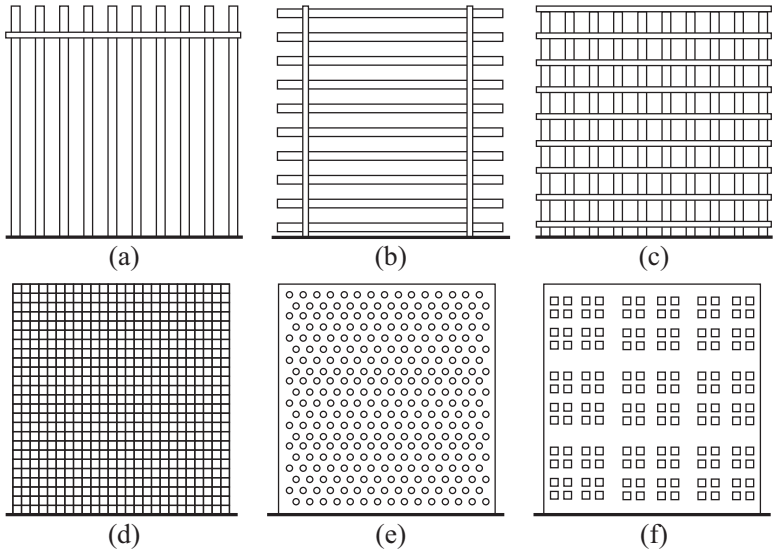

Figure 2.22: Fences with smeared porosity. Homogeneous anisotropic turbulence generators: vertical slats (a), horizontal slats (b). Homogeneous isotropic turbulence generators: grid fence (c), nylon net fence (d), holed fence (e), fractal fence (f). (a-e) redrawn from [70], (f) redrawn from [190].

Fences with *smeared porosity* are fences whose openings have characteristic length(s) several orders of magnitude smaller than the fence characteristic length, i.e. its height. Some schemes of the most common types of smeared porous fences are given in Fig. 2.22. We further subdivide smeared porosity fences as a function of the induced wake turbulence properties. In particular, porous fences will induce anisotropic turbulence when the opening characteristic length distribution is constant but differs between vertical and horizontal dimensions (Fig. 2.22a,b), while they will induce isotropic turbulence when opening characteristic length distribution is the same in both dimensions (Fig. 2.22c-f). The induced wake turbulence, i.e. grid-generated turbulence in the literature [e.g. 297, 155], has a characteristic length scale of the same order of magnitude of the solid element size. Among the latter, fractal porous fences have been recently proposed by [190]: they are expected to induce multiple wake turbulence characteristic length scales.

Fences with *localized porosity*, also called turbulence generators or wind weakeners in the literature, are characterized by openings having characteristic length(s) of the same order of magnitude of, or one order of magnitude smaller than, the fence height. Accordingly, the wake turbulence characteristic length scale is of the same order of magnitude of the characteristic scale of the local mean flow, and strongly interacts with it. Some examples of localized porosity fences are given in Fig. 2.23: an alignment of spire-shaped glass-fiber modules (Fig. 2.23a, [25])

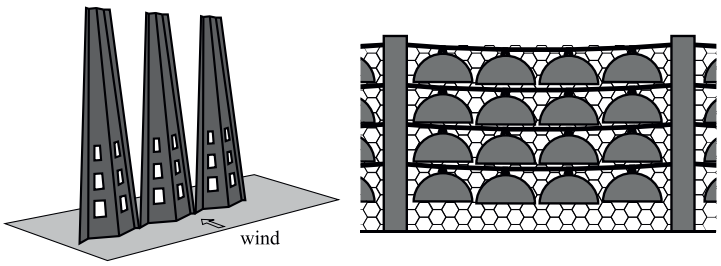

Figure 2.23: Fences with localized porosity: spire-shaped (a, redrawn from [25]), leaf-shaped (b, redrawn from [348]).

analogous to spires usually adopted in boundary layer wind tunnels; an array of leaf-shaped concrete modules hanged by suspension cables (Fig. 2.23b, [348, 46]).

Fences with *deflecting porosity* include solid elements inclined out of the fence plane, such as vanes, slats or plates. Some of these fences were patented in the last decades [e.g. 178, 257], but only recently scientific studies have been devoted to study their aerodynamic and sand morphodynamic behaviour [44, 48]. Fig. 2.24 shows the deflecting porosity fences studied in the cited papers. Both deflecting porosity fences are intended to guide the flow upwards. The working principle of the deflecting inclined elements is twofold: i. guiding the mean bleed flow along target directions, i.e. downward, upward or laterally; ii. reducing the wake turbulence intensity with respect to classic porous fences.

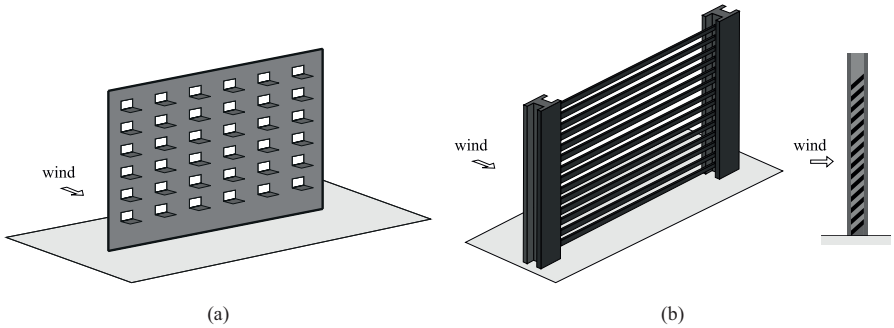

Figure 2.24: Fences with deflecting porosity: guide plates downwind rectangular openings (a, redrawn from [44]), array of inclined slats (b, redrawn from [48]).

Fences with homogenous porosity are one of the oldest type of built SMMs [146]. A traditional example is given in Fig. 2.25(a). Such fences have been developed through the years in order to improve their durability and maintainability, resulting in e.g. polymer nets (Fig. 2.25b). An actual example of fences with localized

porosity made by reinforced concrete panels is given in Fig. 2.25(c).

(a) (b) (c)

Figure 2.25: Fences with smeared porosity: traditional fence protecting a palm plantation (a, explicit publishing permission from the owner of the photos: Nouar Boulghobra), nylon net fence (b, reprinted from [170], with the permission to reuse under a Creative Commons Attribution License). Fences with localized porosity: concrete fence (c, reprinted from [348], with the permission from Elsevier).

Porous fences with smeared porosity are often applied to promote the rapid growth of artificial bell-shaped dunes in coastal regions to protect residential areas from the hazardous effects of both wind and water [266]. Fig. 2.26(a) shows a 6-year long dune growing process. First, a single porous fence is installed where the dune

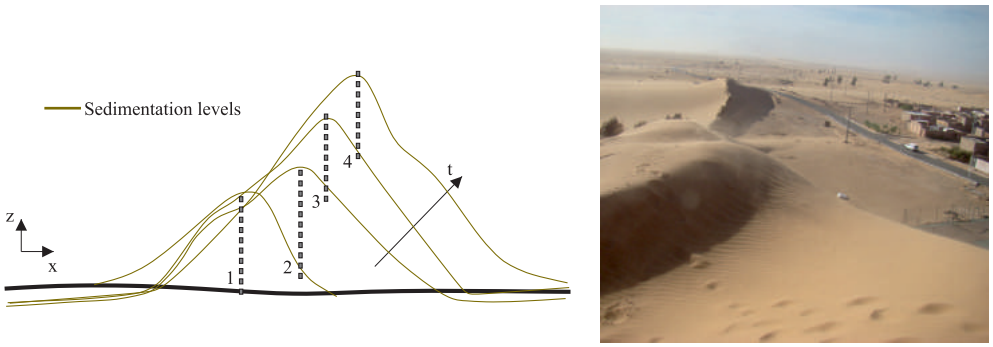

(a) (b)

Figure 2.26: Artificial dune growing: scheme of the process (a, redrawn from [316], sand sedimentation levels scale: $Dz = 5Dx$, Fence 1 (t1) - placed in December 1962, Fence 2 (t2) - placed in January 1963, Fence 3 (t3) - placed in March 1964, Fence 4 (t4) - placed in March 1966, final shape - July 1968), questionable application to stop windblown sand encroaching a village (b, explicit publishing permission from the owner of the photo: Nouar Boulghobra).

is needed. When the accumulation of the sand exceeds the height of the barrier,

a second barrier is positioned on top of the accumulated sand. The process is repeated each time a fence is buried. The numbers depicted in Fig. 2.26(a) indicate the order in which porous fences were positioned. An example of questionable application of artificial dune growing for windblown sand mitigation of a village in the desert is shown in Fig. 2.26(b), where porous fences are used to shape a dune upwind a road. The dune upwind slope acts as a launching pad for the incoming windblown sand. In the figure, it can be seen that, even though a massive dune was created upwind the road, sand is still partially covering it.

Actual porous fences are usually straight and vertical, even if inclined porous windscreens have been investigated [67]. Conversely, the shape of *solid barriers* greatly affects the local wind pattern around them, and the sedimentation process in turn. To our best knowledge, existing solid barriers having different shapes with respect to the SVW are scarcely investigated in scientific literature so far. The parameters driving their design and controlling their performance have been systematically and rigorously discussed only recently [36]. However, solid barriers with other shapes than SVW have been heuristically devised and patented as SMM in the past. Some examples are given in Fig. 2.27. Pettus Newell [229] patented a

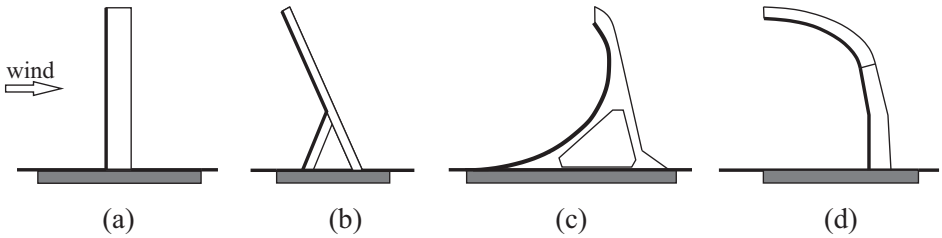

Figure 2.27: Geometry of aerodynamically shaped solid barriers: common Straight Vertical Wall (a), pioneering shape by [229] (b), [228] (c), recent patent Shield for Sand [34] (d). Thick solid lines indicate the cross section of the aerodynamic-effective surfaces.

λ-shaped wooden barrier for railway applications. Analogously, Pensa et al. [228] patented a λ-shaped precast r.c. barrier to be used as SMM for agroforestry applications. Very recently, Bruno et al. [34] have patented a novel solid barriers called *Shield for Sand* (S4S), equipped with an ad-hoc conceived upper windward concave deflector aimed at making the extent of the vortex upwind the barrier as large as possible even for high sedimentation levels. The conceptual design of S4S has been carried out by computational simulations [36], and its performance assessment by wind tunnel test ([33], see Appendix A).
Fig. 2.28 shows the comparison between SVW and S4S induced aerodynamics and morphodynamics for three different sedimentation levels. Both shape and size of the upwind clockwise vortex for about the same level of accumulation change significantly by varying the geometry of the solid barrier. In particular, S4S induces

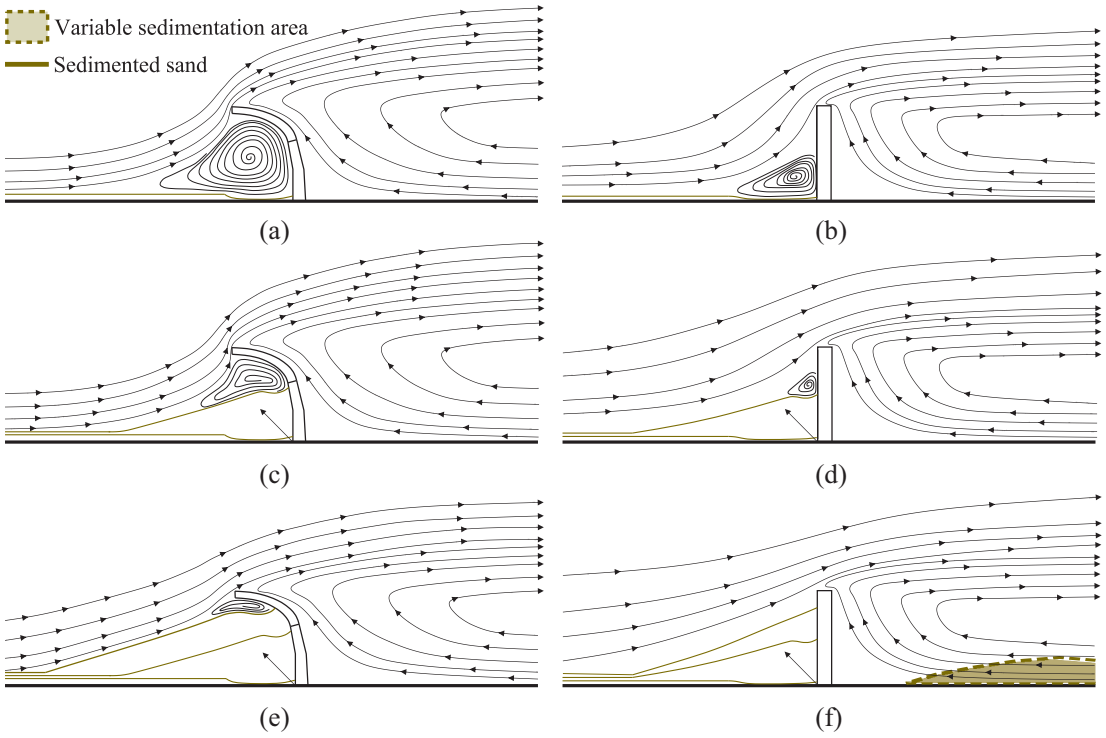

Figure 2.28: Shape induced differences in wind flow mean streamlines (from computational simulations in [36]) and sand sedimentation levels (from wind tunnel tests in [127, 33]): comparison between S4S (a,c,e) and a SVW (b,d,f).

a larger upwind vortex with respect to SVW for low (Fig. 2.28a,b) and moderate (Fig. 2.28c,d) sedimentation levels and higher upwind accumulation potential and trapping efficiency in turn. The vortex upwind SVW vanishes for high sedimentation levels (Fig. 2.28f), while is still present upwind S4S (Fig. 2.28e). The sedimented sand upwind SVW results in a launching pad for incoming windblown sand [127]: windblown sand crosses over the SMM and contaminates the downwind strip and/or the railway, depending on the the wind field in the wake, the position of the reattachment point along the downwind strip, and the width of the strip itself (i.e. variable or uncertain sedimentation area in Fig. 2.28f). Conversely, properly shaped solid windward concave barriers prevent such undesired phenomena until the sedimentation level reaches the barrier height.

To our best knowledge, SVWs are the only kind of solid barriers proposed and tested up to now in actual design practice. For instance, a 4 m-high basic SVW has been proposed as a SMM in the preliminary design of the Segment 1 of the Oman National Railway Network [134]. A 1.5 m-high Jersey-like wall has been recently built along the Mecca-Medina high speed railway in Saudi Arabia [200], showing questionable performances. Some real world SVWs applied as SMM along

railways are given in Fig. 2.29(a-c). The sand sedimentation level around them is low. Conversely, high sedimentation levels around other SVW are shown in Fig. 2.29(d-f). SVWs are made of different materials and components, built ad hoc

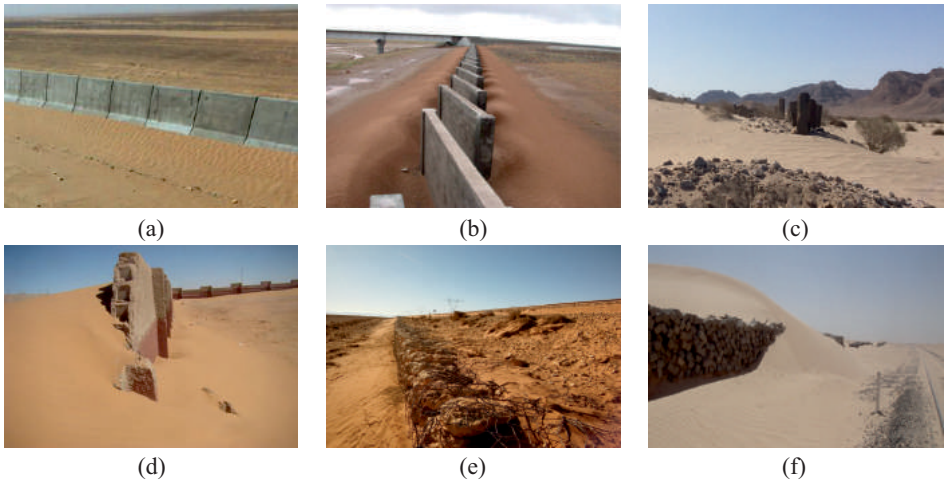

(a) (b) (c)

(d) (e) (f)

Figure 2.29: Straight Vertical Walls examples: precast r.c. modules (a, owner of the photo: R. Méndez, [200]); slanted, overlapped modules (b, reprinted from [348], with the permission from Elsevier]; alignment of vertical sleepers (c, curtsey of Astaldi). Straight Vertical Wall sedimentation patterns: free standing concrete wall (d, explicit publishing permission from the owner of the photo: Nouar Boulghobra, [29]); gabion wall adjacent to the toe of the railway embankment (e, curtsey of Astaldi); horizontally stacked sleepers (f, explicit publishing permission from the owner of the photo: Nouar Boulghobra).

(e.g. Fig. 2.29b,d,e), obtained by adapting elements from other applications (e.g. Jersey barrier in Fig. 2.29a) or by recycling decommissioned ones (e.g. sleepers in Fig. 2.29c,f). Some of the SVWs shown in Fig. 2.29 are not necessarily intended as SMM (courtyard perimeter wall, flood barrier, and sleeper stock in Fig. 2.29d, e, f, respectively). However, they clearly show the attainment of upper limit of the upwind sedimentation (Fig. 2.29d), the subsequent transport of sand grains up the embankment shoulder (Fig. 2.29e), or the progressive burying of the downwind strip and railway track (Fig. 2.29e).

Volume-like

Volume-like path SMMs share the same working principle of Surface-like ones: they decrease the velocity of incoming wind, induce the recirculation flow around

them, and promote sand sedimentation. To our best knowledge, there are no published scientific papers specifically dealing with aerodynamics and sand morphodynamics around dykes or ditches intended as SMMs. Hence, dyke and ditch aerodynamic behaviour is regarded as equivalent to upward-backward facing step and axisymmetric cavity, respectively (schemes in Fig. 2.30a,b). Corresponding qualitative schemes of sand sedimentation levels are shown in Fig. 2.30(c,d). Sand

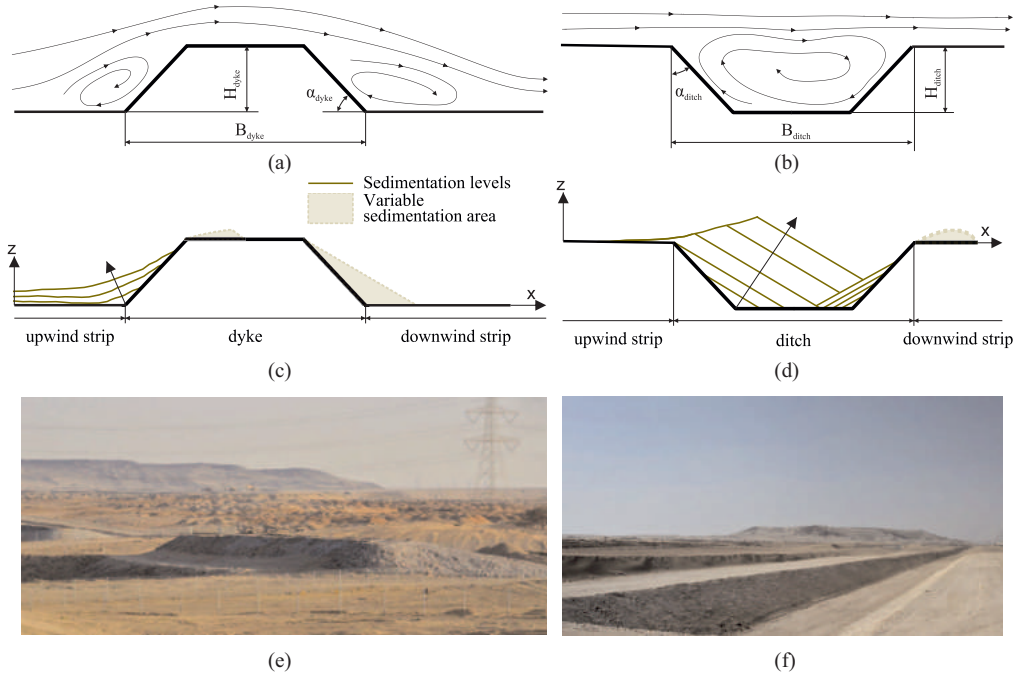

Figure 2.30: Volume-like SMMs. Wind flow mean streamlines around a dyke (a, redrawn from [234]), and a ditch (b, redrawn from [279]). Sand sedimentation levels around a dyke (c, redrawn from [127]), and a ditch (d). Examples of actual volume-like SMMs during field trials: a dyke (e, reprinted from [231]), and a ditch (f, reprinted from [231]).

accumulation over ditches and dykes is mainly affected by their geometric parameters, i.e. height (H), width (B) and slope (α). Dykes induce flow recirculation and consequently sand sedimentation mainly on the upwind slope, while ditches reverse the flow promoting sedimentation mainly inside the cutting. At equilibrium between sedimentation and erosion, the sand accumulated along the upwind shoulder of the dike reduces its slope angle up to about 10 degrees [156]: the upwind vortex disappears, the upwind slope acts as a launching pad for incoming windblown sand, it crosses over the dyke and contaminates the downwind strip. It follows that the accumulation potential of a dike is expected to be relatively small compared to its volume. Conversely, the accumulation potential of a ditch is close to its volume,

provided that its cross section is properly shaped, so that the vortex inside the cutting holds also for high sedimentation levels. From the economic point of view, ditches and dykes involve construction costs higher than surface-like path SMMs, because of the large amount of excavation and earth-moving works. In the recent years, dikes, ditches or a combination of both have been proposed for different railway projects along the Arabian peninsula [230, 231, 35, 55].

In general, maintenance is mandatory to periodically remove sand sedimented around both surface-like and volume-like Path SMMs. Solid barriers have to be cleaned upwind before sand trapping efficiency dramatically decreases. Porous fences have to be unburied both upwind and downwind to avoid dune growing, sand contamination of the infrastructure corridor and the contamination of railway. Analogously, sand accumulated inside volume-like SMM has to be removed from dike shoulder or ditch cutting. Due to the their features and location, solid barriers generally enable easier and cheaper sand removal with respect to other kind of Path SMMs. Apart from common heavy machines, some Sand Removal Machines (SRMs) have been ad-hoc conceived in the last decade in order to remove trapped sand around line-like infrastructures, such as sand cutter and blower [e.g. 267].

2.3.6 Receiver SMM

Receiver SMMs are located directly along or over the infrastructure (e.g. along the embankment shoulder or on railway track). Such measures necessarily interact with and depend on the track superstructure (e.g. rail, sleeper or slab, ballast) and the railway functional requirements (e.g. rail gauge, safety distance from the track). Based on the working principle, receiver SMMs can be further divided into two types:

1. Aerodynamic-based measures aiming at reducing the sand action by controlling windblown sand transport or promoting erosion;

2. Sand-resistant measures, addressed to increase the sand resistance of the track system components rather than avoiding sand sedimentation.

In other words, aerodynamic-based SMMs aim at eliminating accumulated sand around the receiver, while sand-resistant SMMs are intended to increase the receiver resistance to sedimented sand.

Aerodynamic-based

The very first example of measure intended to control the windblown sand transport consists in the jet roof proposed by [245] (Fig. 2.31a). Such a working

principle has been further proposed in patent applications by several inventors for both windblown sand (e.g. [164], Fig. 2.31b) and snow mitigation (e.g. [265], Fig. 2.31c).

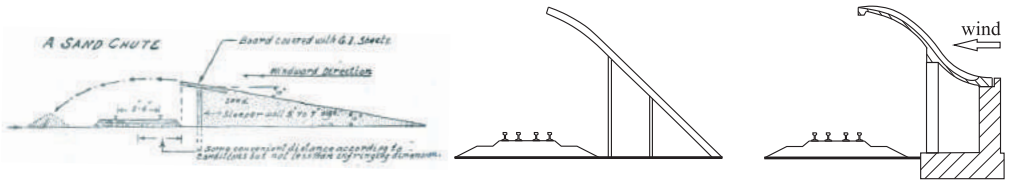

(a) (b) (c)

Figure 2.31: Aerodynamic-based Receiver SMMs: jet roofs. Historical example from [245] (a), patent redrawn from [164] (b), patent redrawn from [265] (c).

The working principle of jet roofs relies on four common steps: i. acceleration of the multiphase flow along the upwind artificial slope; ii. lifting off of the granulated particles at the jet roof trailing edge; iii. crossing of particles over the infrastructure; iv. sedimentation of particles downwind the infrastructure. This conjectured transport mechanism seems physically sound for windblown snow, where the convective contribution of the wind flow largely prevails over the gravitational force acting on very lightweight snowflakes. Conversely, sand physics looks misunderstood: the gravity force applied on the sand grain is orders of magnitude larger than the one on snowflakes. Hence, the trajectories qualitatively sketched by [245] presumably overestimate the flight length of sand grains. We conjecture the sand grains fall and sediment closer downwind the jet-roof trailing edge, i.e. on the railway track. Partially open or fully closed tunnels [e.g. 210, 50], are the straightforward extension of the jet roof concept. They have evident disadvantages with respect to building costs and safety issues when extensively applied along the railway [113].

Among the measures intended to promote sand erosion on the railway track, let us review in particular on-track devices. They include humped sleepers within conventional ballasted track system ([254, 343, 253], Fig. 2.32d) and humped slab track [341]. Humped slabs have been tested in situ along the Namibian railway [254] and the Iran railway [339]. In all cases, protuberances elevate below the rail to support it. The working principle of humped sleepers relies on the well know Venturi effect. This type of devices rely on a growth of a local wind speed induced by the narrowing of the duct in which it flows and the directing of a wind flow towards the track components to be cleaned (Fig. 2.32b,c). Fig. 2.32(d) qualitatively testify the Venturi effect takes place in the opening between consecutive sleepers and below the rail lower flange. On the one hand, this effect involves the local erosion of the sand and prevents the full obstruction of the track. On the other hand, the local deceleration of wind flow between the upwind and downwind rails involves local sand sedimentation, e.g. on signalling balises (Fig. 2.32e,f). In case

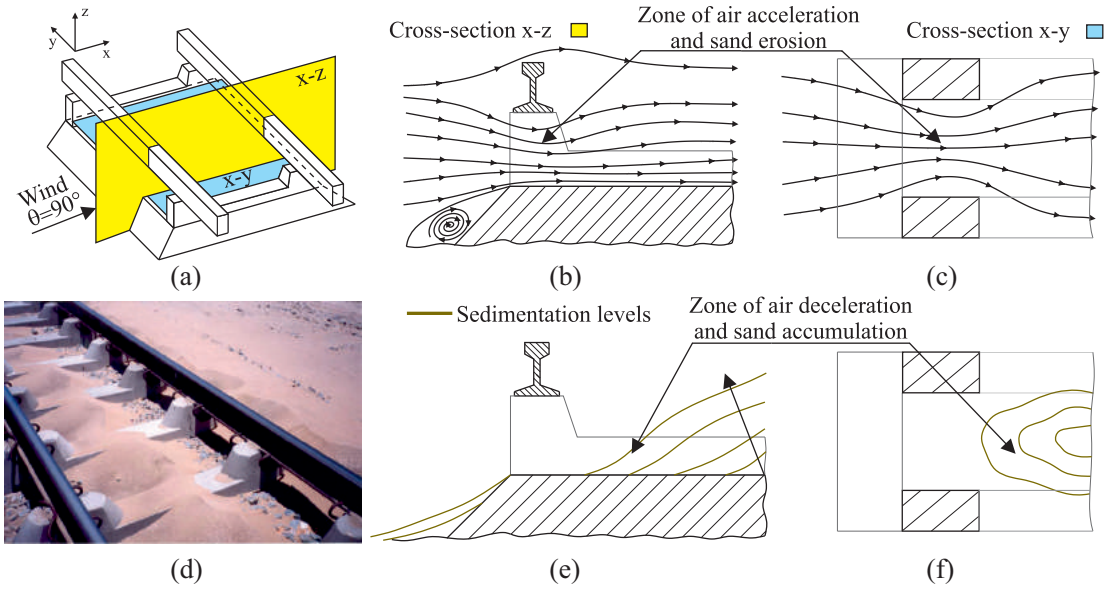

Figure 2.32: Aerodynamic-based Receiver SMMs. Venturi effect-based: humped sleepers scheme (a). Streamlines in the section: x-z (b), x-y (c). humped sleepers (d, reprinted from [253] with the permission to reuse under a Creative Commons Attribution License). Qualitative sand accumulation levels in the section: x-z (e), x-y (f).

of a skewed prevailing wind directions ($\theta \neq 90°$, see Fig. 2.20), we conjecture the Venturi effect weakens since the flow separates in the duct between two successive humps, and sand accumulates below the rails up to the complete clogging of the SMM. In other words, skewed wind does not see the openings of humped sleepers. Further examples of measures based on the Venturi effect are localized porosity fences with higher porosity in their lower part [163] and the so-called bottom-opening walls [50]. Such measures are intended to be installed in proximity of the railway track in order promote sand erosion. According to [50], bottom-opening walls are effective for high wind speeds.

Sand-resistant

Some components of the track superstructure have been recently ad-hoc modified in order to make them more resistant to the sand action. Several ballastless track systems have been tested along desert railways to avoid ballast contamination. Among them, let us recall:

- track systems with longitudinal continuous support, such as Tubular-Track (T-Track) railway system (Fig. 2.33a). The T-Track system has been developed in South Africa since 1989, installed in KSA deserts in 2008 [203] and in Namibian desert. According to [203], T-Track systems have a lot of advantages compared to the ballasted railways. The main reason why they are used in desert areas is because they do not exhibit problems related to ballast fouling. On top of that, initial and maintenance costs are lower;

- track slab systems with discrete rail support (e.g. RHEDA2000®, currently installed in Medina-Mecca high speed line [201], Fig. 2.33b). The most significant advantages are the high stability of the track, reduced maintenance requirements [205], and suitability for the application in sandy deserts, making them suitable for high speed railways. However, initial costs for their construction are higher and it is more difficult to replace parts of the system in case of failure [154].

The combination of slab track system and humped sleepers results in a humped slab track. Its performance is investigated by [341]. According to them, the height of the humps should be about 80 mm in order to avoid track covering for an orthogonal incoming wind direction ($\theta = 90°$), while ballast contamination is naturally avoided. No results are given for skewed incoming winds.

(a) (b) (c)

Figure 2.33: Sand-resistant Receiver SMMs. Ballastless track slab systems: longitudinal continuous support, T-Track system (a, explicit publishing permission from the owner of the photo: Giles Wiggs), continuous slab (b, reprinted from [200], with the permission from El Confidencial). Lubricant free turnout (c, reprinted from [154], with the permission from Voestalpine).

Ballastless systems apart, ballast protection against sand contamination could be alternatively achieved by the application of rigid-polyurethane foam as an in situ stabilization method [e.g. 145, 69]. A recent study from [84] addresses the improvement of ballast performance when ballast fouling takes place through the mixing of tire derived aggregate with ballast.

Further to ballast, others components of the track superstructure have been modified in order to withstand the effects of windblown sand:

- Sand-induced abrasive wear of turnout sliding components and reduced durability of lubricants have been addressed by redesigning the switch mechanism and developing lubricant-free, grease-free, or hinge-free products, e.g. the Plate Integrated Roller System (Piroll®) or the Hydraulic Switching System (Hydrolink®) [154];
- Sand-induced rail grinding has been addressed by increasing the rail head wear and fatigue resistance. Thermal hardening of steel rails of at least R350HT grade are recommended by [232];
- Sand-induced wheel profiling are mitigated, at the present state of art, by two strategies:
  - On one side [122] suggested the adoption of multiple rail profiles along the tangent portions of a railway, in order to produce different contact bands on the wheels and distribute the wear across the wheel tread.
  - On the other side, [86] tested railway wheel made of hardened steels specifically designed for desert environments (SANDLOS H ®) with sanding at the contact interface. Their wearing resistance was proved to be higher than the one of general purpose standard steels.

It is worth stressing that stand alone receiver SMMs are insufficient in most cases to protect the infrastructure against windblown sand since they cannot deal with large sand drifts. In Fig. 2.34 examples of inadequate performances of some receiver SMMs are given. In Fig. 2.34(a,c) there are no path or source SMMs coupled

(a) (b) (c)

Figure 2.34: Failure of Receiver SMMs: T-Track covered by sand (a, explicit publishing permission from the owner of the photo: Ciaran Nash), continuous humped slab covered by sand (b, reprinted from [200], with the permission from El Confidencial), lubricant free turnout jammed by sand (c, courtesy of Astaldi).

with the receiver SMM: ballastless track is successful to prevent ballast contamination, but it is ineffective to mitigate track partial covering (Fig. 2.34a) or dune encroaching; lubricant free turnout avoids wearing of its mechanical components, but the the overall switch is out of service because of the massive sedimentation

between the tapering and the diverging outer rail (Fig. 2.34c). In Fig. 2.34(b) the slab track is coupled with a SVW having low trapping efficiency: ballast is not contaminated, but the track is partially covered by the windblown sand not trapped by the solid barrier. In general, receiver SMMs are useful to deal with small amount of sedimented sand, upwind efficient path SMMs are able to trap most of the incoming sand drift.

Sand removal machines (SRMs) moving on rails have been ad-hoc conceived in the last decade to clean the rail track from sand. Some examples are the 46-6 SRM [38] adopted in the Egypt and Iraq railway network and the the SRM 500 [319] used in Syrian and Kingdom of Saudi Arabia railway networks. Such SRMs have high nominal clearing capacities (up to 2300 tons/hr) required in cleaning railways if no or low efficiency Source or Path SMMs are put in place upwind the infrastructure. Both the 46-6 SRM and SRM 500 use plough and brooms to remove sand from the tracks. The capability of SRMs to discharge the sand as far as possible from the railway/SMM is another crucial aspect. For that purpose, 46-6 SRM and SRM 500 are using slewing conveyor belt capable of discharging the sand from 3 to 5 meters away from the track. In order to prevent the large quantities of removed sand to enter a new erosion-transport-sedimentation cycle, SRMs should be complemented by the complete procedure for sand disposal, by placing it in storage areas far from the railway track, and stabilization.

In the following, lessons learnt are briefly summarized by referring to Source-Path-Receiver classification and to their phenomenological working principles.

- Although Source SMMs are widely adopted against desertification process at regional scales, they are beyond the field of interest, the role, and the economic capabilities of railway owners, designers, and general contractors.

- A number of Path SMMs are proposed in literature and some of them are extensively adopted in practice. Path SMMs appear to be likely adopted along railways since their building components are already employed in the production of other kinds of barriers (e.g. noise or wind barriers) along railway infrastructures. Whilst porous fences are widely studied in literature, solid barriers remains scarcely studied. In particular, porous fence working principle involves a significant amount of sand bleeds through the unburied fence, so that the railway corridor is necessarily contaminated. Conversely, solid barriers comply with the practical requirement of preventing sand accumulation in the railway corridor. Keeping high trapping efficiency upwind the solid barrier even at high accumulation levels is the mandatory design requirement. Such a requirement should be necessarily satisfied by the understanding of the barrier aerodynamic behaviour and its careful aerodynamic design.

- Receiver SMMs have to comply with railway track superstructure functional

requirements. Receiver SMMs are at their infancy to date. This is because they necessarily involve a global rethinking of the superstructure components (i.e. sleepers, rail, signalling devices) and rolling stock in order to be adapted to arid environment conditions. Bearing in mind that these components results form a 150 year long optimization in European and North America countries, such rethinking cannot be envisaged in the short time design process of a single railway project. Midterm research and development programs are required for this purpose.

2.4 Design codes and best practices

The categorization of windblown sand action is missing both in scientific literature and standards. The only remarkable exception is given by the Algerian snow and wind code ([60], Sect. 7). The sand loads are here considered as a variable, direct, fixed, static action in analogy to snow loads resulting from the accumulation of sand transported by the wind. The sand zoning map of the Country is given, analogously to wind and snow ones. Global and local distributed vertical loads are provided for flat and multi-span roofs, respectively:

- a uniformly distributed sand load must be taken in account for flat roofs and roofs with slope lower than 5%;
- in the case of sloping roofs (e.g. gable roofs, shed roofs, domes), a linearly uniformly distributed localized load must be considered along the bottom of the slope (see Fig. 2.35).

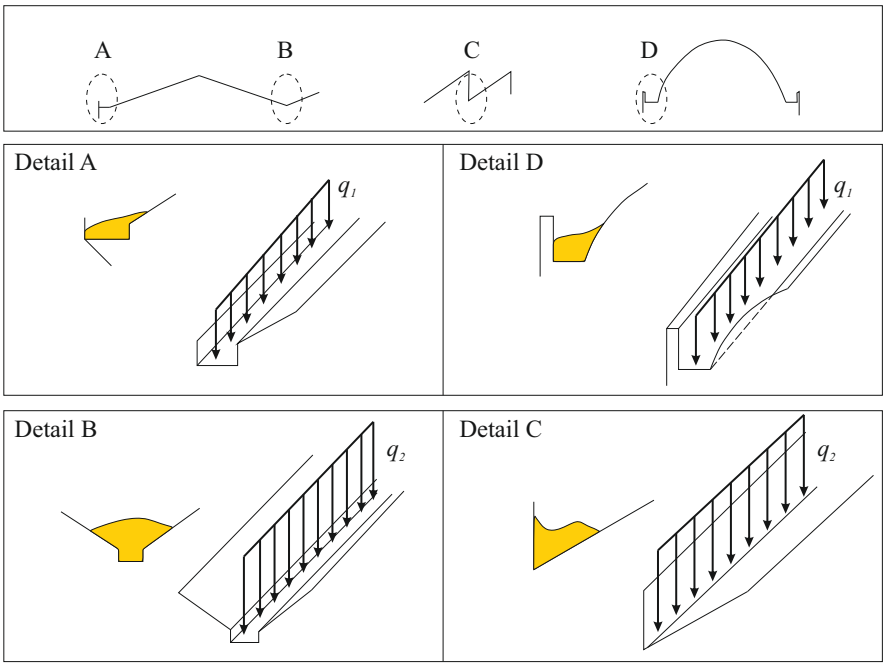

Figure 2.35: Linearly uniformly distributed localized loads redrawn from [60].

Chapter 3

Modelling framework and study outline

Part of the work described in this chapter has been previously published by the author and co-workers in international peer-reviewed journals [241].

The state of art outlined in Chapter 2 highlights two major deficiencies to be investigated in order to systematically design structures and infrastructures against windblown sand:

- windblown sand action and its effects on civil structures and infrastructures are almost completely overlooked in civil and structural engineering, despite the wide range of induced deficiencies, and the need of ad hoc engineering studies and solutions early recognized by e.g. [248, 285]. Furthermore, existing models belonging to the geomorphology field are deterministic despite the very high inborn randomness of the phenomenon and are narrowed to the assessment of the sand transport in open terrain.

- with some remarkable exception, the solid conception, design and performance assessment of SMMs are still missing in the scientific literature and technical practice.

To the author's opinion, the abovementioned deficiencies are due to multiple issues, i.e. (i) the multidisciplinary nature of the problem and lack of dialogue between engineering and fundamental disciplines, such as aeolian research and geomorphology, (ii) the inherent multiscale and multiphysic nature of the involved phenomena, (iii) the scaling and measurements difficulties in experimental tests, (iv) the modelling and numerical difficulties in computational simulations.

The design of civil structures and infrastructures against windblown sand requires, first of all, the definition of windblown sand action. Windblown sand action acts around the boundaries of the affected structure and originates from aeolian processes occurring around it. As a result, it crosses the structural design discipline boundaries and invokes other fields. In order to characterize windblown sand

action one needs to move towards the boundary of the structural design field, in the scarcely explored overlapping between structural engineering and other disciplines in order to look into windblown sand closely, i.e. from a physical and modelling point of view. Being windblown sand the result of the interaction between wind and sand, the fields of Aeolian Research and Geomorphology, Fluid Dynamics, as well as tools from Mathematics and Statistics are explored (see Fig. 3.1). In the next chapters, notions and methods that may appear at first far from the design domain are implemented to quantify windblown sand action on civil structures/infrastructures.

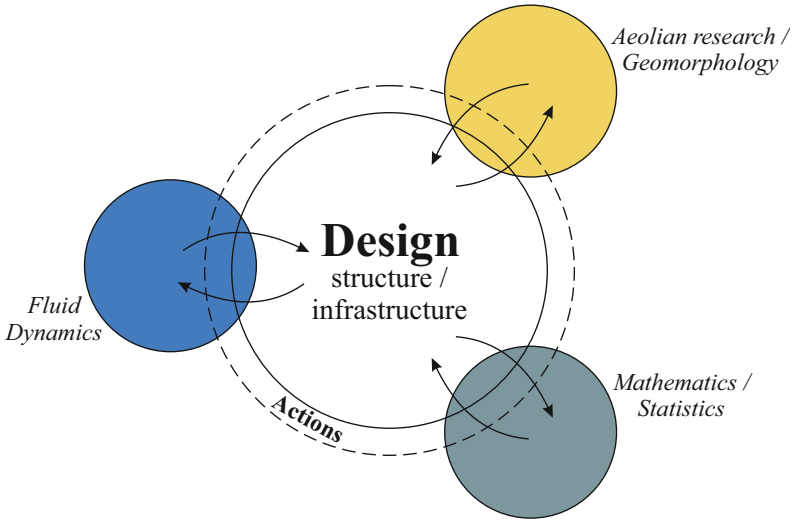

Figure 3.1: Away and back from design of civil structures and infrastructures.

Despite the analogy to snow action reported in Section 2.4, windblown sand accumulation does not translate only into static loads directly applied on structures, but also into indirect actions, once more in analogy to snowdrift, wind-driven ice accretion and other environmental influences that affect durability, impair the performance of the built structure/infrastructure and results in frequent maintenance [81]. In spite of the analogy between sand and snow action, it is useful to put the stress on some differences. i. Wind is necessary to sand lifting, subsequent accumulation and resulting action, while gravity forces in still air are sufficient to drive snowflakes free fall. ii. Sand accumulation can result in both vertical loads on roofs and unprotected floors, and in horizontal loads on wall or diaphragms, because its low cohesion and high density. Conversely, snow accumulation mainly implies vertical load only, while low horizontal static loads results from low cohesion and low snow density (fresh snow), or vice versa (old compact snow). iii. Sand avalanching results in a quasi-steady load, because of the progressive low-speed sliding of the superficial layer only, while snow avalanching results in an impact load because of

massive high-speed sliding. iv. The sand accumulation and related action is monotonically increasing in time, if periodic removal is not included in the maintenance plan, while accumulated snow can be subjected to melting.

Since the definition of windblown sand action is still missing in the scientific literature and standards, a concise categorization of windblown sand action is provided in analogy to the common practice in structural engineering. Windblown sand is here considered an *environmental action*, since it results from the interaction between wind and sand. As a result, it strictly depend on the construction site, and it shows a very high inborn variability, by analogy to wind action. It is a *free action*, since it is directly related to the local wind flow around the affected structure, in analogy to windblown snow. Finally, it is a *variable action*, since it results from a long term accumulation/erosion process by analogy to snow action, but it can be non-monotonic thanks to periodic sand removal due to maintenance operations (see Section 2.3). All these features have repercussions on the modelling framework. A probabilistic approach is required and it must account for both wind and sand fields. Then, a time-variant reliability analysis is needed in order to describe the variable windblown sand action and plan sand removal maintenance operations.

The following chapters deal with the development of a probabilistic approach to windblown sand action and the performance assessment of sand mitigation measures. The modelling framework to assess windblown sand action and its effect on civil structures is organised by analogy with the Davenport Wind Loading Chain widespread in wind engineering (see Fig. 3.2). First, incoming windblown sand upwind the affected structure/infrastructure is assessed. Incoming windblown sand depends on the construction site characteristics, e.g. local wind magnitude and direction, and sand granulometry, by analogy to incoming wind. Windblown sand action is then quantified depending on both aerodynamics and morphodynamics of the affected structure/infrastructure. Finally, the performance level of the affected structure and/or SMM can be assessed on the basis of a time-variant reliability analysis.

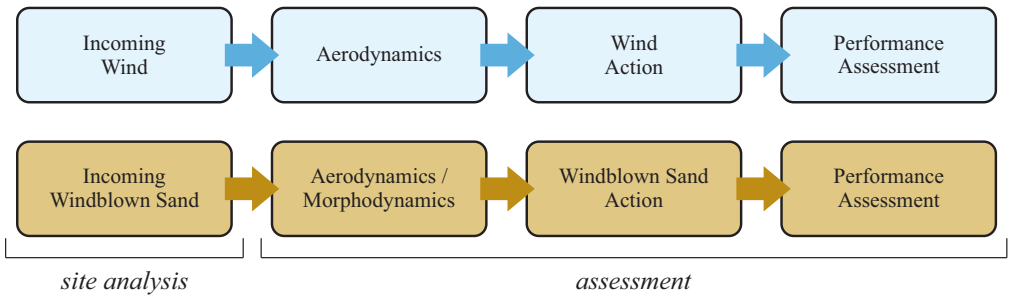

Figure 3.2: Modelling framework.

The thesis develops accordingly to the above objectives through the following chapters. Chapter 4 covers *site analysis* work package. Incoming windblown sand modelling and preliminary findings are discussed. Chapter 5 addresses *assessment* work package. It establishes newborn windblown Sand Limit States for built structures and infrastructures and introduces the modelling of windblown sand action. Finally, the performance assessment of two alternative sand mitigation measures is reported as a case study dealing with a desert railway.

Chapter 4

Incoming windblown sand

Part of the work described in this chapter has been previously published by the author and co-workers in international peer-reviewed journals [244, 243, 242].

This chapter defines incoming windblown sand as the amount per crosswind meter carried by the wind undisturbed by any obstacles, in analogy to the incoming wind velocity in wind engineering practice (e.g. [83], Sect. 4). First, the probabilistic erosion condition is defined and its implications on the transport rate are discussed, then an application to five case studies located in the Arabian Peninsula is presented.

The chapter is organised as follows:

- Modelling
- Application and results

4.1 Modelling

The design of structure and infrastructure in arid environments or coastal zones requires the accurate estimation of the amount of incoming windblown sand that attacks them. Incoming windblown sand varies in both space and time. Indeed, on the one hand, line-like infrastructures cross different regions with a wide variety of geomorphological characteristics. On the other hand, structure/infrastructure design must ensure the service life prescribed by standards. Hence, a probabilistic approach to design is necessary to take into account the inborn variability of the phenomenon.

According to the authors, it is worth pointing out that the current approach within the Fryberger and Dean [94] framework (see Subsection 2.2.3) is:

- deterministic with respect to the sand subfield. Indeed, the expressions of the threshold shear velocity u_{*t} used so far are purely deterministic;

- time-averaged with respect to the wind subfield. The wind speed inborn variability is accounted for, but only the mean value of DP is retained because the rescaling on the reference time is tantamount to averaging.

Let us call such approach as Sand Deterministic - Wind Averaged (SD-WA).

Despite SD-WA approach is generalized in practice, windblown sand phenomenon is affected by several sources of uncertainty. Uncertainty is formally defined as the lack of exact knowledge, regardless of what is the cause of this deficiency [249]. Uncertainty stems from various sources. Overlapping uncertainty classifications can be found in the literature, the typology varying remarkably depending on the context and scope. Nevertheless, every taxonomy reflects a common general classification that distinguishes between *aleatory* and *epistemic* uncertainty [355]. In the following, a complementary categorization referring to the wind and sand subfields is introduced. *Epistemic* uncertainties are associated with the lack of knowledge about the properties and conditions of the phenomena to be modeled. They can be further ascribed to model, parameter and measurement uncertainties. Wind-field epistemic uncertainties are generally well quantified, because of its long-standing modelling, while sand-field ones have been only recently highlighted with respect to threshold shear velocity (e.g. [15, 244]) and sand transport rate (e.g. [16, 242]). *Aleatory* uncertainties refer to inherent randomness of natural phenomena. Wind-related aleatory uncertainties affect the velocity and other environment variables. Sand-related aleatory uncertainties take place at both the microscopic scale, i.e. grain irregular shape, grain size distribution, grain relative position on the sand bed (e.g. [214, 75, 78]), and the macroscopic scale, i.e. soil vegetation covering, soil sediment availability, soil moisture and soil crusting (see e.g. [195, 157, 270, 124]). The statistical description of wind speed is long-standing and well established, as reviewed by e.g. [43]. Conversely only recently the author proposed the statistical description of threshold shear velocity (e.g. [244]).

Both the engineering design needs and the shortcomings of the SD-WA approach pave the way for the probabilistic description of the incoming sand drift. According to the authors, it can be regarded as equivalent to other environmental actions, in analogy to wind action. Hence, let us briefly outline in the following to which extent the incoming wind speed U is analogous to the sand transport rate Q and to the drift potential DP. First, in wind engineering the wind speed is defined in probabilistic terms due to the uncertainty related to inborn wind variability only. The probabilistic representation of sand transport rate is recommended a fortitiori and it is more difficult at the same time, since it is affected by more uncertainties. The variability of both wind and sand features should be taken into account. Second, most of the wind effects on structures, e.g. equivalent static loads or flutter, are related to extreme values of the incoming wind speed. Conversely, windblown sand effects on civil structures are mainly induced by the cumulated values of current values of Q over time, that is DP. In this perspective, windblown sand effects

and related assessment recall wind-induced fatigue. In spite of this analogy, some differences remain. Only a few incoming wind directions are considered in directional wind-induced fatigue assessment (see e.g. [251]), i.e. the ones that induce the highest stresses on the cross section. Conversely, all incoming wind directions are taken into account in assessing the windblown sand drift, since they all contribute in RDP definition.

In the following, the first step towards a probabilistic approach to incoming windblown sand are drawn. First, a statistical description of the threshold shear velocity is investigated and provided in Subsection 4.1.1. Secondly, in Subsection 4.1.2 it is implemented in some common semi-empirical expressions to evaluate the transport rate in order to quantify its uncertainty propagation.

4.1.1 Probabilistic erosion threshold

In the conclusion of their paper, Wu and Chou [327] rise the issue of not yet investigated effects of other random factors on the probabilities of sediment entrainment. To the authors' best knowledge, a comprehensive categorization of such random factors affecting the threshold shear velocity is not given in the literature. However, different sources of uncertainty have been conceptually introduced (e.g. in [114, 355]) and systematically reviewed in related disciplines, including Environmental Modelling [249, 304], Physical Geography [91], Ecology [250], Wind Energy [336]. Having in mind that erosion belongs to the general class of environmental problems [304], in the following the uncertainty classification proposed for the latter is applied to the former. Published papers dealing with threshold shear velocity uncertainties are briefly reviewed accordingly to this general classification.

- *Aleatory uncertainty.* To the authors' best knowledge, the scientific literature in Aeolian Research is primarily focused on aleatory uncertainties. They can be further divided referring to the sand and wind subsystems:
  - *Sand uncertainties.* Beside the grain shape, its surface microstructure [75], and its relative position with respect to the other bed particles [214], other uncertainties at the grain scale affect the grain mineralogy and its surface cleanliness [202]. At the macroscopic scale, the *grain size distribution* is traditionally recognized in literature as an important sand feature affecting u_{*t} (e.g. [78] and included references), beside the mean diameter. In fact, smaller particles interspersed among the large particles provide additional cohesive forces in natural sands, resulting in higher threshold conditions [258]. The early studies on u_{*t} (e.g. [12]) usually assume nominally uniform sand, but this restriction clearly does not hold in a probabilistic framework;
  - *Wind uncertainties.* Beside the ones due to the turbulent flow [322], other uncertainties follows from the inborn variability and/or partially

uncontrolled *environmental conditions* even in wind tunnel facilities, e.g. air temperature and air relative humidity (e.g. [110, 139]);

- *Epistemic uncertainty*. To the authors' best knowledge, such a class of uncertainties is explicitly addressed less often in the Aeolian Research literature. It can be further refined as follows:
  - *Model uncertainties*, that is uncertainty in the necessarily simplified representation of the behaviour of the natural system, in terms of uncertainty in the identification and definition of the variables, hypotheses assumed, interactions left out, and shapes of the functions. With regard to u_{*t} models, first a single quantitative definition of the same "fluid threshold" is not shared in aeolian community. The lack of a shared definition is highlighted by e.g. [270, 288, 40]. Early qualitative definitions suffered the fact that grain motion initiates intermittently in time and not uniformly in space: [11] refers to the "complete bed motion"; [136] refers to "the lowest ... speed at which the majority of exposed particles ... are set in motion" and "general motion of the exposed particles"; [111] to "movement of particles over the entire bed"; [135] to "continuous motion throughout the bed"; [182] establish four velocity thresholds respectively related to the motion of the first grain, or of few grains moving intermittently, gusts moving intermittently or general bed motion. Quantitatively, u_{*t} is commonly set to the value at which a small percentage of grains start to move. According to [270] "inevitably, the practical estimation of u_{*t} involves a certain degree of subjectivity in deciding what is a small percentage". For instance, in [71] "the wind is considered to reach the initiation threshold when more than 5 particles were stuck on the sticky tape". [40] observe "five stages of grain motion, namely first motion, flurries, patches, motion of $\approx$ 50% of the longitudinally central portion of the bed, and motion of $\approx$ 100% of the bed" and finally define threshold as 50% of the bed in motion. The ensemble of the above qualitative and subjective estimates results in an overall source of uncertainty. Second, microscopic models proposed in literature differ in the interparticle cohesive forces accounted for (e.g. van der Waals, electrostatic, capillary, chemical binding, Coulomb forces; [270]) and in their dependency on particle diameter, linear in theory according to [270], but scaling with $d^{4/3}$ according to [54].
  - *Measurement uncertainties*, due to measurements errors and/or to different kind of measurements procedures. Such uncertainties affects both the measurement procedures and techniques adopted to evaluate the bulk granulometry [24, 347], and/or the threshold shear velocity itself

[15, 233]. In fact, the sediment transport can be measured by visual observation [11], camera monitoring equipment [322], impact sensors [247], laser based detection systems [214], or bimodal slope method [102]. Results from these methods are not directly comparable and are significantly scattered (e.g. in [258]);

– *Parameter uncertainties* in the (fixed but poorly known) values of the parameters of a model. For instance, the value of the single parameter of Bagnold model [11] for fluid threshold friction velocity slightly varies among authors for the same nominal conditions (air flow, nearly uniform sand grains of diameters greater or equal to 0.2 mm): $A = 0.10$ in [12], $0.09 \leq A \leq 0.11$ in [51], $A \approx 0.12$ in [354], $0.17 \leq A \leq 0.20$ in [182].

To the author's opinion, four main questions rise in the light of the categorization introduced above and the state of the art briefly reviewed in Subsection 2.2.1: i. How to describe the threshold shear velocity by accounting for the sources of uncertainties introduced above? ii. How can such a description meet the practical engineering need of accurate definition of extreme percentiles of u_{*t}? iii. How many information about the variability of u_{*t} does the deterministic approach neglect? iv. How to overcome the difficulties encountered by probabilistic mechanical models of u_{*t} in handling a number of microscopic r.v.s ?

This Subsection aims at contributing to shed some light on such issues. The deterministic approach is critically reconsidered in the light of a huge collection of experimental measurements. Then, a purely statistical approach to threshold shear velocity is proposed, where the effects of all kinds of uncertainty sources are comprehensively included and merged. Finally, the two approaches are compared.

Data collection and ensemble setting

The data already collected in Fig. 2.6 are complemented by additional experimental measures collected from review papers [153, 78], and studies addressed to the evaluation of sand transport rate for single particle diameters. Table 4.1 lists in chronological order the considered studies. For each of them, the number # of the tested samples is given: an overall collection of 133 setups follows. All studies test nominally dry granular matters. For each setup, the cited papers provide the grain mean, or median, diameter. Except for [90] and [136], granular matter is sand and/or dust grains. In Table 4.1 and in the following the equivalent reference diameter is noted as d for the sake of conciseness.
The complete ensemble of retained sand experimental measurements of u_{*t} is plotted in Fig. 4.1 versus d. On the one hand, the dependency of u_{*t} on d is qualitatively confirmed over the ensemble. On the other hand, a significant dispersion of the data can be easily observed, notably for small and medium sand diameters. In other terms, u_{*t} takes different values at the same d. This feature suggests

Table 4.1: Collected studies: Reference, number of samples, reference diameter

Reference	#	d [mm]
Bagnold (1937) [12]	6	$0.05 \leq d \leq 0.92$
Chepil (1945) [51]	11	$0.02 \leq d \leq 1.57$
Kawamura (1951) [144]	2	0.25, 0.31
Zingg (1953) [354]	5	$0.20 \leq d \leq 0.72$
Chepil (1959) [52]	5	$0.20 \leq d \leq 0.72$
Belly (1964) [20]	1	0.44
Kadib (1964) [141]	1	0.15
Lyles and Krauss (1971) [182]	3	$0.24 \leq d \leq 0.72$
Fletcher (1976) [90]	7	$0.01 \leq d \leq 0.31$
Iversen et al. (1976) [136]	33	$0.01 \leq d \leq 3.09$
Logie (1981) [176]	4	$0.15 \leq d \leq 0.43$
Logie (1982) [175]	1	0.24
Howikawa et al. (1983) [125]	1	0.28
Tian (1988) [294]	3	$0.11 \leq d \leq 0.55$
McKenna Neumann (1989) [195]	3	$0.19 \leq d \leq 0.51$
Darwish (1991) [61]	5	$0.22 \leq d \leq 1.3$
Nalpanis (1993) [209]	2	0.12, 0.19
Nickling and McKenna Neumann (1997) [216]	1	0.20
Dong et al. (2003a) [73]	9	$0.13 \leq d \leq 0.90$
Dong et al. (2003b) [71]	9	$0.13 \leq d \leq 0.90$
Niño et al. (2003) [217]	5	$0.038 \leq d \leq 0.53$
Cornelis and Gabriels (2004) [56]	3	$0.16 \leq d \leq 0.36$
McKenna Neumann (2004) [193]	1	0.27
Roney and White (2004) [258]	12	$0.31 \leq d \leq 0.39$

that setup uncertain/uncontrolled/not detailed parameters other than d affect u_{*t}. Such uncertainties belong to both aleatory uncertainty of the physical setup and epistemic uncertainty. They are detailed in the following for the considered studies.

- In the selected setups the *grain size distribution* is often qualitatively described, e.g. "as uniform as possible" in [12], "very well and poorly sorted" in [20], "naturally graded" in [144]. Such a qualitative description is usually complemented by the nominal size-range of grains (e.g. [12, 71]), while in some papers the cumulative grain size distribution is plotted (e.g. [20, 209, 144, 216, 258]). Recently, [78] have made an effort to evaluate a measure of the diameter variability by evaluating the sorting coefficient for a number of studies. In spite of some difficulties in obtaining such a measure from nominal size-range, it is worth recalling that non negligible variability (e.g.

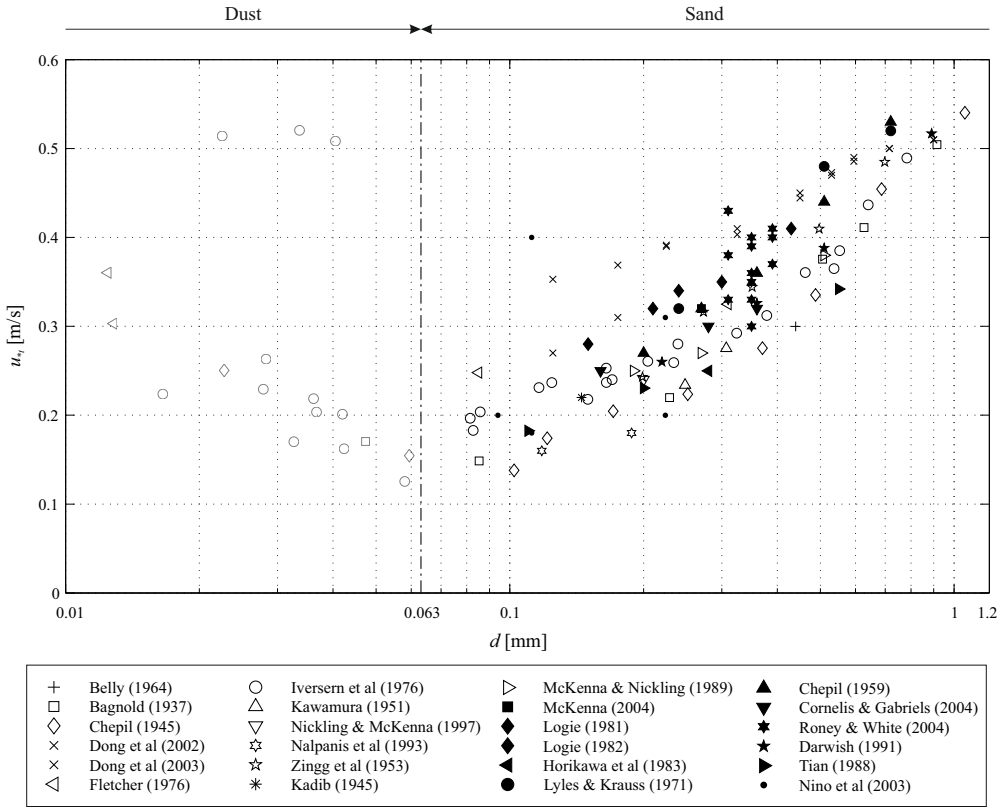

Figure 4.1: Threshold shear velocity measurements collected in literature: dust (empty light grey markers) and sand.

sorting ≈ 0.05, coefficient of variation $c.o.v. \approx 0.12$ in [52]) results also from sieving addressed to obtain sands as uniform as possible. Even greater variability characterizes natural sands (e.g. sorting ≈ 0.65, $c.o.v. \approx 0.35$ in [144]). Other randomness of the grain features (e.g. grain shape, surface microstructure, grain position relative to the other bed particles, grain mineralogy) are not specified in the collected studies.

- *Air humidity* during wind tunnel tests is given and systematically addressed only by [141] to the authors' best knowledge.
- The *quantitative definition of the threshold shear velocity* is not commonly adopted in all the studies. Only [182] provide several u_{*t} values from visual observations depending on the kind of grain motion.
- Analogously, u_{*t} *measurements* and *post processing techniques* are heterogeneous among the studies [24, 347]. Only [258] prove their effects on threshold shear velocity by adopting three different techniques.

The present study is devoted to the characterization of threshold shear velocity for sand only. Hence, setups adopting dust, i.e. having $d < 0.063$ mm according to [133], are discarded (empty light grey markers in Fig. 4.1). It is worth noting that "very coarse" sand ($d > 1.2$ mm) as defined by [93] is not included in the sand ensemble because of the scarceness of available experimental data. An overall sand ensemble having $\# = 109$ results.

Deterministic approach: non-linear regression

Prior to the statistical analysis of the ensemble above, non-linear regression is applied to the collected data in order to refit some of the semi-empirical macroscopic models available in literature. The refitting objective is twofold: on the one hand, the field of application is limited to sands, i.e. on a physics of entrainment relatively simpler than that governing dusts; on the other hand, model parameters are fitted to a number of data higher than that originally adopted by the authors of the models. The models proposed by Bagnold [11] (Eq.4.1) and Shao & Lu [271] (Eq.4.2) are selected because of their compactness, i.e. their dependence from a small number of empirical parameters (A_b, A_s and γ). The two semi-empirical models are reported below for the sake of convenience:

$$u_{*t} = A_b \sqrt{\frac{\rho_p - \rho_a}{\rho_a} g d}, \tag{4.1}$$

$$u_{*t} = A_s \sqrt{\frac{\rho_p - \rho_a}{\rho_a} g d + \frac{\gamma}{\rho_a d}}. \tag{4.2}$$

Beside the single-valued estimates of a goodness-of-fit, for each model the prediction Confidence Intervals (CIs) are evaluated at 5^{th} and 95^{th} percentiles, i.e. the interval within which the true mean value is expected to lie. Fig. 4.2 compares the refitted laws to the original ones, while the corresponding model parameters are summarized in Table 4.2 and 4.3. The following remarks can be outlined:

Table 4.2: Original model parameters

	Bagnold (1941) [11]	Shao and Lu (2000) [271]
A [-]	0.100	0.111
γ [N/m]	-	2.9×10^{-4}

- for both fittings $R^2 \approx 0.75$. On the one hand, this relatively high value confirms grain size is the primary control of u_{*t}. On the other hand, the value is by far lower than unit: hence, u_{*t} cannot be approximated as a deterministic function of d. In other words, the deterministic approach is not able to completely capture the threshold variability.

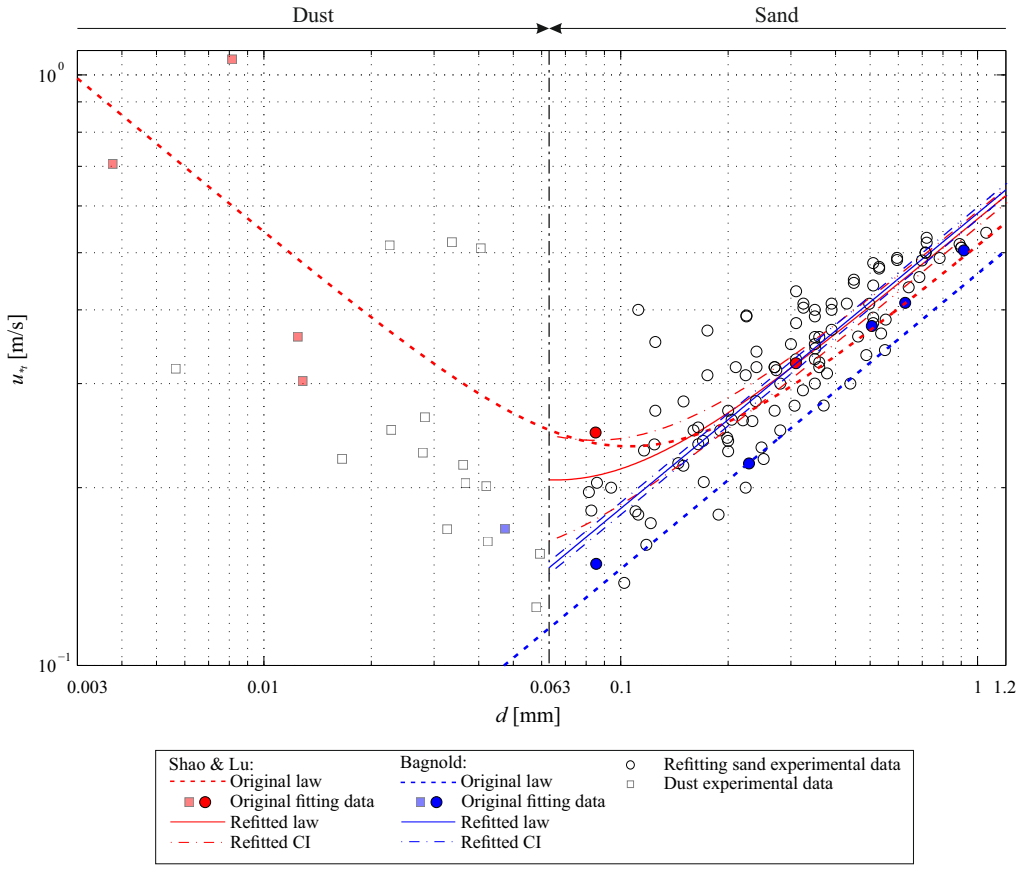

Figure 4.2: Non-linear regression and CIs for [11] and [271]

Table 4.3: Refitted model parameters

	Bagnold (1941) [11]	Shao and Lu (2000) [271]
A [-]	0.127	0.124
γ [N/m]	-	1.12×10^{-4}
R^2	0.74	0.75

- both refitted laws pretty agree for $d > 0.2$ mm, i.e. they share both the asymptotic trend due to the common dependency of u_{*t} on $\sqrt{d}$, and the intercept, i.e. $A_b = 0.127 \approx A_s = 0.124$. This finding is in the spirit of the Shao's model, whose corrective term $\gamma/\rho_a d$ is conceived to modify Bagnold's model at low d only;
- generally speaking, the refitted laws predict higher values of u_{*t} for given

d. It is worth pointing out that the ensemble includes a number of poorly sorted and natural sands, while the ensemble originally adopted by [11] and [271] were limited to sand as uniform as possible. Hence, interspersed small particles provide additional cohesive forces also for medium and coarse natural sands [258];

- regarding the model by [271] at small d, the refitted law predicts u_{*t} values lower than the original law, because fitting is restricted to sands and exclude dusts. In other words, the refitted Shao's law mimics herein only the sand physics, and its trend at low d is not driven by the dust physics, and notably by the very high values $u_{*t} \approx 0.5$ m/s provided by [136] at $d = 0.023, 0.034, 0.041$ mm and $u_{*t} > 1$ m/s provided by [90] at $d = 0.008, 0.009$ mm. A lower value of γ for the refitted law follows;

- CI of the Bagnold fitting is quite narrow (being the model easily reducible to a linear regression model). Conversely, the lower d is, the wider CI in Shao's model is, because of the statistical uncertainty on the parameter γ (Eq. 4.2), which has its main effects for small d.

Statistical approach: copula-based quantile regression

In the following a statistical approach is proposed, having in mind both the number of uncertainty sources and the limitations of the deterministic approach.

Each source of uncertainty and related microscopic parent r.v. are not separately described in statistical terms. Conversely, the threshold shear velocity is modeled as a single, comprehensive, bulk random variable that reflects the effects of all the sources of uncertainty. A continuous dependance of such a random variable on the reference diameter is clearly observed in terms of mean by the deterministic approach. The adopted statistical method is intended to:

- recognize and describe, if any, the dependence of u_{*t} on d not only in terms of mean value but also with reference to higher statistical moments and percentiles;

- discard bias eventually due to the relatively low cardinality of the learning data set and to the non uniform distribution of the reference diameters within it. In fact, the reference diameter that happened to be employed in each original study is not a random variable but a deterministic setup feature. However, the ensemble of sand diameters tested in existing literature does not result from a deterministic research plan.

In order to reach the goals above, it is useful to consider the ensemble of the reference diameter collected from literature as a set of realizations of a random variable. This allows to quantitatively describe in proper statistical terms the structure of

dependence between the random variable of interest u_{*t} and the sand diameter d by means of the copula modeling. In conceptual terms, the copula modeling allows to express the dependence of two random variables (e.g. u_{*t} and d in this case) through subdivision of their joint distribution into two contributions: the marginal distributions of the individual r.v.s and their interdependency, described by the copula [307]. From the joint distribution, one can derive the distributions of u_{*t} conditioned to given values of d, and any corresponding percentiles of interests.

In the following the copula modeling is briefly outlined, having in mind that only recently it has been introduced in some engineering fields (see e.g. [98] in hydrology) and physical sciences (see e.g. [268] in geophysics). For the sake of generality, the r.v.s of our interest, d and u_{*t}, are replaced by two general r.v.s, X and Y, respectively. Given the joint cumulative distribution function $F(x, y)$ of a pair of random variables (X, Y), under suitable assumptions of continuity [212], it can be also written as

$$F(x, y) = C\left\{F_X(x), F_Y(y)\right\}, \ x, y \in \mathbb{R} \tag{4.3}$$

where F_X and F_Y are the cumulative marginal distributions of X and Y, respectively, while $C : [0,1]^2 \to [0,1]$ is the copula of the pair (X, Y).
The copula C, which is the cumulative joint distribution of a pair (U, V) of variables uniformly distributed over [0,1], entirely expresses the dependence structure between X and Y, removing the effects of marginal distributions, and letting immediately observable its main characteristic, like, e.g., positive or negative concordance. Using copulas in estimation of joint distributions, or estimation of relationships among random variables, marginal distributions are firstly evaluated and then a specific copula is fitted with respect to the empirical one available by experimental measurements, i.e. the learning data set. Having removed the effect of marginal behaviours, the copula selection is independent of the marginal distribution choice [298]. Several copulas are reported in literature [212]. For instance, inverted Clayton copula, also known as Heavy Right Tail copula or Burr copula (see, e.g. [307, 308]), is reported below being the employed copula in the following.

$$C(u, v) = u + v - 1 + \left[(1-u)^{-1/\alpha} + (1-v)^{-1/\alpha} - 1\right]^{-\alpha}, \ u, v \in [0,1], \alpha > 0 \tag{4.4}$$

where α is a fitting parameter. Once the copula is fitted according to available measurements, a sample of any cardinality can be generated. Thus, $C(u, v)$ can be transformed back into the original units using the marginal distributions. In fact, the resulting pairs $(x, y) = (F_X^{-1}(u), F_Y^{-1}(v))$ can be deduced by inverting the cumulative distribution functions (see [98] for further details).
From the copula generated sample one can derive conditional probability density functions of Y given X. In turn, point wise percentiles $p_\tau(y)$ of Y can be deduced

from the conditional probability density functions. In fact, given the joint cumulative distribution function $F(x, y)$, it can be first derived the joint density (Eq.4.5) and the conditional density (Eq.4.6)

$$f(x, y) = \frac{\partial^2 F(x, y)}{\partial x \partial y} \tag{4.5}$$

$$f(y \mid x) = \frac{f(x, y)}{f_X(x)} \tag{4.6}$$

from which, any percentile can be obtained as

$$p_\tau(y) = Q_{Y|X}(\tau) \tag{4.7}$$

where $Q_{Y|X}(\tau)$ is the τth quantile of Y given X. Alternatively, the copula modeling allows to directly evaluate high order statistics and perform a quantile regression to obtain any percentile of Y as a function of X. From [30], fixing the conditional probability of Y given $X = x$ at some quantile τ, so that $\partial C(u, v)/\partial u = \tau$, and solving for v, we have [150]:

$$p_\tau(v) = Q_{V|U}\left(\tau \mid u\right) \tag{4.8}$$

and consequently,

$$p_\tau(y) = F_Y^{-1}\left(Q_{V|F(X)}\left(\tau \mid F(x)\right)\right) \tag{4.9}$$

is defined the quantile regression function conditional on X. Hence, in function of τ, one can define any quantile curve of the random variable Y.

In the following the results are presented and discussed by retracing the main methodological steps previously outlined. First, the marginal distributions $F(d)$ and $F(u_{*t})$ are fitted. Secondly, a specific copula is fitted with respect to the learning data set. Finally, the bivariate joint density $f(d, u_{*t})$ is recovered and the conditional probability density functions $f(u_{*t} \mid d)$ are obtained.

Since the marginal distributions of $F(d)$ and $F(u_{*t})$ are a priori unknown, we first aim at assessing which distributions for the diameter and for the threshold shear velocity fit the collected data set. Several guess parametric distributions are considered, such as lognormal, loglogistic, gamma, Weibull. In order to assess the goodness of the fit, Anderson and Darling test is used because of the high weight placed on observations in the tails of distribution [4]. The null hypothesis is not rejected for any tested parametric distribution, being the resulting p-values always greater than its threshold value $p_t = 0.05$. Among tested parametric distributions, lognormal and gamma ones resulted in the highest p-values. In particular, lognormal distribution is highly scored ($p \approx 0.87$) for d, while for u_{*t} the gamma distribution obtains the largest p-value ($p \approx 0.71$). Fig. 4.3 collects the empirical cumulative distributions functions and the best fitting parametric ones (lognormal

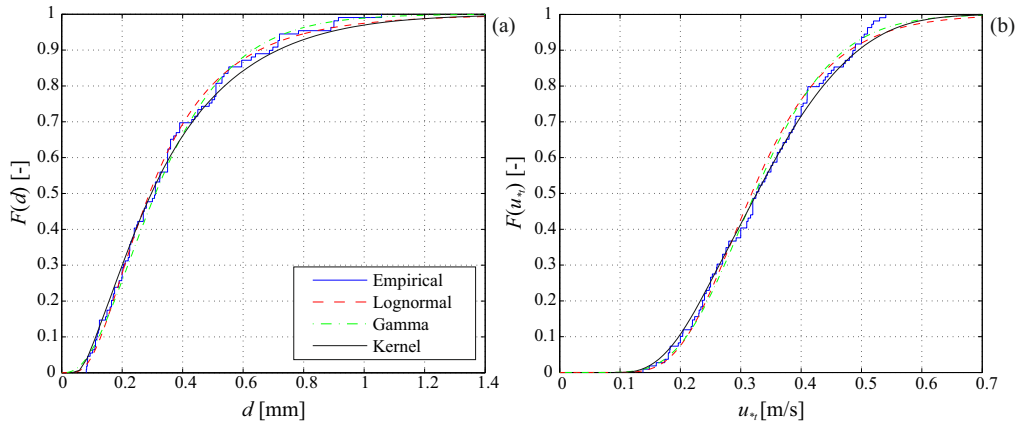

Figure 4.3: Marginal distributions fitting: sand diameter (a) and threshold shear velocity (b)

and gamma). For the sake of generality, also non-parametric distributions based on kernel method are considered. Gaussian kernels are adopted. Their supports are bounded to positive values having in mind the physical meaning of the r.v.s. In particular, the lower bound of d is not forced to be equal to the conventional limit diameter between dust and sand. Indeed, this deterministic nominal value does not comply with the adopted statistical approach. The kernel cumulative distributions functions for d and u_{*t} are also plotted in Fig. 4.3. Both parametric and non-parametric distributions fit well the empirical one at the lower tail but depart at the upper tail, probably not resolved enough by the available data. The kernel distributions best fit around the median values of d and u_{*t}. In the following the non parametric distribution is retained for the sake of generality and because of its goodness-of-fit.

The original learning data set is plotted in terms of d-u_{*t} pairs in Fig. 4.4(a), together with the empirical and non parametric marginal distributions. Hence, it is reduced to the copula scale and shown in terms of scatter plot of the $F(d)$-$F(u_{*t})$ pairs in Fig. 4.4(b). From Fig. 4.4(b) one can observe that the transformed learning data set is strongly correlated with only upper tail dependence. In other words, the points are concentrated in the upper right corner and they open approaching the lower left corner. This empirical qualitative evidence drives the choice of the copula family to be adopted for fitting [268, 98]. On the one hand, elliptical copulas, i.e. Gaussian or Student-t copula, are expected to be inappropriate to describe such a dependence because of their symmetric tail behavior. On the other hand, Archimedean copulas, e.g. Frank, or Clayton copula, being in principle asymmetric, allow for simulating different tail behavior. Because of their flexibility, Archimedean copulas have been previously applied to others physical problems such as in geoscience [268]. For real world, low-cardinality learning data set the choice of

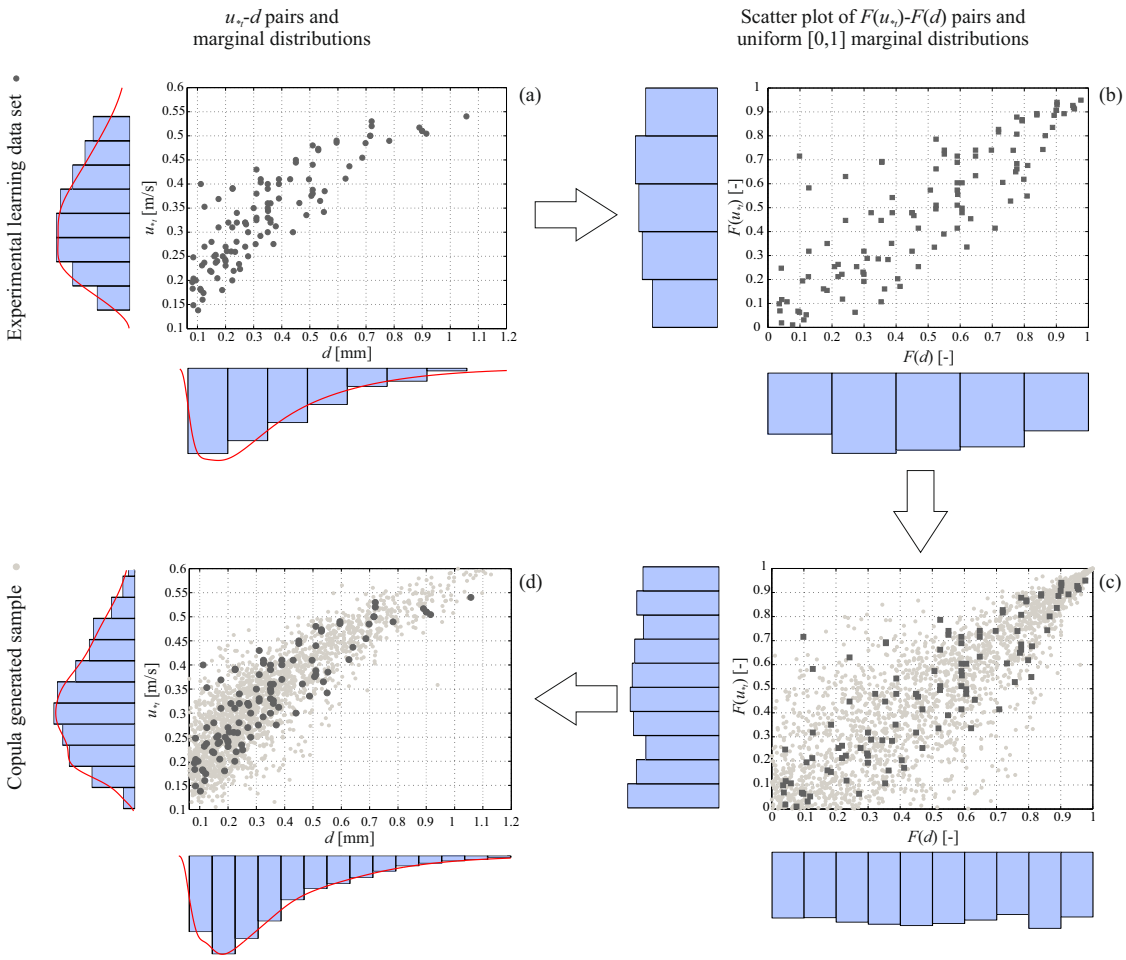

Figure 4.4: Copula fitting to experimental learning data set: plot of experimental learning data set (a), scatter plot of the pairs $F(d)$ and $F(u_{*t})$ (b), random sample from inverted Clayton copula (c), resizing to original scale of the learning data set (d).

the copula can be performed a posteriori by comparing the $F(d)$-$F(u_{*t})$ scatter plot of the observed data set to an artificial data set generated from the fitted copula [99]. Such graphical diagnostics of goodness-of-fit is performed for several guess copulas. The cardinality of the artificial data is set equal to $\# = 2000$ for the sake of clarity in visualization. Results about the copulas not further retained are shown in Fig. 4.5, while the inverted Clayton best fitting copula is assessed in Fig. 4.4(c). Observed data set is highlighted using black marks, while grey marks are used for the artificial data set. Elliptical copulas (t-student and Gaussian ones, Fig. 4.5a,b, respectively) predict high and equal dependence at both upper tail, i.e. close to (1,1), and lower tail, i.e. around (0,0), in line with the theory. Frank copula (Fig.

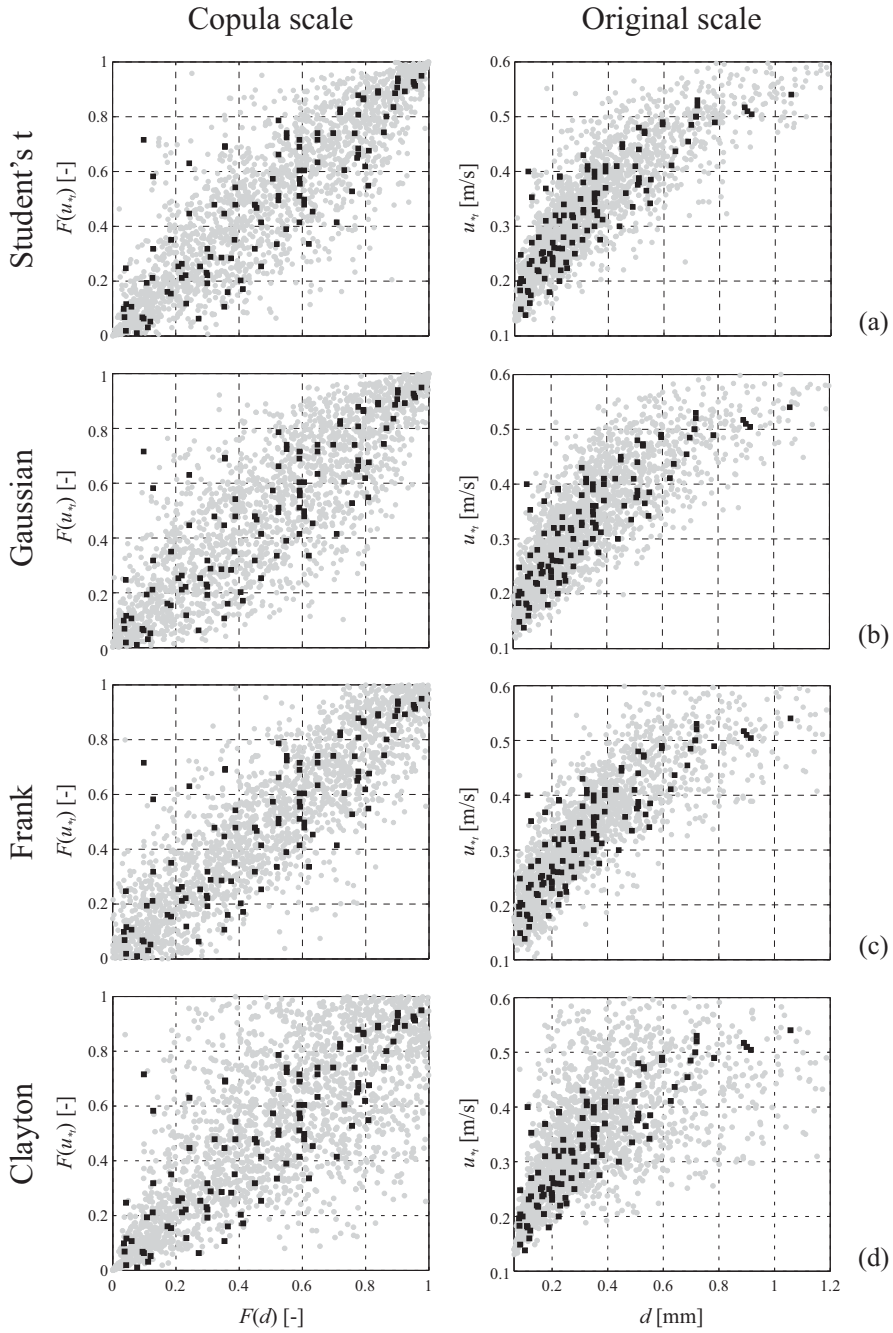

Figure 4.5: Graphical diagnostics of goodness-of-fit for not retained copulas

4.5c) shows no tail dependencies and Clayton copula (Fig. 4.5d) shows lower tail dependence only: both are not suited to replicate the observed dependence. Conversely, the inverted Clayton copula (Fig. 4.4c) replicates the heavy concentration of probability in the upper tail, and lower dependence in the lower tail. Only a light discrepancy can be observed by the fact that the scatter plot of learning data set is slightly asymmetric with respect to the bisector, while the inverted Clayton copula is not. The inverted Clayton best fit results in copula parameter $\alpha = 3.7$ and Kendall's rank correlation $\tau = 0.65$. The convergence of the copula parameter α is checked for increasing number n of the learning data included in the set, being $n \leq 109$. α itself as well as its weighted residual error $\alpha_{res,n} = |(\alpha_n - \alpha_{n-1})/\alpha_n|$ are evaluated for growing sizes n and averaged over 1000 random permutation of the order of the learning data set. The convergences versus n are plotted in Fig. 4.6. The convergence of α (Fig. 4.6a) shows an overall monotonic trend and the convergence rate at complete learning data set ($n = \# = 109$) is very low. The weighted residual error $\alpha_{res,n} \approx 10^{-3}$ at $n = \# = 109$ is low enough for practical applications (Fig. 4.6b). In spite of such an encouraging overall convergence, higher accuracy would need higher cardinality of the learning data set.

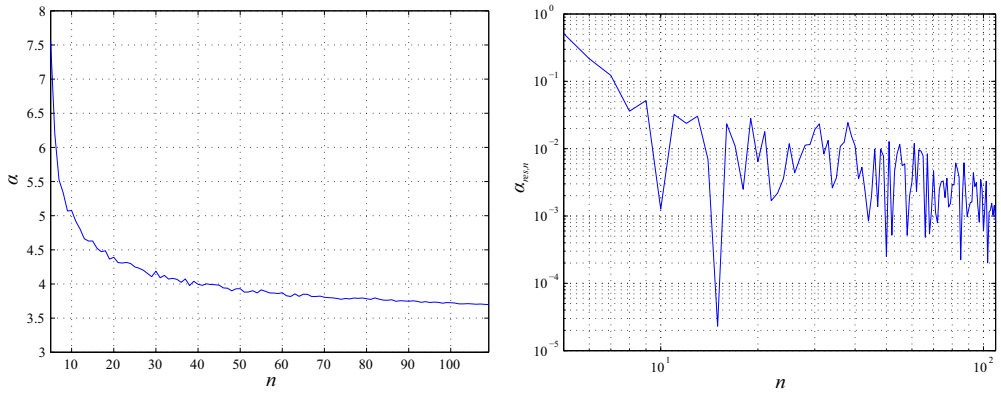

Figure 4.6: Convergence of copula fitting in terms of the parameter α (a) and weighted residual $\alpha_{res,n}$ (b)

Finally, in Fig. 4.4(d), the pairs $F(d) - F(u_{*t})$ are resized back to the original scale of the data calculating the inverted kernel cumulative distribution. The corresponding marginal distributions are plotted in the same Fig.. Both $d - u_{*t}$ pairs and marginal distributions well agree with the ones related to the observed original data.

The cardinality of the artificial sample is increased from $\# = 2.000$ to $\# = 10.000.000$ in order to further proceed in the post processing of the joint and conditional probability density functions. The joint probability density function $f(d, u_{*t})$

of the two random variables d and u_{*t} is recovered by evaluating Eq. (4.5). It is plotted in Fig. 4.7, where the learning data set is superimposed. Hence, the conditional

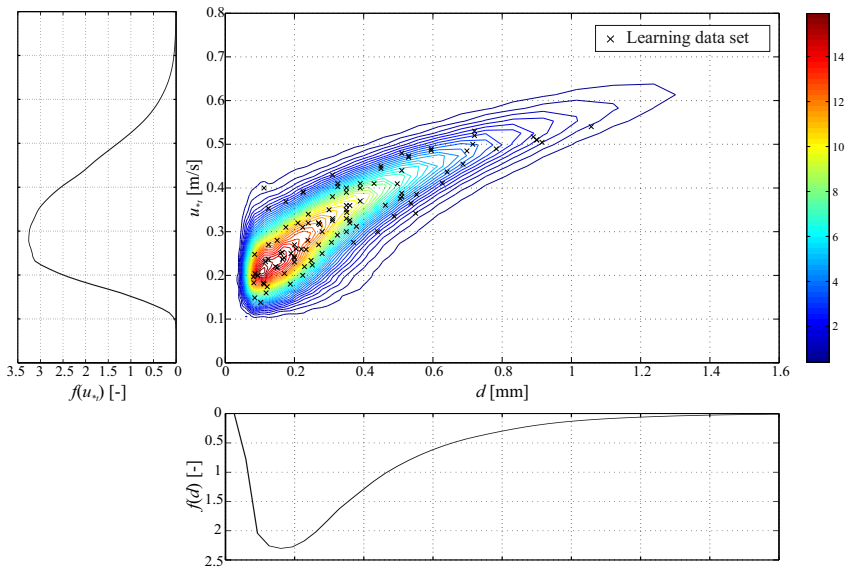

Figure 4.7: Joint and marginal probability density functions derived from copula fitting

probability density functions of the threshold shear velocity $f(u_{*t} \mid d)$ for given values of the diameter d are obtained according to Eq. (4.6). In Fig. 4.8(a), several $f(u_{*t} \mid d)$ are plotted for some selected values of d in the range $0.063 \leq d \leq 1.2$. The coefficient of variation $c.o.v.$ and the skewness sk of the conditional probability density functions are plotted versus the diameter in Figures 4.8(a) and (b). The following remarks can be outlined:

- the higher the diameter is, the higher the mean value of the threshold shear velocity and the lower its variance are;
- the monotonic decrease of the coefficient of variation for growing reference diameter properly reflects the expected decreasing role played by interparticle forces and related uncertainties. The coefficient of variation attains values in the range $0.05 \leq c.o.v. \leq 0.25$, i.e. moderate but not negligible values with respect to other in situ environmental r.v.s (e.g. turbulent wind velocity). The authors conjecture this is due to the fact that wind tunnel setup conditions are more controlled than in situ ones;
- the skewness values indicate that the conditional probability functions are not fully symmetric, except around $d \approx 0.22mm$ where $sk \approx 0$. Skewness is weakly positive (up to $sk = 0.6$) for fine sands ($0.063 \leq d < 0.22mm$),

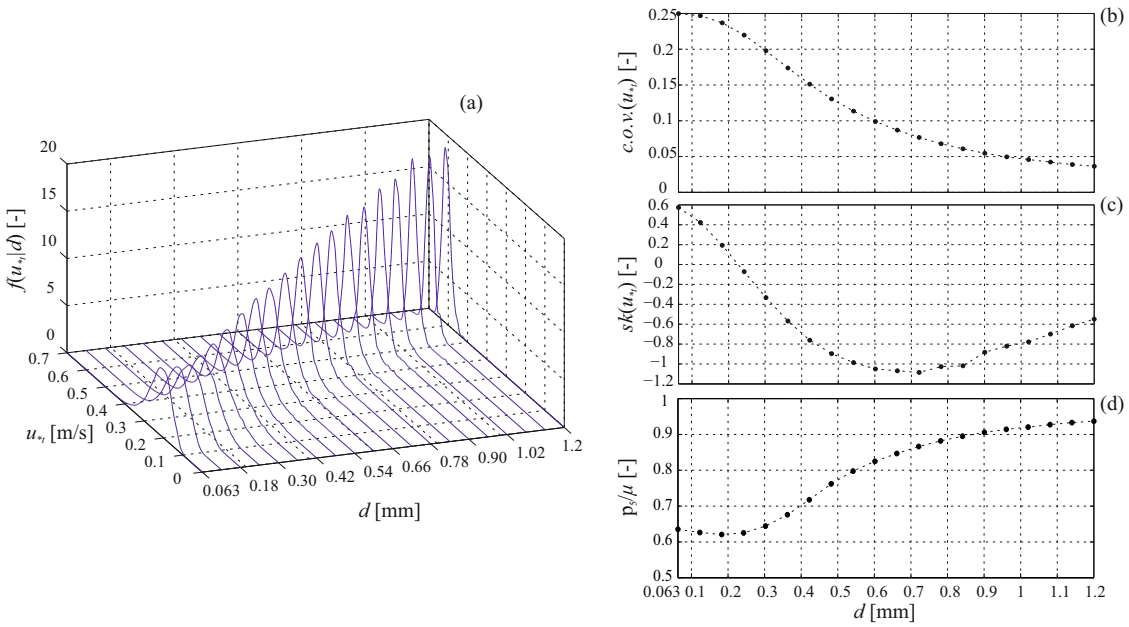

Figure 4.8: Conditional distributions of u_{*t} on d (a), coefficient of variation (b), skewness (c) and 5^{th} percentile - mean value ratio (d) of u_{*t} as a function of d

that is the probability density function is right tailed or, in other terms, not negligible probability density occurs at u_{*t} values quite higher than the mode. The authors conjecture that cohesive resisting force is the main physical cause of such positive skewness. Conversely, skewness is moderately negative (up to $sk \approx -1$) for medium and coarse sands ($0.22 < d \leq 1.2mm$). In such an interval, sk trend versus d is no longer monotonic and increases for diameters higher than about $0.7mm$ (coarse sand). The authors conjecture that Saffman lift force is the main physical cause of such negative skewness [260]. In turn, the lift force is expected to be affected by the uncertain grain relative position with respect to other bed particles.

Any other statistical moment or percentiles can be evaluated for each conditional probability functions. For instance, Fig. 4.8(d) plots the 5^{th} percentile - mean value ratio versus the sand diameter. The quasi-monotonically increasing trend is qualitatively opposite to the decreasing of $c.o.v$. The values vary in the range $0.6 \leq p_5/\mu \leq 0.94$, i.e. the 5^{th} percentile is around 0.65 times the mean value for fine sands and it reaches almost 0.94 times the mean value for coarse sands.

Comparison between deterministic and statistical approach

The main findings of the proposed statistical approach are here critically compared to the results of the deterministic approach. Fig. 4.9 collects the original

learning data set, the refitted deterministic laws of $u_{*t}(d)$ and some statistics obtained from the conditional probability density distributions $f(u_{*t} \mid d)$: the mean value $\mu(u_{*t})$, the 1^{st}, 5^{th}, 25^{th}, 75^{th}, 95^{th} and 99^{th} percentiles.

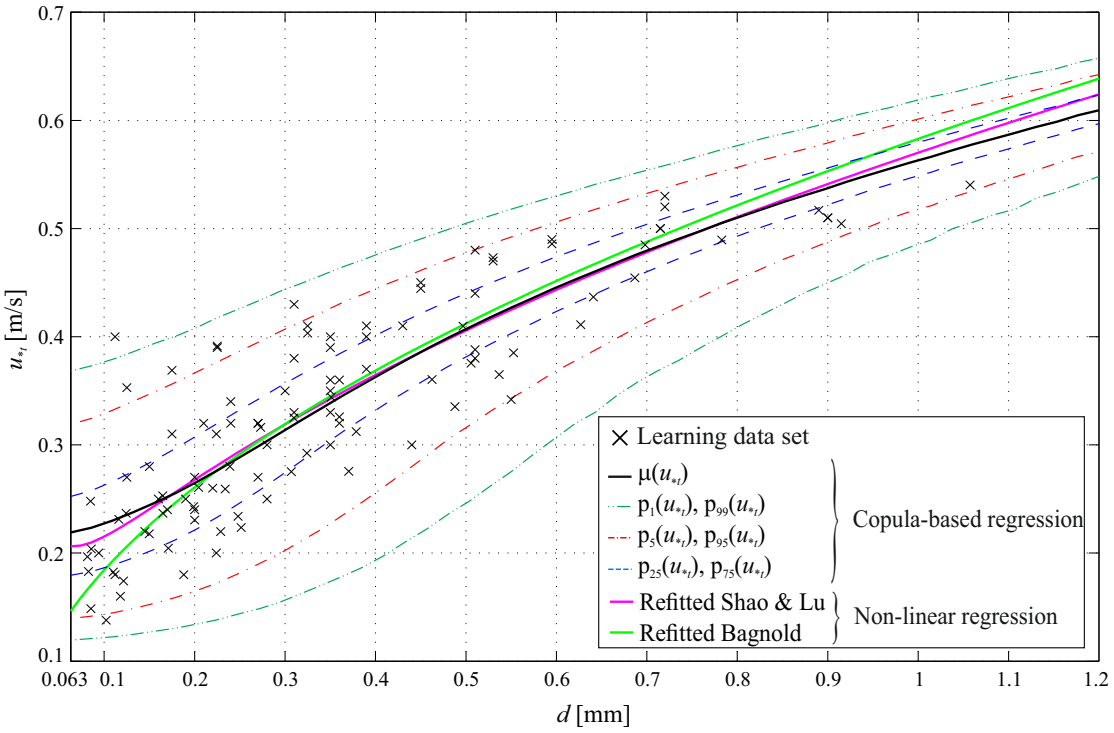

Figure 4.9: Comparison between copula regression and non-linear regression: mean values $\mu(u_{*t})$, $p_1(u_{*t})$, $p_5(u_{*t})$, $p_{25}(u_{*t})$, $p_{75}(u_{*t})$, $p_{95}(u_{*t})$, $p_{99}(u_{*t})$ percentiles versus refitted [11] and [271] laws

It is worth pointing out that:

- the mean value $\mu(u_{*t})$ overall agrees with the refitted law proposed by [271], even if they result from completely different approaches. Generally speaking, the statistical approach provides consistent results in mean terms with the traditional and most established deterministic laws: this outcome is expected because of the common learning data set, but is not for granted;
- in addition, the proposed statistical approach enriches substantially the description of u_{*t} versus d. Indeed, for a given diameter any value of the threshold shear velocity is associated to a probability of not-exceedance;
- in lieu of adopting the nominal value of u_{*t}, a given safety level can be set in engineering practice, and the corresponding value of the threshold shear

velocity adopted in the estimation of the sand transport rate.

4.1.2 Probabilistic sand transport rate

According to the authors, the emerging differences (see Subsection 2.2.2) among semi-empirical sand transport rate models, or Q-models, can be regarded as the result of the inherent *uncertainty* in the saltation phenomenon. A comprehensive description of uncertainties concerning the prediction of aeolian sand transport rate is not available in the literature. Similarly to Subsection 4.1.1, uncertainty is here classified distinguishing between *aleatory* and *epistemic* uncertainty [355], both of which are relevant to the sand transport case.

Aleatory uncertainty arises not only in nature but also in the laboratory environment, where the properties of aeolian processes can be nominally controlled in both space and time. [283] discussed aleatory uncertainty and suggested that a satisfactory solution for sand transport rate variability can only be given in terms of probabilistic models because of the large degree of unpredictability in the subfields involved in the phenomenon, such as fluctuating wind, irregular shape of sand grains, grain size distribution and relative position of grains on the sand bed.

Epistemic uncertainty, and in particular *model*, *measurement* and *parameter* uncertainties, are discussed in the studies of [270] and [16]. According to the authors, the uncertainty concerning the mode of u_{*t} to be used in sand transport equations can be considered as an *epistemic model* uncertainty too because it is related to the lack of knowledge about the Q-model. Indeed, the mode of u_{*t} to be adopted is not unequivocally established in the literature, an issue that has been somewhat overlooked in the geomorphological literature to date. Two threshold velocities have been recognized: the fluid threshold and the impact threshold (see Subsection 2.2.1). However, there is no unanimity in the literature as to which threshold is the most appropriate for modelling sand transport rate: some authors prefer the impact threshold, others suggest the fluid threshold, and still others recommend a combination of the two. [237] and [153] recommend the impact threshold defined as a linear function of the fluid threshold (85% and 80% of the fluid threshold, respectively). Similarly, [5] and [225] also prefer the impact threshold and provide models for its estimation. Conversely, [270] refers to the fluid threshold only, whilst [274] adopt the fluid threshold for small Q and, for increasing Q, an exponential decreasing u_{*t} to a minimum equal to the impact threshold (85% of the fluid threshold). [152] provides a more sophisticated model for sand transport which considers a hysteretic threshold between the impact and fluid threshold that depends on the history of the system.

The uncertainties reviewed up to this point are innate in Q-models. The author expects that the *uncertainty propagation* to Q from other models also occurs, also due to the uncertainty in u_{*t}. A few authors have recently raised this issue. [270] attributes the Q-model randomness not only to their empirical parameters

but also to variability in the threshold shear velocity. Moreover, since a method to determine a single quantitative definition of u_{*t} is not agreed upon (see [286]), [270] notes that any estimate of u_{*t} must involve a degree of subjectivity. In particular, he conjectured that such uncertainties in defining u_{*t} could outweigh the differences inherent in the functional forms of the sand transport rate models. The quantification of uncertainty in u_{*t} has recently been assessed by [244], and [78] and [318] note that such uncertainty in threshold estimates can be expected to propagate to sand transport rate predictions.

Given these points, two main questions are pertinent: i. How does the degree of uncertainty in sand transport rate (Q) vary with respect to the uncertainty in estimates for the threshold shear velocity (u_{*t})? ii. How do different sand transport rate models behave when threshold shear velocity is considered as a statistically random variable?

Four key, semi-empirical models of sand transport rate are here adopted to evaluate the impact of uncertainty propagation. Threshold shear velocity is assumed as the only random variable affecting sand transport rate and, as a result, instead of having a single deterministic value of sand transport rate for given values of u_* and d, a range of different values describing a probability distribution are obtained.

Methods

The methods for evaluating uncertainty propagation from the parametric uncertainty of the threshold shear velocity to the model prediction of sand transport rate are here described and justified. From here on, the threshold shear velocity conditional probability density function $f(u_{*t} \mid d)$ is expressed as $f_{u_{*t}}$ for the sake of conciseness.

Uncertainty propagation from threshold shear velocity to predictions of sand transport rate is investigated by comparing dimensionless statistical metrics of both Q and u_{*t}. Both numerical and analytical solutions could be applied to evaluate uncertainty propagation [280]. Analytically, for a given grain diameter and shear velocity, the cumulative distribution functions F_Q for sand transport rate can be obtained from the following procedure:

$$F_Q(s) = P[Q \leq s] = P[Q(u_{*t}) \leq s] = P\left[u_{*t} \leq Q^{-1}(s)\right] = F_{u_{*t}}\left[Q^{-1}(s)\right], \ \forall d, u_* \tag{4.10}$$

So, deriving each term, one can find the probability density functions f_Q:

$$f_Q(s) = f_{u_{*t}}\left[Q^{-1}(s)\right] \cdot \left[Q^{-1}(s)\right]', \ \forall d, u_* \tag{4.11}$$

It is worth noting from Eq. (4.11) that the inversion of most of the sand transport rate models can only be performed numerically. Hence, a numerical approach is preferred because a fully analytical solution is not achievable. A classical Monte Carlo

(MC) sampling based method [41] was preferred to other numerical approaches because of its very low computational cost. Furthermore, other numerical approaches (such as functional expansion-based methods like Karhunen-Loeve or polynomial chaos expansions) offer results that are too sophisticated for the relatively simple task covered by the present study. The MC method relies on repeated random sampling in order to obtain numerical probabilistic results. Hence, a set of numerical realizations of the random prediction $Q(u_*, u_{*t})$ was evaluated by varying $u_* \in [0.1{,}2]\ m/s$ and by sampling the random parameter u_{*t} according to $f_{u_{*t}}$. In applying the MC method, it is important to check the convergence of the numerical realizations. Indeed, the rate of convergence of MC is always $1/n^{0.5}$, where n is the number of numerical realizations. It follows that the cardinality # of Q and u_{*t} affects the obtained results and must be chosen in order to reach the convergence of the first statistical moments of Q. Convergence can be checked by means of the weighted absolute error φ_{abs} as well as the weighted residual φ_{res} of the generic parameter φ. They are respectively defined for growing cardinality n as $\varphi_{abs} = |\varphi_{\#} - \varphi_n| / \varphi_{\#}$ and $\varphi_{res,n} = |\varphi_n - \varphi_{n-1}| / \varphi_n$.

In the framework of the MC method, sand transport rate is obtained by referring to some well-known modified Bagnold sand transport models reported in the literature. Semi-empirical modified Bagnold-type sand transport models proposed by [144], [221], [161] and [153] were evaluated to assess the effects of uncertainty on transport predictions. These models are reported in Table 4.4. For the model of [221], v_t is the particle's terminal velocity. [45] parametrized this as a function of the sand grain diameter getting $v_t = -0.775352 + 4.52645 d^{0.5}$, where v_t is expressed in m/s and d in mm.

Table 4.4: Summary of the adopted sand transport rate models

Reference	Q-model	C
Kawamura (1951) [144]	$C\frac{\rho_a}{g}u_*^3\left(1-\frac{u_{*t}^2}{u_*^2}\right)\left(1+\frac{u_{*t}}{u_*}\right)$	2.78
Owen (1964) [221]	$C\frac{\rho_a}{g}u_*^3\left(1-\frac{u_{*t}^2}{u_*^2}\right)$	$0.25+\frac{v_t}{3u_*}$
Lettau and Lettau (1978) [161]	$C\sqrt{\frac{d}{d_r}}\frac{\rho_a}{g}u_*^3\left(1-\frac{u_{*t}}{u_*}\right)$	6.7
Kok et al. (2012) [153]	$C\frac{\rho_a}{g}u_{*t}u_*^2\left(1-\frac{u_{*t}^2}{u_*^2}\right)$	5

It is worth stressing that the models proposed by [144] and [153] do not explicitly take into account the grain diameter only because their semi-empirical parameter refers to $d \approx 0.25$ mm. In this study their semi-empirical parameter is considered constant as an approximation. In fact, [144] does not define the relation between C and d, while [153] provide a relation that cannot be easily computed. However, this assumption doesn't reflect on the uncertainty propagation to Q when expressed in dimensionless statistics such as coefficient of variation and skewness.

In this study, the fluid (or static) threshold shear velocity is adopted for several reasons. First, since it represents the starting point for erosion it is considered highly relevant for modelling purposes and application of model results. Secondly, unlike the impact threshold, appropriate probability density functions for the fluid threshold shear velocity are available from the literature (e.g. [75, 244]). Thirdly, the fluid threshold is likely to be more variable than the impact threshold because it is more dependent upon variability in surface properties. Therefore, the analysis carried out in this paper will provide estimates of the maximum likely uncertainty propagation. Fourthly, when assuming the impact threshold as a linear function of the fluid threshold (i.e. $80\% - 85\%$ of the fluid threshold), the adoption of the fluid rather than the impact threshold doesn't affect the uncertainty propagation to Q when expressed in dimensionless statistics.

In order to account for the uncertainty in u_{*t}, conditional probability density functions of threshold shear velocity, $f_{u_{*t}}$ were taken from Subsection 4.1.1. Given that u_{*t} varies as a function of d, one $f_{u_{*t}}$ exists for each value of d. The range $d \in [0.063, 1.2]$ mm (i.e. from fine to coarse sand) was investigated by means of fifty linearly spaced non-parametric conditional probability density functions $f_{u_{*t}}$.

Preliminary findings

The convergence of the first three Q statistical moments for an increasing cardinality n of $Q(u_*, u_{*t})$ is here first discussed.
The weighted absolute error φ_{abs} as well as the weighted residual φ_{res} of the generic parameter φ were averaged over 100 random permutations of the order of $Q(u_*, u_{*t})$ for an assigned value of $u_*/\mu(u_{*t})$.
The rate of convergence is the same for each grain diameter, shear velocity and Q-model tested. However, the residuals differ with different Q-models and parameters. For example, in Fig. 4.10 the convergence of absolute and residual error is given with reference to the [144] model for $u_*/\mu(u_{*t}) = 1.5$ and $d = 0.25$ mm. Fig. 4.10(a) confirms that the rate of convergence of the absolute error clearly follows the slope $1/n^{0.5}$, in agreement with MC theory [41]. Fig. 4.10(b) plots the weighted residual to evaluate the total number of realizations # required to reach a desired accuracy. For the set-up above, even a modest cardinality $n = 5e{+}2$ allows $\mu_{res,n} \approx \sigma_{res,n} \approx 10^{-3}$ for the mean value and standard deviation of Q. This is a low residual error if compared with common engineering applications. As regards sk, $n = 2e{+}3$ allows a transport rate of about $sk_{res,n} \approx 10^{-3}$. Having in mind the low computational cost of a single realization and for the sake of precision, a cardinality $\# = 1e{+}6$ is adopted in this study.

Overall, a probability density function of Q can be determined for each sand transport rate model and for each value of d and u_*. By way of example, two estimates of f_Q result from varying the Q-models, u_* and d are shown in Fig. 4.11(a),(b) and (c), respectively. The adopted $f_{u_{*t}}$ (dotted line) is also shown for

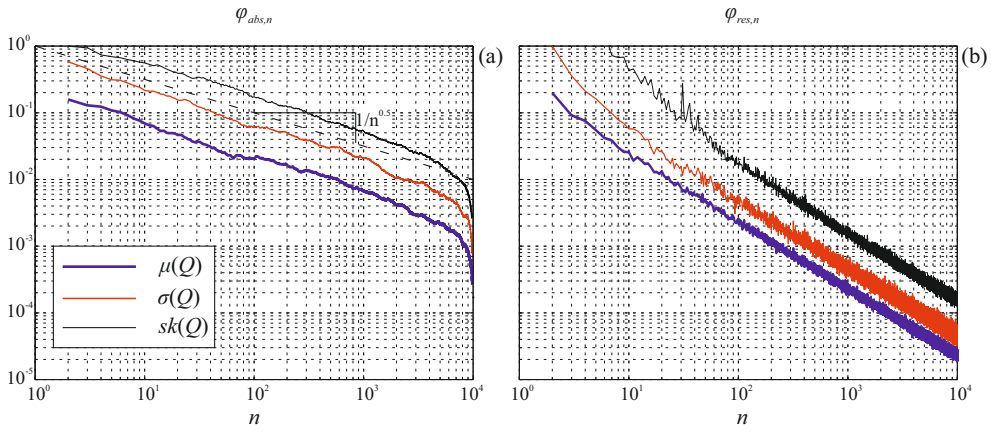

Figure 4.10: Assessment of the MC convergence: weighted absolute error (a) and weighted residual error (b) of the mean value μ, standard deviation σ and skewness sk of sand transport rate estimated by means of the [144] model for $d = 0.25$ mm and $u_*/\mu(u_{*t}) = 1.5$

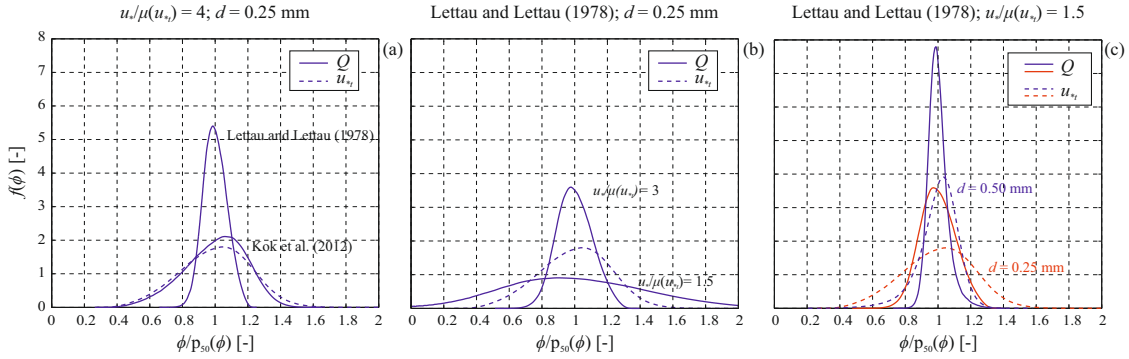

Figure 4.11: Comparison between normalized $f_{u_{*t}}$ and f_Q evaluated by varying Q-models (a), u_* (b) and d (c). The changes of both variance and skewness from $f_{u_{*t}}$ to f_Q are due to the uncertainty propagation.

each f_Q. The probability density functions are plotted over the normalized axis $\phi/p_{50}(\phi)$ of the generic variable ϕ. From Fig. 4.11, it is clear that different models, as well as different values of u_* and d, induce a significant variation in both variance and skewness of Q. As a result, the range of predicted values of Q also changes considerably. An increasing or decreasing variance with respect to the mean value of Q represents an amplification or reduction in the uncertainty, respectively. The skewness quantifies the degree of non-Gaussianity in that uncertainty.

Sensitivity analysis

For a given Q-model, a probability density function of Q corresponds to any point in the parameter plane $d - u_*$. In this study, this plane is sampled by 50 linearly spaced values of $d \in$ [0.063,1.2] mm and 50 linearly spaced values of $u_* \in$ [0.1,2] m/s. This results in as many as 2500 numerical estimates of f_Q for each Q-model, and in 10 billion realizations of Q in total. Given the considerable number of estimated densities f_Q, the uncertainty in sand transport rate is represented by means of its statistical moments, for the sake of brevity and clarity. The mean value μ, the 95^{th} percentile p_{95}, the standard deviation σ and the skewness sk of Q for each Q-model are plotted using contour plots in the parameter plane in Fig. 4.12.

Qualitatively, the results do not appear to differ significantly in average terms. The general trend of $\mu(Q)$ is the same for each sand transport model and also similar to $p_{95}(Q)$. $\mu(Q)$ monotonically increases with increasing u_* for a given d. Conversely, the trend over d for a given u_* is no more globally monotonic except for results from the [144] model. Here $\mu(Q)$ decreases with increasing d for small u_* even if the trend may be locally non-monotonic, while $\mu(Q)$ increases with increasing d for large u_*. Strong discrepancies between the models arise for higher order statistics $\sigma(Q)$ and $sk(Q)$, both qualitatively and quantitatively. However, some similarities in model behaviours can be recognized. First, results from [144] and [153] are qualitatively similar (Fig. 4.12c,d and Fig. 4.12o,p, respectively). Indeed, both $\sigma(Q)$ and $sk(Q)$ show local maxima and minima. Secondly, high moments from [221] and [161] (Fig. 4.12g,h and Fig. 4.12k,l, respectively) reveal common trends. In particular, it is worth noting that $sk(Q)$ remains constant for increasing values of u_* above a common threshold of u_* for each grain size. In sum, while the model proposed by [221] behaves qualitatively like the one of [161], the model proposed by [144] behaves qualitatively like the one of [153]. Whilst some similarities can be identified in the qualitative general trend, the quantitative discrepancies remain significant.

In order to systematically discuss uncertainty propagation from u_{*t} to Q, Q statistics are compared to those of u_{*t}. μ and σ are condensed into the coefficient of variation *c.o.v.*, and p_{95} is normalized with respect to p_{50} in order to deal with dimensionless statistical metrics. In this way, metrics referring to u_{*t} can be directly compared with those of Q. For the sake of graphical clarity, the comparison is made by reducing the 3D plots in Fig. 4.12 to 2D plots, where the generic statistical metric φ is plotted versus one parameter for given values of the other.

In Fig. 4.13, $\varphi(Q)$ are plotted over d for each Q-model and for some sampled values of u_* (black continuous lines). The corresponding statistical metrics of u_{*t} versus d are plotted for comparison (dash dot lines). It is worth recalling that $\varphi(u_{*t})$ does not depend on u_* or the Q-model. Even if Q has a first order dependency on u_*, a stronger determinant is the effective shear velocity (Eq. 4.12), which takes

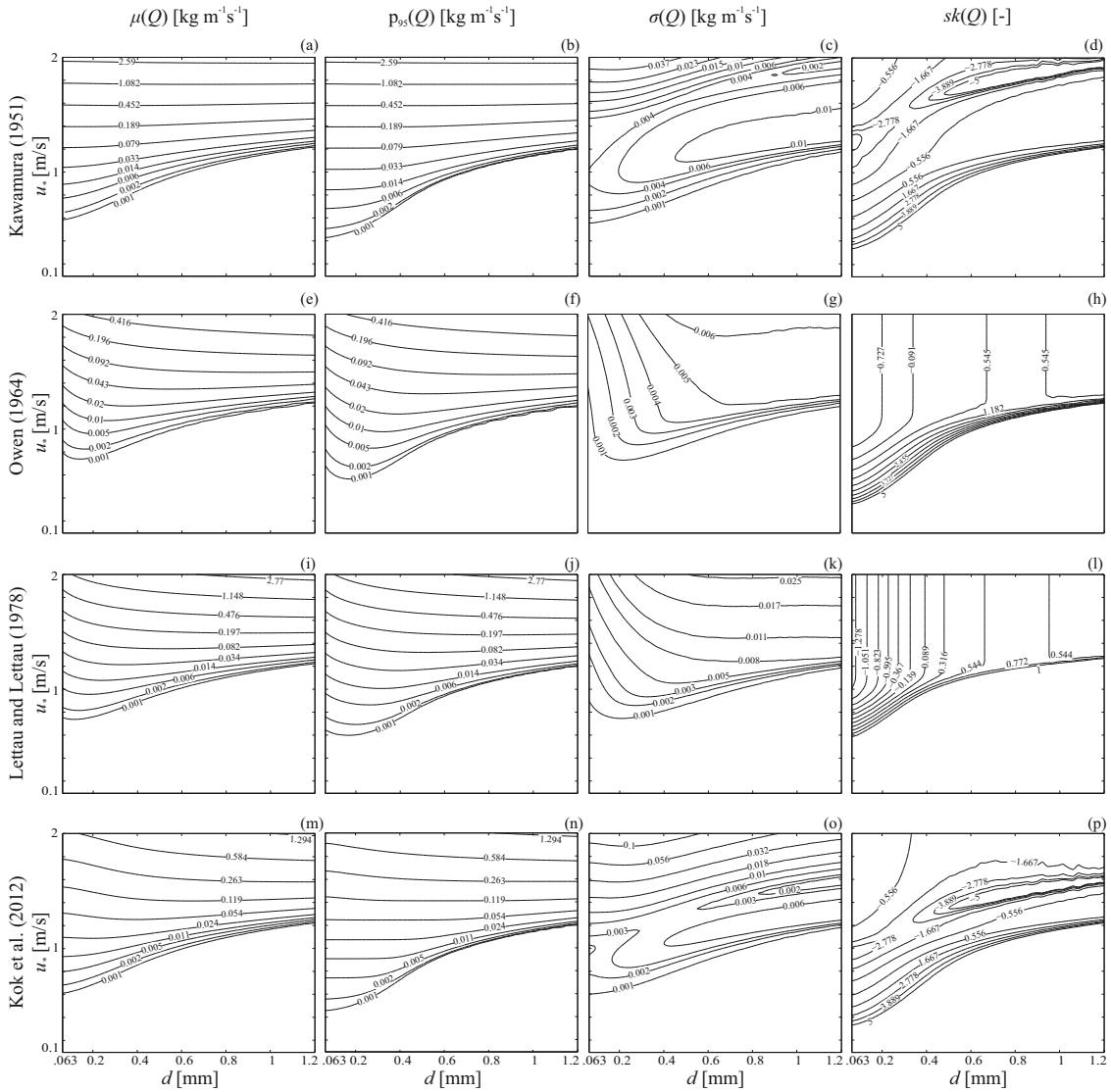

Figure 4.12: Contour plots of the first three statistical moments and 95^{th} percentile of Q. Mean value μ, 95^{th} percentile p_{95}, standard deviation σ and skewness sk according to different Q-models

into account the threshold value u_{*t}. Hence, in Fig. 4.13 the statistical metrics of Q are also plotted for given values of the averaged effective ratio $u_*/\mu(u_{*t})$ (dashed lines).

The variability of the sand transport rate over d with respect to its mean value, i.e. $c.o.v.(Q)$, is controlled by u_* (Fig. 4.13a,d). For slow winds (small u_*), the variability of Q is shown to increase with grain size for a given shear velocity for all the examined Q-models. For fast winds (large u_*), the results vary substantially

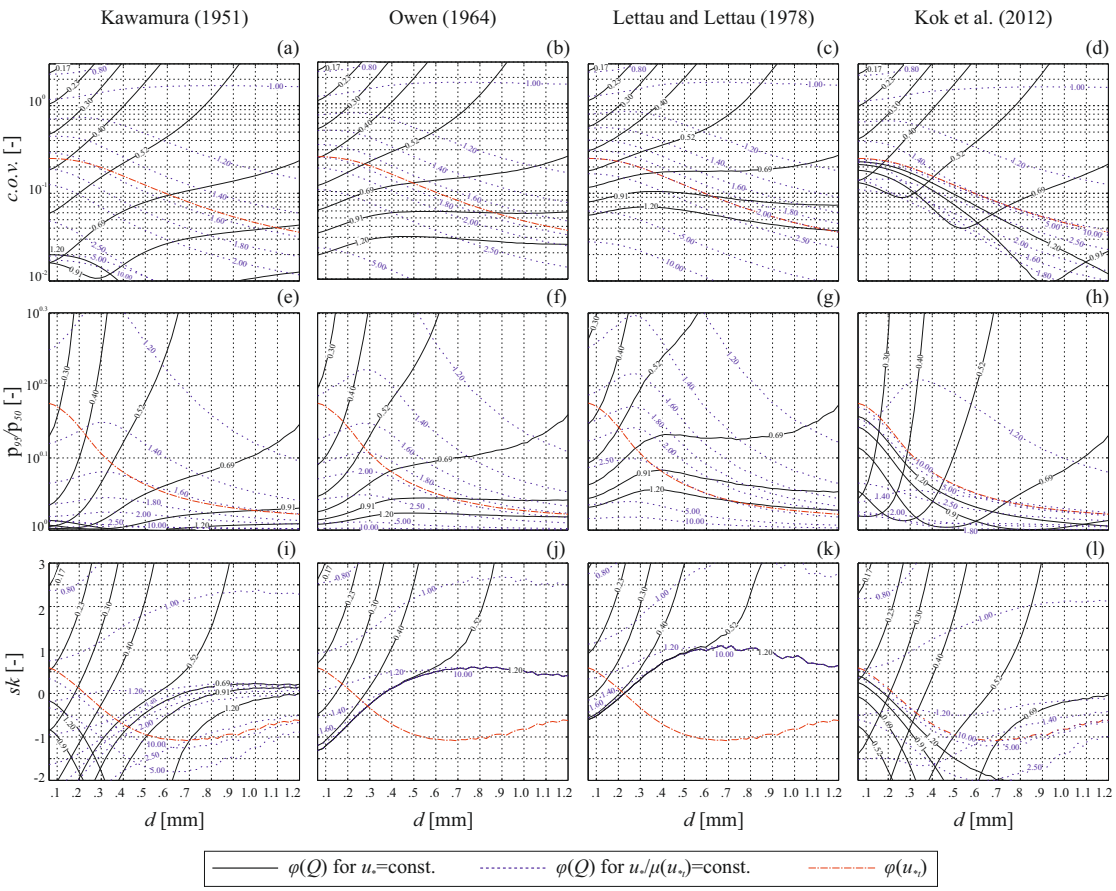

Figure 4.13: Uncertainty propagation from u_{*t} to Q. Q and u_{*t} statistical metrics versus d according to each Q-model

depending on the Q-model. The influence of grain diameter on the variability of Q ($c.o.v.(Q)$) decreases considerably for the [221] and [161] models, while d strongly affects the variability of Q in the [144] and [153] models. The $c.o.v.(Q)$ dependence on d is much clearer for fixed $u_*/\mu(u_{*t})$ ratios. Three fundamental states of the threshold shear velocity can be identified. First, when $u_* > \mu(u_{*t})$ the variability of Q decreases with increasing particle size, i.e. the low variability applies for coarse sands and large effective shear velocity. Secondly, when $u_* \approx \mu(u_{*t})$ the variability of Q is not particularly affected by d. Thirdly, when $u_* < \mu(u_{*t})$ the variability increases with increasing grain diameter d. For a given value of d, the typical relationship is lower variability in Q at higher values of u_*, except in the case of the [153] model (Fig. 4.13d).

The trend of $p_{95}/p_{50}(Q)$ versus d and u_* qualitatively follows the trend of $c.o.v.(Q)$ (Fig. 4.13e-h). Indeed, $p_{95}/p_{50}(Q)$ describes the variability of Q as a

function of the tail event $p_{95}(Q)$, i.e. a large sand transport rate with a low chance of occurrence. Curves are simply stretched in the ordinate direction because $p_{95}/p_{50}(Q)$ address a characteristic variability rather than the standard variation as measured by *c.o.v.* Analogously to *c.o.v.*, all the models approach $p_{95}/p_{50}(Q) = 1$ with increasing $u_*/\mu(u_{*t})$, except for the [153] model where $p_{95}/p_{50}(Q)$ tends to $p_{95}/p_{50}(u_{*t})$.
Turning to the skewness (Fig. 4.13i-l), the behaviour of the models is qualitatively the same up to $u_* \approx 0.5$ m/s: $sk(Q)$ increases over d, changing sign for $0.3 \leq u_* \leq 0.5$. Conversely, the trend of $sk(Q)$ over d for about $u_* > 0.5$ m/s varies significantly between the models and this is difficult to interpret. It is worth pointing out that $sk(Q)$ versus d for the [221] and [161] models does not vary for $u_* > 0.5$ m/s. Conversely, $sk(Q)$ for the [144] and [153] models changes its trend leading to local minima.

To better understand the behaviour of the models with varying u_*, statistical metrics are evaluated over $u_*/\mu(u_{*t})$ ratios for three fixed values of the sand grain diameter. In Fig. 4.14, *c.o.v.*, p_{95}/p_{50} and sk for Q are plotted over $u_*/\mu(u_{*t}) \in [0.5,50]$ at $d = \{0.1, 0.25, 0.5\}$ mm. Values of u_* equal to fifty times the mean threshold shear velocity are out of scope for real world saltation phenomena. In fact, $u_* \approx 1 \div 2$ m/s for extreme winds and this equates to $u_*/\mu(u_{*t}) \approx 2 \div 10$ in Fig. 4.14. However, large u_* values are considered herein to assess the asymptotic behaviour of the statistical metrics. The values of the corresponding statistical metrics for u_{*t} are also reported for comparison.
Generally, all the Q-models show approximately the same trend for all statistical metrics up to $u_*/\mu(u_{*t}) \approx 1$ (i.e. small or null Q). Conversely, each model shows a different behaviour at larger ratios at higher wind speeds. Hence, the uncertainty will propagate differently for $u_*/\mu(u_{*t}) > 1$. *c.o.v.*(Q) and $p_{95}/p_{50}(Q)$ (Fig. 4.14a-f) provide a reasonable measure of the variability of Q, and some information on the uncertainty propagation from u_{*t} to Q, i.e. if variability is damped or amplified. Focusing on *c.o.v.*(Q), the uncertainty in u_{*t} is amplified where $u_*/\mu(u_{*t}) < 1.5$. Conversely, the uncertainty is damped where $u_*/\mu(u_{*t}) > 1.5$, except in the case of the [153] model. In the case of $u_*/\mu(u_{*t}) > 1.5$, the variability resulting from the [221] and [161] models decreases and tends monotonically to zero, while the variability resulting from the [144] and [153] models exhibit local minima before tending to the curve of [161] and *c.o.v.*(u_{*t}), respectively. The model that shows the fastest convergence rate to zero is the one proposed by [221]. The trend of $p_{95}/p_{50}(Q)$ highlights once again that the variability in Q decreases for increasing values of u_*, except for data derived from the model of [153].

The skewness values (Fig. 4.14g-i) better highlight the different behaviour of each model against $u_*/\mu(u_{*t})$. In general, the sand transport rate predictions are non-Gaussian. For small $u_*/\mu(u_{*t})$, they are all highly positively skewed. Indeed, f_Q will show an extremely large frequency of null transport (i.e. a peak for $Q = 0$) and very low frequencies of non-null transport (i.e. right-tailed distribution). For

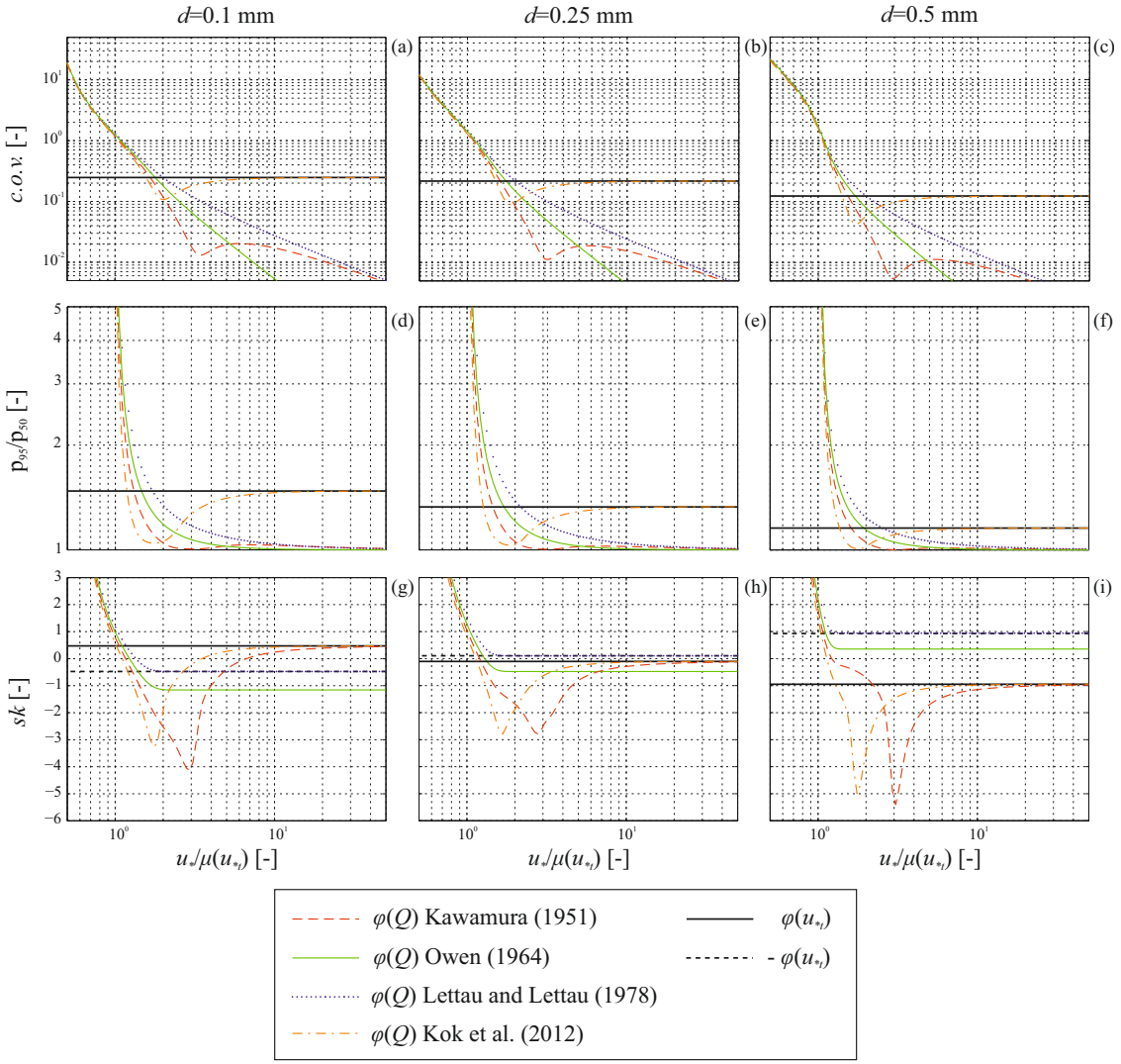

Figure 4.14: Uncertainty propagation from u_{*t} to Q. Q statistical metrics versus $u_*/\mu(u_{*t})$ ratio for each Q-model

intermediate $u_*/\mu(u_{*t})$, the results from the [144] and [153] models are highly negatively skewed, while the skewness from the [161] and [221] models is related to $sk(u_{*t})$. For large $u_*/\mu(u_{*t})$, the degree of non-Gaussianity decreases to values related to $sk(u_{*t})$.

The above results are determined by MC-based numerical experiments. The non-trivial trends observed suggest there is value in interpreting them in analytical terms by basic a-posteriori uncertainty propagation analysis. In order to do so, the

adopted modified Bagnold type models are generalized to the same basic form:

$$Q = \Phi \, \frac{\rho_a}{g} \, u^3_{*,eff} \left(u_*, u_{*t} \right) \tag{4.12}$$

where Φ is the dimensionless semi-empirical parameter and $u^3_{*,eff}$ is the effective shear velocity determined as a function of u_* and u_{*t}. The expressions of $u^3_{*,eff}$ is given in the second column of Table 4.5, for each Q-model.
In deterministic terms, $u^3_{*,eff}$ is a third order polynomial of the variables u_* and u_{*t}. In probabilistic terms, $u^3_{*,eff}$ is a transformation of the random variable u_{*t} and a function of the deterministic variable u_*. The analytical study of the statistical metrics of Q is unfeasible, since uncertainty propagation depends on the combination of u_* and u_{*t} in a non-trivial way. Some light can be shed by the analytical evaluation of the limits of the statistical metrics of Q for $u_* \to +\infty$. Given Eq. 4.12, the limit of Q metrics is equivalent to the one of $u^3_{*,eff} \left(u_*, u_{*t} \right)$. The limits of $c.o.v.(Q)$, $sk(Q)$ and $\mathrm{p}_{95}/\mathrm{p}_{50}(Q)$ are obtained having in mind the basic properties of the same statistical metrics. For example, by referring to the $c.o.v.(Q)$ resulting from the [153] model we have:

$$\begin{aligned} \lim_{u_* \to +\infty} c.o.v.(Q) = \lim_{u_* \to +\infty} \frac{\sigma(Q)}{\mu(Q)} = \lim_{u_* \to +\infty} \frac{\sigma\left(u^3_{*,eff} \right)}{\mu\left(u^3_{*,eff} \right)} = \\ = \lim_{u_* \to +\infty} \frac{u_*^2 \sigma\left(u_{*t} \right)}{u_*^2 \mu\left(u_{*t} \right)} = \frac{\sigma(u_{*t})}{\mu(u_{*t})} = c.o.v.(u_{*t}) \end{aligned} \tag{4.13}$$

Conversely, by referring to the $c.o.v.(Q)$ resulting from all the other models:

$$\lim_{u_* \to +\infty} c.o.v.(Q) = \lim_{u_* \to +\infty} \frac{\sigma(Q)}{\mu(Q)} = \lim_{u_* \to +\infty} \frac{\sigma\left(u^3_{*,eff} \right)}{\mu\left(u^3_{*,eff} \right)} = \lim_{u_* \to +\infty} \frac{\sigma\left(u^3_* \right)}{\mu\left(u^3_* \right)} = 0 \tag{4.14}$$

Tables 4.5 and 4.6 reports the full list of $u^3_{*,eff} \left(u_*, u_{*t} \right)$ and the analytical limits for each Q-model and statistical metric, respectively. In particular, they confirm the right-sided asymptotic tendencies of Fig. 4.14.

Previously, we explored the asymptotic behaviour of the statistical metrics of Q. However, the limits for $u_* \to +\infty$ are not relevant in the practice. Hence, we reduced the range of the shear velocity under investigation so to assess realistic values of the coefficient of variation. In doing this, we set the roughness length $z_0 = 0.003 \ m$ and the interval $u_* \in [0.1{,}1]$ m/s. Such an interval corresponds to approximate wind speed values between 2 (light breeze) and 8 (gale) on the Beaufort scale, i.e. a scale that relates wind speed to observed weather conditions [117]. Furthermore, we adopted an additional condition on the mean value of Q in order to discard very large $c.o.v.$ which correspond to very low sand transport rates. Hence, values of $\mu(Q) \geq 10^{-3} kg \ m^{-1} s^{-1}$ are used in the analysis. The resulting

Table 4.5: Effective shear velocity

Reference	$u^3_{*,eff}(u_*, u_{*t})$
Kawamura (1951)	$u_*^3\left(1-\frac{u_{*t}^2}{u_*^2}\right)\left(1+\frac{u_{*t}}{u_*}\right)$
Owen (1964)	$u_*^3\left(1-\frac{u_{*t}^2}{u_*^2}\right)$
Lettau and Lettau (1978)	$u_*^3\left(1-\frac{u_{*t}}{u_*}\right)$
Kok et al. (2012)	$u_*^2 u_{*t}\left(1-\frac{u_{*t}^2}{u_*^2}\right)$

Table 4.6: Limits of dimensionless statistical metrics of Q for $u_* \to +\infty$

Reference	$\lim_{u_*\to+\infty} c.o.v.(Q)$	$\lim_{u_*\to+\infty} \frac{p_{95}}{p_{50}}(Q)$	$\lim_{u_*\to+\infty} sk(Q)$
Kawamura (1951)	0	0	$sk(u_{*t})$
Owen (1964)	0	0	$-sk(u_{*t}^2)$
Lettau and Lettau (1978)	0	0	$-sk(u_{*t})$
Kok et al. (2012)	$c.o.v.(u_{*t})$	$\frac{p_{95}}{p_{50}}(u_{*t})$	$sk(u_{*t})$

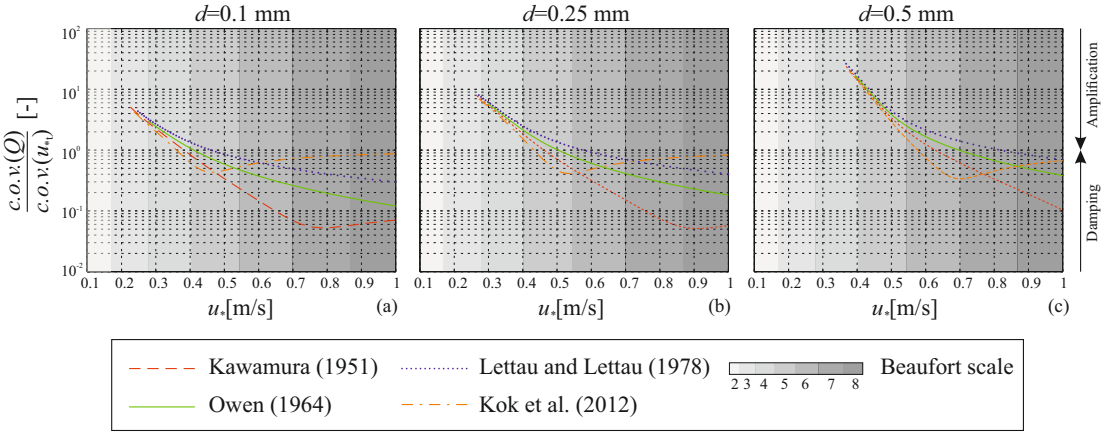

Figure 4.15: Uncertainty propagation from u_{*t} to Q for realistic values of u_*. $c.o.v.(Q)/c.o.v.(u_{*t})$ versus $u_*/\mu(u_{*t})$ for each Q-model and $u_* \in [0.1,1]$ m/s

values of the ratio $c.o.v.(Q)/c.o.v.(u_{*t})$ are reported in Fig. 4.15 for each model, and for three values of the sand grain diameter, namely $d \in \{0.1,0.25,0.50\}$ mm. Fig. 4.15 quantifies the actual magnitude of the uncertainty propagation. In particular, $c.o.v.(Q)/c.o.v.(u_{*t}) > 1$ reflects uncertainty amplification, while $c.o.v.(Q)/c.o.v.(u_{*t}) < 1$ reflects uncertainty damping. Generally, $c.o.v.(Q)/c.o.v.(u_{*t})$ covers a range from

1 to 2 orders of magnitude. The variability in Q changes significantly in the adopted range of wind speed, ranging from small values below unity for gales (damped uncertainty from u_{*t} to Q) to very high values above unity and up to 20 for breezes (amplified uncertainty), notably for coarser sands. Indeed, $c.o.v.(Q)/c.o.v.(u_{*t})$ increases with increasing d for small values of $u_*/\mu(u_{*t})$. Conversely, $c.o.v.(Q)/c.o.v.(u_{*t})$ remains almost constant with increasing d for large values of $u_*/\mu(u_{*t})$. Hence, the variation in particle size mostly affects the uncertainty propagation when u_* is close to $\mu(u_{*t})$.

Discussion

The obtained results indicate that the uncertainty in threshold shear velocity u_{*t} propagates into predictions of sand transport rate Q. The numerical uncertainty propagation investigated in this study can be viewed as a reflection of both *physical* and *statistical* processes. From a physical point of view, the variability of u_{*t} affects the mechanics of the sand saltation. From a statistical point of view, the modelling, measurement, and parametric uncertainty in u_{*t} propagates to Q. However, the characteristics of this propagation vary depending upon the Q-model, the sand grain diameter d, and the wind shear velocity u_*.

The discrepancies in uncertainty propagation among Q-models can be ascribed to the general form of $u^3_{*,eff}$. For the sake of clarity, the effective shear velocity was split between $u^3_{*,eff} = \mathcal{U}_* \Psi_*$, where $\mathcal{U}_*$ representing *sustained saltation* and Ψ_* representing *triggering of saltation*. In particular, $\mathcal{U}_*$ express the scaling of the particle speed, while Ψ_* express the effective shear velocity translation as a function of u_{*t}. The resulting values of $\mathcal{U}_*$ and Ψ_* for each Q-model are reported in Table 4.7.

Table 4.7: General form of the effective shear velocity $u^3_{*,eff} = \mathcal{U}_* \Psi_*$. Saltation sustaining $\mathcal{U}_*$ and saltation triggering Ψ_* according to each sand transport rate model

Reference	$\mathcal{U}_*$	Ψ_*
Kawamura (1951)	$u_* + u_{*t}$	$u_*^2 - u_{*t}^2$
Owen (1964)	u_*	$u_*^2 - u_{*t}^2$
Lettau and Lettau (1978)	u_*^2	$u_* - u_{*t}$
Kok et al. (2012)	u_{*t}	$u_*^2 - u_{*t}^2$

The physical interpretation of the obtained results is clear from Table 4.7. The [153] model propagates the same amount of uncertainty of u_{*t} to Q for strong winds. In formulas, for the generic dimensionless statistical metric φ, it holds that $\lim_{u_* \to +\infty} \varphi(Q) = \varphi(u_{*t})$. Conversely, the other models behave differently: the

uncertainty is damped from u_{*t} to Q for strong winds and the variation tends to zero. An interpretation of these marked differences in behaviour of the models can be obtained with reference to the saltation sustaining $\mathcal{U}_*$ and the saltation triggering Ψ_*.
$\mathcal{U}_*$ drives the uncertainty propagation for strong winds since $\lim_{u_*\to+\infty}\varphi(\Psi_*) = 0$. [153] explicitly adopt the impact threshold for $\mathcal{U}_*$. Under this assumption the asymptotic trend of Q statistical metrics looks physically sound since saltation is carried out by grain impacts and the particle terminal velocity does not depend on u_* (see [153] and related references). [221] and [161] adopt u_* and u_*^2, respectively. Hence, saltation is sustained purely by wind entrainment. [144] adopts the sum of u_* and u_{*t}. However, the statistical metrics of the [144] model tend to the ones of [221] and [161] for strong winds. In this sense, the models of [144], [221] and [161] are consistent with the adoption of the fluid threshold. Under this assumption saltation is initiated purely by wind entrainment and uncertainty in the fluid threshold has a greater impact at wind speeds close to the threshold. This issue represents a source of epistemic model uncertainty since uncertainty in threshold choice is not a resolved debate in the scientific literature. The author hopes that the present study contributes to the discussion on this open issue and stimulates debate. It is worth pointing out that the effective shear velocity in [144] is the summation of the $u_{*,eff}^3$ from [221] and [153]. Indeed, the statistical metrics of Q resulting from the [144] model are hybrid (see Fig. 4.14).

As regards Ψ_*, it is the same for all the Q-models except for [161]. Indeed, for the [144], [221] and [153] models Ψ_* reflects the general physical scaling $Q \propto \tau_{eff} = \rho_a(u_*^2 - u_{*t}^2)$, where τ_{eff} is the effective shear stress. Conversely, the [161] model shows a linear translation. The authors believes that the reasons for this discrepancy could be ascribed to the empirical fitting of the Q-model.

In the light of the obtained results, three main observations can be made:

1. Differences in the propagation of uncertainty between different sand transport models are significant and can reach up to an order of magnitude. [264], [275, 274] and [272] have highlighted the discrepancies between models in deterministic terms. The adoption of one model over another gives rise to differences not only in the mean values, but also much larger differences in terms of variance, skewness and extreme percentiles (see Fig. 4.12). These kinds of discrepancies between model predictions become more noticeable in the range $u_*/\mu(u_{*t}) \in [2,5]$ (see Fig. 4.14). This range is of practical interest for real world windblown sand events.

2. Differences in uncertainty propagation caused by varying u_* show that for slow wind speeds the uncertainty in Q is amplified with respect to the uncertainty in u_{*t}. Slow wind speeds occur frequently in nature due to the Weibull probability density function of wind speed. Hence, amplification in Q uncertainty is a potentially large practical issue if not accounted for correctly. In

contrast, in strong winds the uncertainty of u_{*t} does not significantly affect Q, except in the model results of [153] (see Fig. 4.14a-c). The physical interpretation of the local and global minima of the statistical metrics occurring for intermediate values of $u_*/\mu(u_{*t}) \in [2,3]$ in [144] and [153] is not straightforward (Fig. 4.14). Analytically, they result from the presence of u_{*t} in the saltation sustaining term $\mathcal{U}_*$. In the practice, the global minima of the skewness imply an underestimation of Q for related wind speeds by employing the [144] and [153] models with respect to the [221] and [161] models.

3. Differences in uncertainty propagation caused by varying the sand grain diameter, d, highlight that, for slow winds the variability in Q increases for coarse sands whilst, for strong winds, the variability in Q is less affected by d, except in the model results of [153] (see Fig. 4.13a-d). For realistic values of u_*, errors in the estimation of d propagate to Q prediction primarily for slow winds (Fig. 4.15). However, it is worth pointing out that the effect of d on the nominal sand transport rate remains an open issue [71, 305].

In light of the above observations, the choice of a Q-model should be performed not only to achieve the best prediction of the mean sand transport rate, but also in consideration of the uncertainty propagation in practical estimation of probabilistic sand transport rate. However, care must be taken since the choice of the model considerably affects the uncertainty of Q predictions. Further experimental investigations on sand transport rate uncertainty could shed some light on these issues.

4.2 Application and results

A general probabilistic approach is proposed and applied to real world sites in Arabian Peninsula. Each site is characterized by its actual wind field and sand granulometry. In particular, variability of both sand characteristics at microscopic scale (comprehensively reflected by threshold shear velocity) and wind speed (i.e. wind direction and intensity) are considered. Other sources of uncertainties reviewed above are not included because the lack of their statistical description. As a result, instead of a single pair of values describing mean RDP magnitude and direction, their probability distributions are obtained. Three main questions may rise to the authors' mind: i. How does the uncertainty of both threshold shear velocity and mean wind velocity jointly propagate to RDP? ii. Does the probability distribution of RDP change significantly form a site to another in the same region? iii. Does the gap between characteristic and mean value of RDP make the approach of interest for engineering practice? The present section aims at contributing in shedding some light on such issues. In the following, the framework proposed by [94] is first recalled. Then, the proposed probabilistic approach to assess sand drift

is shown step-by-step.

[94] define the directional drift potential and the resultant drift potential on the basis of the model proposed by [161], where the sand transport rate Q_θ in a given direction θ is expressed as

$$\begin{aligned} Q_\theta &= 6.7\sqrt{\frac{d}{d_r}}\frac{\rho_a}{g}u_{*,\theta}^3\left(1-\frac{u_{*t}}{u_{*,\theta}}\right) \quad \text{if} \quad u_{*,\theta} > u_{*t} \\ Q_\theta &= 0 \qquad\qquad\qquad\qquad\qquad\quad \text{if} \quad u_{*,\theta} \leq u_{*t}, \end{aligned} \tag{4.15}$$

being $u_{*,\theta}$ the shear velocity in the corresponding wind direction.
The directional drift potential D_θ [i.e. DP in the notation of 94] is rephrased as

$$D_\theta = \frac{1}{\rho_b}\frac{T}{T_r}\sum_{i=1}^{N_\theta} Q_{\theta,i}\Delta t = \frac{T}{T_r}\sum_{i=1}^{N_\theta} D_{\theta,\Delta t,i} \quad (\text{or } D_\theta = 0 \text{ if } N_\theta = 0)\,, \tag{4.16}$$

where ρ_b is the packed bulk sand density, T is the reference time and T_r is the recording time set as a multiple of T. Δt is the sampling interval of the wind speed, not necessarily equal to the 10-minute averaging time, for the sake of generality. The drift potential over the sampling interval $D_{\theta,\Delta t}$ $[m^3 m^{-1}\Delta t^{-1}]$ is estimated postulating Q_θ $[Kg\ m^{-1}s^{-1}]$ constant over Δt.
N_θ follows as the number of occurrences in the reference time in which the wind will blow in the direction θ, and it is expressed as

$$N_\theta = \frac{T}{T_r}\frac{T_\theta}{\Delta t}, \qquad \text{constrained by} \quad \sum_{\theta=1}^{2\pi/\Delta\theta} N_\theta + N_0 = N, \tag{4.17}$$

where T_θ is the time over which the wind blows in the direction θ, $\Delta\theta$ is the sector width on which the wind is recorded, N_0 and N are the number of occurrences of calm wind and the number of total occurrences in the reference time T, respectively.
Finally, the resultant drift potential R [i.e. RDP in the notation of 94] can be easily obtained from the vector sum of D_θ:

$$R = \sum_{\theta=1}^{2\pi/\Delta\theta} D_\theta. \tag{4.18}$$

In the following, resultant drift potential magnitude and direction are defined as $|R|$ and $\hat{R}$, respectively.
It may be useful to highlight that [94] provide also an index of the directional variability of windblown sand drift, i.e. the ratio between the resultant drift potential magnitude and the sum of drift potential modulus:

$$R/D = \frac{|R|}{\sum_{\theta=1}^{2\pi/\Delta\theta}|D_\theta|}. \tag{4.19}$$

In particular, the lower the ratio, the higher the directional variability.

In the proposed probabilistic approach the input quantities u_{*t} and $u_{*,\theta}$ are random variables. Hence, the [94] framework has to be adapted in order to deal with such random variables. Such a newborn approach is here called Sand Wind Probabilistic (SWP). The steps followed in SWP approach are sketched in the flow chart in Fig. 4.16 and described in the following.

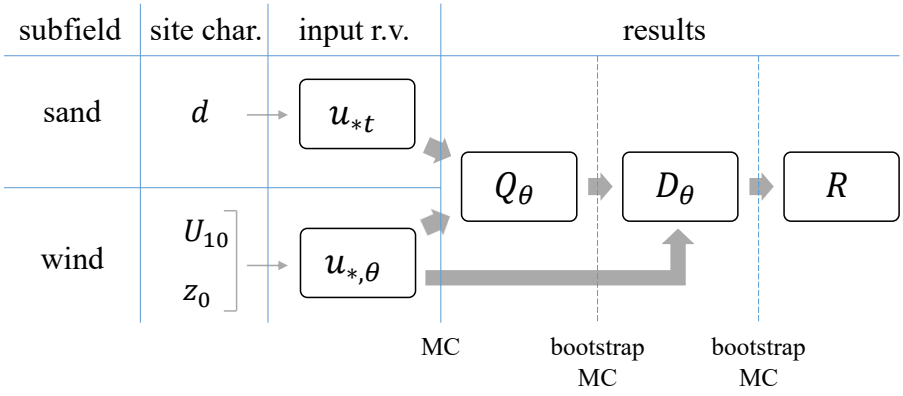

Figure 4.16: Flow chart of the proposed SWP approach

The site characteristics are needed as input data, with respect to both sand subfield (mean sand diameter d) and wind subfield (aerodynamic roughness z_0 and time series of 10-minute averaged wind speed $U_{10}(t)$). The input random variables u_{*t} and $u_{*,\theta}$ are described from the probability density functions $f(u_{*t})$ and $f(u_{*,\theta})$, respectively. To the authors' best knowledge, there are no experimental evidence or systematic studies in literature about a dependence between $u_{*,\theta}$ and u_{*t}. As a result, the directional shear velocity and the threshold shear velocity are considered independent random variables. Indeed, u_{*t} depends entirely on the sand characteristics, while $u_{*,\theta}$ depends only on the wind velocity for a given z_0. $f\,(u_{*,\theta})$ is simply obtained by rescaling the probability density function $f\,(U_{10,\theta})$, being $u_{*,\theta} = 0.41U_{10,\theta}/ln(z/z_0)$. Hence, Weibull-type $f\,(u_{*,\theta})$ results. The conditional probability density functions $f\,(u_{*t} \mid d)$ are obtained in Subsection 4.1.1.

The sand transport rate model proposed by [161] is adopted because it is widespread in scientific and technical literature (e.g. [94, 9, 15, 338, 171]), and judged performing better than other sand transport models [274]. Q_θ results from the transformation of the continuous random variables $u_{*,\theta}$ and u_{*t}. Q_θ is expected to be a mixed random variable. In fact, Q_θ is characterized by a discrete part, i.e. $Q_\theta = 0$, and a continuous part, i.e. $Q_\theta > 0$, because of the nature of the adopted sand transport rate model (Eq. 4.15).

Analytically, given the independent random variables $u_{*,\theta}$ and u_{*t}, the probability density function $f(Q_\theta)$ for a given value of d can be evaluated by differentiating its

distribution function $F(Q_\theta)$, which, for $q \geq 0$ and $u_{*,\theta} > u_{*t}$, can be expressed as

$$\begin{aligned} F_{Q_\theta}(q) &= P[Q_\theta \leq q] = \\ &= P\left[\left\{6.7\sqrt{\frac{d}{d_r}}\frac{\rho_a}{g}u_{*,\theta}^3\left(1-\frac{u_{*t}}{u_{*,\theta}}\right) \leq q\right\} \bigcap \{u_{*,\theta} > u_{*t}\}\right] = \\ &= \int\int_{\left\{(v_1,v_2)\ :\ v_1>v_2;\ v_1^3\left(1-\frac{v_2}{v_1}\right)\ \leq\ \frac{q}{6.7}\sqrt{\frac{d_r}{d}}\frac{g}{\rho_a}\right\}} f_{(u_{*,\theta},u_{*t})}(v_1,v_2)dv_1dv_2 = \\ &= \int_0^\infty \left[\int_{v_1-\frac{1}{v_1^2}\frac{q}{6.7}\sqrt{\frac{d_r}{d}}\frac{g}{\rho_a}}^{v_1} f_{(u_{*,\theta},u_{*t})}(v_1,v_2)dv_2\right] dv_1 = \\ &= \int_0^\infty \left(F_{u_{*t}}(v_1) - F_{u_{*t}}\left(v_1 - \frac{1}{v_1^2}\frac{q}{6.7}\sqrt{\frac{d_r}{d}}\frac{g}{\rho_a}\right)\right) f_{u_{*,\theta}}(v_1)dv_1. \end{aligned} \tag{4.20}$$

However, apart for the untractable analytical solution of this double integration, $f(Q_\theta)$ cannot be expressed in explicit form because $f(u_{*t} \mid d)$ is given by a non-parametric kernel density function [244].
Numerically, Monte Carlo (MC) simulations can be applied [41]. This approach presents three substantial advantages. First, MC convergence is independent from the number of random variables involved. In fact, it converges with a rate equal to $1/\sqrt{m}$, where m is the number of realizations, regardless of the number to random variables. Second, the very low cost of each single numerical realization of Q_θ allows to perform a large number of realizations for each wind direction. Finally, MC allows to describe the mixed random variable Q_θ in a straightforward manner.

It is worth pointing out that N_θ (Eq. 4.17) is a random quantity because T_θ is. For this reason, the probability distribution of the directional drift potential $g\,(D_\theta)$ should be expressed as a mixture of convolutions

$$\begin{aligned} g\,(D_\theta) = \sum_{n=1}^{\infty} \left(f_1 * \ldots * f_i * \ldots * f_n\right)(D_{\theta,\Delta t})\, P\left[N_\theta = n\right] \\ \text{with} \quad f_i = f \quad \text{for} \quad i = 1,\ldots,N_\theta, \end{aligned} \tag{4.21}$$

whose corresponding mean μ and variance σ^2 are

$$\begin{aligned} \mu\,(D_\theta) &= \mu\,(N_\theta)\,\mu\,(D_{\theta,\Delta t}) \\ \sigma^2\,(D_\theta) &= \mu\,(N_\theta)\,\sigma^2\,(D_{\theta,\Delta t}) + \mu^2\,(D_{\theta,\Delta t})\,\sigma^2\,(N_\theta)\,. \end{aligned} \tag{4.22}$$

In particular, the variance results from the sum of two terms, the first due to the variance of $D_{\theta,\Delta t}$ and the second to the variance of N_θ. It should be pointed out that adoption of a non-random N_θ implies an underestimation of the uncertainty of D_θ, being in this case $\sigma^2\,(N_\theta) = 0$. It should be also observed that the constraint on the whole set $\{N_\theta,\ \theta = 1,2,\ldots,n\}$ (see Eq. 4.17) induces a negative dependence

between the variables N_θ, and consequently in the set $\{D_\theta,\ \theta = 1,2,\dots,n\}$, which plays a key role in the final distribution of R. Unfortunately, the description of such an effect of the dependence between the variables N_θ can not be provided in a simple and tractable analytical manner. For these reasons, a Monte Carlo approach, based on bootstrapping techniques [79] from the data set of observed values to generate samples, has been adopted. For each simulation, first the vector $N = (N_1, N_2, \dots, N_n)$ of registered occurrences of wind in the considered directions has been obtained from the data set. Then, for each direction $\{\theta = 1,2,\dots,n\}$, a sample of cardinality N_θ of realizations of $D_{\theta,\Delta t}$ has been randomly chosen. Finally, the matrix $\boldsymbol{D} = (D_1, D_2, \dots, D_n)$ has been simulated through

$$\boldsymbol{D} = \begin{bmatrix} D_1 \\ D_2 \\ \vdots \\ D_\theta \\ \vdots \\ D_n \end{bmatrix} = \begin{bmatrix} \sum_{i=1}^{N_1} D_{1,\Delta t,i} \\ \sum_{i=1}^{N_2} D_{2,\Delta t,i} \\ \vdots \\ \sum_{i=1}^{N_\theta} D_{\theta,\Delta t,i} \\ \vdots \\ \sum_{i=1}^{N_n} D_{n,\Delta t,i} \end{bmatrix}, \tag{4.23}$$

where any $D_{\theta,\Delta t,i}$ is a realization of $D_{\theta,\Delta t}$ previously extracted from the data set.

Analytically, R is the vector sum of the components D_θ of the matrix $\boldsymbol{D}$ (Eq. 4.18), thus a realization of the resultant drift potential R can be immediately assessed once the realization of $\boldsymbol{D}$ is given. A set of numerical realizations of R can be computed by repeating the same procedure multiple times, and the distribution of R can be estimated through such a sample.

In the following, the proposed SWP approach is applied to five Sites located in the Arabian Peninsula. In Subsection 4.2.1, the layout of the study is shown. Geographical location and aeolian sand grain size of the chosen sites are reported. In Subsection 4.2.2, SWP approach is applied to Site 1. Obtained results are shown in terms of both intermediate, i.e. Q_θ and D_θ, and final, i.e. R, results in order to follow and comment step-by-step the full adopted procedure. Finally, in Subsection 4.2.3, final results from Sites 1-5 sites are summarized and compared.

4.2.1 Study layout

The site selection obeys to three criteria. Sites with a complete enough anemometric database are first retained. Among them, sites are selected to sample the huge variability of both sand and wind subfields in Arabian Peninsula. Finally, sites are chosen in reason of their proximity to railway lines having in mind the vulnerability of such infrastructures to windblown sand.

In Fig. 4.17, Sites 1-5 are represented on Arabian Peninsula (blue dots). On the same Fig., some operating/under construction/planned railway tracks are sketched.

In particular, the 950 km long Saudi Landbridge links Jeddah with the Saudi Arabia capital Riyadh. The 2750 km North South Railway Line links northern Saudi Arabia with Riyadh and the port city Ras Al-Khair. The 450 km long Haramain High Speed Rail links the cities of Medina and Mecca. Ethiad Rail is part of the United Arab Emirates' national 1200 km railway network.
Sites coordinates and mean sand grain size d are reported in Table 4.8. Mean grain sizes are derived from sedimentology studies of arabian sand dunes [263, 80, 116, 77]. In particular, Sites 1, 3 and 4 are sensitive to the sand of Ad Dahna desert, made of medium grained, well sorted quartz sand. Site 2 is sensitive to the sand of Jeddah plain. Site 5 is sensitive to the fine grained, moderately well sorted sand of Rub' al Khali desert.

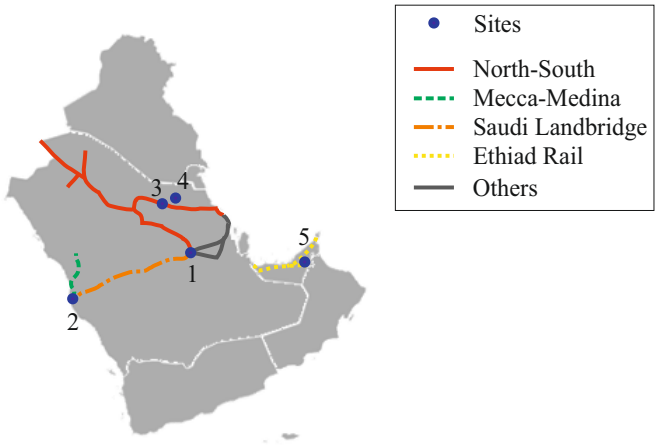

Figure 4.17: Sketch of the selected sites (blue dots) and railways tracks (lines)

Table 4.8: Sites of incoming sand drift estimation

Site number	Site name	Latitude	Longitude	d $[mm]$
1	Riyad	24°4'1.20"N	47°34'58.80"E	0.35
2	Jeddah	21°41'60.00"N	39°10'58.80"E	0.25
3	Hafr Al-Batin	27°55'1.20"N	45°31'1.20"E	0.30
4	Al Qaisumah	28°19'1.20"N	46°7'58.80"E	0.30
5	Al Ain	24°12'2.99"N	55°45'40.00"E	0.16

The aerodynamic roughness is set equal to $z_0 = 4e{-}3\ m$ in all Sites. The wind velocity dataset refers to $T_r = 5$ years from January 2008 to December 2012 for all stations as well. The 10-min average wind direction is measured in the horizontal

plane with a sampling interval $\Delta\theta = 10°$ at all the selected anemometric stations. $n = 36$ directions result. The 10-min average wind velocity is recorded with a sampling interval in time $\Delta t = 1$ hour at all the anemometric stations (sampling rate 24/144). The actually available datasets at the selected anemometric stations include missing data due to anemometric breakdowns and/or operational problems. Missing data are in average equal to 4% of the complete dataset. They are evaluated to be almost uniformly distributed along the day. Both the sampling rate and missing data are sources of incompleteness of the dataset. In the literature (see e.g. [39]) is widely accepted that randomly distributed data incompleteness is usually not influential on the probability distribution of the 10-min average wind velocity, while it may lead to underestimations of the extreme values. It is worth recalling that windblown sand drift potential R is mainly induced by the cumulated values of current values of Q over time, resulting from the 10-min average wind velocity in turn. Hence, data incompleteness is not expected to affect the obtained results. Finally, the resultant drift potential R is expressed over a reference time $T = 1$ year.
The results discussed in the next Subsections are obtained by MC approach. Hence, results convergence should be discussed every time a random variable is introduced and numerically generated. Convergence is classically evaluated by referring to weighted residuals of the first statistical moments of each random variable. The cardinality of the set of realizations for each random variable is chosen in order to reach a weighted residual lower or at least equal to $1e{-}2$. In the following, the cardinality of each random variable is reported for the sake of completeness, while convergence studies are not reported for the sake of brevity.

4.2.2 Results for site 1

The characteristics of the in-situ sand subfield is summarized by $d = 0.35$ mm (Table 4.8). The related input random variable is the threshold shear velocity. Its probability density function $f(u_{*t}|d = 0.35\,mm)$ is derived from Subsection 4.1.1. Related u_{*t} statistics are reported in Table 4.9 in terms of mean value μ, standard deviation σ and coefficient of variation $c.o.v$. It is worth recalling that $f(u_{*t}|d)$ is the same in each wind direction, since it depends solely on sand characteristics.
The wind subfield is obtained by mean wind speed in-situ measurements. U_{10} variability is assessed in terms of both *non-directional* and *directional* statistics. *Non-directional* statistics is summarized in Fig. 4.18. U_{10} time history is shown in Fig. 4.18(a). Both mean wind speed $\mu(U_{10})$ and mean threshold velocity $\mu(U_t)$ are plotted on the same graph. U_{10} variability is described by the Hybrid Weibull (HW) model [290]. HW probability density function $f\,(U_{10})$ is defined as follows:

$$f_{(\lambda,k)}\,(U_{10}) = \begin{cases} F_0 & \text{for } U_{10} = 0 \\ (1 - F_0)\,\dfrac{k}{\lambda}\left(\dfrac{U_{10}}{\lambda}\right)^{k-1} e^{-U_{10}/\lambda^k} & \text{for } U_{10} > 0 \end{cases} \tag{4.24}$$

where F_0 is the rate of zero values, i.e. the frequency of calm wind, k is the shape parameter and λ is the scale parameter. HW $f\,(U_{10})$ is plotted in Fig. 4.18(b).

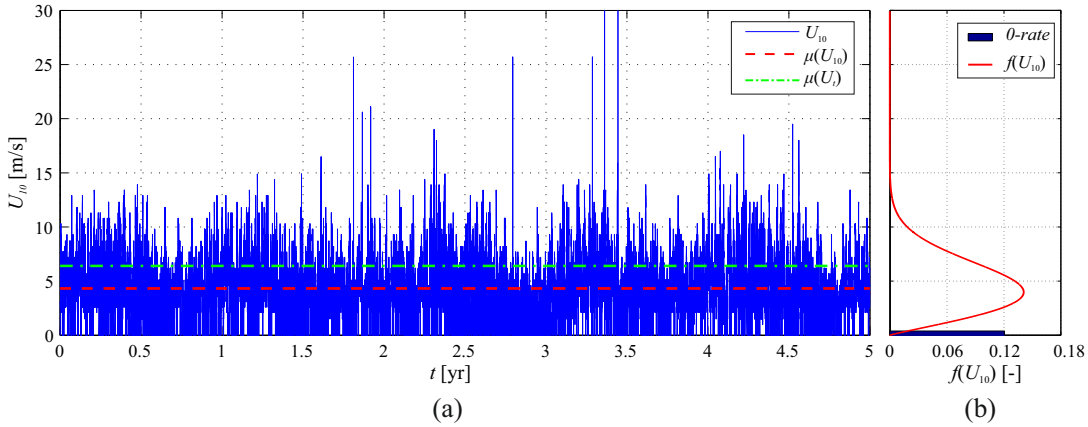

Figure 4.18: Site 1. Non-directional statistics of mean wind speed: Wind time history (a) and Hybrid Weibull fitting (b)

Wind shear velocity is recovered from mean wind speed in-situ measurement. HW $f(U_{10})$ is rescaled into HW $f(u_*)$. u_* statistical parameters and moments are reported in Table 4.9, where they can be compared with u_{*t} ones. In particular, the threshold shear velocity is higher than the shear velocity in mean terms, while the highest variability is addressed to the wind subfield.

Table 4.9: Site 1. Statistical parameters and moments of the non-parametric $f(u_{*t}|d = 0.35\,mm)$ and Hybrid Weibull $f(u_*)$

Random variable	F_0 [−]	k [−]	λ [$m\ s^{-1}$]	μ [$m\ s^{-1}$]	σ [$m\ s^{-1}$]	$c.o.v.$ [−]
u_{*t}	-	-	-	0.34	0.06	0.18
u_*	0.12	2.09	0.29	0.25	0.13	0.50

Directional statistics is shown by means of the wind rose and the polar diagram in Fig. 4.19. Calm wind, i.e. $U_{10,\theta}$ null values, is filtered since it is non-directional by nature and does not contribute in defining directional statistics. Fig. 4.19(a) shows a very broad wind directionality. However, North and South-SouthEast are the directions having the highest occurrence frequency. In Fig. 4.19(b), the empirical probability density function of the wind speed in North direction is shown as an example. Fig. 4.19(c) depicts the variation of probability density function of both wind speed $U_{10,\theta}$ and erosion threshold U_t by means of their directional mean values values and extreme percentiles (i.e. 5^{th} percentile p_5 and 95^{th} percentile

p_{95}), as a function of wind direction $\theta = 1, \ldots, n$. $\mu(U_t)$ is higher than $\mu(U_{10,\theta})$ for every direction, but the 95^{th} percentile of the wind speed $p_{95}(U_{10,\theta})$ overcomes the corresponding percentile of the threshold velocity $p_{95}(U_t)$ for winds blowing from around North and from South-SouthWest.

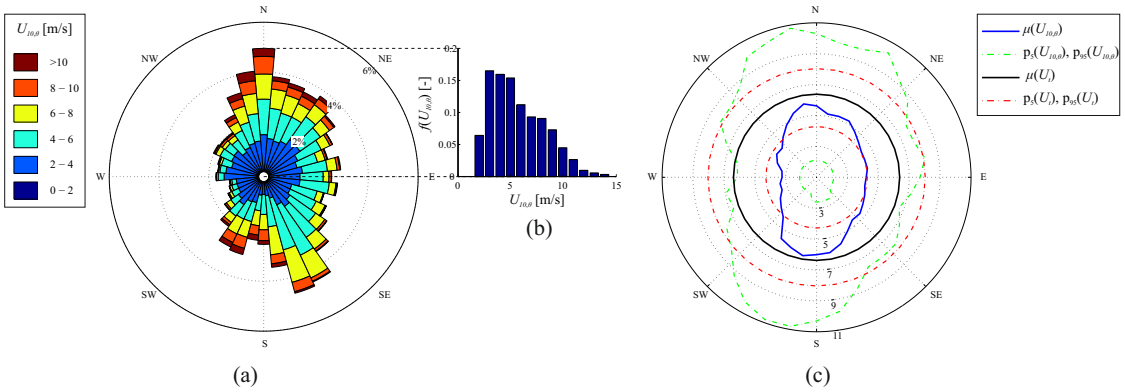

Figure 4.19: Site 1. Directional statistics of mean wind speed: wind rose (a), empirical probability density function of the wind speed in North direction (b), polar diagram of U_{10} and U_t statistics (c)

$U_{10,\theta}$ is converted into $u_{*,\theta}$ dataset. Classic Weibull probability density function $f(u_{*,\theta})$ are fitted for each direction. Numerical realizations of u_{*t} and $u_{*,\theta}$, consistent with $f(u_{*t})$ and $f(u_{*,\theta})$ respectively, are generated in order evaluate the sand transport rate Q within MC approach. u_{*t} and $u_{*,\theta}$ cardinality $\# = 1e{+}6$ is adopted for each direction. Sand transport rate results are organized in the form of sand rose in Fig. 4.20(a) in analogy with the wind rose in Fig. 4.19(a). In fact, the length of each bin is the same in both roses. The wind rose and the sand rose have the same direction frequencies. Hence, the relative length of each bin is the same in both roses. This is due to the fact that one realization of Q for a given direction results from the corresponding realization of U_{10} along the same direction θ. Conversely, the probability density function $f(Q_\theta)$ for each direction does not result from a simple rescaling of the corresponding $f(u_{*,\theta})$, because of the piece-wise, non-linear transformation (Eq. 4.15). In particular, for $0 < u_{*,\theta} < u_{*t}$, $Q_\theta = 0$ even if this does not correspond to wind calm conditions. Hence, the color pattern in each bin significantly varies. An example is explicitly given by the empirical probability density functions for North direction (Fig. 4.19b and 4.20b). Fig. 4.20(c) depicts the mean value and the 95^{th} percentile of the sand transport rate as a function of θ. $\mu(Q_\theta)$ and $p_{95}(Q_\theta)$ are higher for winds blowing from around North and from South-SouthWest, that are the direction for which $p_{95}(U_{10,\theta}) > p_{95}(U_t)$ (see Fig.4.19c).

The following remarks can be outlined. First, the distribution is no longer a continuous distribution: its hybrid nature is due to the first part of the piece-wise

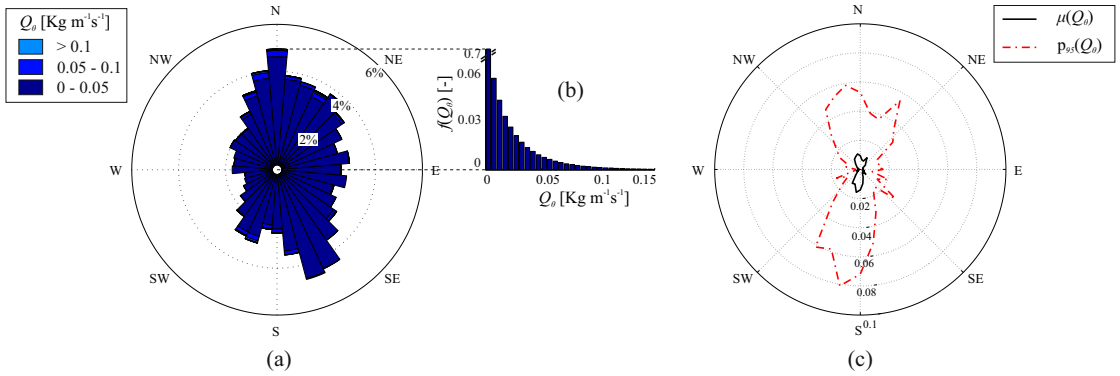

Figure 4.20: Site 1. Sand transport rate statistics: sand transport rate rose (a), sand transport rate empirical probability density function in North direction (b), polar diagram of sand transport rate statistics (c)

transformation, i.e. $Q_\theta = 0$ if $u_{*,\theta} \leq u_{*t}$. Second, the distribution is no longer a Weibull-type one, due to the non-linear transformation. In particular, distributions are strongly right-sided skewed. Finally, the sand transport rate directional statistics are strongly bimodal, with North and South prevailing directions, in contrast with the very broad wind directionality (Fig.4.19-a). This is due to the fact that the sand transport rate Q_θ depends on the effective shear velocity $u^3_{*,\theta,eff} = u^3_{*,\theta} - u^2_{*,\theta}u_{*t}$. Referring to Fig. 4.19(c), low-speed winds from West and East do not contribute to Q_θ, while high-speed winds from North and South almost solely contribute to Q_θ.

The drift potential over the sampling interval $D_{\theta,\Delta t}$ $[m^3\ m^{-1}hr^{-1}]$ is simply obtained from Q_θ $[Kg\ m^{-1}s^{-1}]$ considering the packed bulk sand density $\rho_b = 1.8e{+}3\ kg\,m^{-3}$.

The number of occurrences N_θ is assessed by bootstrapping a sample of cardinality $N = 8768$ (i.e. the number of Δt in T) from the actual wind velocity dataset. The wind direction frequencies N_θ/N are shown by box plots in Fig. 4.21(a). On the same graph, calm wind frequency is plotted too. It should be highlighted that the influence of calm wind on D_θ is taken into account by N_θ. In fact, wind direction frequencies are computed considering the frequency of calm wind (see Eq.4.17).

Once $D_{\theta,\Delta t}$ and N_θ are assessed over each direction, the drift potentials D_θ over $T = 1$ year are obtained following Equation 4.23. In particular, Equation 4.23 is applied by bootstrapping a sample of $D_{\theta,\Delta t}$ and N_θ realizations, both having cardinality $\# = 1e{+}5$. The same cardinality $\#_{D_\theta}$ for each D_θ follows from MC. In Fig. 4.21(b), drift potential mean values and percentiles are plotted as a function of θ to summarize directional statistics and related $f(D_\theta)$. The non-parametric probability density function $f(D_\theta)$ which describes the incoming sand drift from North in $T = 1$ year, is shown in Fig. 4.21(c) by way of example.

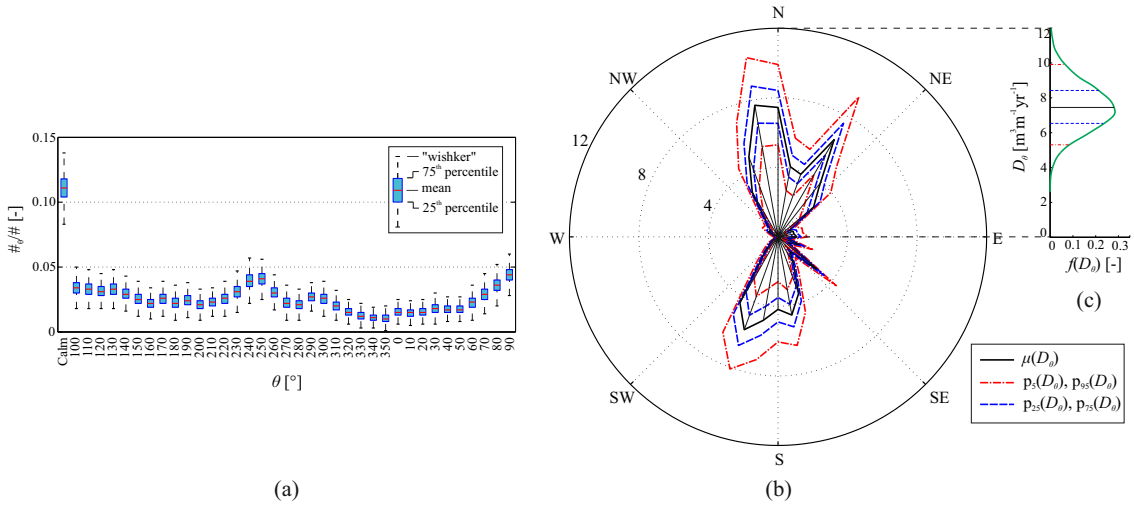

Figure 4.21: Site 1. Wind direction frequencies by N_θ/N box plot (a). Drift potential D_θ directional statistics (b), drift potential probability density function in North direction (c).

Three remarks follow. First, N_θ variability is low, at least for this site. Hence, the variance of D_θ is mainly due to the variance of $D_{\theta,\Delta t}$, while the variance of N_θ is relatively small (see Eq.4.22). Second, the drift potential directional statistics are strongly bimodal with North and South prevailing directions in accordance with the sand transport rate ones (see Fig.4.20c). Finally, the cumulative sum of the very skewed $f(Q_\theta)$ gives rise to almost symmetric $f(D_\theta)$. This is compliant to the central limit theorem: the sum of independent random variables tends to a normally distributed random variable even if the original random variables are not.

Fig. 4.22 provides a synopsis of the uncertainty propagation from erosion threshold and wind speed to sand transport rate and drift potential. The coefficient of variation and skewness modulus of these random variables are plotted as a function of the direction θ in Figures 4.22 (a) and (b), respectively. The *c.o.v.* of the input random variables ($U_{10,\theta}$, U_t) is relatively small (*c.o.v.* $\approx 1e{-}0.5$). Uncertainty is magnified by an order of magnitude proceeding to Q_θ (*c.o.v.* $\approx 1e{+}0.5$), while *c.o.v.* is damped again passing from Q_θ to D_θ (*c.o.v.* $\approx 1e{-}0.5$). Indeed, on the one hand, transformation of random variables done in order to assess Q (i.e. Eq.4.15) magnifies the uncertainty of the initial random variables $U_{10,\theta}$ and U_t. On the other hand, the random sum of identically and independent distributed random variables (Eq.4.23) damps *c.o.v.* The *c.o.v.* of the random variables above shows slight differences over θ. U_t does not depend on θ at all, *c.o.v.* $(U_{10,\theta})$ is almost constant for this site, *c.o.v.*(Q_θ) and *c.o.v.*(D_θ) in turn are higher for winds blowing from East and West, i.e. the less frequent wind directions. The skewness modulus shows approximately the same behavior of *c.o.v.* $|sk(Q_\theta)|$ increases significantly with respect to

$|sk(U_t)|$ and $|sk(U_{10,\theta})|$, while $|sk(D_\theta)|$ decreases again. In particular, $|sk(D_\theta)|$ is lower for winds blowing from around North and South directions.

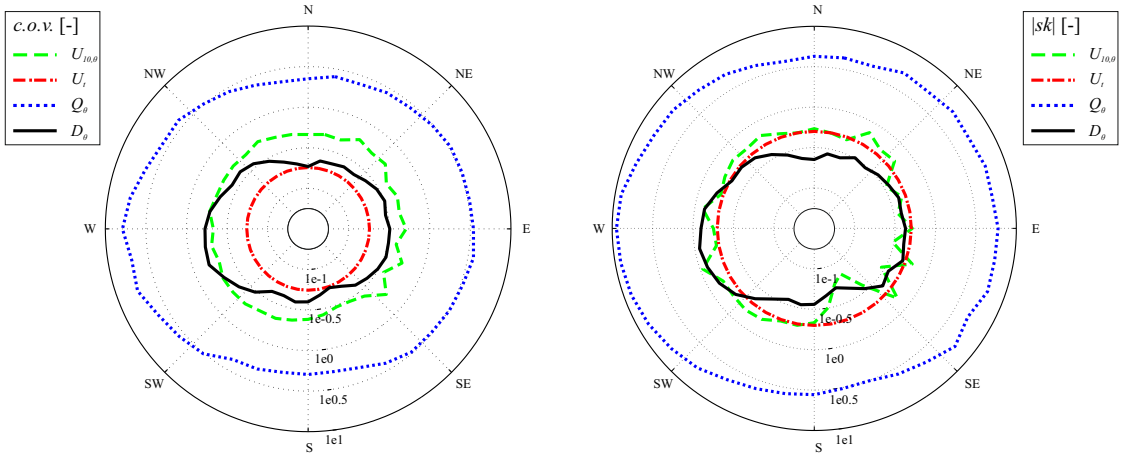

Figure 4.22: Site 1. Uncertainty propagation from U_{10} and U_t to Q_θ and D_θ in terms of polar diagrams of coefficient of variation (a) and skewness (b)

Finally, in Fig. 4.23(a), each black dot represents a single realization the resultant drift potential R. The radial coordinate of the dots is the vector magnitude $|R|$, while the angular coordinate is the vector direction $\hat{R}$. Each realization of R is numerically obtained from one realization of $\boldsymbol{D}$ through Equations 4 and 9 by bootstrapping [79]. The ensemble of black dots graphically visualizes the whole set of numerical realizations of R. The cardinality of R is $\#_R = 5e{+}4$. In the following we call "realization cloud" the ensemble of black dots. The mean resultant drift potential vector $\mu(R)$ is depicted by the red arrow on the same graph. R can be described in probabilistic terms by the joint probability density function $f(|R|, \hat{R})$ of the two random variables $|R|$ and $\hat{R}$. $f(|R|)$ and $f(\hat{R})$ marginal densities are shown in Fig. 4.23(b) and (c), respectively.
The realization cloud appears to be comma-shaped in circular coordinates, i.e. tear-shaped in cartesian coordinates. This shape indicates a significant skewness of $\hat{R}$, as testified by its marginal distribution. The radial width of the realization cloud provides a qualitative graphical reading of the variability of R magnitude. The circumferential extent of the cloud qualitatively describe the variability of R direction. For this site, the variability of $\hat{R}$ is by far higher than the one of $|R|$. This is confirmed by the marginal distributions in Figures 4.23(b) and (c). From a qualitative point of view, it is worth pointing out that the only mean value (red arrow) is a poor description of the sand drift phenomenon. Conversely, realization cloud and related high-order statistics provide a more complete description. In general, SD-WA approach loses fundamental information of R, while the proposed

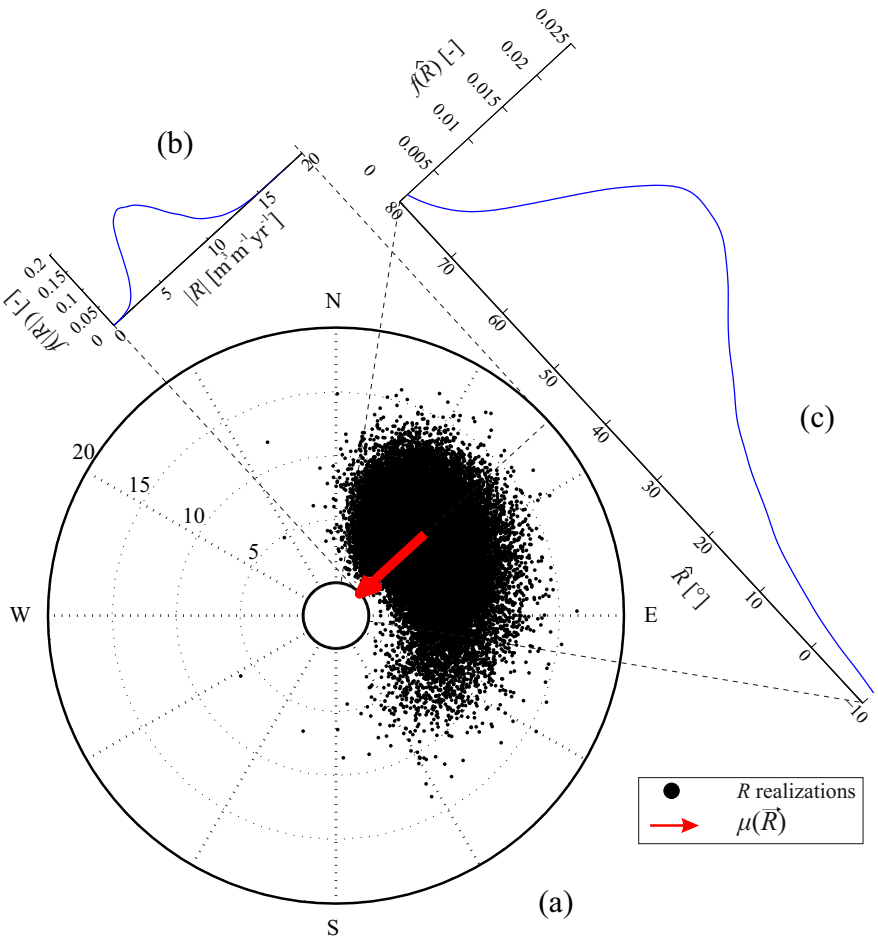

Figure 4.23: Site 1. Resultant drift potential (a), resultant drift potential magnitude marginal density (b) and resultant drift potential direction marginal density (c).

SWP approach provides complete statistics.
The quantitative statistics of R for this Site and all remaining Sites are reported in the following Subsection.

4.2.3 Comparative analysis Sites 1-5

In the following, all the selected Sites are accounted for. Both wind and windblown sand fields are probabilistically evaluated and critically compared.

In Fig. 4.24, U_{10} wind roses and polar diagrams of resultant drift potential R are represented on Arabian Peninsula map. Realization clouds of the resultant drift potential and marginal densities are plotted as well. On the same graphs,

the mean values of R are reported (red arrows). In short, Fig. 4.24 collects the results of the initial and final step of the proposed procedure. Wind rose shape testifies a variety of wind regimes: wide unimodal, i.e. Site 2, acute bimodal, i.e. Site 3, obtuse bimodal, i.e. Sites 1 and 5, complex, Site 4. Realization cloud shape, dimension and density change significantly moving from a site to another. The realization clouds appear to be comma-shaped in polar diagrams (i.e. tear-shaped in cartesian coordinates), or kidney-shaped (i.e. elliptical-shaped in cartesian coordinates). Comma shape (Sites 1 and 5) indicates a significant skewness of $\hat{R}$, while kidney shape (Sites 2,3,4) indicates weakly skewed magnitude and direction. The wider the realization cloud in radial and/or circumferential direction, the higher the variation of R, in magnitude and direction, respectively. Variations of both $|R|$ and $\hat{R}$ are small at Sites 2 and 3, so that kidney-shaped cloud appear as elliptical. Site 4 is remarkably characterized by very high variation of $\hat{R}$ and a small variation of $|R|$. The marginal densities $f(|R|)$ and $f(\hat{R})$ clearly reflect these differences. In particular, while in some cases they recall Gaussian distributions (Sites 2 and 3), in others they appear asymmetric, mainly with respect to the direction ($f(\hat{R})$ at Sites 1 and 5). In general, the relation between wind rose and realization cloud is not straightforward, because of the non-linear relation between U_{10} and Q. Furthermore, wind roses graphically point out wind direction frequencies much more effectively than wind speed frequencies. However, it is worth pointing out that the more complex the wind rose, the wider the realization cloud.

Non-dimensional statistics of both $|R|$ and $\hat{R}$ are reported in Table 4.10 to summarize the obtained results and quantitatively compare the Sites. Variation and skewness of $|R|$ and $\hat{R}$ are assessed in order to understand how much the random variables are dispersed and how far are from Gaussianity. The variability of $|R|$ is expressed by means of *c.o.v.*, while the variability of $\hat{R}$ is directly expressed by the angular deviation σ. It is worth to point out that since $\hat{R}$ is a circular random variable, circular statistics is assessed [89, 22]. The lowest variability is addressed to Site 2, i.e. the Site with unimodal wind regime, while the highest variability is addressed to e.g. Sites 1 and 4, i.e. the Sites with obtuse bimodal or complex wind regimes. Concerning probability density functions symmetry, Sites 1 and 5 show the most skewed distributions, while Site 3 one is almost symmetric.

The design of infrastructures in arid environments should be based on sand drift magnitude related to a low probability of exceedance. Hence, characteristic values (i.e. extreme percentiles) of both R magnitude and direction are included in Table 4.10. The ratio between 95^{th} percentile and mean value p_{95}/μ is assessed as regards R magnitude. The study gives rise to characteristic values up to ≈ 1.6 times the mean value (Site 1). In other words, the evaluation of $|R|$ in mean terms only significantly underestimates the amount of transported sand. The angular distance $|\mathrm{p}_{95} - \mathrm{p}_5|$ is evaluated, regarding $\hat{R}$. Both percentiles are referred to anti-clockwise circular direction from East. In other words, $|\mathrm{p}_{95} - \mathrm{p}_5|$ provides a quantitative measure of the variability of $\hat{R}$ based on characteristics directions. This measure

is the well posed probabilistic reading of the estimate of drift direction variability proposed by [94] in deterministic terms through Equation 4.19. The highest $|p_{95} - p_5|$ angular distance is observed for Site 4, i.e. $\approx 88°$, while the lowest, $\approx 8°$, is observed for Site 2.

Table 4.10: Sites 1-5. Statistics of resultant drift potential magnitude and direction

	$\lvert R\rvert$ $[m^3 m^{-1} yr^{-1}]$			$\hat{R}$ [°]		
	$c.o.v.$ [−]	sk [−]	p_{95}/μ[−]	σ [°]	sk [−]	$\lvert p_{95} - p_5\rvert$[°]
Site 1	0.32	0.37	1.57	20.77	2.61	77.22
Site 2	0.06	0.02	1.09	2.52	0.38	8.28
Site 3	0.10	0.01	1.16	3.88	-0.05	12.78
Site 4	0.27	0.11	1.46	24.09	0.60	87.80
Site 5	0.10	0.28	1.17	7.11	1.05	23.22

4.2.4 Concluding remarks

The present study introduces a new Sand-Wind Probabilistic (SWP) approach to evaluate incoming windblown sand drift potentials and resultant drift potentials. The approach adapts the general framework proposed by [94] in order to deal with the sources of uncertainty related to both wind and sand subfields. The input uncertainties on U_{10} and u_{*t} propagate to the final result, i.e. R, passing through the definition of Q_θ and D_θ.

The following concluding remarks can be outlined, bearing in mind the three kickoff questions raised at the beginning of Section 4.2:

- uncertainty of both threshold shear velocity and mean wind velocity are magnified passing to the directional sand transport rate Q_θ by about an order of magnitude. Subsequently, uncertainty is damped from Q_θ to the drift potential D_θ, and it is further damped to the resultant drift R. Magnification is due to the cubic dependency of Q versus u_* and u_{*t}, while damping results from cumulating in time and vector summing over directions;

- the probability distribution of the resultant drift potential changes significantly form a site to another in the same region. Complex wind regimes are particularly prone to cause windblown sand drift with high inborn variability. For instance, the highest $c.o.v(|R|)$ and $\sigma(\hat{R})$ are referred to sites showing obtuse bimodal or complex wind roses. Changes in the sand granulometry and related shear threshold velocity probability distribution from one site to another also affect R;

- the proposed SWP probabilistic approach allows to obtain characteristic values of R, while the Sand Deterministic-Wind Averaged (SD-WA) approach adopted up to now in scientific literature and engineering practice does not provide sufficient statistics to describe correctly the phenomenon. The gap between characteristic and mean value of RDP makes the approach of interest for engineering practice and grounds the probabilistic approach to design of civil infrastructure in arid regions. Regarding sites with complex wind regimes, on the one hand, the characteristic value of $|R|$ is about 1.5 times the mean value. On the other hand, the angular distance between the mean direction and the characteristic values of $\hat{R}$ is about 40°;

- in this study, Q_θ, D_θ and R are estimated by neglecting the effect of wind turbulence fluctuations and by considering neutral atmospheric conditions, flat orography and absence of obstacles. These features represent, however, standard conditions for desert environments. Furthermore, u_*t refers to dry, loose, bare sand and ignores environmental effects, such as soil moisture, salt concentration and sand crusting. Indeed, a statistical description of such environmental effects on u_{*t} is not practically feasible since they dramatically vary in both space and time. Nevertheless, they can be taken into account a posteriori through the adoption of environmental factors.

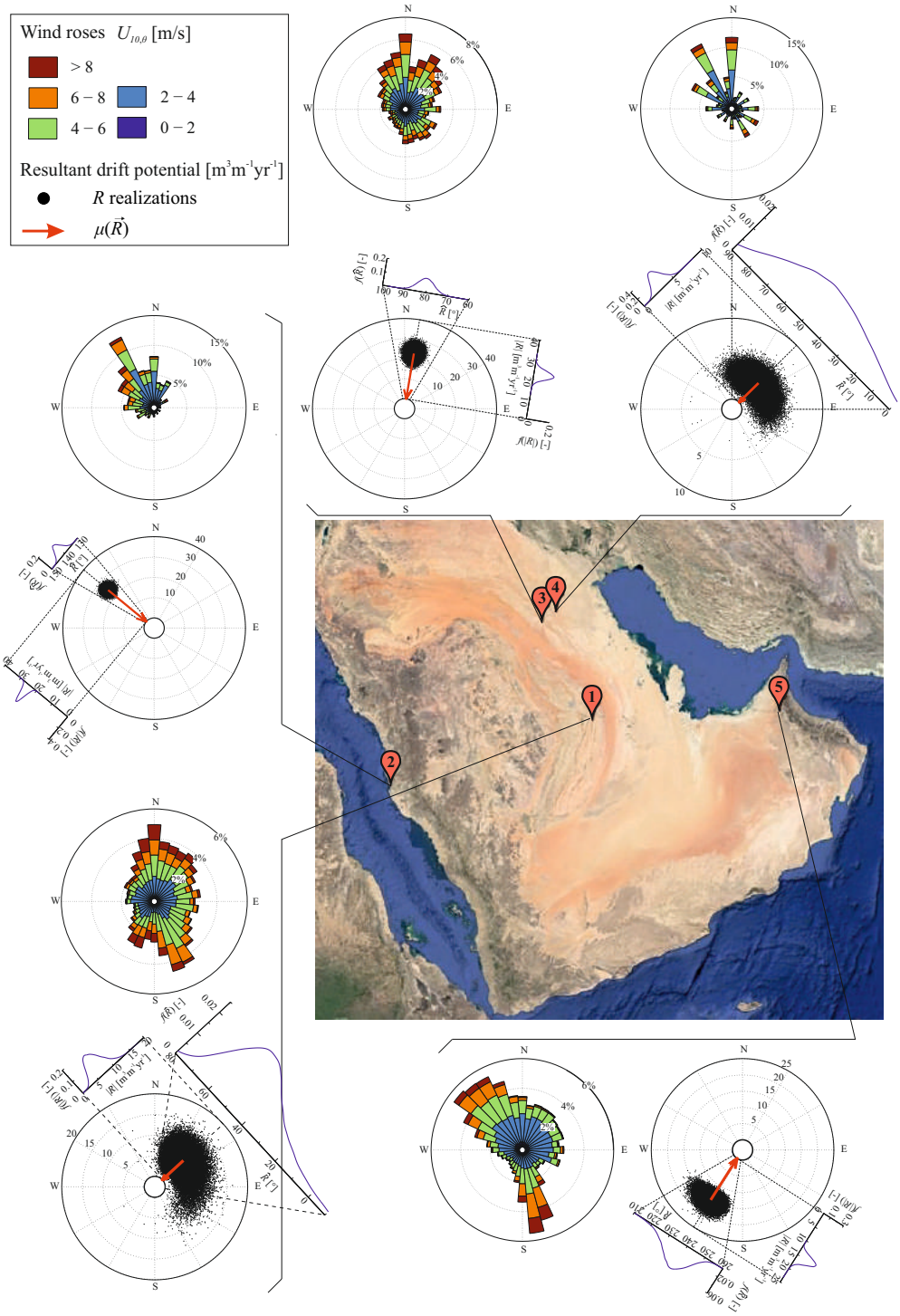

Figure 4.24: Sites 1-5. Wind roses and resultant drift potentials around Arabian Peninsula

Chapter 5

Windblown sand action

Part of the work described in this chapter has been previously published by the author and co-workers in international peer-reviewed journals [33, 241].

This chapter refers to windblown sand as an environmental action. Analogously to snow drift, windblown sand results from the interaction between wind and sand, and implies sand erosion, transport, sedimentation and avalanching around any kind of built structure. The analogy above was early recognized in a phenomenological and physical modelling perspective by e.g. [3, 149], where both sand grains and snow flakes are intended as particulate materials. Such an analogy has not been transferred to structural engineering in order to define windblown sand action. This entails that windblown sand action and its effects on civil structures and infrastructures are almost completely overlooked in structural engineering, despite the wide range of induced deficiencies, and the need of ad hoc engineering studies and solutions early recognized by e.g. [248, 285].

The chapter first introduces some real world documented example of windblown sand action collected by the author by providing their original phenomenological reading. A limit state design approach against windblown sand is introduced through the definition of newborn windblown Sand Limit States. Windblown sand action modelling is outlined. Finally, an application to a case study is carried out. The chapter is structured as follows:

- Phenomenological analysis
- Windblown Sand Limit States
- Modelling
- Application and results

5.1 Phenomenological analysis

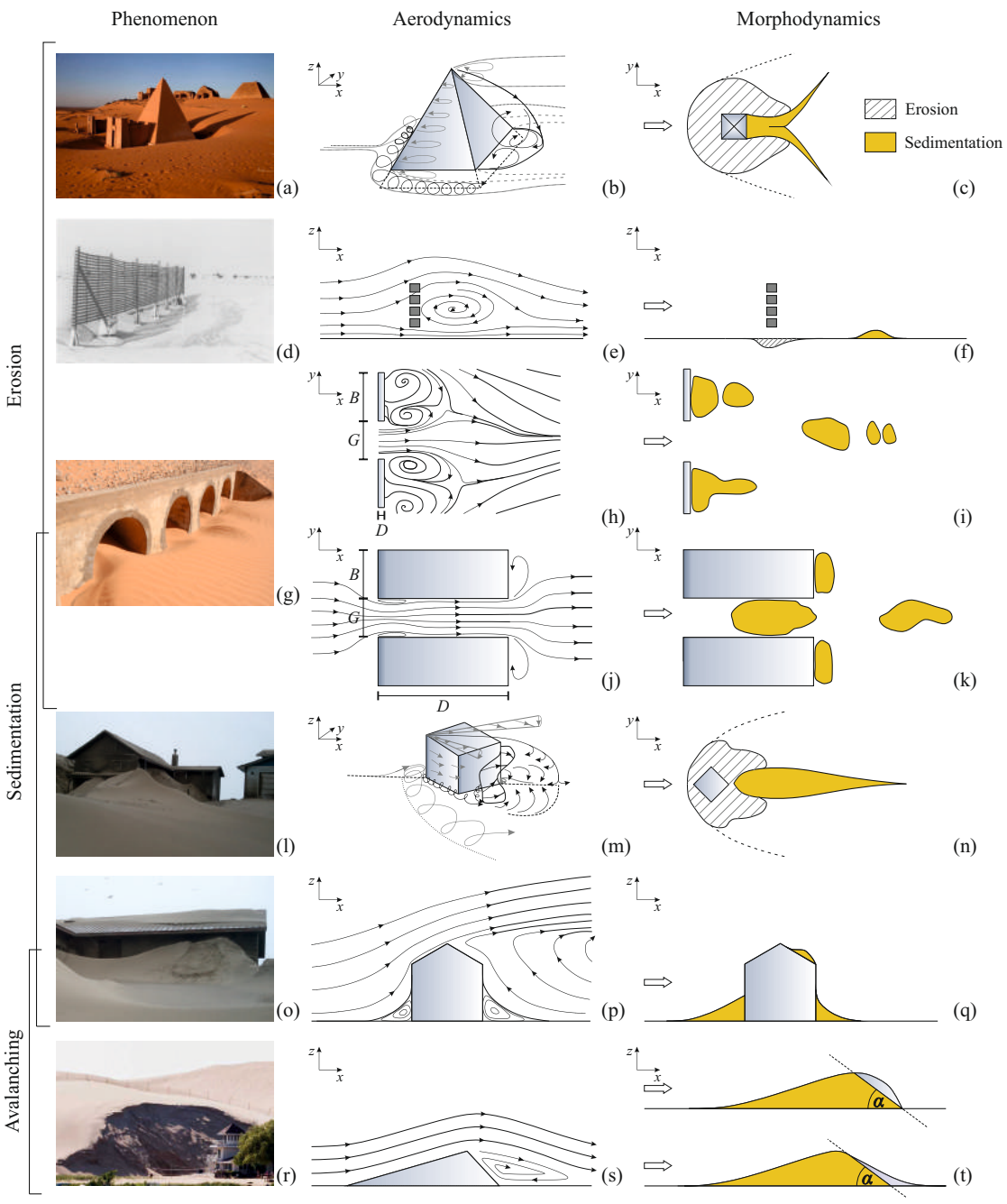
Phenomenon
Aerodynamics
Morphodynamics
Erosion
Sedimentation
Avalanching
Erosion
Sedimentation
(a)
(b)
(c)
(d)
(e)
(f)
(g)
(h)
(i)
(j)
(k)
(l)
(m)
(n)
(o)
(p)
(q)
(r)
(s)
(t)
B
G
H
D
α

Figure 5.1: Windblown sand around built structures. Scour effect around a Meroe Pyramid in Sudan (a, explicit publishing permission from the owner of the photo: Boris Kester, www.traveladventures.org), 3D flow pattern around a pyramidal obstacle (b, redrawn from [129]), sand erosion pattern (c, redrawn from [196]). Venturi effect under a porous sand fence (d, reprinted from [316], with the permission from the Geological Society of London), wind flow mean streamlines (e), eroded and sedimented sand (f). Partial obstruction of embankment culverts (g), D<<B: time-averaged streamlines between two solid barriers (h, redrawn from [180]), sand accumulation zones (i, redrawn from [179]); D>B: time-averaged streamlines in a conduct (j), sand accumulation zones (k). Shadow dune in the lee of a house in Waldport, Oregon (l, explicit publishing permission from the owner of the photo: Jason Durrett), qualitative flow around a cube with 45° incidence angle (m, redrawn from [303]), sand sedimentation pattern (n, redrawn from [196]). Sand accumulation on a gable roof in Waldport, Oregon (o, explicit publishing permission from the owner of the photo: Jason Durrett), flow pattern around a building with 30° roof pitch (p, redrawn from [223]), sand sedimentation pattern (q). Sand avalanching from a migrating dune at the Silver Lake, Michigan (r, explicit publishing permission from the owner of the photo: Andraya Croft), flow around an ideal transverse dune (s), dune shape before and after avalanche (t).

In the following, a concise phenomenological analysis of windblown sand around built structures is given to ground its successive modelling. The windblown sand action results from the wind flow field and sand morphodynamics around the affected structure. Some real world case studies are collected in Fig. 5.1, left column. For each of them, the local wind field topology is schematized by referring to the huge literature in the field of surface-mounted bluff body aerodynamics (e.g. [137, 187], Fig. 5.1, central column). Correspondingly, the local sand morphodynamics around built structures are depicted by translating the experimental studies on natural obstacles, such as boulders and clumps of vegetation (e.g. [188] and references therein, Fig. 5.1, right column). The case studies are selected as examples of the three main aeolian phenomena arising around built structures: erosion, sedimentation, and avalanching.

Erosion implies scour around built structures. Scour is a well known effect in structural, fluvial and coastal engineering. Indeed, it takes place in a variety of design scenarios, e.g. around bridge piers [238], or around marine and offshore structures [100]. A remarkable three-dimensional aeolian scour is shown in Fig. 5.1(a) around one of the Meroe pyramids in Sudan. The wind flow pattern around an isolated pyramid is characterized by an upwind horseshoe vortex (Fig. 5.1b), similarly to others bluff bodies and wind incidences (e.g. [287], Fig. 5.1m). Such a vortex results from the interaction between the atmospheric boundary layer and the boundary layer along the frontal and side surfaces of the mounted body. The reversed flow close to the ground induces sand erosion in front of and around the

pyramid (Fig. 5.1c). Sedimentation only occurs around the wake midline, where vortices of opposite sign are close to each other [196].
Fig. 5.1(d) shows a simpler example of two-dimensional aeolian scour at the toe of a 2 m high porous fence, 3 months after its installation [316]. The bottom opening induces the well known Venturi effect, i.e. the acceleration of the wind flow across the gap (Fig. 5.1e). It involves local erosion of the sedimented sand at the fence foundation, and local sedimentation of the transported sand where the flow decelerates [50] (Fig. 5.1f).
An analogous Venturi effect and related erosion take place across the gap between two solid barriers (plan view, Fig. 5.1h), if the depth/gap ratio D/G is much lower than unit. Once more, sand sedimentation occurs where the wind speed decreases, i.e. downwind the barrier free end [180] and in the wake far from the gap [179] (Fig. 5.1i).

Sedimentation and progressive sand accumulation around structures can occur under different circumstances. Fig. 5.1(g) shows the partial obstruction of culverts across a railway embankment. Unlike the gapped barrier above, here the D/G ratio is higher than unit. The separation bubbles just downstream the duct leading edges act as a virtual convergent/divergent segment, and induce the flow deceleration along the remaining length of the duct, other than in the culvert far wake (Fig. 5.1j). A massive sand accumulation along the duct and the culvert obstruction follows, in addition to the sedimentation at the shoulder recirculation regions and in the wake far from the culvert (Fig. 5.1k).
Fig. 5.1(l) shows the accumulated sand downwind a low rise house in Waldport, Oregon. The flow topology depicted in Fig. 5.1(m) is confirmed by a number of wind tunnel tests around surface-mounted finite-height prisms at various incidences, from [187] to [303]. The near wake topology is characterized by a closed arch-vortex, that entrains the surrounding fluid from both sides and from the top towards the axis of symmetry of the wake. In such a way, the sedimented sand shapes as an elongated, alongwind symmetric, and narrow dune (Fig. 5.1n, also called "sand shadow" in geomorphology literature). Such kinds of sand shadow have been reported in the geomorphology literature for a variety of natural obstacles, e.g. in the lee of small boulders and bushes but also mountains (e.g. [237, 329]).
Fig. 5.1(o) shows sand accumulated on the downwind pitch of a gable roof. According to the flow pattern in Fig. 5.1(p) the flow separates along the ridge and does not reattach onto the roof [223]. The local low-speed wind in the reversed flow regions promotes sand sedimentation on the roof right downwind the ridge, other than around the upwind and downwind vertical walls of the building (Fig. 5.1q).

Sand *avalanching* re-shapes the accumulated sand, where the accumulation profile locally exceeds the sand natural angle of repose. The angle of repose for medium-fine sands is typically $\alpha = 32° - 34°$ [237]. Sand avalanches can take place at different scales. In Fig. 5.1(o) a small avalanche comes down from a

steep accumulation profile downwind a house. In Fig. 5.1(r) a dozen meter-long sand avalanche develops along the whole downwind face of a large migrating dune. The flow around a transverse dune is schematically depicted in Fig. 5.1(r): the boundary layer separates at the dune crest, and an elongated reversed flow region takes place downwind it (Fig. 5.1s). The sand sedimentation rate is very high just downwind the crest, and deceases towards the dune downwind toe. Recurrent avalanches slide down from a line close downwind the crest (also called "brick" line, in geomorphology literature, Fig. 5.1t).

5.2 Windblown Sand Limit States

The lack of a common categorization of windblown sand induced effects on structures and infrastructures has resulted in the proposition of a new general framework, shown in the upper part of Fig. 5.2. In general terms, under a given windblown sand drift (input) the overall structure/infrastructure (system) is characterised by a resulting level of performance (output). Windblown *Sand Limit States* (SLSs) are defined as threshold performance levels, beyond which the structure/infrastructure no longer fulfills relevant design criteria under windblown sand action. SLSs are classified into Sand Ultimate Limit States (SULSs) and Sand Serviceability Limit States (SSLSs), analogously to safety formats widespread in structural engineering [81]. SULSs are defined as the threshold performance level beyond which structure/infrastructure is no longer safe, while attaining SSLSs implies its loss of functionality. SLSs may be specified separately for structures and infrastructures, since windblown sand action is strictly bound to them. In the present section, the focus is put on railway infrastructures, defined as a set of four *railway components*: i. Civil works; ii. Track superstructure; iii. Rolling stock; iv. Signalling system. In the case of civil structures, SLSs account for both direct and indirect windblown sand action. Attaining SULS involves structural failure, while attaining SSLS involves structural durability issues, service requirements no longer met, and human discomfort. Conversely, in the case of civil infrastructures, SLSs mainly account for indirect windblown sand action and strongly depend on the affected component. In general, attaining SULS involves service interruption and/or users unsafe conditions, while attaining SSLS involves infrastructure partial loss of capacity and/or users discomfort. In the following, attainable SLSs are discussed by referring to generic structures and in particular railways infrastructures. The windblown SLSs are adopted as a main classification criterion, while the railway components attaining them as the secondary (see Fig. 5.2).

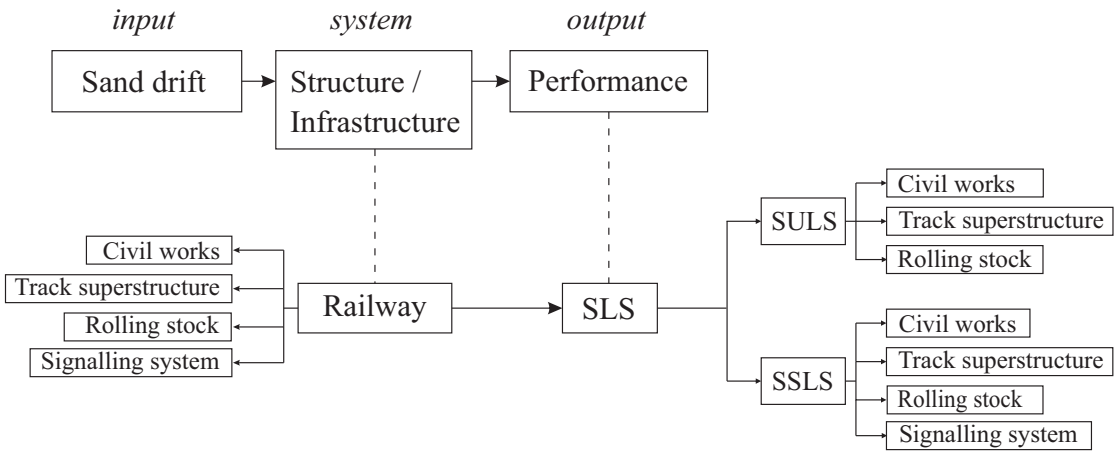

Figure 5.2: Framework scheme of the safety standards.

5.2.1 Sand Ultimate Limit States

SULSs are mainly induced by accumulated sand volume. This schematically occurs under two different environmental conditions. First, when migrating dunes, e.g. barchan ones, encroach a built structure. Secondly, when the structure is near or in a sandy plane. In this case, the structure acts as an obstacle to the incoming sand drift and induces sand sedimentation around it. In both cases, the attainment of SULS causes structural failure. Fig. 5.3 shows a coastal dune encroaching a house: the active lateral sand pressure induces the collapse of the structure.

Figure 5.3: Sand Ultimate Limit States. House collapse due to active lateral sand pressure from an encroaching sand dune at the Silver Lake in Michigan, before and after the attainment of the SULS.

Railway SULS is mainly attained by civil works, e.g. embankment or cutting buried by sand. Because of the state of civil works, the track superstructure and

rolling stock attains it in turn. To our best knowledge, the remaining reviewed system components (i.e. signalling system) do not suffer SULSs. Under SULS, the windblown sand completely inhibits infrastructure operation. Hence, SULSs are attained on the whole or a section of the railway.

Civil works

Schematically, railway body is susceptible to be buried by windblown sand under two conditions:

- the railway line crosses a migrating dune field, i.e. an area covered by transverse or barchan dunes (Fig. 5.4a). Such dunes advance with little or no change in shape and dimension [299]. The velocity of barchan dunes varies with the dune height. For example, a 3 m high dune propagates at a velocity from 15 to 60 m/yr, while a 15 m high dune with a velocity ranging from 4 to 15 m/yr [6]. Dune encroachments across railway lines are reported by [207] and [68];

- the railway line crosses a sandy plane, where the ground surface is covered by a thin sand sheet. The railway body (embankment and/or cutting) acts as an obstacle to the incoming wind flow, inducing a deceleration of the flow at the upwind toe and a recirculation region downstream [e.g. 328]. The reduction of the wind velocity and the shear stress promotes sedimentation of the windblown sand over the infrastructure, resulting in a partial (Fig. 5.4b) or full covering of the railway body. The degree of coverage depends, besides the incoming sand transport rate, on time. Regardless of the degree of coverage, the sedimented sand induces the railway SULS when it compromises the infrastructure safety or operation. A number of site observations well documents railway covering in the literature, e.g. [346, 231, 96, 47].

Track superstructure

Analogously to civil works, track superstructure of at-grade sections (ballast bed, slab or rails) promotes sedimentation of the windblown sand over the track. Windblown sand can jam the railroad switches (also named turnouts, Fig. 5.4c). The sand accumulates in the gap between the linked tapering rail and the diverging outer rail (Fig. 5.4d), and prevent the correct operation of switches, analogously to snow and ice in cold conditions. In such a condition, service interruption is mandatory since switches malfunction may lead to train derailment or head-on collision.

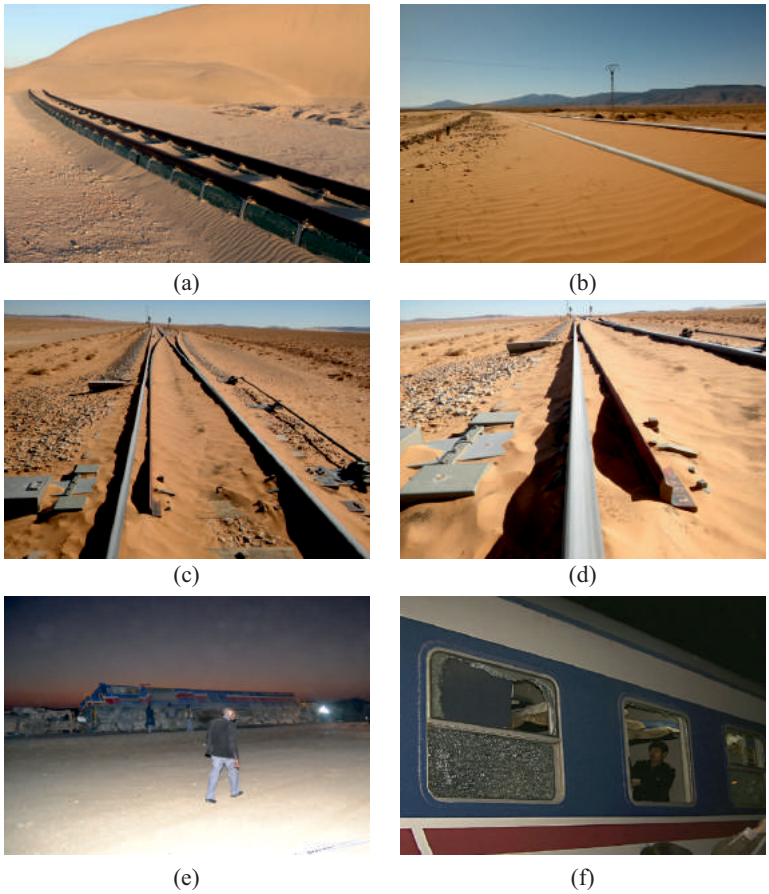

Figure 5.4: Sand Ultimate Limit States. Civil works: full sand coverage by an encroaching dune (a, explicit publishing permission from the owner of the photo: Giles Wiggs), partial sand coverage blown from sandy plane (b). Track superstructure: jammed turnout (c), detail of the sand accumulation in the gap (d). Rolling stock: running train derailment (e, reprinted from [63] with the permission from the editor), train window breaking (f, reprinted from [47] with the permission from Elsevier).

Rolling stock

The following conditions are recognized as SULSs of rolling stock:

- the sand covering of the railway platform can induce derailment of running trains (Fig. 5.4e), as reported by e.g. [211], [63];
- in general, the overturning of running trains is mainly due to crosswind (see [14] for a review). The contribution of the sand suspended in the crosswind

flow has been recently studied by [332] and [312, 313] by means of computational fluid dynamic simulations. According to [312], for very high crosswind speed (about 50 m/s) the overturning moment caused by sand grains impacts on the running train is about 20% of the aerodynamic overturning moment. To the authors' best knowledge, there are not experimental evidences to date;

- parked trains acting as a further obstacle to windblown sand and promoting sand sedimentation around them. Trains parked even for relatively short time can get trapped during windblown sand events with high sand drift (e.g. one night according to [96]). In the mentioned case, sand had to be manually removed to allow the train departure;

- breaking of the train windows by windblown sand in conjunction with high wind speed (Fig. 5.4f, [47]). An experimental study has demonstrated that windblown sand, and especially sand grain of about 5-6 mm in diameter, can significantly reduce the window glass ultimate pressure [333].

5.2.2 Sand Serviceability Limit States

Fig. 5.5 collects some iconic examples of SSLS. Windblown sand encroaching the Algerian town of In-Salah is shown in Fig. 5.5(a). According to [28], dozens of buildings including houses, schools and administrative buildings were completely and permanently abandoned due to serviceability issues induced by encroaching sand. The sand accumulates not only against buildings facades (Fig. 5.5b) but also enters indoor spaces (Fig. 5.5c) obstructing the use of the building. Two remarkable examples of attained SSLS in coastal regions are Bayshore district in Oregon and Shoyna village in Russia. In Bayshore district, houses are built along the backside of a foredune. Because of the strong winds, sand frequently and regularly buries them [159] (see Fig. 5.1l,o). Shoyna village was settled in the 1930s. Sand dunes started migrating by the action of westerly wind from the 1950s. Nowadays, more than half of the village is buried under sand and population decreased accordingly [143].
Structures built in windblown sand-prone zones can be also subject to windblown sand induced wear. The wear induced by sand on common construction materials in desert environment, such as concrete and adobe blocks, has been investigated by [115, 335, 172].

Railway SSLS is attained by every component of the railway infrastructure. Under SSLS, windblown sand affects only a component of the railway. However, SSLSs reverberate on the overall railway system performances, notably its speed. Significant speed reduction along sandy block are reported by [211, 342, 208].

(a) (b) (c)

Figure 5.5: Sand Serviceability Limit States. Windblown Sand Serviceability Limit States. Sand encroaching In-Salah, Algeria (a, from Google Earth year 2002), sand sedimented against a single building in In-Salah (b, explicit publishing permission from the owner of the photo: Nouar Boulghobra), indoor sand infiltration in In-Salah (c, reprinted by permission from RightsLink: Springer [29], owner of the photo: Nouar Boulghobra).

Civil works

The sole SSLS attained by civil works is the partial obstruction of railway embankment culverts by the sedimented windblown sand. Even if this is a recurrent issue on the field (Fig. 5.6a), it is scarcely studied in scientific literature, except by [276].

Track superstructure

The following track superstructure SSLSs are identified:

- ballast contamination (or ballast fouling) due to windblown sand is the most common example of attained track superstructure SSLSs. The sand acts as an external source of fine materials (i.e. surface spillage in [269]) infiltrating from the upper surface of the ballast bed. In usual conditions, surface spillage contributes to about 7% of the ballast contamination, but it largely prevails in desert environment. Attainment of ballast contamination SSLS is generally defined by referring to a permitted level of fouling, quantitatively expressed by a suitable fouling metric, e.g. Fouling index [269], Void Contaminant Index [291], or Percentage Void Contamination (PVC, [87]). Different allowable limits of PVC have been applied for different track standards and ballast depths. As an example, according to [130], in a concrete sleeper track with a 250 mm thick ballast, an allowable limit of PVC at 30% is used to specify a ballast-cleaning process considering a minimum requirement for the depth of clean ballast of 100 mm. Figures 5.6 (d-h) shows different levels of ballast contamination along the same railway line: clean 0% $\leq$PVC$<$ 20% ballast

(Fig. 5.6d); moderately (20% ≤PVC< 30%) to fouled (PVC ≥ 30% ballast (Fig. 5.6e,f); fully buried ballast (Fig. 5.6g); fully covered ballast (Fig. 5.6h). In the literature, there is a number of well documented ballast contamination site observations (e.g. [346, 343, 96, 300]). Ballast layer fouling leads to:

  - increasing of the stiffness and decreasing of the damping of ballast bed and rail support modulus. That causes an increase of train-induced vibrations and additional damage to superstructure components of the track, such as sleepers, rail pads and rails (see e.g. in situ observation by [343] along the Iranian Bafgh-Mashhad railway, and laboratory full-scale box tests by [131]). The received share of axle load for under wheel sleeper and sleeper bending moments are subsequently higher in sand-fouled ballast than in clean one [340]. Ballast fouling percentages of 12% and 50% involve a growth of the rail support modulus of about 182% and 454%, respectively [85];
  - accumulation of permanent deformation, increasing surface deviation of the track [76];
  - rail corrugation, as observed in situ by [300] along the Aqaba Railway, Jordan (Fig. 5.6b). This is a phenomenon characterized by route-wise periodic patterns of wavelets on the rail head [301]. Besides negatively affecting train induced dynamics, such anomalies also result in environmental noise pollution. Affected rails are called squealing or roaring [184];
  - decreasing of the ballast drainage capacity, as observed in situ by [7] (Fig. 5.6c). The test results by [291] show that a 5% increase of the Void Contaminant Index decreases the hydraulic conductivity by a factor of around 1500 for ballast contaminated by fine clayey sand;

- corrosion and degradation of fastening system, r.c. sleeper and rail due to the salt content of the sand sedimented around them (Fig. 5.6i, j and k, respectively). To our best knowledge, no specific studies about windblown desert sand are published on the topic, apart from qualitative observations of corrosion test in a saline mist chamber on a specially coated clip and its metallic screw [42];

- sand induced effects on the dynamic behaviour of fastening systems. Laboratory dynamic bending load tests conducted by [42] on a single fastening system show that sand penetrates in the gaps between the upper surface of the pad and the rail foot. A significant increase of the overall stiffness of the fastening system follows (about +44%);

- windblown sand sedimented around railroad switches enters and becomes trapped in their components. This, in turn, leads to abrasive wear [326],

increasing of the friction between sliding/rolling components (Fig. 5.6l), decreasing of the performance and durability of grease and lubricant [154];

- rail grinding induced by the thin sand layer sedimented on the wheel-rail contact interface. This SSLS has been first recognized along the heavy-haul North-South Railway in KSA [96, 154, 122], and more recently along the Haramain High Speed railway [86]. The thickness of the sand layer on the head of the rail is estimated of the order of the millimeter. The sand covered rail head is easily recognizable by its matte surface, compared to the shiny sand free rail head (e.g. the right and left hand rails in Fig. 5.6m, respectively). When a train travels on a rail covered by a thin sandy layer, it crushes sand grains and increases wearing (Fig. 5.6n). To our best knowledge, the reasons why sand sediments on a rail head are scarcely investigated in scientific literature. [122] conjectures this is due to the aerodynamic effects of the passing trains: the underside of the vehicle induces lifting of the sand previously sedimented in between rails, analogously to the well known ballast lifting by high speed trains. Analogous effects are expected in the wake of the train. These train-induced lifting is expected to induce the sand covering of both rails, because related aerodynamic phenomena are symmetric in average. However, in situ observations (e.g. [96]) often reveal the asymmetric sand covering of the rails, i.e. covered downwind and sand-free upwind rail head (e.g. Fig. 5.6m). We propose in the following an aerodynamic reading of this evidence. The incoming wind flow separates at the head of the upwind rail. Here, the flow acceleration avoids sand sedimentation and promotes erosion. Conversely, the low-speed flow recirculation in the track gauge promotes the windblown sand sedimentation around the downwind rail gauge face and on its head. This qualitative reading should be confirmed by future quantitative studies. The sandy layer increases the friction coefficient up to approximately twice the value commonly seen in Europe or North America [122]. This induces adhesive vertical and gauge face wearing rates 18 to 24 times higher than an analogous North American railway [122]. A worn rail head with crack patterns on its surface is shown in Fig. 5.6(o). Because of the asymmetric sand sedimentation, [96] estimates the head of the downwind rail wears at 2-3 times the rate of the upwind rail, and the rate of rail replacement is expected 3 to 1 for the downwind to upwind rail respectively.

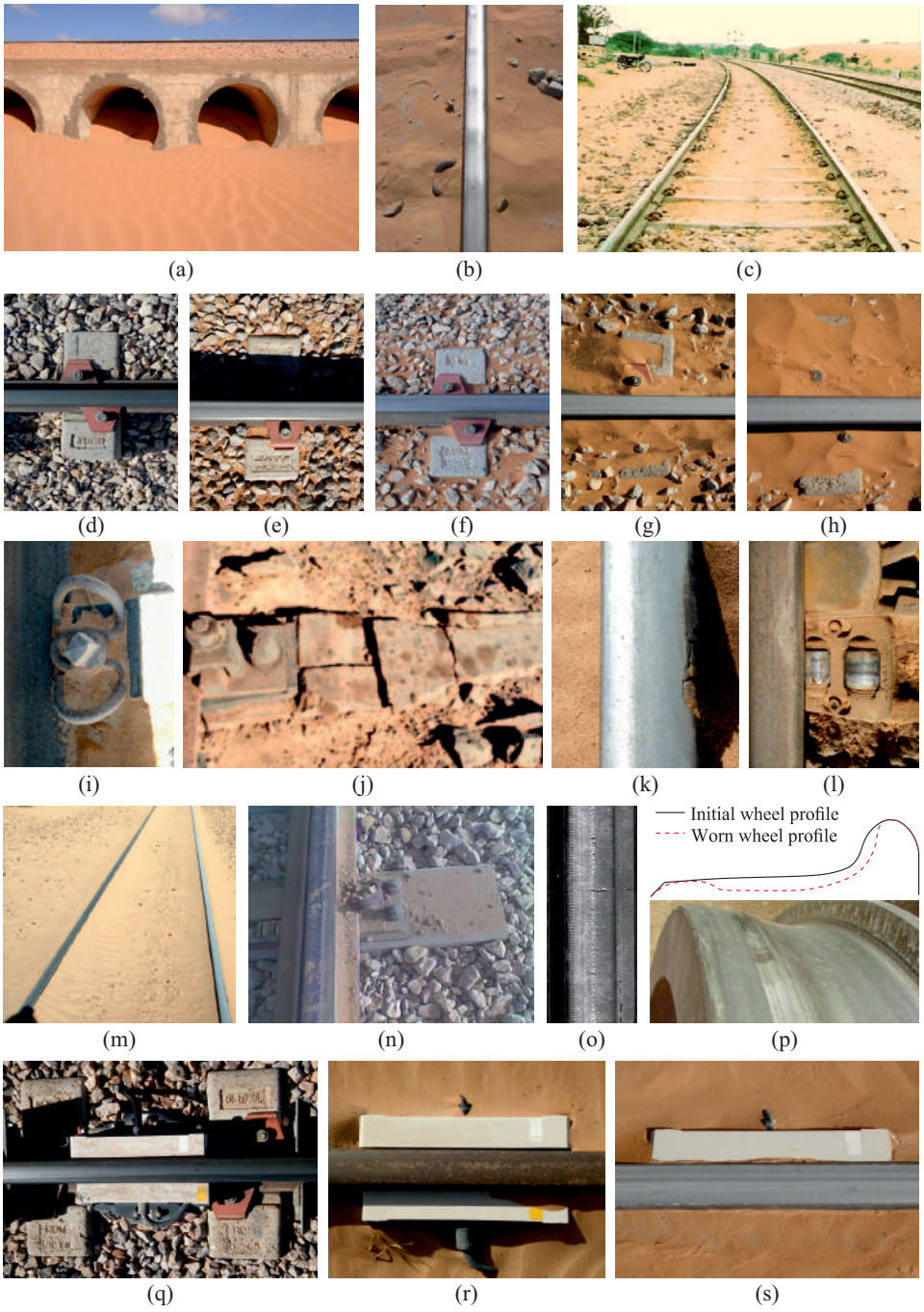

(a) (b) (c)

(d) (e) (f) (g) (h)

(i) (j) (k) (l)

(m) (n) (o) (p)

(q) (r) (s)

Figure 5.6: Sand Serviceability Limit States. Partial obstruction of embankment culverts (a). Ballast contamination induced problems: Rail corrugation (b, reprinted from [301] with the permission from Elsevier, photocredit: W. R. Tyfour), Track drainage malfunction (c, reprinted from [84] with the permission from Elsevier). Levels of ballast contamination (d-h). Corrosion of track superstructure elements due to salt content in sand: contamination of fasteners and rail web (i), degradation of sleepers (j, reprinted from [84] with the permission from Elsevier), corrosion of rail head (k, courtesy of Astaldi). contamination of turnout moving components (l). Sand wearing induced issues: thin sand layer on the downwind rail head, incoming wind from left to right (m, courtesy of Astaldi), detail of the downwind rail head (n, reprinted from [154] with the permission from Voestalpine), waring-induced cracks on the rail head (o, reprinted from [154] with the permission from Voestalpine), wheel profiling (p, reprinted from [154] with the permission from Voestalpine). Sand accumulation around Wheel Detectors: sand free WD (q), partially buried WD (r), fully covered WD (s).

Rolling stock

The rolling stock may attain the following SSLSs:

- sand-induced wheel profiling results from the same aerodynamic phenomenon that induces rail grinding, i.e. windblown sand sedimentation on the wheel-rail contact interface. Severe wheel wear problems have been observed on rolling stock operating along the heavy-haul North-South Railway in KSA [96, 154, 122] and along the the Haramain High Speed railway [86]. The wheels adopted in four months track test along the Haramain line recorded very low performances in terms of durability, reaching the end of life within around 130,000 km [86]. Analogously, [96] estimates that the wheel wears 2-3 times faster than the normal rate, and wheel replacement is 2-3 times more frequent. Both flange wear and hollow wheel occur (Fig. 5.6p, after [154]). A sound metallurgical analysis of the damage mechanism is given by [86] on the basis of optical micrographs: the wear originates in the thin sand layer, that induces very deep layer of cold plastic deformed material and surface cracks that are filled by sand. Once the sand has penetrated the cracks, further plastic strain tends to incorporate it into the steel matrix, and enhances the crack propagation. According to [122], the wearing process is amplified along almost completely tangent alignments usually occurring in railway lines across deserts. Here, the wheel running bands consistently makes contact with the same portion of the rail profile;

- sand impact on high-speed running trains. Premature wear of train elements, especially the leading vehicle, may occur because of the high relative speed

caused by the motion of high-speed trains in sand-laden air. Such a limit state has not been observed up to now in the field, but preliminary investigations have been recently proposed in the literature by [227].

Signalling system

A number of signalling devices are often mounted on modern railways to detect and transmit rolling stock information. All of them are prone to be buried by sedimented sand, and damaged by mechanical sand removal operations. Conversely, sedimented sand is expected to affect their operability to a different extent, depending on their working principles. Even if to our best knowledge scientific studies or technical specifications are not available in the literature, some devices are recalled in the following:

- Wheel Detectors (WDs) are part of Axle Counting System, rail-mounted on the gauge side of the rail, and usually based on inductive sensor technology. Such sensors are traditionally [95] and widely used to measure train position or speed in desert environments. Because of their working principles, they are generally independent of sedimented sand [128]. Sand free, partially buried and fully covered WDs are shown in Fig. 5.6(q-s), respectively;

- balises are wayside transmission units which communicate with a train passing over them. They are mounted along the center line of the track, and based on Magnetic Transponder Technology. Its main function is to transmit and/or receive signals through the air gap between the balise and the train [302]. The sand covering induces the impairment in the balise performance, analogously to other debris [293]. According to [302], the influence of debris is twofold: i. the Input /Output characteristics of balise are affected; ii. the mutual coupling between balise and on board antenna unit is affected. The European mandatory requirements for achieving air-gap interoperability specify detailed functional and non-functional requirements for the balise and consider specific environmental conditions [302]. In particular, balise must fulfill the Input/Output characteristics when applying a 20 mm thick dry sand covering. In our opinion, for the time being, such a thickness can be tentatively adopted to quantify the SSLS of balises;

- Hot box and and hot wheel defect detectors are mounted across the whole gauge, and based on infrared optics. Their working principle is expected to be strongly affected by sedimented sand covering.

The following partial remarks can be synthetically drawn about Sand Limit States:

- bearing in mind the magnitude of the incoming windblown sand drift (Chapter 4), and the length and lifetime of a railway line, its verification at both SULS and SSLS can be obtained only under planned maintenance operation of the sand mitigation measures and of the railway itself;
- the verification of the railway line and its components at SULS is mandatory in order to cope with safety issues;
- the undesired effects at SSLS can be mitigated, but not completely removed.

Finally, in the light of the SMMs categorization in Section 2.3, it is worth highlighting that the proposed Source-Path-Receiver scheme corresponds to the Sand Limit States categorization. Correlation between SPR classification and SLSs is shown in Table 5.1. In particular, Source and Path SMMs are mainly addressed to reduce the sand drift responsible for SULS. However, even if such SMMs exhibit high sand trapping performance, it is not likely that they completely trap the whole incoming windblown sand and cope with SSLS. Receiver SMMs definitely cope with SSLS once the Path and Source SMMs remove the threat of SULS.

Table 5.1: Correlation between types of mitigation measure and Sand Limit States.

	1. Source	2. Path	3. Receiver
SULS	✓	✓	
SSLS			✓

5.3 Modelling

In the following, we propose a framework for the definition and probabilistic quantification of the windblown sand as an environmental variable action. The metric describing windblown sand action can vary depending on the SLS. However, for most SLSs, the local windblown sand action can be directly related to the volume of sedimented sand around the generic structure.

Fig. 5.7(a) shows the modelling scheme and related state variables of the local windblown sand action on a general structure. Under unsteady state conditions, the incoming sand transport rate Q_{in} splits into the sedimentation rate Q_s and the outgoing (i.e. filtered) transport rate Q_{out}. The fully probabilistic modelling of Q_{in} is provided in Chapter 4. In the light of the above, Q_{in} is here expressed via the

model by [161], here reported in probabilistic terms:

$$\begin{aligned} f(Q_{in}) =& C\sqrt{\frac{d}{d_r}\frac{\rho}{g}} f(u_*)^3 \left[1 - \frac{f(u_{*t}|d)}{f(u_*)}\right] \quad \text{if} \quad u_* > u_{*t} \\ f(Q_{in}) =& 0 \quad \text{if} \quad u_* \leq u_{*t}. \end{aligned} \tag{5.1}$$

We define the local sand action around the generic structure as the accumulated sand volume V. V results from the time-cumulated sedimentation rate Q_s, that is related to the incoming windblown sand Q_{in} by the sedimentation coefficient C_s. C_s is defined in turn as the ratio between Q_s and Q_{in}. In general, C_s depends on both the incoming sand transport rate yaw angle θ and the overall shape of the specific obstacle Γ analogously to the force coefficients for the wind action ([83], Sect. 7). However, it is worth stressing a substantial difference: the overall shape of the obstacle Γ is now described by a virtual geometry that varies over time and depends on the initial geometry of the structure Γ_0 and on V. Hence, we can write $C_s = C_s(\theta, \Gamma_0, V)$. It is worth stressing that C_s referred to path SMMs translates into their sand trapping efficiency (see Section 2.3). As a result, high values of C_s are preferred for such design solutions, i.e. most of the sand is trapped by the path SMM. Conversely, low values of C_s are preferred for generic structures. This implies that most of the sand overtakes the structure and less sand sediments around it.

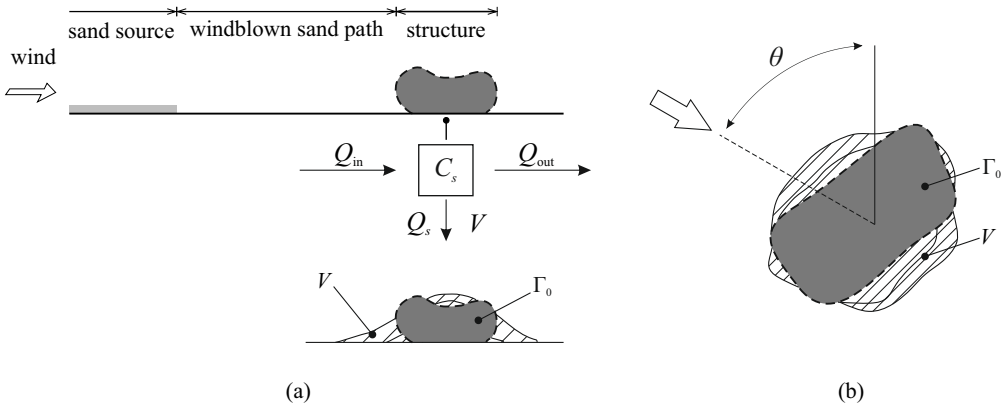

Figure 5.7: Sand action conceptual scheme (a) and dependance with respect to wind yaw angle θ (b).

Given the lack of a closed form for C_s, its semi-empirical expression can be obtained from wind tunnel tests and/or computational simulations. Qualitatively speaking, for fixed θ and Γ_0, Q_{out} is expected to increase with increasing accumulated sand volume while Q_{in} tends to zero. It follows that $C_s(V)$ has a monotonic decreasing trend and $C_s \in [0,1]$. In probabilistic modelling terms, Q_s and Q_{out} can

therefore be obtained as PDFs as follows

$$f(Q_s) = C_s\left(\theta, \Gamma_0, V\right) f(Q_{in}) \tag{5.2}$$

$$f(Q_{out}) = \left[1 - C_s\left(\theta, \Gamma_0, V\right)\right] f(Q_{in}) \tag{5.3}$$

The windblown sand action is then modeled as a random variable because of the large uncertainty involved in the phenomenon. The PDF of the total volume accumulated over a time period t can be obtained as the mixture of convolutions:

$$g(V(t)) = \sum_{n=1}^{\infty} \left(f_1 * f_i * \ldots * f_n\right) Q_s \mathrm{P}\left[N_\theta = n\right] \tag{5.4}$$

where $f_i = f$ for $i = 1, \ldots, N_\theta$, and N_θ is the number of occurrences in which the wind blows from the direction θ over t.

In order to assess the structure performance, V must be referred to the structure resistance. For most SLSs, it can be expressed as a resistant sand volume V_R. The attainment of V_R implies structure/infrastructure failure, e.g. the overturning of a wall for lateral sand pressure or the full coverage of the railway track superstructure, or alternatively SMM failure, i.e. too low SMM efficiency. For a generic structure/infrastructure, V_R can be defined according to a chosen SLS, while for a given path SMM, V_R can be defined as the SMM nominal capacity $\bar{V}$, i.e. the maximum volume of sand that can be trapped, or better as a ratio of $\bar{V}$. In any case, sand maintenance removal is required before V_R is reached. It is worth stressing that the definition of structure/infrastructure resistance through the bulk quantity V_R alone is not suitable when the windblown sand action is assessed on a localized component, e.g. a railroad switch. In such cases, the shape of sedimented sand profile plays a major role since the resistance is better quantified by the local thickness of the sand accumulated on the component.

Given the time-variant sand action $V(t)$, a time-variant reliability analysis is required in order to assess the characteristic time of failure of a generic structure subject to windblown sand action. The basic condition for a satisfactory state in a reliability analysis framework can be defined as [199]:

$$V(t) < V_R(t) \tag{5.5}$$

The probability of exceedence $p_f(t)$ of the sand action with respect to the resistant volume is equal to:

$$p_f(t) = P\left[V(t) \geq V_R(t)\right] = \int_0^{+\infty} F_{V_R}(x,t) f_V(x,t)\, dx \tag{5.6}$$

where F_{V_R} is the Cumulative Distribution Function (CDF) of V_R. In general, V_R is time-constant and can be described by its nominal value whatever the nature of

the structure is, since its degree of uncertainty is much lower than the one of V. Hence, Eq. (5.6) becomes:

$$p_f(t) = P\left[V(t) \geq V_R\right] = 1 - F_V\left(V_R, t\right) \tag{5.7}$$

where F_V is the CDF of V. The characteristic time of failure T_k can be defined as the time during which the condition (5.5) is violated only with a given probability $p_{f,k}$, i.e. $p_f(T_k) = p_{f,k}$. Assuming the monotonous function $V(t)$, p_f is also monotonous and its inverse function can be defined. Hence, the characteristic time of failure can be derived as

$$T_k = p_f^{-1}\left(p_{f,k}\right) \tag{5.8}$$

In summary, Fig. 5.8 shows a generic trend of the time-variant sand action through its PDF $f_V(t)$, the mean value $\mu_V(t)$, and the increasing trend of $p_f(t)$.

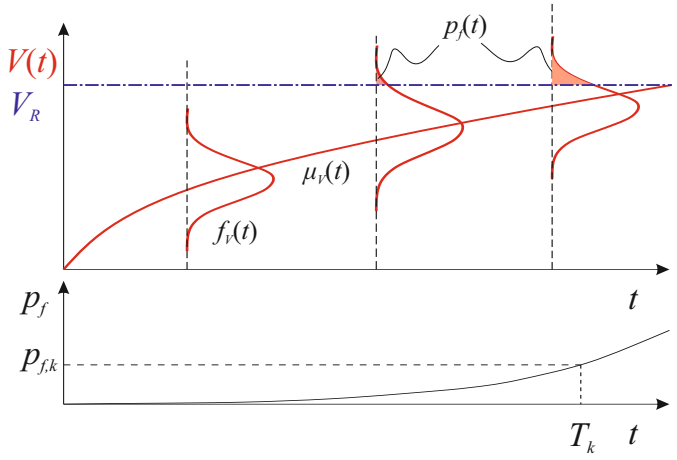

Figure 5.8: Time-variant sand action and related probability of failure.

5.3.1 Towards a semi-probabilistic approach

In a limit state design perspective and within a semi-probabilistic approach to windblown sand action, partial safety factors for windblown sand action are required and can be derived from the same proposed fully probabilistic approach. The partial safety factor γ for windblown sand action is defined equal to

$$\gamma = \frac{V_d\left(T_d\right)}{V_k\left(T_k\right)} \tag{5.9}$$

where $V_k(T_k)$ is the characteristic value of windblown sand action defined as the k-th percentile of V for $t = T_k$ and $V_d(T_d)$ is the design value of windblown sand

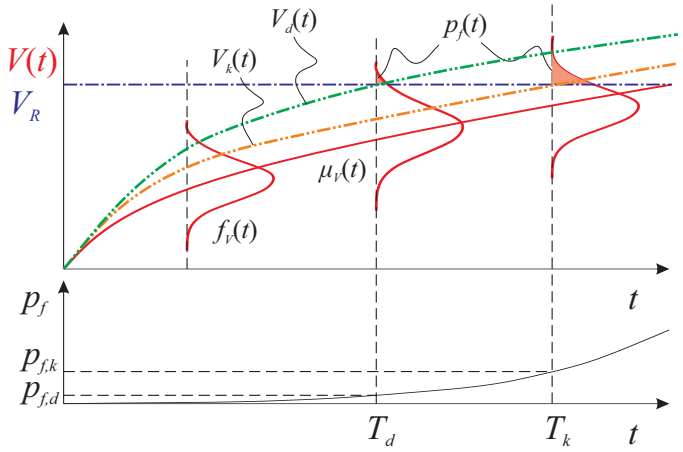

Figure 5.9: Semi-probabilistic approach to windblown sand action.

action defined as the d-th percentile of V for $t = T_d$ with $d > k$. The trends of the characteristic values V_k and design values V_d are sketched in Fig. 5.9.
The design time of failure T_d can be assessed once a target very low design probability of failure $p_{f,d}$ is chosen as:

$$T_d = p_f^{-1}\left(p_{f,d}\right) \tag{5.10}$$

The value of the probability of failure $p_{f,d}$ to be adopted results from cost-benefit analysis for each specific class of structures. However, the calibration of such probabilities is out of the scope of the present work.

5.4 Application and results

The proposed modelling framework is beyond the current state of the art reviewed in Chapter 2. The lack of long term and detailed in situ measurements does not allow proper validation. Very scarce laboratory measurements only partially allow the quantification of the sedimentation coefficient. Nevertheless, in the following an effort is accomplished to put the framework at work aimed at demonstrating the technical feasibility of the approach in an engineering design perspective. The proposed application refers to a desert railway infrastructure protected by two alternative design solutions. The study layout is outlined in Subsection 5.4.1, while the obtained results are discussed in Subsection 5.4.2.

5.4.1 Study layout

The selected site is located in the Arabian peninsula near the Hafr-al-Batin city, along the 2750 km long North-South Railway line linking Al-Haditha and Jalamid

with the new port city Ras Al-Khair (Fig. 5.10 a). The railway alignment around the site develops along the West-East direction, and it crosses the sand migration prevailing path from the An-Nafud desert to the Rub-al-Khali sand sea through the Ad-Dahna corridor. It follows that Q_{in} mainly attacks the railway from the North side and South side. The sand consists of medium sized, well sorted quartz grains. The mean sand grain diameter is set equal to d=0.35 mm [77]. The aerodynamic roughness z_0 is set equal to $z_0 = 4e-3$ m, a common value for sandy desert terrains. The wind speed dataset refers to the 10-min average wind velocity U_{10} recorded by an anemometric station from Jan 2007 to Dec 2012 with a time sampling $\Delta t = 1$ hr. The wind speed is measured over 36 directions with sampling yaw angle $\Delta\theta = 10°$.

The available dataset includes some missing data due to malfunctions or operational problems of the anemometric station. Missing data are estimated equal to 9% and are evaluated to be almost uniformly distributed along the hours of the day. Both time sampling and missing data are sources of incompleteness of the dataset. In the literature, randomly distributed data incompleteness is recognised as not influential on the probability distribution of U_{10}, while it may lead to underestimations of the extreme values [39].

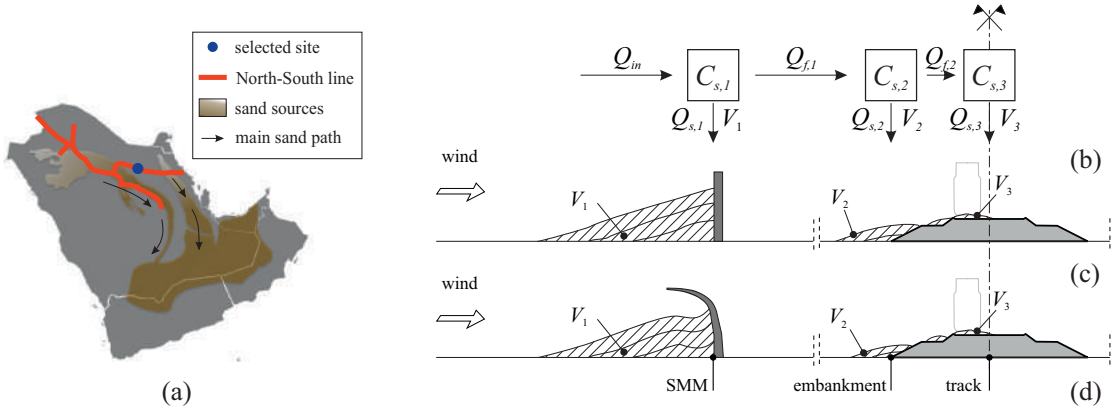

Figure 5.10: Selected site (a), modelling framework and related state variables (b), scheme of the setup geometry with SVW (c) and with S4S (d) as SMM for increasing V.

Fig. 5.10(b) shows the modelling framework and the related state variables for a single side of the railway corridor. Such a scheme results directly from the general one in Fig. 5.7, by putting in series three objects, each of them inducing a local windblown sand action, i.e. V_1 acting on the SMM, V_2 acting on the embankment, and V_3 acting on the track superstructure. The same mirrored scheme holds for the opposite side of the railway. The setup geometries are shown in Fig. 5.10(c,d). Two types of path SMMs are alternatively tested: a common Straight

Vertical Wall (SVW) [32], and the Shield for Sand (S4S) aerodynamically shaped barrier [36]. The height of the SMMs and of the embankment are set equal to 4 m and 2.5 m, respectively. A double-track railway is considered, with a 0.25 m width ballast bed.

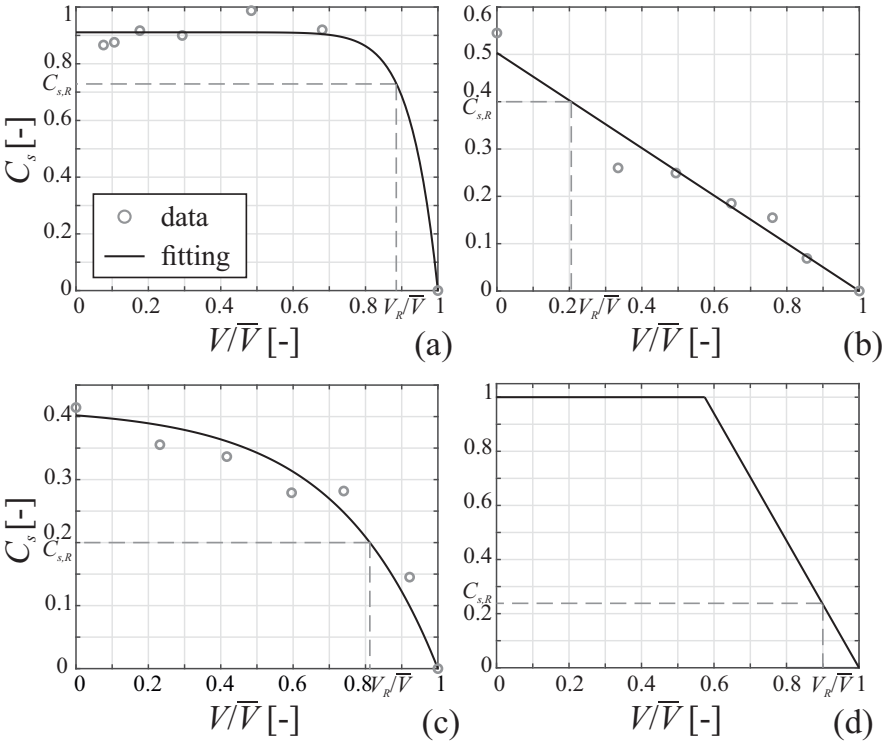

Figure 5.11: Sedimentation coefficients versus $V/\bar{V}$: Shield for Sand (a), Straight Vertical Wall (b), embankment shoulder (c), track superstructure (d).

The sedimentation coefficients C_s of both SMMs, the embankment, and the track superstructure are plotted as a function of the dimensionless sand action $V/\bar{V}$ for $\theta = 90°$ in Fig. 5.11. The experimental values of C_s referred to a basic SVW and a generic embankment are derived from the wind tunnel tests made by Hotta and Horikawa [127]. Conversely, the values of C_s referred to S4S have been directly obtained by the authors in the framework of a wind tunnel test intended for the estimation of its efficiency for increasing V, see Appendix A. Hence, the experimental data is fitted with continuous monotonic decreasing functions that exhibit $C_s(V/\bar{V} = 1) = 0$, i.e. null Q_s and maximum Q_f when the nominal capacity is reached. To our best knowledge, they are the only studies that provide time-varying V, and therefore C_s, but only for $\theta = 90°$. Unfortunately, the literature particularly lacks of studies addressed to track superstructure induced sand morphodynamics. Therefore, $C_{s,3}$ is purely conjectured constant up to the filling of

ballast voids (PVC=100%, see Subsection 5.2.2), and then linearly decreasing up to $V = \bar{V}$. As such, we conjecture that first the sand fills the ballast voids, and then it accumulates uniformly on the surface of the railway superstructure

During the lifetime of the infrastructure, the sand sedimented around any SMMs, embankment, and track superstructure need to be periodically removed in order to avoid failure. In this study, V_R is set on the basis of a performance-based criterion. The SMMs V_R is defined as the sand volume that induces a decrease of the efficiency equal to 20% the initial value, i.e. $C_{s,1}(V_R/\bar{V}) = 0.8C_{s,1}(V/\bar{V} = 0)$. The embankment V_R is set as the sand volume that induces a decrease of $C_{s,2}$ equal to 50% the initial value, i.e. $C_{s,2}(V_R/\bar{V}) = 0.5C_{s,2}(V/\bar{V} = 0)$. The results discussed in the following refer to the attainment of SULS for full covering of the track superstructure. As a result, the track superstructure V_R is set equal to $V_R = 0.9\bar{V}$. The dimensionless resistant volume $V_R/\bar{V}$ and the correspondent sedimentation coefficient $C_{s,R}$ are drawn as dashed lines in Fig. 5.11.

In order to assess the non-linear model outlined by Eq. (5.2-5.4), a Monte Carlo simulation based on bootstrapping technique is performed on the basis of $f(U_{10})$ and $f(u_{*t})$. $f(U_{10})$ is derived from the wind speed dataset. $f(u_{*t})$ is obtained directly from Subsection 4.1.1. Q_{in} is modeled as a stationary, non-Gaussian random process. As a result, Q_{in} is decomposed into a series of independent incoming sand transport rates. The low-frequency, high-amplitude cycles due to macro-meteorological fluctuations of the wind speed, i.e. time-correlations at the annual, synoptic, and diurnal time scales, are discarded. In the light of these remarks, and bearing in mind the cumulative nature of V, windblown sand action recalls somehow wind-induced fatigue loading by means of the "state approach" commonly adopted in the practice [252, 243]. The Monte Carlo simulation accounts for about 22e+6 realizations for each specific obstacle under both SMM setups. The probability of failure is set equal to $p_{f,k} = 5\%$ so that failure is defined with respect to the characteristic value of the sand action V_k, i.e. its 95th percentile $p_{95}(V)$.

5.4.2 Results

The incoming sand transport rate is assumed in the worst case scenario, i.e. perpendicular to the obstacle, by analogy with common wind engineering practice. As a result, Q_{in} derives from the side-PDFs of the incoming wind speed, i.e. the non-directional PDFs of U_{10} blowing from North and South sides of the railway. Wind statistics are collected in Fig. 5.12. The wind rose recalls a obtuse bimodal regime (Fig. 5.12b). Time series of the Northerly and Southerly recorded wind speed are plotted in Fig. 5.12(c) and condensed in Fig. 5.12(d) as classic Weibull PDFs. Finally, Fig. 5.12(e) plots the discrete distribution of the wind direction θ categorized as North, South and Calm. It is worth highlighting that, although northerly winds are more common, the North and South $f(U_{10})$ are tantamount.

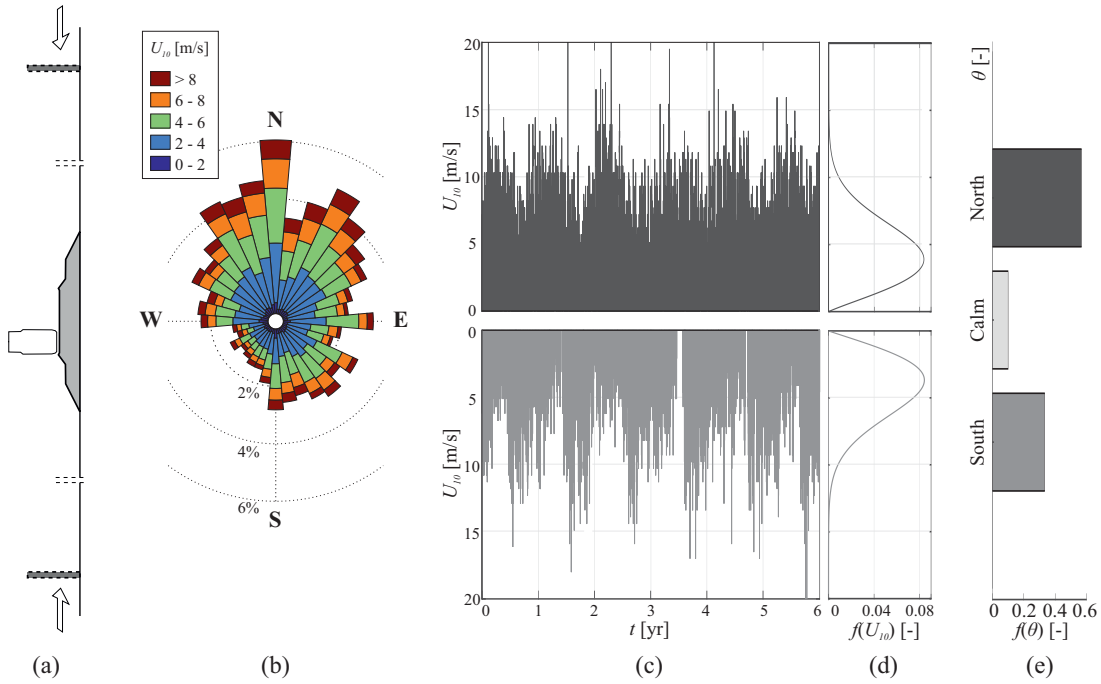

Figure 5.12: Incoming wind statistics. Geometrical setup (a), wind rose (b), North and South U_{10} time series (c), probability density functions (d), North and South direction occurrences (e).

Fig. 5.13 collects the main results derived from windblown sand action modelling framework with incoming sand transport rate from the North side of the railway and SVW setup. Fig. 5.13(a-c) plots a 1-year long realization of the incoming (Q_{in}) and filtered ($Q_{f,1}$, $Q_{f,2}$) sand transport rate versus time t in order to show the model workflow. The filtering effect on the sand transport rate is clearly depicted by the fall of its magnitude each time an obstacle is overcome. Fig. 5.13(d-f) collects the realizations of the windblown sand action V and related statistics, i.e. mean values μ and i-th percentiles p_i, versus time. It is worth highlighting that while V_1 and V_2 directly result from northerly Q_{in}, V_3 results from both northerly and southerly Q_{in}. Discarding the macro-meteorological features of the wind velocity helps us distinguish the effect of the trend of C_s on the evolution of V. The general trend of V is nonlinear monotonic increasing and tends to a horizontal asymptote defined by the obstacle nominal capacity $\bar{V}$. Indeed, the monotonic decreasing trend of C_s induces a monotonic decreasing gradient of V up to zero. Once V reaches $\bar{V}$, the equilibrium condition reflected by the null value of C_s does not allow the sand to accumulate anymore. Furthermore, the randomness of V initially increases and then diminishes approaching $\bar{V}$. Fig. 5.13(g-i) provides a close-up view of $f(V)$ in proximity to the characteristic time of failure T_k while

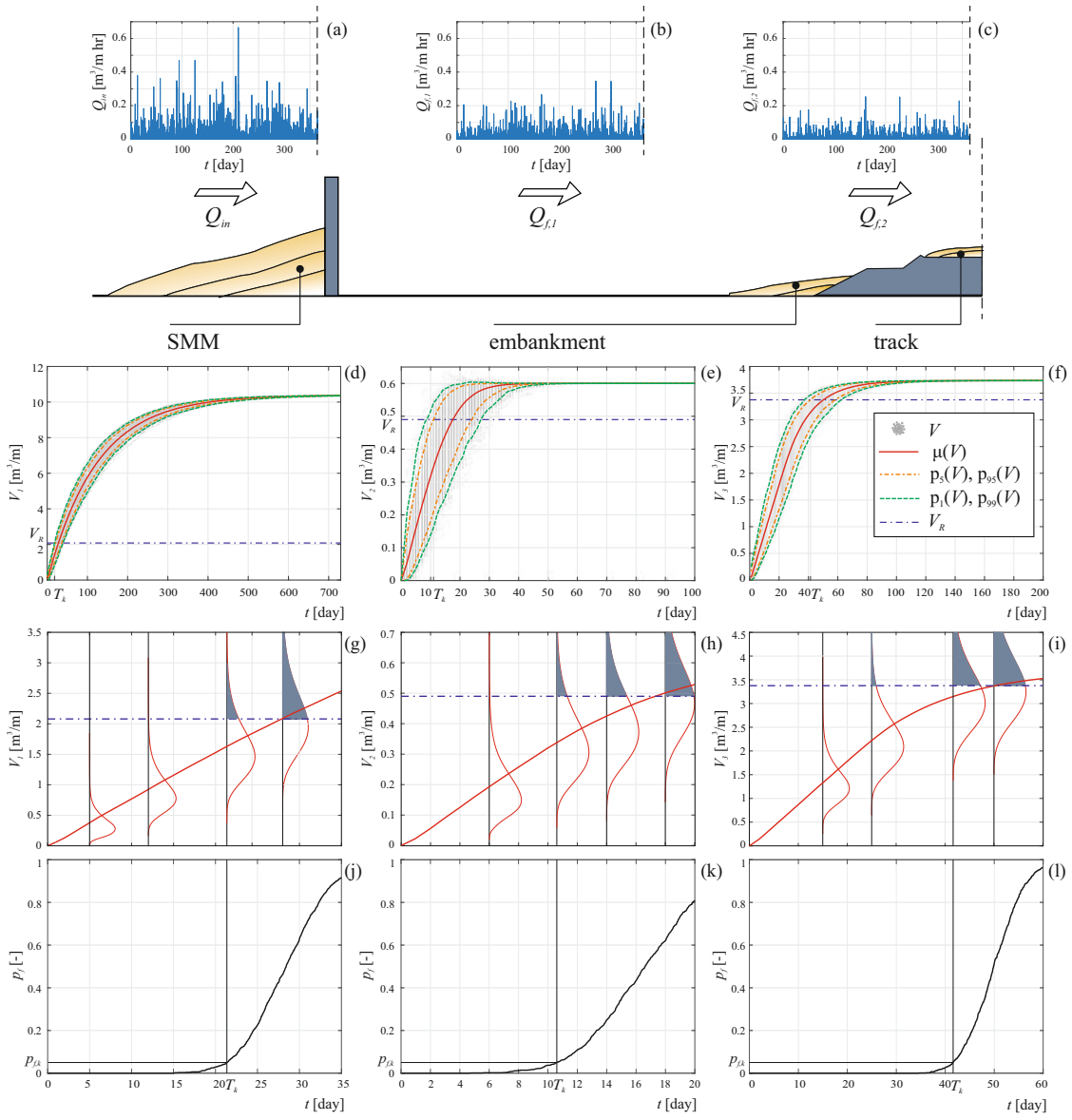

Figure 5.13: North side of the SVW railway setup. Incoming sand transport rate (a), sand transport rate filtered by SVW (b), sand transport rate filtered by the embankment (c). Windblown sand action on SVW (d), embankment (e), track superstructure (f). Close up view of the windblown sand action in the interest time-period on SVW (g), embankment (h), track superstructure (i). Probability of failure referred to SVW (j), embankment (k), track superstructure (l).

Fig. 5.13(j-l) plots the related growing probability of failure p_f. Generally, $f(V)$ are non-Gaussian with time-varying skewness from positive to negative values. Failure

is reached in chronological order on the embankment, on the SVW and finally on the track.

Fig. 5.14 collects the characteristic times of failure for the SMMs T_{k1}, the embankment T_{k2}, and the track superstructure T_{k3} resulting from the adoption of SVW or S4S along both North and South railway sides. For a given SMM, the higher the side incoming wind occurrence (Fig 5.12 e), the lower the characteristic time of failure. For both sides, the S4S barrier performs better than SVW in terms of higher T_k because of its higher nominal capacity and sedimentation coefficient. This result is supported by the purely aerodynamic study performed on both solid barriers by [32] in terms of sand accumulation potentials.

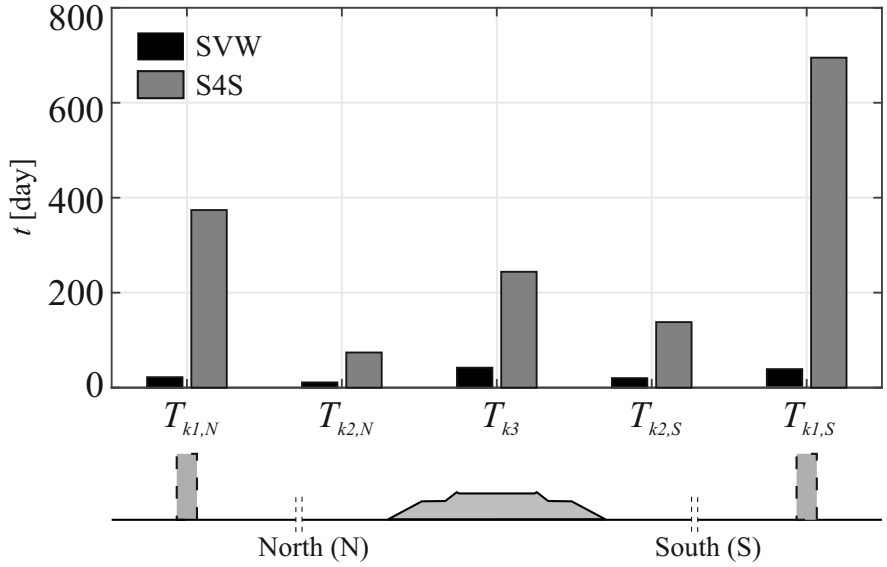

Figure 5.14: Characteristic times of failure related to SVW and S4S design solutions.

The obtained characteristic times of failure does not account for macro-meteorological effects. As a result, they can be rather interpreted as average characteristic times of failure. The time-scales of T_k can help establish if the contribution of low-frequency, high-amplitude cycles related to macro-meteorological fluctuations of the mean wind speed can be relevant. Indeed, while the SVW setup can be mainly sensitive to diurnal and synoptic time-scales, the S4S setup can also be sensitive to larger time-scales, i.e. seasonal and annual ones.

5.4.3 Concluding remarks

The technical applicability of the proposed framework to assess windblown sand action has been demonstrated by referring to a desert railway infrastructure protected by two alternative design solutions against windblown sand. The obtained results allow to assess the characteristic values of the windblown sand action, the performances of the sand mitigation measures in terms of characteristic time of failure, and plan sand removal maintenance operations on any infrastructure component. The following concluding remarks can be outlined in a design perspective:

- The proposed model allows to quantify the performances of alternative design solutions and to select the best option. In the addressed test case, Shield for Sand increases considerably the time of failure up to 2 years, and it will in turn lower sand removal costs.
- The higher the wind occurrence (in the addressed test case on the North side of the railway), the lower the sand removal period, for a given SMM capacity. Conversely, by fixing a priori sand removal period, the higher the wind occurrence, the higher the required capacity to be met by properly sizing the SMM.

Chapter 6

Conclusions

Windblown sand action and its effect on civil structures have remained for the time being overlooked in structural engineering despite the broad spectrum of windblown sand induced issues reviewed in this thesis. A number of sand mitigation measures have been proposed in the domain of railway infrastructures showing inadequate performances. The present thesis aims at reducing the existing gaps by introducing the definition of, and by proposing a modelling framework for the quantification of windblown sand action on civil structures and infrastructures. The same proposed modelling framework allows to estimate the performances of alternative sand mitigation measures.

The proposed modelling framework accounts for a probabilistic description of the windblown sand action, given the high variability of the phenomenon. The framework has been conceived on the basis of the wind engineering analysis chain commonly adopted in wind engineering. The incoming windblown sand is defined as the amount of sand transported by the undisturbed wind upwind the affected structure. It depends on the construction site characteristics, i.e. the wind flow that attacks the structure and the sand granulometry in its vicinity. The incoming windblown sand is defined and quantified by means of sand transport rate, drift potential, the resultant drift potential. While the transport rate provides an instantaneous value of the transported sand, the drift potential provides a cumulated value useful for get an idea of the structure susceptibility to windblown sand action. The local windblown sand action is then defined as the amount of sand sedimented around the affected structure. It results from the incoming windblown sand and the affected structure aerodynamic and induced sand morphodynamics. As a result, the modelling of local windblown sand action envisages the definition of a sedimentation coefficient that translates the total amount of incoming windblown sand into the actual amount of sedimented sand around the affected structure, by analogy to the force coefficients for the wind action. Such a coefficient depends on the incoming sand transport rate yaw angle, and on the virtual geometry of the whole obstacle, i.e. the evolving surface described by both the structure and the

sedimented sand. Given the lack of closed form solutions, it can be estimated by means of wind tunnel tests or computational simulations. Finally, the reliability of the affected structure can be assessed by relating the local windblown sand action to its resistance to windblown sand. This allows to forecast characteristic times of failure, to plan periodic sand removal operations, and to properly size sand mitigation measures in order to meet a chosen sand removal period. Finally, a case study addressing the comparison and performance assessment of two path sand mitigation measures, i.e. Shield for Sand and a basic Straight Vertical Wall, is reported. The time-variant windblown sand action is assessed. Their performances are quantified by means of characteristic times of failure, from which sand removal periods and windblown sand related maintenance costs result, in turn.

In conclusion, the author would like to point out that this thesis opens the door to windblown sand action and its mitigation from an engineering perspective. Furthermore, it contributes for the first time to the systematization of this existing engineering problem making use of notions and techniques from other fields, in a multidisciplinary framework.

In the light of this newborn, wide research field, the following research perspective are suggested in order to further develop the proposed model and fill further gaps of knowledge not addressed in the present thesis.

- A potential future optimization of the modelling framework consists in the inclusion of macro-meteorological broadband random component together with annual, synoptic, diurnal cycles of the wind speed into the modelling of the incoming sand transport rate. This can be done by simulating synthetic mean wind speed time series by adopting both its fitted probability density function and the wind power spectrum associated with the macro-meteorological peak [295].

- In a limit state design perspective, a semi-probabilistic approach to windblown sand action can be derived from the same proposed fully probabilistic approach, provided that the design probability of failure is known. In this framework, the effects of uncertain, highly variable environmental conditions such as soil moisture, sand salt concentration or sand crusting, could be taken into account by semi-empirical factors.

- Further experimental studies are strongly encouraged to assess the sand sedimentation pattern, and the sedimentation coefficients in turn, around multiple structure geometries and under different environmental setups, e.g. incoming sand transport rate yaw angle, and diverse wind flow features, such as Reynolds number.

- The proposed approach needs to be validated in-situ by means of long-term measurement of both incoming sand transport and local sand accumulation.

Full-scale field tests would allow to estimate scaling effects on the sedimentation coefficient, if any, and compare the performances under the operational environmental conditions for a given construction site.

The author hopes that future independent studies will be addressed to assess the accuracy of the proposed model by means of experimental campaigns and further develop this contribution in order to achieve a more robust probabilistic framework for the evaluation of windblown sand action on structures.

Appendix A

Shield for Sand

Part of the work described in this chapter has been previously published by the author and co-workers in international peer-reviewed journals [36].

This appendix aims at presenting the industrial development of the PCT International Patent Application published at number WO 2016/181417 A1 "Shield for Sand (S4S): a deflecting module for an anti-sand barrier, a barrier thus obtained and a protection method from windblown sand". The patent is owned by Politecnico di Torino and its commercialization is in charge of the Research Support and Technology Transfer Department (TRIN). The activity set out in this appendix have been carried out within the "Sand Mitigation along Railway Tracks" (SMaRT) project n. 10317, in the framework of the "Proof of Concept" programme at Politecnico di Torino co-funded by Compagnia di San Paolo & Windblown Sand Modelling and Mitigation (WSMM) group. The project financed the activity for the passage of the technology from an early stage of development to a sufficiently evolved one. The author was involved in the project team as young researcher member as explicitly required by the call. Confidential information concerning the intellectual property of the patent are not included herein.

In the following, S4S is briefly presented discussing its innovative working principles, its components, and its industrial development plan. Then, wind tunnel tests to demonstrate S4S working principles and assess its efficiency and sedimentation coefficient are illustrated.

A.1 Main features and working principles

In 2015, Bruno et al. [34] have proposed a novel concept of solid barrier called Shield for Sand (S4S), patented by Politecnico di Torino (Fig. A.1). S4S cross-section geometry is generally characterized by three parts: 1. a foundation; 2. a lower quasi-vertical part; and 3. an upper windward concave deflector (Fig. A.1a). The values of the cross section main geometrical parameters depend on the specific

construction site, i.e. the magnitude of the incoming sand drift.

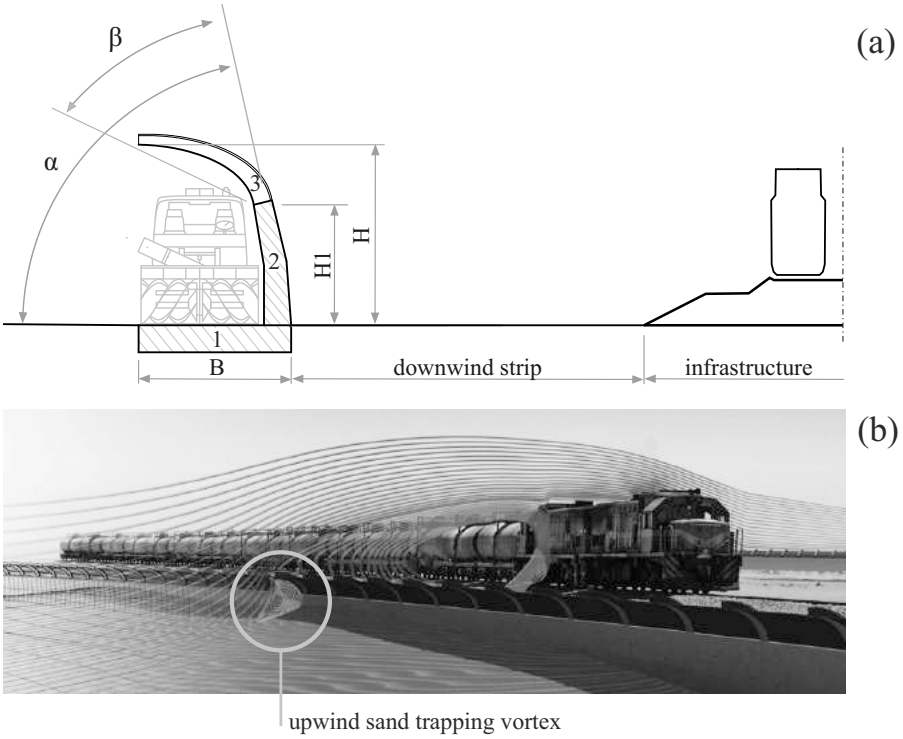

Figure A.1: S4S: rendering along a mitigated railway with simulated streamlines (a) and geometry of the barrier (b)

The three parts and their shape ensure functional requirements and the barrier working principles. The foundation opposes the overturning moment induced by both wind-induced load and passive trapped sand pressure. The quasi-vertical part allows an easy clearance of the accumulated sand by means of removal machines: for the sake of clarity, Fig. A.1(a) includes the front view of an actual sand blower machine [267]. The upper windward concave deflector is the key component in ensuring S4S innovative working principles: it maximizes the size of the upwind recirculation vortex by promoting the local downward deflection of the wind flow upwind the barrier (Fig. A.1b). The local reversed flow strongly decreases the velocity gradient close to the ground, and consequently the wind shear velocity u_*. Sedimentation is guarantee where u_* is lower than a threshold value u_{*t} (Subsection 2.2.1). As a result, the upwind vortex induced by S4S acts as a sand trapping one. Qualitatively, the larger the upwind vortex, the higher the sand trapping performances, that is: i. sand is accumulated along the upwind strip only, ii. the volume of the trapped sand is as large as possible; iii. the trapping vortex still holds also

for high levels of accumulated sand, and high trapping efficiency in turn.

Alternative construction methods, embodiments and materials can be specified for each part of S4S notwithstanding the general principles above. Options should comply with the construction requirements for civil engineering applications (simplicity of construction/prefabrication/assembling and maintenance, durability), and using building components possibly already employed in the industrial chain of other kind of barriers (such as noise or wind barriers) in the Country where the barrier is built. For instance, the render in Fig. A.1(b) depicts a solid reinforced concrete continuous vertical wall, while the windward concave deflector is formed by point wise curved steel pillars and a steel deflecting panel fixed at its intrados.

The development of a patented technology shall reach an appropriate level of maturity to allow its actual application under operational environmental conditions. The so-called Technology Readiness Level (TRL) is a method of estimating, managing and developing of a technology. Conceived by NASA in the Seventies [259], TRL is today widely adopted in a number of technological fields and by Research & Development institutions, e.g. the H2020 EU framework program. TRLs are based on a scale ranging from 1 to 9. For simplicity, TRL scale can be roughly subdivided into three parts, which refer to corresponding distinct stages of development of the selected technology.

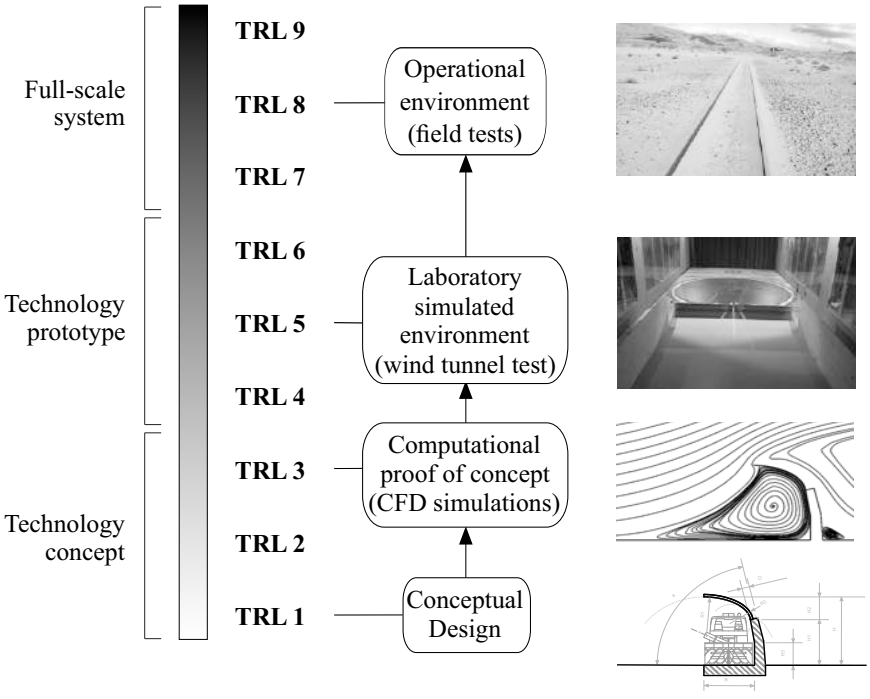

Figure A.2: S4S Technology Readiness Level

In Fig. A.2, the general TRL scale is summarized and referred to the S4S development process. In the first part (TRL1-3), the S4S technology concept is investigated by means of basic research on windblown sand phenomena [235] and engineering constraints to be fulfilled. S4S barrier is patented [34]. The concept is proved by assessing its working principle and aerodynamic performances by means of Computational Fluid Dynamics (CFD) simulations [32]. This part corresponds to the conceptual and preliminary design phases in Civil Engineering. In the second part (TRL4-6), S4S prototype is tested in laboratory environment conditions in order to validate/demonstrate the technology. In particular, wind tunnel tests with windblown sand are performed on a scaled mockup and its trapping performances are measured [37]. This part corresponds to the detailed design phase in Civil Engineering. In the third part (TRL7-9), the full-scale system is tested under operational environmental conditions towards system qualification, production process lunching and commercial deployment. This part corresponds to the as-built design phase in Civil Engineering.

A.2 Wind tunnel testing

The Wind Tunnel (WT) tests were performed on a scale mockup of S4S in the closed circuit L-1B WT (Fig. A.3) of the von Karman Institute for Fluid Dynamics, Belgium (hereafter referred as VKI), in 2017. The L-1B WT allows for the simulation of controlled Atmospheric Boundary Layer (ABL) and Saltation Boundary Layer (SBL) running over the barrier. The final objective of the WT tests is to determine the efficiency of S4S under controlled environmental conditions as close as possible to the real operational ones.

A.2.1 Design and realisation of the mockup

The mockup has to respond to aerodynamic constraints induced by the WT. A 1:10 scale mockup of S4S is designed. The height and length of the mockup are set equal to $h = 30$ cm and $l = 184$ cm, respectively. The mockup is conceived composed by three sections in order to make the construction and the transport easier:

- two side non-transparent sections 90 cm long made of wood and aluminum;
- one central transparent section 4 cm long made of acrylic sheet.

The two side section were made at the MOD Lab Arch of the Department of Architecture and Design (DAD), Politecnico di Torino, with the assistance of the author. The central section was made directly at VKI. The acrylic sheet allows for measurements of the sand accumulation levels below the upper windward concave

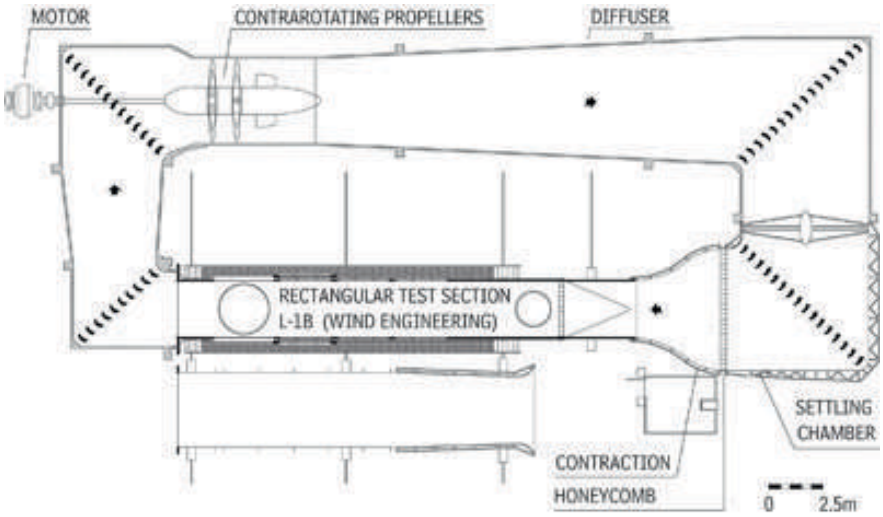

Figure A.3: Plan view of the VKI L-1B wind tunnel

deflector. The whole mockup was assembled at VKI.

The side sections consist of curved wooden pillars equally spaced by lower horizontal wooden beams at the base. An aluminum sheet with simple curvature is attached to the upper windward concave profile. The anchorage between the mockup and the WT floor is ensured by adopting steel angled supports on the downwind side of the barrier. A small prototype of the mockup 24 cm long was first made in order to test the construction process, its resistance and deformation (see Fig. A.4). The base of the prototype was anchored to a small multilayer wooden panel in order to replicate the same anchorage of the WT. A uniformly distributed load equivalent to 5 kg was then applied to each pillar in order to simulate the wind load (Fig. A.4c). The prototype allowed to optimize the building process and confirmed the resistance and deformation requirements.

Being the construction process the same, it is described in detail for the mockup side sections only. The curved pillars were printed by means of a laser-cutting printer (see Fig. A.5a). A single pillar is made of two glued wooden layers 8 mm thick, each. The wooden skeleton was then assembled starting from 5 curved pillars and 4 wooden base beam placed between them (see Fig. A.5b). A 1 mm thick aluminum sheet was manually bent and glued to the wooden skeleton (Fig. A.5c). In Fig. A.5(d), 5 clamped wooden ribs were positioned in correspondence of each pillar in order to avoid displacement while the glue was drying. Finally the angled supports are screwed on the downwind side of the mockup (Fig. A.5e).

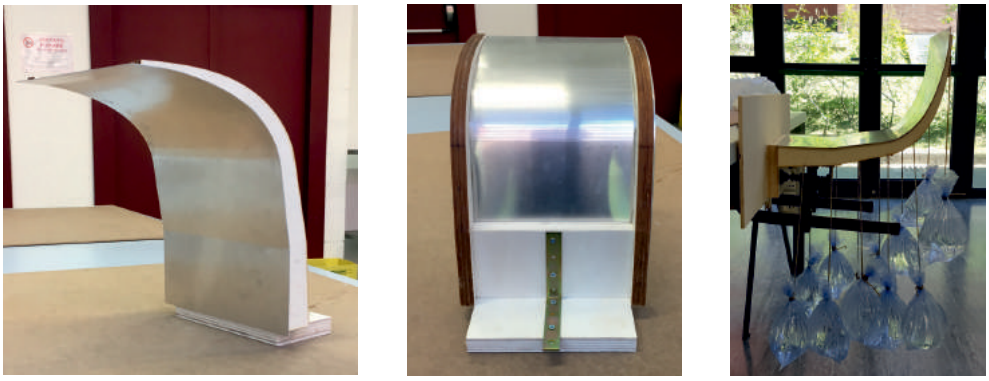

(a) (b) (c)

Figure A.4: Prototype of the mockup and static load test

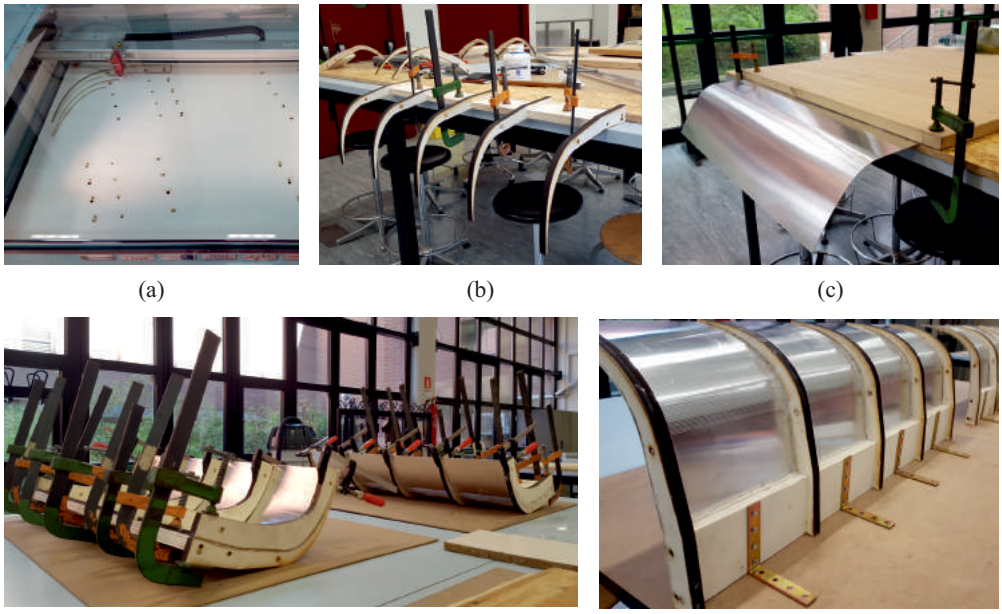

(a) (b) (c)

(d) (e)

Figure A.5: Building of the mockup side sections

A.2.2 Wind Tunnel setup

The WT test is performed for 6 different levels (n0-n5) of accumulated sand upwind the barrier as sketched in Fig. A.6, from no sand accumulated, i.e. level n0, to maximum level tested of sand accumulation, i.e. level n5. This allow the estimation of the efficiency of S4S for increasing trapped sand volume. Each sand level is set with a 15° degrees slope angle in order to set an initial slope close to

the natural one (e.g. [156]). The WT tests are intended to last until steady state conditions are reached. A uniform sand fetch 1 cm thick is spread upwind the barrier before each test in order to supply sand to the SBL.

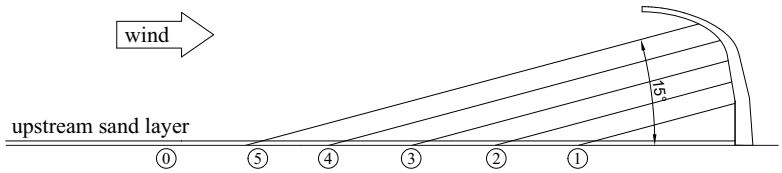

Figure A.6: Sand accumulation levels

The test is performed in the 3x2 m test section of the VKI L-1B. A low-roughness ABL condition is set in order to simulate open terrain conditions [83]. The reference wind velocity U_{ref} is measured at the inlet of the test section via Prandtl pitot tube. The mockup is installed just before the turntable at the end of the test section (see Fig. A.7). Two Plexiglas plates with a height of 505 mm are placed next to the lateral free-ends of the barrier to reduce end-tip aerodynamic effects.

Measurement setup

The measurement equipment allows for the detection of the profile of accumulated sand upwind the barrier, the incoming sand flux upwind the mockup, and the outgoing sand flux that overcomes the top of the barrier. Each measurement is taken in the WT centerline so that they are not affected from end-tip aerodynamic effects. A pulsed laser source is located on the top of the WT, generating a laser sheet shooting at 2Hz. Two cameras are positioned outside the WT. The accumulation profile of the trapped sand is captured by the Charged-Coupled Device imaging of the pulsed-laser sheet scattered from the accumulated sand (i.e. camera #1). The same pulsed-laser sheet images are then used to obtain the concentration fields of the sand particles, via the so-called Particle Tracking Velocimetry (PTV) algorithms (i.e. camera #2). The Field of View (FoV) of the cameras are approximately 50x50 cm and 85x60 cm, respectively (see Fig. A.8).

Boundary layer characterization

The reference wind velocity U_{ref} is set in order to obtain a steady, fully developed SBL. Some exploratory tests are performed with a uniform sand layer 1 cm thick and without the mockup installed. The PTV technique is adopted to detect saltating grains and provide a visual representation of the height of the saltation layer as a function of U_{ref} (see Fig. A.9). The reference wind velocity $U_{ref} = 9$ m/s is selected. The corresponding mean velocity profile and turbulence intensity in absence of saltating sand are then measured via PIV technique.

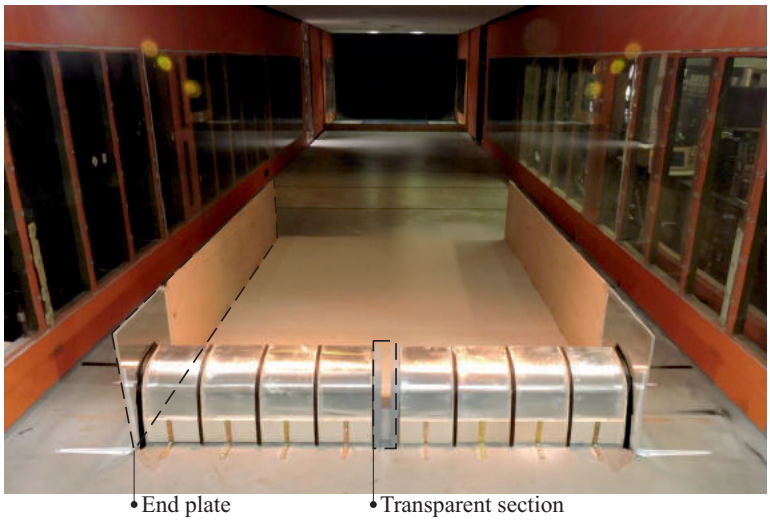

(a)

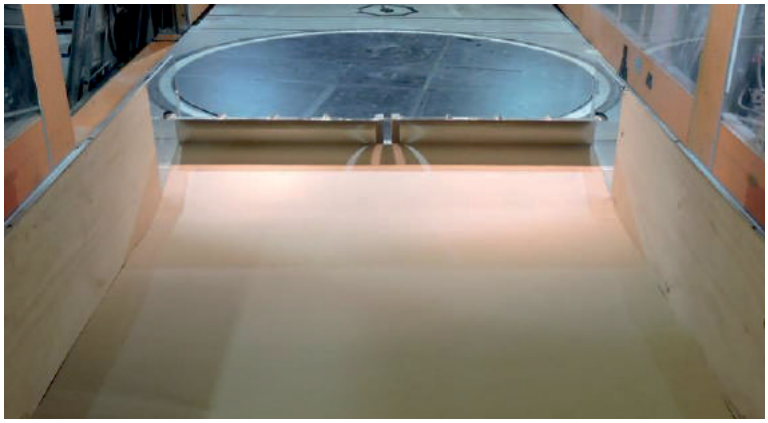

(b)

Figure A.7: Mockup arrangement in the VKI L-1B WT. Back view (a) and front view (b)

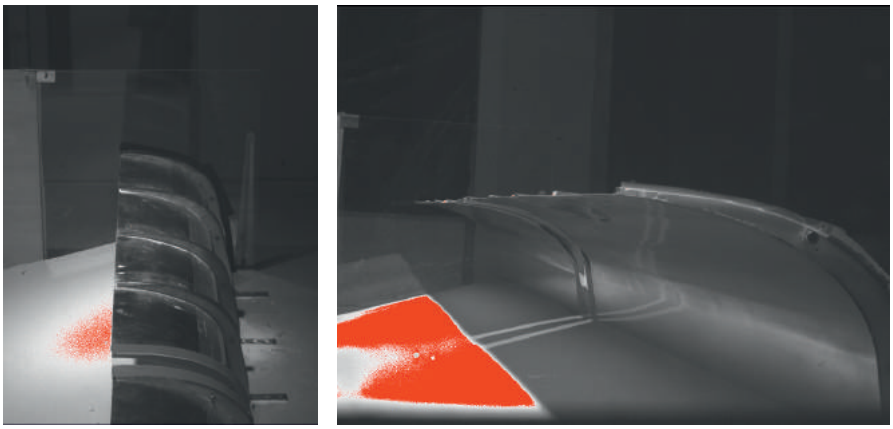

(a) (b)

Figure A.8: Field of View of the two cameras: camera #1 (a) and camera #2 (b)

From the adopted scaling law follows Reynolds number $Re = U_{ref}h/\nu = 1.8e{+}5$, and Froude number for particles saltating in the wind tunnel test section $Fr = U_{ref}^2/gH_{WT} = 4.1$, where H_{WT} is the height of the WT test section. Re value is within the supercritical aerodynamic regime, where significant Re effects do not take place. Fr value fulfills the limit criterion set by Owen and Gillette [222, 321], being lower than 20.

A.2.3 Efficiency assessment

The efficiency of the mockup is evaluated by measuring as a function of time:

- the profile of the sand accumulated upwind the barrier;
- the sand grains concentration and velocity profiles incoming and passing over the barrier.

Each measurement is performed twice for each sand accumulation level in order to ascertain the repeatability of the tests. The tests are stopped when the sand is eroded in the sand fetch resulting in patches without sand (see Fig. A.10a-f), i.e. out of equilibrium condition. The tests duration for each sand level and run is reported in Table A.1.

The pictures in Fig. A.10(g-l) shows profiles at the beginning and end of each test highlighted by the laser scattered from the accumulated sand. These profiles reflect the morphodynamics that takes place upwind the barrier and qualitatively confirm the working principles of S4S. In particular, the upwind recirculation vortex induced by S4S promotes reversed sand erosion near the barrier, while the lowering of the wind speed promotes sand sedimentation upwind the eroded zones. Even if

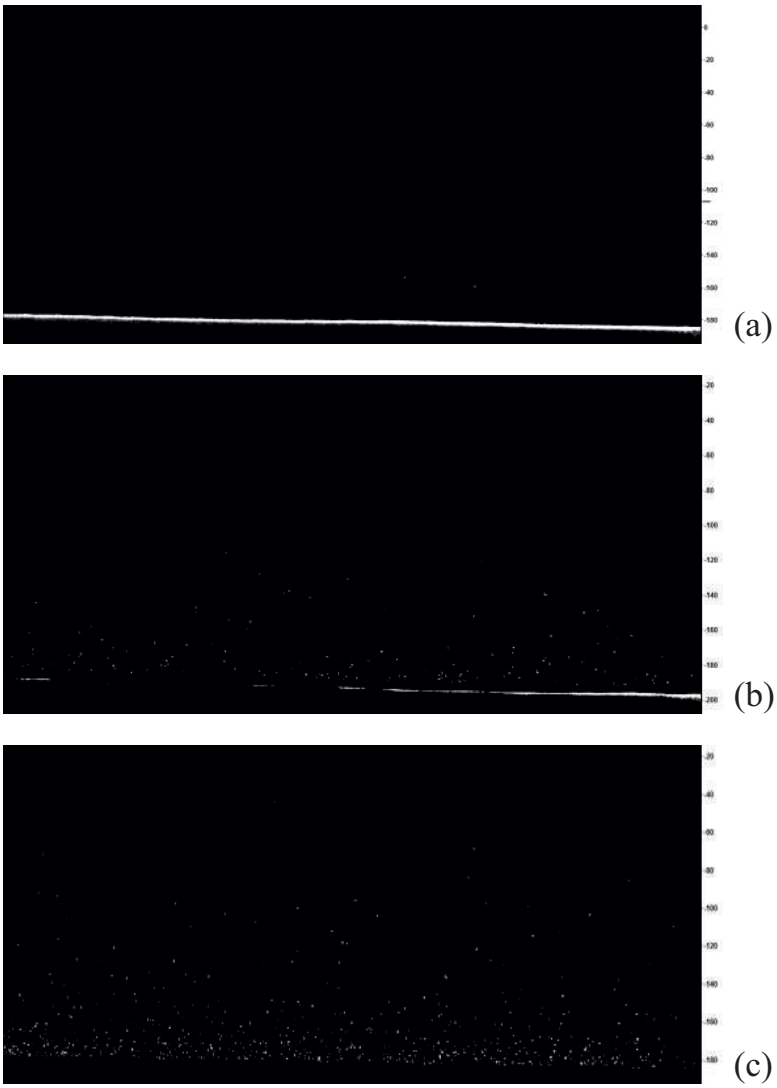

Figure A.9: Saltation boundary layer in function of U_{ref}: 8 m/s (a), 9 m/s (b), 10 m/s (c)

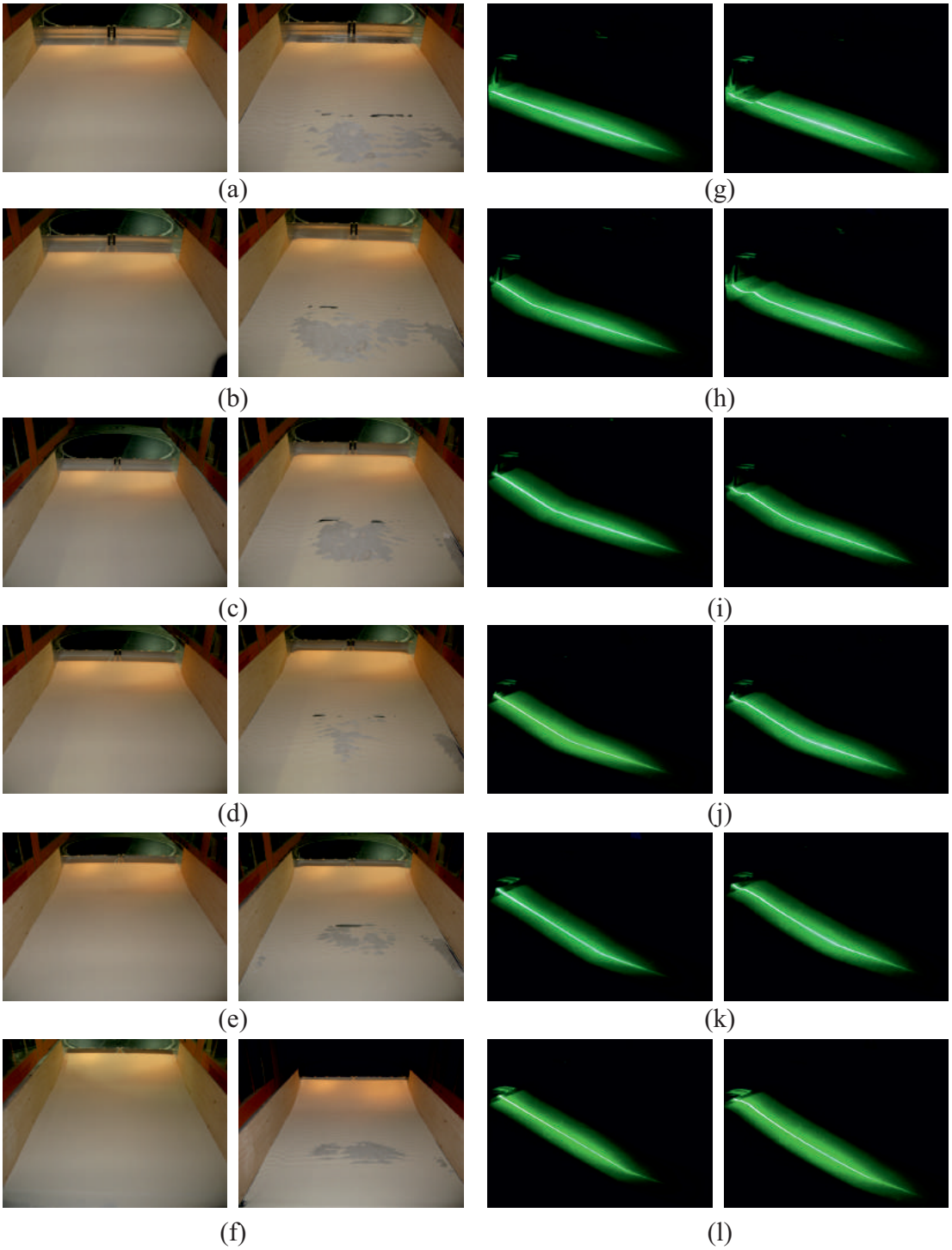

Figure A.10: Sand fetch before (left column) and after (right column) each test (a-f), upwind sand accumulation profiles before (left column) and after (right column) each test (g-l).

Table A.1: Tests duration

Sand level	Run	Duration [s]
n0	1	1350
	2	1350
n1	1	1350
	2	1350
n2	1	1575
	2	1350
n3	1	1125
	2	1350
n4	1	1350
	2	1092
n5	1	856
	2	1240

the erosion zone gets necessarily shorter as the sand level increases, sedimentation remarkably still holds also for the highest sand level.

The determination of the incoming sand concentration is performed at the same location as the determination of the incoming mean wind velocity profile, without the mockup installed. Instead, the outgoing concentration profiles are measured for each sand accumulation level simultaneously with the acquisition of the sand accumulation profiles. For both cases, the instantaneous concentration fields are extracted from the PTV pictures. In turn, the images are filtered and sand particles are detected thanks to PTV algorithm. The FoV is divided into horizontal bins and particles within each bin are counted and divided by the bin volume. Finally, the result obtained is multiplied by the mean particle volume and the sand density.

Fig. A.11 shows both the incoming and outgoing mean sand concentrations φ for each sand accumulation level together with upwind sand accumulation profiles at initial (t_0) and final (t_{end}) conditions. The mean concentration profiles are plotted preserving the same scale in order to have a not misleading graphic representation of the amount of incoming and outgoing sand. The incoming φ profile follows a typical decreasing exponential trend [270] and it is obviously the same for each sand level. The height of the SBL is determined as the height below which 99% of the total concentration take place and is equal to $\delta = 14.4$ cm. The mean outgoing φ profile changes slightly as a function of the sand level.

The efficiency η of the S4S mockup is here obtained through the following relation:

$$\eta = \frac{\Phi_{in} - \Phi_{out}}{\Phi_{in}}, \tag{A.1}$$

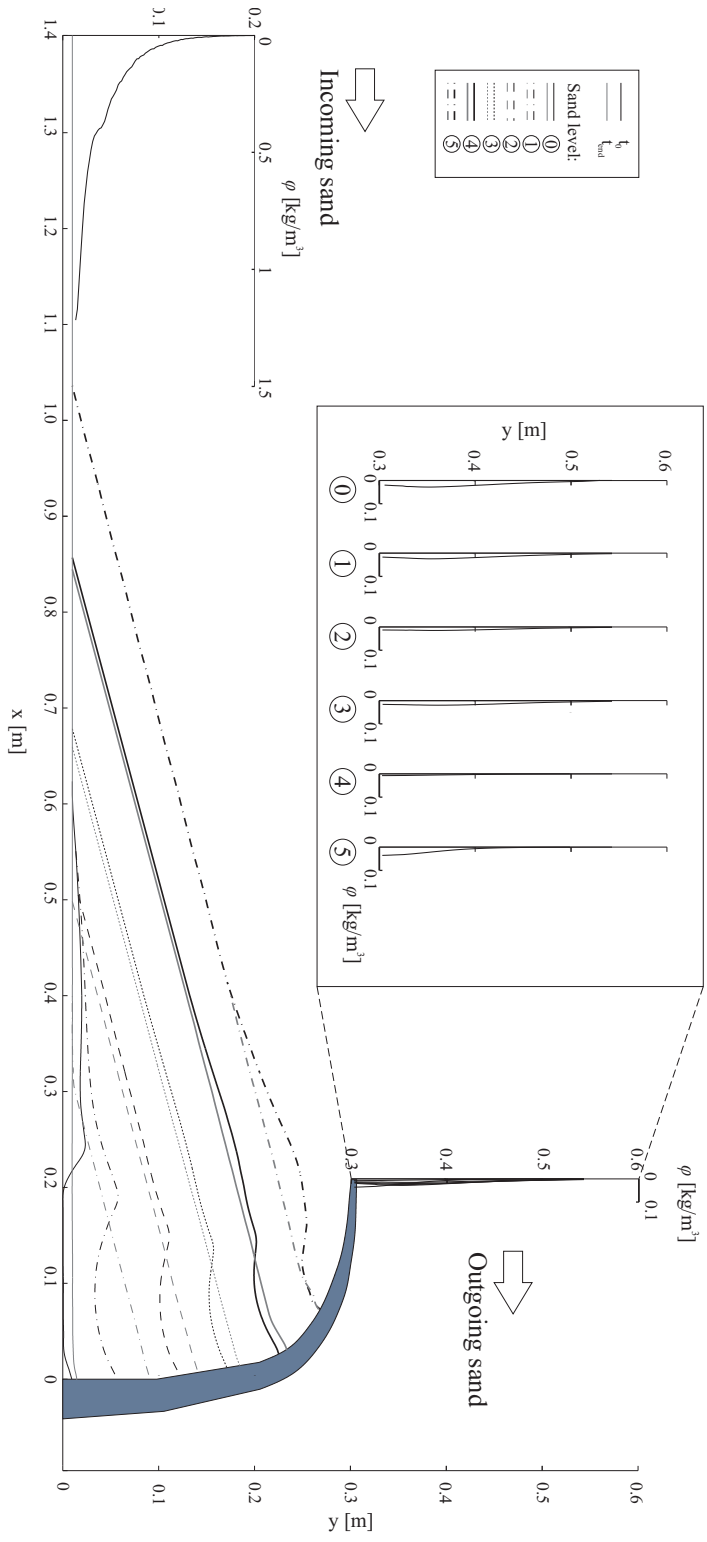

Figure A.11: Incoming and outgoing mean sand concentration profiles and sand accumulation profiles upwind the mockup.

where Φ_{in} is the integral of the mean incoming sand concentration and Φ_{out} is the integral of the mean outgoing sand concentration, both evaluated as

$$\Phi = \int_0^{+\infty} \varphi(z) dz. \tag{A.2}$$

In Fig. A.12, the efficiency assessed from the wind tunnel measurements is plotted as a function of the filling height ratio h_s/h where h_s is the height of the intersection between the final sand accumulation level (t_{end}) and the barrier profile. The measured efficiency is approximately constant and about 90% for each tested sand level. The dotted curve represents the fitted efficiency trend of S4S. In particular, it is roughly constant for $0 < h_s/h < 0.9$, then it must decrease steeply in order to reach a null efficiency for the maximum level of sand accumulation, i.e. $h_s = h$. In summary, wind tunnel tests demonstrate S4S traps more than 90% of the incoming sand, and that keeps such high performances up to its maximum capacity. These qualities imply a very small fraction of sand reaches the downwind strip, and permit low frequency sand removal operations, respectively.

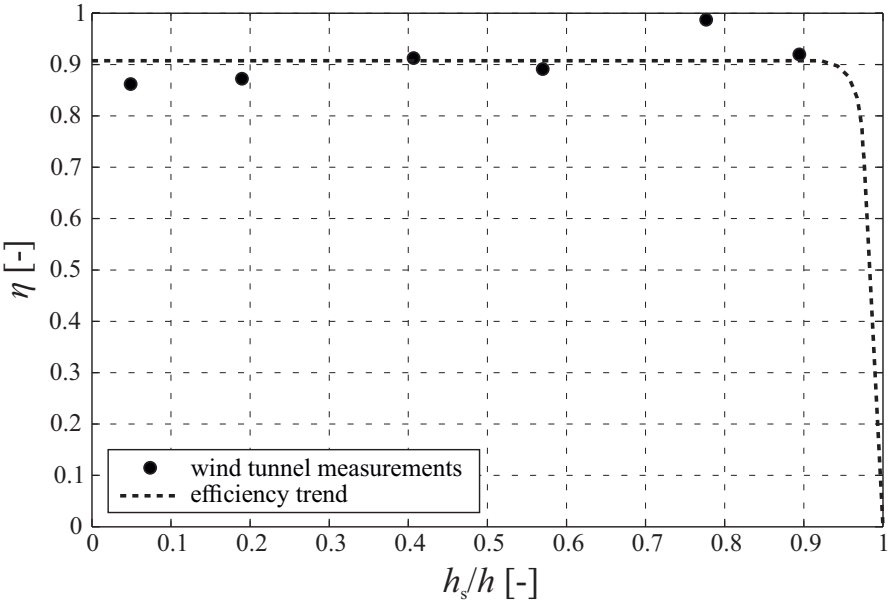

Figure A.12: Efficiency of the S4S mockup

The sedimentation coefficient C_s of S4S results from the incoming and outgoing sand transport rate. Being the instantaneous sand particle concentration ψ and velocity v two random variables, the mean sand transport rate Q is given by

$$\mu(Q) = \int_0^{+\infty} \mu[q(z,t)] dz = \int_0^{+\infty} \mu[\psi(z,t)]\, \mu[v(z,t)] + Cov[\psi(z,t), v(z,t)] dz, \tag{A.3}$$

where $Cov\left[\psi\left(z,t\right),v\left(z,t\right)\right]$ is the covariance between the concentration and the velocity of the sand particles. $Cov\left[\psi\left(z,t\right),v\left(z,t\right)\right]\neq 0$ since ψ and v are dependent random variables. Since the performed WT tests provided only the average value of the v profile of the outgoing flux, we cannot obtain accurate values of Q_{out} for the time being. In order to compute approximated values of C_s, C_s is obtained on the basis of the sole concentration profiles $\varphi(z)$ and the contribute of $v(z,t)$ profiles is neglected. As a result, $C_s \equiv \eta$.

Bibliography

[1] R. M. Al Rumaih. "Conquering the deserts". In: *Railway Gazette International* 165.8 (2009), pp. 46–48.

[2] A. A. Alghamdi and N. S. Al-Kahtani. "Sand Control Measures and Sand Drift Fences". English. In: *Journal of Performance of Constructed Facilities* 19.4 (Nov. 2005), pp. 295–299. DOI: 10.1061/(ASCE)0887-3828(2005)19:4(295).

[3] R.L. Anderson and B. Hallet. "Sediment Transport by Wind: Toward a General Model". In: *Geological Society of America Bulletin* 97.5 (1986), pp. 523–535. DOI: 10.1130/0016-7606(1986)97<523:STBWTA>2.0.CO;2.

[4] T. Anderson and D. A. Darling. "Asymptotic theory of certain goodness of fit criteria based on stochastic processes". In: *Ann. Math. Stat.* 23 (1952), pp. 193–212.

[5] B. Andreotti. "A two-species model of aeolian sand transport". In: *Journal of Fluid Mechanics* 510 (2004), pp. 47–70. DOI: 10.1017/S0022112004009073.

[6] B. Andreotti, P. Claudin, and S. Douady. "Selection of dune shapes and velocities. Part 1: Dynamics of sand, wind and barchans". In: *The European Physical Journal B - Condensed Matter* 28 (2002), pp. 321–339. DOI: 10.1140/epjb/e2002-00236-4.

[7] S. Anurag. "Problems in maintenance of Indian railway in deserts and possible solutions". In: *UIC workshop on desert railways*. 2008, pp. 67–82.

[8] I. Asi et al. "Stabilization of Dune Sand Using Foamed Asphalt". In: *ASTM Geotechnical Testing Journal* 25.2 (2002), pp. 168–176. DOI: 10.1520/GTJ11360J.

[9] J. M. Al-Awadhi and A. A. Al-Awadhi. "Modeling the aeolian sand transport for the desert of Kuwait: Constraints by field observations". In: *Journal of Arid Environments* 73.11 (2009), pp. 987–995. DOI: 10.1016/j.jaridenv.2009.04.023.

[10] R. A. Bagnold. "The Movement of Desert Sand". In: *Proceedings of the Royal Society A: Mathematical, Physical and Engineering Sciences* 157.892 (1936). DOI: 10.1098/rspa.1936.0218.

[11] R. A. Bagnold. *The Physics of Blown Sand and Desert Dunes*. Methuen, 1941. DOI: 10.1007/978-94-009-5682-7.

[12] R. A. Bagnold. "The Transport of Sand by Wind". In: *The Geographical Journal* 89 (1937), pp. 409–438. DOI: 10.2307/1786411.

[13] W. Baines. "Effects of velocity distribution on wind loads and flow patterns on buildings". In: *Wind effects on buildings and structures*. 1963.

[14] C Baker. "A review of train aerodynamics Part 2 - Applications". In: *The Aeronautical Journal* 118.1202 (2014), pp. 345–382. DOI: 10.1017/S0001924000009179.

[15] T. E. Barchyn and C. H. Hugenholtz. "Comparison of four methods to calculate aeolian sediment transport threshold from field data: Implications for transport prediction and discussion of method evolution". In: *Geomorphology* 129 (2011), pp. 190–203. DOI: 10.1016/j.geomorph.2011.01.022.

[16] T. E. Barchyn et al. "Fundamental mismatches between measurements and models in aeolian sediment transport prediction: The role of small-scale variability". In: *Aeolian Research* 15 (2014), pp. 245–251. DOI: 10.1016/j.aeolia.2014.07.002.

[17] C. G. Bates. *Windbreaks: Their Influence and Value*. Tech. rep. US Dept. of Agriculture, Forest Service., 1911.

[18] B. Belkacemi. "French Railways in Algeria, 1850-1990: A Contribution to the Study of Colonial History". PhD thesis. University of East Anglia, 1984.

[19] R. Bellefontaine et al. "The African Great Green Wall project - What advice can scientists provide?" In: *CSFD Topical issue, French Scientific Committee on Desertification*. Montpellier, 2012.

[20] P. Y. Belly. *Sand movement by wind*. Tech. rep. US Army - Corps of engineers, 1964.

[21] B. Ben Salem. "Mulching Technique of Dune Fixation: the layer system". In: *Sand Dune Stabilization, Shelterbelts and Afforestation in Dry Zones*. Food and Agriculture Organization of the United Nations. Rome, 1985.

[22] P. Berens. "CircStat: A MATLAB Toolbox for Circular Statistics". In: *Journal of Statistical Software* 31.10 (2009). DOI: 10.18637/jss.v031.i10.

[23] A. Bernardino et al. "Water Channel Study of Flow and Turbulence past a Two Dimensional Array of Obstacles". In: *Boundary Layer Layer Meteorology* 155.1 (2015), pp. 73–85. DOI: 10.1007/s10546-014-9987-2.

[24] S. J. Blott and K. Pye. "Particle size distribution analysis of sand-sized particles by laser diffraction: an experimental investigation of instrument sensitivity and the effects of particle shape". In: *Sedimentology* 53 (2006), pp. 671–685. DOI: 10.1111/j.1365-3091.2006.00786.x.

[25] K. K. Bofah and K. G. Al-Hinai. "Field tests of porous fences in the regime of sand-laden wind". In: *Journal of Wind Engineering and Industrial Aerodynamics* 23 (1986), pp. 309–319. DOI: 10.1016/0167-6105(86)90051-6.

[26] K. K. Bofah, C. Kramer, and H. J. Gerhardt. "Design considerations for buildings in a sandy and dusty environment". In: *Journal of Wind Engineering and Industrial Aerodynamics* 38 (1991), pp. 161–166. DOI: 10.1016/0167-6105(91)90038-X.

[27] R. Bogle, M. H. Redsteer, and J. Vogel. "Field measurement and analysis of climatic factors affecting dune mobility near Grand Falls on the Navajo Nation, southwestern United States". In: *Geomorphology* 228 (2015), pp. 41–51. DOI: 10.1016/j.geomorph.2014.08.023.

[28] N. Boulghobra. "Climatic data and satellite imagery for assessing the aeolian sand deposit and barchan migration, as a major risk sources in the region of In-Salah (Central Algerian Sahara)". In: *Arabian Journal of Geosciences* 9.450 (2016). DOI: 10.1007/s12517-016-2491-x.

[29] N. Boulghobra, M. Saifi, and L. Fattoum. "Sand encroachment in the Saharan Algeria; the not declared disaster - Case study: In-Salah region in the Tidikelt". In: *Planet@Risk* 3.1 (2015), pp. 72–76. URL: https://planet-risk.org/index.php/pr/article/view/172.

[30] E. Bouyé and M. Salmon. "Dynamic Copula Quantile Regressions and Tail Area Dynamic Dependence in Forex Markets". In: *The European Journal of Finance* 15.7-8 (2009), pp. 721–750. DOI: 10.1080/13518470902853491.

[31] L. Bruno and D. Fransos. "Sand transverse dune aerodynamic: 3D coherent flow structures from a computational study". In: *Journal of Wind Engineering and Industrial Aerodynamics* 147 (2015), pp. 291–301. DOI: 10.1016/j.jweia.2015.07.014.

[32] L. Bruno, D. Fransos, and A. Lo Giudice. "Solid barriers for windblown sand mitigation: Aerodynamic behavior and conceptual design guidelines". In: *Journal of Wind Engineering and Industrial Aerodynamics* 173 (2018), pp. 79–90. DOI: 10.1016/j.jweia.2017.12.005.

[33] L. Bruno, M. Horvat, and L. Raffaele. "Windblown sand along railway infrastructures: A review of challenges and mitigation measures". In: *Journal of Wind Engineering and Industrial Aerodynamics* 177 (2018), pp. 340–365. DOI: 10.1016/j.jweia.2018.04.021.

[34] L. Bruno, L. Preziosi, and D. Fransos. "A deflecting module for an anti-sand barrier, a barrier thus obtained and a protection method from windblown sand. WO 2016/181417 A1". PCT International Application WO 2016/181417 A1. 2016.

[35] L. Bruno, L. Preziosi, and D. Fransos. "Saudi Landbridge Railway Project - Sand Mitigation Study - Sand Mitigation Measure Efficiency Final Report". Internal report to Italferr S.p.a. July 2014.

[36] L. Bruno et al. "Shield for Sand: An Innovative Barrier for Windblown Sand Mitigation". In: *Recent Patents on Engineering* 12.1 (2018). DOI: 10.2174/1872212112666180309151818.

[37] L. Bruno et al. *Wind Tunnel Tests of the Shield for Sand barrier, final internal Technical Report*. Tech. rep. Proof of Concept programme, Politecnico di Torino, 2017.

[38] Al-Burhan Group. *Sand Removal Machine 46-6*. URL: http://www.alburhangroup.com/products.php.

[39] M. Burlando et al. "Wind climate analysis in complex terrain". In: *Journal of Wind Engineering and Industrial Aerodynamics* 123 (2013), pp. 349–362. DOI: 10.1016/j.jweia.2013.09.016.

[40] D. M. Burr et al. "Higher-than-predicted saltation threshold wind speeds on Titan". In: *Nature* 517 (2015).

[41] R. E. Caflisch. "Monte Carlo and quasi-Monte Carlo methods". In: *Acta Numerica* 7 (1998), pp. 1–49. DOI: 10.1017/S0962492900002804.

[42] I. A. Carrascal et al. "Dynamic behaviour of high-speed rail fastenings in the presence of desert sand". In: *Construction and Building Materials* 117 (2016), pp. 220–228. DOI: 10.1016/j.conbuildmat.2016.05.023.

[43] J. A. Carta, P. Ramírez, and S. Velázquez. "A review of wind speed probability distributions used in wind energy analysis: Case studies in the Canary Islands". In: *Renewable and Sustainable Energy Reviews* 13.5 (2009), pp. 933–955. DOI: 10.1016/j.rser.2008.05.005.

[44] G. Chen et al. "3D numerical simulation of wind flow behind a new porous fence". In: *Powder Technology* 230 (2012), pp. 118–126. DOI: 10.1016/j.powtec.2012.07.017.

[45] W. Chen and D. W. Fryrear. "Aerodynamic and geometric diameter of airborne particles". In: *Journal of Sedimentary Research* 71 (2001), pp. 365–371. DOI: 10.1306/2DC4094A-0E47-11D7-8643000102C1865.

[46] J. Cheng and C. Xue. "The sand-damage-prevention engineering system for the railway in the desert region of the Qinghai-Tibet plateau". In: *Journal of Wind Engineering and Industrial Aerodynamics* 125 (2014), pp. 30–37. DOI: 10.1016/j.jweia.2013.11.016.

[47] J. Cheng et al. "Characteristics of the disastrous wind-sand environment along railways in the Gobi area of Xinjiang, China". In: *Atmospheric Environment* 102 (2015), pp. 344–354. DOI: 10.1016/j.atmosenv.2014.12.018.

[48] J. Cheng et al. "Disturbance of the inclined inserting-type sand fence to wind–sand flow fields and its sand control characteristics". In: *Aeolian Research* 21 (2016), pp. 139–150. DOI: 10.1016/j.aeolia.2016.04.008.

[49] J. Cheng et al. "Effect of hanging-type sand fence on characteristics of wind-sand flow fields". In: *Wind and Structures* 22.5 (2016), pp. 555–571. DOI: 10.12989/was.2016.22.5.555.

[50] J. Cheng et al. "Unloading Characteristics of Sand-drift in Wind-shallow Areas along Railway and the Effect of Sand Removal by Force of Wind". In: *Scientific Reports* 7.41462 (Jan. 2017). DOI: 10.1038/srep41462.

[51] W. S. Chepil. "Dynamics of wind erosion: II. Initiation of soil movement". In: *Soil Sci.* 60 (1945), pp. 397–411. DOI: 10.1097/00010694-194511000-00005.

[52] W. S. Chepil. "Equilibrium of soil grains at threshold of movement by wind". In: *Soil Sci. Soc. Proc.* 23 (1959), pp. 422–428.

[53] W. S. Chepil. "Properties of soil which influence wind erosion: IV. State of dry aggregate structure". In: *Soil Sci.* 72 (1951), pp. 387–401.

[54] P. Claudin and B. Andreotti. "A scaling law for aeolian dunes on Mars, Venus, Earth, and for subaqueous ripples". In: *Earth and Planetary Science Letters* 252 (2006), pp. 30–44. DOI: 10.1016/j.epsl.2006.09.004.

[55] V. Conforti et al. "New challenges for the design of High Speed and Heavy Haul rail". In: *Proceedings 11th World Congress on Railway Research*. Milan, Italy, May 2016.

[56] W. M. Cornelis and D. Gabriels. "A simple model for the prediction of the deflation threshold shear velocity of dry loose particles". In: *Sedimentology* 51 (2004), pp. 39–51. DOI: 10.1111/j.1365-3091.2004.00609.x.

[57] W. M. Cornelis and D. Gabriels. "Optimal windbreak design for wind-erosion control". In: *Journal of Arid Environments* 61.2 (2005), p. 315. DOI: 10.1016/j.jaridenv.2004.10.005.

[58] S. Corti, F. Molteni, and T. N. Palmer. "Signature of recent climate change in frequencies of natural atmospheric circulation regimes". In: *Nature* 398 (1999), pp. 799–802. DOI: 10.1038/19745.

[59] P. Croce et al. "Climate change: Impact on snow loads on structures". In: *Cold Regions Science and Technology* (2017). in press. DOI: 10.1016/j.coldregions.2017.10.009.

[60] D.T.R. C 2-4.7. *Document Technique Réglementaire C 2-4.7: Règlement Neige & Vent (version 2013)*. 2013.

[61] M. Darwish. "Threshold friction velocity: moisture and particle size effect". MA thesis. Texas Tech University, 1991.

[62] H. Davarzani et al. “Study of the effect of wind speed on evaporation from soil through integrated modeling of the atmospheric boundary layer and shallow subsurface”. In: *Water Resources Research* (2014). DOI: 10.1002/2013WR013952.

[63] M. Davel Wallis. “Freight Train Derails”. In: *Namib Times* (2014). URL: http://namibtimes.net/freight-train-derails/.

[64] A. G. Davenport. “The response of slender line-like structures to gusty wind”. In: *Preoceedings of the Institution of Civil Engineers*. Vol. 23. 1962, pp. 389–408.

[65] C. Demartino et al. “Effects of ice accretion on the aerodynamics of bridge cables”. In: *Journal of Wind Engineering and Industrial Aerodynamics* 138 (2015), pp. 98–119. DOI: 10.1016/j.jweia.2014.12.010.

[66] DGII-D3. *Scientific Support Activity in the Field of Structural Stability of Civil Engineering Works. Snow Loads - FINAL REPORT*. Tech. rep. COMMISSION OF THE EUROPEAN COMMUNITIES, 1998.

[67] W. Dierickx, W. M. Cornelis, and D. Gabriels. “Wind Tunnel Study on Rough and Smooth Surface Turbulent Approach Flow and on Inclined Windscreens”. In: *Biosystems Engineering* 86.2 (2003), pp. 151–166. DOI: 10.1016/S1537-5110(03)00120-X.

[68] K Dierks. *Namibia’s Railway System*. Sept. 2004. URL: http://www.klausdierks.com/Namibia_Rail/.

[69] Tolga Dölçek. “Mechanical Behavior of Polyurethane Stabilized Fouled Ballast (PSFB)”. MA thesis. Geological Engineering at the University of Wisconsin, 2014. URL: http://minds.wisconsin.edu/bitstream/handle/1793/69518/MS_Thesis_Dolcek_Tolga.pdf.

[70] Z. Dong et al. “A wind tunnel simulation of the mean velocity fields behind upright porous fences”. In: *Agricultural and Forest Meteorology* 146.11 (2007), pp. 82–93. DOI: 10.1016/j.agrformet.2007.05.009.

[71] Z. Dong et al. “Aeolian sand transport: a wind tunnel model”. In: *Sedimentary Geology* 161 (2003), pp. 71–83. DOI: 10.1016/S0037-0738(03)00396-2.

[72] Z. Dong et al. “Controlling blown sand along the highway crossing the Taklimakan Desert”. In: *Journal of Arid Environments* 57.3 (2004), pp. 329–344. DOI: 10.1016/j.jaridenv.2002.02.001.

[73] Z. Dong et al. “The flux profile of a blowing sand cloud: a wind tunnel investigation”. In: *Geomorphology* 49.3-4 (2003), p. 219. DOI: 10.1016/S0169-555X(02)00170-8.

[74] Z. Dong et al. "Wind tunnel simulation of the three-dimensional airflow patterns around shrubs". In: *Journal of Geophysical Research* 113 (2008), F02016. DOI: 10.1029/2007JF000880.

[75] S. Z. Duan, N. Cheng, and L. Xie. "A new statistical model for threshold friction velocity of sand particle motion". In: *Catena* 104 (2013), pp. 32–38. DOI: 10.1016/j.catena.2012.04.009.

[76] A. Ebrahimi and A. K. Keene. "Maintenance Planning of Railway Ballast". In: *Proceedings of the AREMA Conference*. Minneapolis, Sept. 2011.

[77] H. Stewart Edgell. *Arabian Desert*. Springer, 2006.

[78] B. L. Edwards and S. L. Namikas. "Characterizing the sediment bed in terms of resistance to motion: Toward an improved model of saltation thresholds for aeolian transport". In: *Aeolian Research* 19 (2015), pp. 123–128. DOI: 10.1016/j.aeolia.2015.10.004.

[79] B. Efron and R. J. Tibshirani. *An Introduction to the Bootstrap*. New York: Chapman & Hall/CRC, 1993.

[80] J. Ehlen. *Physical Characteristics of Some Solis from the Middle East*. Tech. rep. U.S. Army Topographic Engineering Center (TEC-0032), May 1993.

[81] EN 1990. *Eurocode - Basis of structural design - EN 1990*. European Committee for Standardization, 2002.

[82] EN 1991-1-3. *Eurocode 1: Actions on structures Part 1-3 General actions - Snow Loads - EN 1991-1-3*. European Committee for Standardization, 2002.

[83] EN 1991-1-4. *Eurocode 1: Actions on structures - Part 1-4: General actions - Wind actions - EN 1991-1-4*. European Committee for Standardization, 2005.

[84] M. Esmaeili, P. Aela, and A. Hosseini. "Experimental assessment of cyclic behavior of sand-fouled ballast mixed with tire derived aggregates". In: *Soil Dynamics and Earthquake Engineering* 98 (July 2017), pp. 1–11. DOI: 10.1016/j.soildyn.2017.03.033.

[85] M. Esmaeili, J. A. Zakeri, and S. A. Mosayebi. "Effect of sand-fouled ballast on train-induced vibration". In: *International Journal of Pavement Engineering* 15.7 (2013), pp. 635–644. DOI: 10.1080/10298436.2013.818146.

[86] M. Faccoli et al. "Effect of desert sand on wear and rolling contact fatigue behaviour of various railway wheel steels". In: *Wear* 396-397 (2018), pp. 146–161. DOI: 10.1016/j.wear.2017.05.012.

[87] F. Feldman and D. Nissen. "Alternative testing method for the measurement of ballast fouling: percentage void contamination." In: *Proceedings of the Conference on Railway Engineering*. Railway Technical Society of Australia. Wollongong, Australia, Oct. 2002, pp. 101–109.

[88] E. A. Finney. *Snow control on the highways*. Tech. rep. Michigan Engineering Experiment Station Bulletin No. 57, 1934.

[89] N. I. Fisher. *Statistical Analysis of Circular Data*. Cambridge University Press, 1995. DOI: https://doi.org/10.1017/CBO9780511564345.

[90] B. Fletcher. "Incipient motion of granular materials". In: *J. Phys. D Appl. Phys.* 9 (1976), pp. 2471–8. DOI: 10.1088/0022-3727/9/17/007.

[91] A. M. Foley. "Uncertainty in regional climate modelling: A review". In: *Progress in Physical Geography* 34.5 (2010), pp. 647–670. DOI: 10.1177/0309133310375654.

[92] P. G. Fookes and E. M. Lee. "Desert environments: landscapes and stratigraphy". In: *Geology Today* 25.5 (2009), pp. 172–180. DOI: 10.1111/j.1365-2451.2009.00722.x.

[93] G. M. Friedman and F. E. Sanders. *Principles of sedimentology*. New York: Wiley, 1978.

[94] S. G. Fryberger and G. Dean. "A Study of Global Sand Seas". In: ed. by McKee E. D. 1979. Chap. Dune forms and wind regime, pp. 137–155.

[95] K. Futsuhara and M. Mukaidono. "Realization of a fail-safe train wheel sensor using electromagnetic induction". In: *IEEE Transactions on Instrumentation and Measurement* 38.2 (1989), pp. 421–426.

[96] G. Al-Gassim. *SAR - North South Railway Challanges*. Ed. by Al-Gassim. 2013. URL: http://fr.slideshare.net/imadhammoud/gassim-al-gassim-sar-environmental-challenges.

[97] Saudi Gazette. "Tracks lost in sand, trains suspended". In: *Saudi Gazette* (Sept. 2013). URL: http://saudigazette.com.sa/article/48288/Tracks-lost-in-sand-trains-suspended.

[98] C. Genest and A. C. Favre. "Everything You Always Wanted to Know about Copula Modeling but Were Afraid to Ask". In: *Journal Of Hydrologic Engineering(ASCE)* 12 (2007), pp. 347–368. DOI: 10.1061/(ASCE)1084-0699(2007)12:4(347).

[99] C. Genest and J. Nešlehová. "Copulas and Copula Models". In: *Wiley StatsRef: Statistics Reference Online*. John Wiley & Sons, Ltd, 2014. DOI: 10.1002/9781118445112.stat07523. URL: http://dx.doi.org/10.1002/9781118445112.stat07523.

[100] B. Gerwick Jr and R. Bittner. *Construction of Marine and Offshore Structures*. CRC Press, 2007.

[101] A. Giannoulis et al. "Wind loading on vertical panels with different permeabilities". In: *Journal of Wind Engineering and Industrial Aerodynamics* 107-108 (2012), pp. 1–16. DOI: 10.1016/j.jweia.2012.02.014.

[102] D. A. Gillette, B. Marticorena, and G. Bergametti. "Change in aero- dynamic roughness height by saltating grains: Experimental assessment, test of theory, and operational parameterization". In: *Journal of Geophysical Research Atmospheres* 103.D6 (1998), pp. 6203–6209. DOI: 10.1029/98JD00207.

[103] J. A. Gillies and N. Lancaster. "Large roughness element effects on sand transport, Oceano Dunes, California". In: *Earth Surface Processes and Landforms* 38 (2013), pp. 785–792. DOI: 10.1002/esp.3317.

[104] J. A. Gillies, W. G. Nickling, and J. King. "Aeolian sediment transport through large patches of roughness in the atmospheric inertial sublayer". In: *Journal of Geophysical Research* 111.F02006 (2006). DOI: 10.1029/2005JF000434.

[105] J. A. Gillies et al. "Using solid element roughness to control sand movement: Keeler Dunes, Keeler, California". In: *Aeolian Research* 18 (2015), pp. 35–46. DOI: 10.1016/j.aeolia.2015.05.004.

[106] F. Giorgi. "Climate change hot-spots". In: *Geophysical Research Letters* 33 (2006), p. L08707. DOI: 10.1029/2006GL025734.

[107] L. Gomez and R. Mèndez. "Saudis kick up storm over Spanish group's high-speed desert rail project". In: *El Paìs* (Feb. 2015).

[108] M. C. Good and P. N. Joubert. "The form drag of two-dimensional bluff-plates immersed in turbulent boundary layers". In: *Journal of Fluid Mechanics* 31.3 (1968), pp. 547–582. DOI: 10.1017/S0022112068000327.

[109] A. S. Goudie. "Dust storms: Recent developments". In: *Journal of Environmental Management* 90 (2009), pp. 89–94. DOI: 10.1016/j.jenvman.2008.07.007.

[110] R. Greeley and J. D. Iversen. *Wind as a Geological Process on Earth, Mars, Venus, and Titan*. New York: Cambridge University Press, 1985. DOI: 10.1017/CBO9780511573071.

[111] R. Greeley et al. "Mars: Wind friction speeds for particle movement". In: *Geophys. Res. Lett.* 3.8 (1976), pp. 417–420. DOI: 10.1029/GL003i008p00417.

[112] Z. Guo et al. "Wind Erosion Induced Soil Degradation in Northern China: Status, Measures and Perspective". In: *Sustainability* 6.12 (2014), pp. 8951–8966. DOI: 10.3390/su6128951.

[113] A. Haack. "Current safety issues in traffic tunnels". In: *Tunnelling and Underground Space Technology* 17 (2002), pp. 117–127. DOI: 10.1016/S0886-7798(02)00013-5.

[114] J. Y. Halpern. *Reasoning About Uncertainty*. MIT Press, 2003.

[115] Y. Hao, Y. Feng, and J. Fan. "Experimental study into erosion damage mechanism of concrete materials in a wind-blown sand environment". In: *Construction and Building Materials* 111 (2016), pp. 662–670. DOI: 10.1016/j.conbuildmat.2016.02.137.

[116] A. Al-Harthi. "Geohazard assessment of sand dunes between Jeddah and Al-Lith, western Saudi Arabia". In: *Environmental Geology* 42 (2002), pp. 360–369. DOI: 10.1007/s00254-001-0501-z.

[117] L. Hasse. "BASIC ATMOSPHERIC STRUCTURE AND CONCEPTS | Beaufort Wind Scale". In: *Reference Module in Earth Systems and Environmental Sciences* (2015), pp. 1–6. DOI: 10.1016/B978-0-12-382225-3.00466-7.

[118] W. He et al. "Numerical simulation of wind-sand movement in the reversed flow region of a sand dune with a bridge built downstream". In: *The European Physical Journal E* 41 (2018), p. 53. DOI: 10.1140/epje/i2018-11660-5.

[119] M. Heffernan. "Engineering Earth - The Impacts of Megaengineering Projects". In: ed. by S.D. Brunn. Springer Netherlands, 2010. Chap. Shifting Sands: The Trans-Saharan Railway. DOI: 10.1007/978-90-481-9920-4.

[120] J. C. Henry. "American Railroad on the Arabian Desert". In: *Popular Mechanics* 97.4 (1952), pp. 107–110.

[121] P. A. Hesp and R. Hyde. "Flow dynamics and geomorphology of a trough blowout". In: *Sedimentology* 43 (1996), pp. 505–525. DOI: 10.1046/j.1365-3091.1996.d01-22.x.

[122] T. Hewitt. "Designing a heavy haul desert railway: lessons learned". In: *11th International Heavy Haul Conference, (IHHA 2015), Operational Excellence*. Perth, Western Australia, Australia, 21st-24th June 2015, pp. 228–237. URL: http://railknowledgebank.com/Presto/content/Detail.aspx?ctID=Y3RDb3B5X29mX1RoZXNlcw==&rID=MjgyNw==&ssid=c2NyZWVuSURfMTc2MzM=.

[123] S. W. Hong, I. B. Lee, and I. H. Seo. "Modelling and predicting wind velocity patterns for windbreak fence design". In: *Journal of Wind Engineering and Industrial Aerodynamics* 142 (2015), pp. 53–64. DOI: 10.1016/j.jweia.2015.03.007.

[124] B. M. Hoonhout and S. de Vries. "A process-based model for aeolian sediment transport and spatiotemporal varying sediment availability". In: *Journal of Geophysical Research: Earth Surface* 121 (2016), pp. 1555–1575. DOI: 10.1002/2015JF003692.

[125] K. Horikawa et al. *On the sand transport rate by wind on a beach*. Tech. rep. 1983, pp. 101–120.

[126] S. Hotta and S. Harikai. "STATE-OF-THE-ART IN JAPAN ON CONTROLLING WIND-BLOWN SAND ON BEACHES". In: *Proceedings of the International Conference on Coastal Engineering*. 32. 2010.

[127] S. Hotta and K. Horikawa. "Function of Sand Fence Placed in Front of Embankment". In: *Coastal Engineering 1990* 2 (1991), pp. 2754–2767. DOI: 10.1061/9780872627765.211.

[128] M. Howard. "The new generation of inductive sensors". In: *World Pumps* 2013.2 (Feb. 2013), pp. 10–11. DOI: 10.1016/S0262-1762(13)70055-5.

[129] M. Ikhwan and B. Ruck. "Flow and pressure field characteristics around pyramidal buildings". In: *Journal of Wind Engineering and Industrial Aerodynamics* 94.10 (2006), pp. 745–765. DOI: 10.1016/j.jweia.2006.02.005.

[130] B. Indraratna, L. Su, and C. Rujikiatkamjorn. "A new parameter for classification and evaluation of railway ballast fouling". In: *Canadian Geotechnical Journal* 48.2 (2011), pp. 322–326. DOI: 10.1139/T10-066.

[131] D. Ionescu et al. "Deformation and Degradation Characteristics of Sand-Contaminated Railway Ballast". In: *Proceedings of the Third International Conference on Railway Technology: Research, Development and Maintenance*. Ed. by J. Pombo. 26. Stirlingshire, UK: Civil-Comp Press, 2016. DOI: 10.4203/ccp.110.26.

[132] ISO 12494:2017. *Atmospheric icing of structures*. International Organization for Standardization.

[133] ISO14688-1:2002. *Geotechnical investigation and testing - Identification and classification of soil - Part 1: Identification and description*. Interantional Organization for Standardization.

[134] S.p.a. Italferr. *Preliminary Design for Oman National Railway Project - Segment 1 - Oman / UAE border at Al Buraimi - Geotechnical Study: Sand Mitigation Report*. Aug. 2014.

[135] J. D. Iversen and B. R. White. "Saltation threshold on earth, mars and venus". In: *Sedimentology* 29.1 (1982), pp. 111–119. DOI: 10.1111/j.1365-3091.1982.tb01713.x.

[136] J. D. Iversen et al. "Saltation threshold on Mars: The effect of interparticle force, surface roughness, and low atmospheric density". In: *Icarus* 29 (1976), pp. 381–93. DOI: 10.1016/0019-1035(76)90140-8.

[137] P. S. Jackson. "The flow round obstacles in boundary layers". PhD thesis. University of Cambridge, 1973.

[138] J. W. Johnson, ed. *Federal Inter-Agency Sedimentation Conference*. 970. United States Department of Agriculture Miscellaneous Publication. 1965.

[139] R. Jones et al. "Adhesion forces between glass and silicon surfaces in air studied by AFM: effects of relative humidity, particle size, roughness and surface treatment". In: *Langmuir* 18 (2002), pp. 8045–8055. DOI: 10.1021/la0259196.

[140] N. Junquera. "Shifting sands and 60 million pilgrims: The trials of building an Arabian railway". In: *El Paìs* (May 2014).

[141] A. A. Kadib. *Sand Transport by Wind - Addendum II to Sand movement by Wind*. Tech. rep. US Army Coastal Eng. Res. Center, Washington, DC. U.S. Army - Corps of Engineers, 1964.

[142] R. N. Kaul. "Sand dune fixation and afforestation: traditional procedures for dune fixation: the hedge system". In: *Sand Dune Stabilization, Shelterbelts and Afforestation in Dry Zones*. Food and Agriculture Organization of the United Nations. Rome, 1985.

[143] Kaushik. *The Sand Buried Village of Shoyna*. 2016. URL: http://www.amusingplanet.com/2016/07/the-sand-buried-village-of-shoyna.html.

[144] R. Kawamura. *Study of sand movement by wind*. Tech. rep. NASA technical translation, 1951.

[145] A. Keene, T. Edil, and J. Tinjum. "Mitigating Ballast Fouling and Enhancing Rail Freight Capacity". In: *Technical Repor CFIRE 04-07, National Center for Freight and Infrastructure Research and Education* (Nov. 2012). University of Winsconsin-Madison. URL: http://www.wistrans.org/cfire/documents/FR_CFIRE0407.pdf.

[146] R. C. Kerr and J. O. Nigra. *Analysis of Aeolian Sand Control*. Arabian American Oil Company, 1951.

[147] R. C. Kerr and J. O. Nigra. "Eolian Sand Control". In: *Bulletin of the American Association of Petroleum Geologists* 36.8 (1952), pp. 1541–1573.

[148] Z. Kilibarda and V. Kilibarda. "Seasonal geomorphic processes and rates of sand movement at Mount Baldy dune in Indiana, USA". In: *Aeolian Research* 23A (2016), pp. 103–114. DOI: 10.1016/j.aeolia.2016.10.004.

[149] R. J. Kind. "Mechanics of Aeolian Transport of Snow and Sand". In: *Journal of Wind Engineering and Industrial Aerodynamics* 36 (1990), pp. 855–866. DOI: 10.1016/0167-6105(90)90082-N.

[150] R. Koenker. *Quantile Regression*. Cambridge University Press, 2005.

[151] J. F. Kok. *Analytical calculation of the minimum wind speed required tosustain wind-blown sand on Earth and Mars*. Jan. 2010. URL: http://arxiv.org/ftp/arxiv/papers/1001/1001.4840.pdf.

[152] J. F. Kok. "Difference in the Wind Speeds Required for Initiation versus Continuation of Sand Transport on Mars: Implications for Dunes and Dust Storms". In: *Physical Review Letters* 104 (2010). DOI: 10.1103/PhysRevLett.104.074502.

[153] J. F. Kok et al. "The physics of wind-blown sand and dust". In: *Reports on Progress in Physics* 75.10 (2012), p. 106901. DOI: 10.1088/0034-4885/75/10/106901.

[154] J. Kóllmann. "Railway Operations under Harsh Environmental Conditions – Sand, Dust & Humidity Problems and Technical Solutions / Mitigation Measures". In: *AHK Workshop Be a Partner of Qatar Rail*. Berlin, Apr. 2013. URL: http://docplayer.net/22407097-Railway-operations-under-harsh-environmental-conditions.html.

[155] T. Kurian and J. H. M. Fransson. "Grid-generated turbulence revisited". In: *Fluid Dynamics Research* 41.021403 (2009). DOI: 10.1088/0169-5983/41/2/021403.

[156] N. Lancaster. *Geomorphology of Desert Sand Dunes*. Cambridge, England: Routledge, 1995. DOI: 10.4324/9780203413128.

[157] N. Lancaster and A. Baas. "Influence of vegetation cover on sand transport by wind: field studies at Owens Lake, California". In: *Earth Surface Processes and Landforms* 23 (1998), pp. 69–82. DOI: 10.1002/(SICI)1096-9837(199801)23:1<69::AID-ESP823>3.0.CO;2-G.

[158] S. Lee and H. Kim. "Laboratory measurements of velocity and turbulence field behind porous fences". In: *Journal of Wind Engineering and Industrial Aerodynamics* 80 (1999), pp. 311–326. DOI: 10.1016/S0167-6105(98)00193-7.

[159] C. Lehman. *Oregon Creates New Unit Of Government Just To Control Sand*. 2015. URL: http://nwnewsnetwork.org/post/oregon-creates-new-unit-government-just-control-sand.

[160] C. W. Letchford and J. D. Holmes. "Wind loads on free-standing walls in turbulent boundary layers". In: *Journal of Wind Engineering and Industrial Aerodynamics* 51 (1994), pp. 1–27. DOI: 10.1016/0167-6105(94)90074-4.

[161] K. Lettau and H. Lettau. *Experimental and micro-meteorological field studies of dune migration*. Tech. rep. 101, 110-147. Exploring the World's Driest Climate (IES Report, 101, 110-147), 1978.

[162] B. Li, J. T. Ellis, and D. J. Sherman. "Estimating the impact threshold for wind-blown sand". In: *Journal of Coastal Research* 70 (Apr. 2014), pp. 627–632. DOI: 10.2112/SI70-106.1.

[163] B. Li and D. J. Sherman. "Aerodynamics and morphodynamics of sand fences: A review". In: *Aeolian Research* 17 (2015), pp. 33–48. DOI: 10.1016/j.aeolia.2014.11.005.

[164] G. Li and P. Mayi. "Wind-preventing sand-throwing wall". CN/102002916 B. 2012.

[165] F. Lianchan. "Railways Built in Deserts and Sand-Prevention in China". In: *Journal of the China Railway Society* 3 (1984). In Chinese.

[166] F. Lianchan, L. Jiqing, and D. Yaoquan. "Review on the Prevention of Sand Damages to Railway Line in Desert Areas of China". In: *Journal of Desert Research* 3 (1994). In Chinese.

[167] T. Lihui et al. "Characteristics of erosion and deposition of straw checkerboard barriers in alpine sandy land". In: *Environmental Earth Sciences* 74.1 (2015), pp. 573–584. DOI: 10.1007/s12665-015-4059-6.

[168] I. Lima et al. "Optimal array of sand fences". In: *Scientific Reports* 7 (2017). DOI: 10.1038/srep45148.

[169] B. Liu et al. "Controlling windblown sand problems by an artificial gravel surface: A case study over the gobi surface of the Mogao Grottoes". In: *Geomorphology* 134.3-4 (2011), pp. 461–469. DOI: 10.1016/j.geomorph.2011.07.028.

[170] B. Liu et al. "Numerical evaluation of the scale problem on the wind flow of a windbreak". In: *Scientific Reports* 4 (2014), p. 6619. DOI: 10.1038/srep06619.

[171] L. Liu et al. "The role of maximum wind speed in sand-transporting events". In: *Geomorphology* 238 (2015), pp. 177–186. DOI: 10.1016/j.geomorph.2015.03.007.

[172] L. Liu et al. "Wind tunnel measurements of adobe abrasion by blown sand: profile characteristics in relation to wind velocity and sand flux". In: *Journal of Arid Environments* 53.3 (2003), pp. 351–363. DOI: 10.1006/jare.2002.1049.

[173] Y. Liu. "Establishment and effect of protecting system along the Batou-Lanzhou Railway in the Shapotou Study Area". In: *Journal of Desert Research* 7.4 (1987). In Chinese with English Abstract, pp. 1–11.

[174] I. Livingstone et al. "The Namib Sand Sea digital database of aeolian dunes and key forcing variables". In: *Aeolian Research* 2.2-3 (2010), pp. 93–104. DOI: 10.1016/j.aeolia.2010.08.001.

[175] M. Logie. "Influence of roughness elements and soil moisture on the resistance of sand to wind erosion". In: *Catena* Suppl. 1 (1982), pp. 161–174.

[176] M. Logie. "Wind tunnel experiments on dune sands". In: *Earth Surf. Proc. Land.* 6.3-4 (1981), pp. 365–374. DOI: 10.1002/esp.3290060315.

[177] C Longjun. "UN Convention to Combat Desertification". In: *Encyclopedia of Environmental Health* 504-517 (2011).

[178] R. W. Luebke. "Fencing for controlling accumulation and drifting of snow,sand or other heavier-than-air particles suspended in air currents". US3473786A. 1967.

[179] W. Luo et al. "Influence of the gap ratio on variations in the surface shear stress and on sand accumulation in the lee of two side-by-side obstacles". In: *Environ. Earth Sci.* 75 (2016), p. 766. DOI: 10.1007/s12665-016-5588-3.

[180] W. Luo et al. "Near-wake flow patterns in the lee of adjacent obstacles and their implications for the formation of sand drifts: A wind tunnel simulation of the effects of gap spacing". In: *Geomorphology* 213 (2014), pp. 190–200. DOI: 10.1016/j.geomorph.2014.01.008.

[181] W. Luo et al. "Wind tunnel simulation of the three-dimensional airflow patterns behind cuboid obstacles at different angles of wind incidence, and their significance for the formation of sand shadows". In: *Geomorphology* 139-140 (2012), pp. 258–270. DOI: 10.1016/j.geomorph.2011.10.027.

[182] L. Lyles and R. K. Krauss. "Threshold velocities and initial particle motion as influenced by air turbulence". In: *Trans. ASAE* (1971), pp. 14563–14566.

[183] R. Ma et al. "Effectiveness of shelterbelt with a non-uniform density distribution". In: *Journal of Wind Engineering and Industrial Aerodynamics* 98 (2010), pp. 767–771. DOI: 10.1016/j.jweia.2010.07.001.

[184] J. Mandula, B. Salaiova, and M. Koval'akova. "Prediction of noise from tram traffic in urban units". In: *Journal of Scientific Papers of Rzeszów University of Technology* 32[180].2 (2000), pp. 237–244. URL: https://www.infona.pl/resource/bwmeta1.element.baztech-article-BTB2-0047-0097/tab/summary.

[185] R. L. Martin and J. F. Kok. "Wind-invariant saltation heights imply linear scaling of aeolian saltation flux with shear stress". In: *Sci. Adv.* 3 (2017), e1602569. DOI: 10.1126/sciadv.1602569.

[186] M. L. Martínez and N. P. Psuty, eds. *Coastal Dunes: Ecology and Conservation*. Springer-Verlag Berlin Heidelberg, 2004. DOI: 10.1007/978-3-540-74002-5.

[187] R. Martinuzzi and C. Tropea. "The Flow Around Surface-Mounted, Prismatic Obstacles Placed in Fully Developed Channel Flow". In: *Journal of Fluids Engineering* 115 (1993), pp. 85–92. DOI: 10.1115/1.2910118.

[188] J. R. Mayaud and N. P. Webb. "Vegetation in Drylands: Effects on Wind Flow and Aeolian Sediment Transport". In: *Land* 6.3 (2017), p. 64. DOI: 10.3390/land6030064.

[189] J. R. Mayaud et al. "Modelling aeolian sand transport using a dynamic mass balancing approach". In: *Geomorphology* 280 (2017), pp. 108–121. DOI: 10.1016/j.geomorph.2016.12.006.

[190] S. McClure et al. "Shelter effects of porous multi-scale fractal fences". In: *Journal of Wind Engineering and Industrial Aerodynamics* 163 (2017), pp. 6–14. DOI: 10.1016/j.jweia.2017.01.007.

[191] I. McEwan and J. Heald. "Discrete particle modeling of entrainment from flat uniformly sized sediment beds". In: *Journal of Hydraulic Engineering* 127.7 (2001), pp. 588–597. DOI: 10.1061/(ASCE)0733-9429(2001)127:7(588).

[192] C. McKenna Neuman. "Effects of temperature and humidity upon the entrainment of sedimentary particles by wind". In: *Boundary Layer Meteorol.* 108.1 (2003), pp. 61–89. DOI: 10.1023/A:1023035201953.

[193] C. McKenna Neuman. "Effects of temperature and humidity upon the transport of sedimentary particles by wind". In: *Sedimentology* 51 (2004), pp. 1–17. DOI: 10.1046/j.1365-3091.2003.00604.x.

[194] C. McKenna Neuman and O. Bédard. "A wind tunnel study of flow structure adjustment on deformable sand beds containing a surface-mounted obstacle". In: *Journal of Geophysical Research: Earth Surface* 120 (2015). DOI: 10.1002/2015JF003475.

[195] C. McKenna Neuman and W. G. Nickling. "A theoretical and wind tunnel investigation of the effect of capillary water on the entrainment of sediment by wind". In: *Can. J. Soil Sci.* 69 (1989), pp. 79–96. DOI: 10.4141/cjss89-008.

[196] C. McKenna Neuman, R. S. Sanderson, and S. Sutton. "Vortex shedding and morphodynamic response of bed surfaces containing non-erodible roughness elements". In: *Geomorphology* 198 (2013), pp. 45–56. DOI: 10.1016/j.geomorph.2013.05.011.

[197] W. T. McLaughlin and R. L. Brown. *Controlling Coastal Sand Dunes in the Pacific Northwest*. Tech. rep. US Dept. of Agriculture, 1942.

[198] MEED Insight. *Middle East Rail and Metro Projects Report 2014*. Tech. rep. 2014.

[199] E. R. Melcher and A. T. Beck. *Structural Reliability Analysis and Prediction*. Wiley, 2018. DOI: 10.1002/9781119266105.

[200] R. Méndez. *La arena invade tramos del AVE Medina-La Meca*. 2016. URL: https://www.elconfidencial.com/empresas/2016-03-07/la-arena-invade-tramos-del-ave-a-la-meca-ante-la-paralisis-del-consorcio-espanol_1163269/.

[201] P. Merino. "Arabia Saudi: Un reto exigente para la internacionalización de la tecnología española". In: *Lineas* 80 (2014), pp. 58–67. URL: http://www.adif.es/es_ES/comunicacion_y_prensa/doc/UltimoNumero.pdf.

[202] J. P. Merrison. "Sand transport, erosion and granular electrification". In: *Aeolian Res.* 4 (2012), pp. 1–16. DOI: 10.1016/j.aeolia.2011.12.003.

[203] J. van der Merwe. *T-Track System*. 2013. URL: http://ttracksaudi.com.

[204] D. Mestoul, R. Bensalem, and L. Adolphe. "Modeling of urban form against sand accumulation in the city of Gourara in southern Algeria". In: *Energy Procedia* 122 (2017), pp. 913–918. DOI: doi.org/10.1016/j.egypro.2017.07.405.

[205] G. Michas. "Slab Track Systems for High-Speed Railways". MA thesis. Stockholm, Sweden: Royal Institute of Technology (KTH), 2012. URL: https://pdfs.semanticscholar.org/69f8/d0e5d9c8572bad83cfdfae1eb2f00262b20d.pdf.

[206] N. J. Middleton and T. Sternberg. "Climate hazards in drylands: A review". In: *Earth-Science Reviews* 126 (2013), pp. 48–57. DOI: 10.1016/j.earscirev.2013.07.008.

[207] D. J. Mitchell et al. "Wind Erosion and Dune Stabilisation in Ningxia, China". In: (1996). URL: http://www.uft.uni-bremen.de/Revitalisierung/texte/1996%20mitchell%20china%20sand%20stabil.pdf.

[208] D. Mohan and L. Yuanyuan. *Raging sandstorm in Inner Mongolia: Lince was forced to open next day the railway passenger line*. In Chinese. China Radio International. 2010. URL: http://gb.cri.cn/27824/2010/12/30/5187s3108418.htm.

[209] P. Nalpanis, J. C. R. Hunt, and C. F. Barret. "Saltating particles over flat beds". In: *J. Fluid Mech.* 251 (1993), pp. 661–685. DOI: 10.1017/S0022112093003568.

[210] F. Naser, C. Baker, and F. Schmid. "A review of railway windblown sand mitigation techniques and a structural analysis of a novel tunneling solution". In: *International Workshop on Railway Aerodynamics*. University of Birmingham, Apr. 2013.

[211] V. Nathawat and A. Sharda. "Challenges of Track Maintenance in Desert Area - Problems and Remedies". In: *Permanent Way Bulletin* 32.1 (2005), pp. 1–8.

[212] R. B. Nelsen. *An Introduction to Copulas*. Springer Series in Statistics. Springer-Verlag, 2007. DOI: 10.1007/0-387-28678-0.

[213] J Nicholson. *The Hejaz Railway*. Stacey International, 2005. DOI: 10.1080/03068370600906481.

[214] W. G. Nickling. "The initiation of particle movement by wind". In: *Sedimentology* 35 (1988), pp. 499–511. DOI: 10.1111/j.1365-3091.1988.tb01000.x.

[215] W. G. Nickling and C. McKenna Neuman. "Geomorphology of Desert Environments". In: ed. by A. J. Parsons and A. D. Abrahams. Springer: Netherlands, 2009. Chap. Aeolian sediment transport. DOI: 10.1007/978-1-4020-5719-9.

[216] W. G. Nickling and C. McKenna Neuman. "Wind tunnel evaluation of a wedge-shaped aeoilian sediment trap". In: *Geomorphology* 18 (1997), pp. 333–345. DOI: doi:10.1016/S0169-555X(96)00040-2.

[217] Y. Niño, F. Lopez, and M. Garcia. "Threshold for particle entrainment into suspension". In: *Sedimentology* 50 (2003). DOI: 10.1046/j.1365-3091.2003.00551.x.

[218] M. P. O'Brien and B. D. Rindlaub. "The transportation of sand by wind". In: *Civil Engineering* 6 (1936), pp. 325–327.

[219] M. O'Rourke, A. DeGaetano, and J. D. Tokarczyk. "Analytical Simulation of Snow Drift Loading". In: *Journal of Structural Engineering* 131.4 (2005), pp. 660–667. DOI: 10.1061/(ASCE)0733-9445(2005)131:4(660).

[220] T. R. Oke. *Boundary Layer Climates*. Vol. 435. Routledge, 1987. URL: https://bayanbox.ir/view/6693893538424427706/T.-R.-Oke-Boundary-Layer-Climates-Second-Editio-BookFi.org.pdf.

[221] P. R. Owen. "Saltation of uniform grains in air". In: *Journal of Fluid Mechanics* 20.2 (1964), pp. 225–242. DOI: 10.1017/S0022112064001173.

[222] P. R. Owen and D. Gillette. "Wind tunnel constraint on saltation". In: *Proc. International Workshop on the Physics of Blown Sand*. Vol. 2. University of Aarhys, Denmark, 1985, pp. 253–269.

[223] Y. Ozmen, E. Baydar, and J.P.A.J. van Beeck. "Wind flow over the low-rise building models with gabled roofs having different pitch angles". In: *Building and Environment* 95 (2016), pp. 63–74. DOI: 10.1016/j.buildenv.2015.09.014.

[224] M. Page. *Clean-up work underway as winds blow huge piles of sand onto roads and paths in Cleethorpes*. Mar. 2018. URL: https://www.grimsbytelegraph.co.uk/news/clean-up-work-underway-winds-1286702.

[225] T. Pahtz, J. F. Kok, and H. J. Herrmann. "The apparent roughness of a sand surface blown by wind from an analytical model of saltation". In: *New Journal of Physics* 14.043035 (2012). DOI: 10.1088/1367-2630/14/4/043035.

[226] H. Parry. *Massive eighty foot tall sand dunes threaten to SWALLOW UP homes on the banks of Lake Michigan*. July 2017. URL: http://www.dailymail.co.uk/news/article-4719294/Sand-dunes-threaten-swallow-homes-near-Lake-Michigan.html.

[227] C. Paz et al. "Numerical study of the impact of windblown sand particles on a high-speed train". In: *Journal of Wind Engineering and Industrial Aerodynamics* 145 (2015), pp. 87–93. DOI: 10.1016/j.jweia.2015.06.008.

[228] M. Pensa, P. Spirito Petrosimo, and G. Spirito Petrosimo. "Barriera Antivento, particolarmente per venti carichi di sabbia". IT/1224625. 1990.

[229] J. Pettus Newell. "Sand Guards for Railroad Tracks". US/731320. 1903.

[230] D. A. Phillips. "Analysis of Potential Sand Dune Impacts on Railway Tracks and Methods of Mitigation". In: *GCC Transport and Railway Conference*. Doha, Qatar, Oct. 2011, pp. 17–19. URL: http://www.iktissadevents.com/files/events/gtrc/1/presentations/d2-s8-duncan-phillips.pdf.

[231] J. S. Plaza, M. Lombardero Barceló, and P. Rodríguez de Lema Tapetado. "Sand and Wind: an outline of the study of aeolian action on infrastructure with reference to Haramain High Speed Railway, Makkah–Al-Madinah". In: *Revista de Obras Públicas* 159.3537 (Nov. 2012), pp. 7–36. URL: http://ropdigital.ciccp.es/detalle_articulo.php?registro=19202&anio=2012&numero_revista=3537.

[232] P. Pointner, A. Joerg, and J. Jaiswal. *Definitive guidelines on the use of different rail grades*. Deliverable report D4.1.5GL. EU-Project "Innovative Track Systems" (Innotrack, TIP5-CT-2006-031415), 2009.

[233] A. Poortinga et al. "Measurement uncertainties in quantifying aeolian mass flux: evidence from wind tunnel and field site data". In: *PeerJ* 2:e454 (2014). DOI: 10.7717/peerj.454.

[234] A. K. Pozarlik and J. B. W. Kok. "Numerical Simulation of a Turbulent Flow Over a Backward Facing Step With Heated Wall: Effect of Pulsating Velocity and Oscillating Wall". In: *International Journal of Thermal Sciences* 4.4 (2012). DOI: 10.1115/1.4007278.

[235] L. Preziosi, D. Fransos, and L. Bruno. "A multiphase first order model for non-equilibrium sand erosion, transport and sedimentation". In: *Applied Mathematics Letters* 45 (2015), pp. 69–75. DOI: 10.1016/j.aml.2015.01.011.

[236] K. Pye. *Aeolian dust and dust deposits*. Academic Press, 1987. DOI: 10.1016/C2013-0-05007-4.

[237] K. Pye and H. Tsoar. *Aeolian Sand and Sand Dunes*. Springer, 2009. DOI: 10.1007/978-3-540-85910-9.

[238] W. Qi and F. Gao. "Physical modeling of local scour development around a large-diameter monopile in combined waves and current". In: *Coastal Engineering* 83 (2014), pp. 72–81. DOI: 10.1016/j.coastaleng.2013.10.007.

[239] G. Y. Qiu et al. "Principles of sand dune fixation with straw checkerboard technology and its effects on the environment". In: *Journal of Arid Environments* 56.3 (2004), pp. 449–464. DOI: 10.1016/S0140-1963(03)00066-1.

[240] J. Qu et al. "Field observations on the protective effect of semi-buried checkerboard sand barriers". In: *Geomorphology* 88.1 (2007), pp. 193–200. DOI: 10.1016/j.geomorph.2006.11.006.

[241] L. Raffaele and L. Bruno. "Windblown sand action on civil structures: Definition and probabilistic modelling". In: *Engineering Structures* 178 (2019), pp. 88–101. DOI: 10.1016/j.engstruct.2018.10.017.

[242] L. Raffaele, L. Bruno, and G. F. Wiggs. "Uncertainty propagation in aeolian processes: From threshold shear velocity to sand transport rate". In: *Geomorphology* 301 (2018), pp. 28–38. DOI: 10.1016/j.geomorph.2017.10.028.

[243] L. Raffaele et al. "Incoming windblown sand drift to civil infrastructures: A probabilistic evaluation". In: *Journal of Wind Engineering and Industrial Aerodynamics* 166 (2017), pp. 37–47. DOI: 10.1016/j.jweia.2017.04.004.

[244] L. Raffaele et al. "Windblown sand saltation: A statistical approach to fluid threshold shear velocity". In: *Aeolian Research* 23 (2016), pp. 79–91. DOI: 10.1016/j.aeolia.2016.10.002.

[245] M. A. Rahim. "Behaviour of Drift sand and Method of Dealing with it". In: *Pakistan Engineering Congress*. Vol. 32. 271. 1945.

[246] K. R. Rasmussen, J. D. Iversen, and P. Rautahemio. "The effect of surface slope on saltation threshold". In: *Sedimentology* 41 (1994), pp. 721–728. DOI: 10.1111/j.1365-3091.1994.tb01419.x.

[247] S. Ravi et al. "On the effect of air humidity on soil susceptibility to wind erosion: the case of air-dry soils". In: *Geophysical Research Letters* 31 (2004), p. L09501. DOI: 10.1029/2004GL019485.

[248] J. H. Redding and J. A. Lord. "Designing for the effects of windblown sand along the new Jessah-Riyadh-Dammam expressway". In: *Symposium on Geotechnical Problems in Saudi Arabia*. 1981, pp. 363–395.

[249] J. C. Refsgaard et al. “Uncertainty in the environmental modelling process - A framework and guidance”. In: *Environmental Modelling & Software* 22 (2007), pp. 1543–1556. DOI: 10.1016/j.envsoft.2007.02.004.

[250] H. M. Regan, M. Colyvan, and M. A. Burgman. “A taxonomy and treatment of uncertainty for ecology and conservation biology”. In: *Ecological Applications* 12.2 (2002), pp. 618–628. DOI: 10.1890/1051-0761(2002)012[0618:ATATOU]2.0.CO;2.

[251] M. P. Repetto and G. Solari. “Directional Wind-Induced Fatigue of Slender Vertical Structures”. In: *Journal of Structural Engineering* 130.7 (2004), pp. 1032–1040. DOI: 10.1061/~ASCE!0733-9445~2004!130:7~1032!.

[252] M. P. Repetto and A. Torrielli. “Long term simulation of wind-induced fatigue loadings”. In: *Engineering Structures* 132 (2017), pp. 551–561. DOI: 10.1016/j.engstruct.2016.11.057.

[253] K. Riessberger. “Heavy Haul in Sand Environment”. In: *IHHA 2015 Conference*. Perth, Australia, June 2015. URL: http://railknowledgebank.com/Presto/content/GetDoc.axd?ctID=MTk4MTRjNDUtNWQ0My00OTBmLTllYWUtZWFjM2U2OTE0ZDcz&rID=MjgyOQ==&pID=Nzkx&attchmnt=VHJ1ZQ==&uSesDM=False&rIdx=Mjg4OA==&rCFU=.

[254] K. Riessberger and W. Swanepoel. “Specialised Sleepers Combat Sand”. In: *Railway Gazette International* (Sept. 2005), p. 555. URL: https://trid.trb.org/view.aspx?id=789500.

[255] M. J. P. M. Riksen et al. “Constructing notches in foredunes: Effect on sediment dynamics in the dune hinterland”. In: *Geomorphology* 15 (2016), pp. 340–352. DOI: 10.1016/j.geomorph.2015.10.021.

[256] A. A. Rizvi. “Planning Responses to Aeolian Hazards in Arid Regions”. In: *Journal of King Saud University, Architecture & Planning* 1 (1989), pp. 59–74.

[257] J. Rodríguez Hernández et al. “Protective barrier for snowstorms”. EP2354312A1. 2008.

[258] J. A. Roney and B. R. White. “Definition and measurement of dust aeolian thresholds”. In: *J. Geophys. Res.* 109.F01013 (2004). DOI: 10.1029/2003JF000061.

[259] S. R. Sadin, F. P. Povinelli, and R. Rosen. “The NASA technology push towards future space mission systems”. In: *Acta Astronautica* 20 (1989), pp. 73–77. DOI: 10.1016/0094-5765(89)90054-4.

[260] P. G. Saffman. “Lift on a small sphere in a slow shear flow”. In: *J. Fluid Mech.* 22 (1965), p. 385. DOI: 10.1017/S0022112065000824.

[261] M. Saifi, N. Boulghobra, and L. Fattoum. "The Green Dam in Algeria as a tool to combat desertification". In: *Planet@Risk* 3.1 (2015). Davos: Global Risk Forum GRF Davos, pp. 68–71.

[262] A. B. Salman et al. "Environmental impact and natural hazards on Kharga Oasis monumental sites, Western Desert of Egypt". In: *Journal of African Earth Sciences* 58.2 (2010), pp. 341–353. DOI: 10.1016/j.jafrearsci.2010.03.011.

[263] A.M. Al-Sari and W. Uddin. "Eolian Sand Problem: an Engineering Evaluation". In: *Proceedings Symposium Geotechnical Problems in Saudi Arabia*. 1981.

[264] R. D. Sarre. "Aeolian sand transport". In: *Progress in Physical Geography* 11 (1987), pp. 157–182.

[265] A. Sato and M. Ono. "Snowstorm guard fence structures and jet roofs. US4958806A". US 4958806 A. 1990. URL: https://www.google.com/patents/US4958806.

[266] R. P. Savage and W. W. Woodhouse. "Creation and stabilization of coastal barrier dunes". In: *11th International Conference on Coastal Engineering*. London, 1968. DOI: 10.1061/9780872620131.043.

[267] Aebi Schmidt. *Santera 3000 Technical Sheet*. 2013. URL: https://www.aebi-schmidt.com/en/products/street-cleaning/sand-cutter-blower-santera-3000.

[268] C. Schölzel and P. Friederichs. "Multivariate non-normally distributed random variables in climate research - introduction to the copula approach". In: *Nonlinear Processes in Geophysics* 15.5 (2008), pp. 761–772. DOI: 10.5194/npg-15-761-2008.

[269] E. T. Selig and J. M. Waters. *Track geotechnology and substructure management*. London: Thomas Telford Services Ltd, 1994.

[270] Y. Shao. *Physics and Modelling of Wind Erosion*. Springer, 2008. DOI: 10.1007/978-1-4020-8895-7.

[271] Y. Shao and H. Lu. "A simple expression for wind erosion threshold friction velocity". In: *J. Geophys. Res.* 105 (2000), pp. 22437–43. DOI: 10.1029/2000JD900304.

[272] D. J. Sherman and B. Li. "Predicting aeolian sand transport rates: A reevaluation of models". In: *Aeolian Research* 3 (2012), pp. 371–378. DOI: 10.1016/j.aeolia.2011.06.002.

[273] D. J. Sherman and K. F. Nordstrom. "Hazards of Wind-Blown Sand and Coastal Sand Drifts: A Review". In: *Journal of Coastal Research* 12 (1994), pp. 263–275. URL: www.jstor.org/stable/25735603.

[274] D. J. Sherman et al. "Recalibrating aeolian sand transport models". In: *Earth Surf. Process. Landforms* 38 (2013), pp. 169–178. DOI: 10.1002/esp.3310.

[275] Douglas J Sherman et al. "Wind-blown sand on beaches: an evaluation of models". In: *Geomorphology* 22.2 (1998), pp. 113–133. DOI: 10.1016/S0169-555X(97)00062-7.

[276] L. Shi et al. "Three - dimensional Simulation Analysis of Response Law of Windblown Sand Flow around the Railway Culvert". In: *Journal of Railway Engineering Society* 33.9 (2016), pp. 14–18.

[277] Oriental Shuraa. *TerraFirma TF-2000 - Technical Data Sheet*. 2014. URL: http://www.terrafirma.biz/.

[278] E. Simiu and R. H. Scanlan. *Winds Effects on Structures: Fundamentals and Applications to Design*. 3rd ed. New York: Wiley, 1996.

[279] J. Sinha et al. "Computational Investigation of Control Effectiveness on a Near Transition Open and Closed Axisymmetric Cavity". In: *Advances in Aerospace Science and Applications* 4.1 (2014), pp. 45–52. URL: https://www.researchgate.net/publication/261988204_Computational_Investigation_of_Control_Effectiveness_on_a_Near_Transition_Open_and_Closed_Axisymmetric_Cavity.

[280] R. C. Smith. *Uncertainty Quantification: Theory, Implementation, and Applications*. SIAM, 2014.

[281] T. A. G. Smyth. "A review of Computational Fluid Dynamics (CFD) airflow modelling over aeolian landforms". In: *Aeolian Res.* 22 (2016), pp. 153–164. DOI: 10.1016/j.aeolia.2016.07.003.

[282] G. Solari. "Thunderstorm response spectrum technique: Theory and applications". In: *Engineering Structures* 108 (2016), pp. 28–46. DOI: 10.1016/j.engstruct.2015.11.012.

[283] M. Sørensen. "Stochastic Models of Sand Transport by Wind and Two Related Estimation Problems". In: *International Statistical Review* 61.2 (1993), pp. 245–255. DOI: 10.2307/1403627.

[284] C. J. Stigter et al. "Agroforestry solutions to some African wind problems". In: *Journal of Wind Engineering and Industrial Aerodynamics* 90 (2002), pp. 1101–1114. DOI: 10.1016/S0167-6105(02)00224-6.

[285] A. S. Stipho. "Aeolian sand hazards and engineering design for desert regions". In: *Quarterly Journal of Engineering Geology* 25 (1992), pp. 83–92. DOI: 10.1144/GSL.QJEG.1992.025.02.02.

[286] J. E. Stout. "A method for establishing the critical threshold for aeolian transport in the field". In: *Earth Surf. Process. Landf.* 29 (2004). DOI: 10.1002/esp.1079.

[287] D. Sumner. "Flow above the free end of a surface-mounted finite-height circular cylinder: A review". In: *Journal of Fluids and Structures* 43 (2013), pp. 41–63. DOI: 10.1016/j.jfluidstructs.2013.08.007.

[288] C. Swann, R. C. Ewing, and D. J. Sherman. "A Threshold Continuum for Aeolian Sand Transport". In: *Proceedings American Geophysical Union Fall Meeting, abstract EP24A-04*. San Francisco, 14-18 December 2015.

[289] R. D. Tabler. *Controlling Blowing and Drifting Snow with Snow Fences and Road Design*. Tech. rep. National Cooperative Highway Research Program Transportation Research Board of the National Academies, 2003. URL: https://www.esf.edu/willow/lsf/Litterature/Tabler%202003%20-%20Controlling%20Blowing%20and%20Drifting%20Snow.pdf.

[290] E. S. Takle and J. M. Brown. "Note on the Use of Weibull Statistics to Characterize Wind-Speed Data". In: *J. Appl. Meteorol.* 17 (1978), pp. 556–559. DOI: 10.1175/1520-0450(1978)017<0556:NOTUOW>2.0.CO;2.

[291] N. Tennakoon et al. "Assessment of ballast fouling and its implications on track drainage". In: *11th Australia - New Zealand Conference on Geomechanics: Ground Engineering in a Changing World*. Ed. by G. A. Narsilio, A. Arulrajah, and J. Kodikara. ANZ Geomechanics. 2012, pp. 421–426.

[292] Terratech. *Railway Sand Drift Abatement*. 2010. URL: http://www.terratechinfo.com/soil-stabilization-polymer/projects/specialty-applications/railway-sand-drift-abatement.

[293] T. Thake. "ERTMS implementation in Saudi Arabia". In: *International Strategic Rail Forum*. Abu Dhabi, Apr. 2012.

[294] Y. Tian. "Wind erosion: threshold velocity for initial particle movement". MA thesis. Texas Tech University, 1988.

[295] A. Torrielli, M. P. Repetto, and G. Solari. "Long-term simulation of the mean wind speed". In: *Journal of Wind Engineering and Industrial Aerodynamics* 99 (2011), pp. 1139–1150. DOI: 10.1016/j.jweia.2011.08.003.

[296] A. Tresca et al. "MANAGEMENT OF AEOLIAN SAND TRANSPORT ON A DIKE, DUNKIRK SEAPORT, FRANCE". In: *Coastal Engineering Proceedings*. Vol. 33. 2012. URL: https://icce-ojs-tamu.tdl.org/icce/index.php/icce/article/view/6682.

[297] R. Tresso and D. R. Munoz. "Homogeneous, Isotropic Flow in Grid Generated Turbulence". In: *Journal of Fluids Engineering* 12256.1 (1999), pp. 51–56. DOI: 10.1115/1.483226.

[298] P. K. Trivedi and D. M. Zimmer. *Copula Modeling: An Introduction for Practitioners*. Vol. 1. now Publisher, 2005. DOI: 10.1561/0800000005.

[299] H. Tsoar, D. G. Blumberg, and Y. Stoler. "Elongation and migration of sand dunes". In: *Geomorphology* 57 (2004), pp. 293–302. DOI: 10.1016/S0169-555X(03)00161-2.

[300] W. R. Tyfour. "Effect of moving sand as a ballast contaminant on rail corrugation: field experience". In: *International Journal of Environmental Engineering* 6.1 (2014), pp. 15–28. DOI: 10.1504/IJEE.2014.057836.

[301] W. R. Tyfour. "Predicting the Effect of Grinding Corrugated Rail Surface on the Wear Behavior of Pearlitic Rail Steel". In: *Tribology Letters* 29.3 (2008), pp. 229–234. DOI: 10.1007/s11249-008-9300-y.

[302] UNISIG. *FFFIS for Eurobalise, SUBSET-036 issue 3.0.0, Mandatory Specification, ERTMS*. UNISIG, 2012.

[303] S. Unnikrishnan, A. Ogunremi, and D. Sumner. "The effect of incidence angle on the mean wake of surface-mounted finite-height square prisms". In: *International Journal of Heat and Fluid Flow* 66 (2017), pp. 137–156. DOI: 10.1016/j.ijheatfluidflow.2017.05.012.

[304] L. Uusitalo et al. "An overview of methods to evaluate uncertainty of deterministic models in decision support". In: *Environmental Modelling & Software* 63 (2015), pp. 24–31. DOI: 10.1016/j.envsoft.2014.09.017.

[305] A. Valence et al. "The physics of Aeolian sand transport". In: *Comptes Rendus Physique* 16.1 (2015), pp. 105–117. DOI: 10.1016/j.crhy.2015.01.006.

[306] H. F. del Valle et al. "Sand dune activity in north-eastern Patagonia". In: *Journal of Arid Environments* 72.4 (2008), pp. 411–422. DOI: 10.1016/j.jaridenv.2007.07.011.

[307] G. G. Venter. "Tails of Copulas". In: *Proceedings of the Casualty Actuarial Society*. 2002.

[308] D. J. de Waal and P. H. A. J. M. van Gelder. "Modelling of extreme wave heights and periods through copulas". In: *Extremes* 8 (2005), pp. 345–356. DOI: 10.1007/s10687-006-0006-y.

[309] I. J. Walker. "Secondary airflow and sediment transport in the lee of a reversing dune". In: *Earth Surf. Proc. Land.* 24.5 (1999), pp. 437–448. DOI: 10.1002/(SICI)1096-9837(199905)24:5<437::AID-ESP999>3.0.CO;2-Z.

[310] I. J. Walker and W. G. Nickling. "Simulation and measurement of surface shear stress over isolated and closely spaced transverse dunes in a wind tunnel". English. In: *Earth Surf. Proc. Land.* 28.10 (Sept. 2003), pp. 1111–1124. DOI: 10.1002/esp.520.

[311] K. Wang, J. Jiang, and W. Zhang. "Establishment of Protective System and its Ecological Benefit Along Both Sides of Jing-Tong Railway". In: *Journal of Desert Research* 9.3 (1989), pp. 1–12.

[312] T. T. Wang et al. "The Influence of Wind-Blown Sand on High-Speed Train Aerodynamic Performance". In: *Proceedings of the Third International Conference on Railway Technology: Research, Development and Maintenance*. Ed. by J Pombo. Civil-Comp Press, 2016. DOI: 10.4203/ccp.110.51.

[313] T. Wang et al. "Numerical simulation of sand load applied on high-speed train in sand environment". In: *J. Cent. South Univ.* 24 (2017), pp. 442–447. DOI: 10.1007/s11771-017-3446-4.

[314] T. Wang et al. "Shelter effect efficacy of sand fences: A comparison of systems in a wind tunnel". In: *Aeolian Research* 30 (2018), pp. 32–40. DOI: 10.1016/j.aeolia.2017.11.004.

[315] X. M. Wang et al. "Has the Three Norths Forest Shelterbelt Program solved the desertification and dust storm problems in arid and semiarid China?" In: *Journal of Arid Environments* 74 (2010), pp. 13–22. DOI: 10.1016/j.jaridenv.2009.08.001.

[316] A. Watson. "The control of windblown sand and moving dunes: a review of the methods of sand control in deserts, with observations from Saudi Arabia". In: *Quarterly Journal of Engineering Geology* 18 (1985), pp. 237–252. DOI: 10.1144/GSL.QJEG.1985.018.03.05.

[317] N. P. Webb and C. L. Strong. "Soil erodibility dynamics and its representation for wind erosion and dust emission models". In: *Aeolian Res.* 3 (2011), pp. 165–179. DOI: 10.1016/j.aeolia.2011.03.002.

[318] N. P. Webb et al. "Threshold wind velocity dynamics as a driver of aeolian sediment mass flux". In: *Aeolian Research* 20 (2016), pp. 45–58. DOI: http://dx.doi.org/10.1016/j.aeolia.2015.11.006.

[319] Rainer Wenty. "The SRM 500 - A high-output sand removal machine for combating sand drifts". In: *Rail Engineering International* 4 (2017), pp. 9–10.

[320] B. R. White. "Laboratory Simulation of Aeolian Sand Transport and Physical Modeling of Flow Around Dunes". In: *Annals of arid zone* 35.3 (1996), pp. 187–213.

[321] B. R. White and H. Mounla. "An experimental study of Froude number effect on wind-tunnel saltation". In: *Acta Mechanica* 1 (1991), pp. 145–157. DOI: 10.1007/978-3-7091-6706-9_9.

[322] J. J. Williams, G. R. Butterfield, and A. G. Clark. "Aerodynamic entrainment threshold: effects of boundary layer flow conditions". In: *Sedimentology* 41 (1994), pp. 309–328. DOI: 10.1111/j.1365-3091.1994.tb01408.x.

[323] J. J. Williams, G. R. Butterfield, and A. G. Clark. "Rates of aerodynamic entrainment in a developing boundary layer". In: *Sedimentology* 37 (1990), pp. 1039–1048. DOI: 10.1111/j.1365-3091.1990.tb01844.x.

[324] C. Winchester and C. J. Allen. "Railway Wonders of the World". In: Amalgamated Press., 1935. Chap. Through Desert and Jungle.

[325] C. Winchester and C. J. Allen. "Railway Wonders of the World". In: Amalgamated Press, 1935. Chap. In Northern Africa.

[326] M. Woldman et al. "Investigating the influence of sand particle properties on abrasive wear behaviour". In: *Wear* 294-295 (2012), pp. 419–426. DOI: 10.1016/j.jweia.2015.06.008.

[327] F. C. Wu and Y. Chou. "Rolling and Lifting Probabilities for Sediment Entrainment". In: *Journal of Hydraulic Engineering* 129.2 (2003). DOI: 10.1061/(ASCE)0733-9429(2003)129:2(110).

[328] J. Xiao, Z. Yao, and J. Qu. "Influence of Golmud-Lhasa Section of Qinghai-Tibet Railway on Blown Sand Transport". In: *Chinese Geographical Science* 25.1 (2015), pp. 39–50. DOI: 10.1007/s11769-014-0722-1.

[329] J. Xiao et al. "Morphology and formation mechanism of sand shadow dunes on the Qinghai-Tibet Plateau". In: *J. Arid Land* 7.1 (2015), pp. 10–26. DOI: 10.1007/s40333-014-0074-9.

[330] S. Xie, J. Qu, and Y. Pang. "Dynamic wind differences in the formation of sand hazards at high- and low-altitude railway sections". In: *Journal of Wind Engineering and Industrial Aerodynamics* 169 (2017), pp. 39–46. DOI: 10.1016/j.jweia.2017.07.003.

[331] S. Xie et al. "Formation mechanism and suitable controlling pattern of sand hazards at Honglianghe River section of Qinghai–Tibet Railway". In: *Natural Hazards* 76.2 (2015), pp. 855–871. DOI: 10.1007/s11069-014-1523-7.

[332] H. Xiong et al. "Numerical study on the aerodynamic performance and safe running of high-speed trains in sandstorms". In: *J. Zhejiang University-SCIENCE A Appl. Phys. Eng.* 12 (2011), pp. 971–978. DOI: 10.1631/jzus.A11GT005.

[333] L. Xu et al. "Experiment test of wind-sand flow destruction to train tempered glass". In: *Journal of Central South University (Science and Technology)* 7 (2014), pp. 2489–2495.

[334] Y. Xu and Y. M. Mustafa. "Using CFD-Based Virtual Sensor Data to Study the Structure of Air Flow behind A Porous Fence". In: *The Eighth International Conference on Sensor Technologies and Applications*. 2014. URL: https://www.researchgate.net/publication/287310511_Using_CFD-based_virtual_sensor_data_to_study_the_structure_of_air_flow_behind_a_porous_fence.

[335] H. Xue et al. “Analysis of the Damage to the Aeolian sand Concrete Surface Caused by Wind-Sand Erosion”. In: *Journal of Advanced Concrete Technology* 15 (2017), pp. 724–737. DOI: 10.3151/jact.15.724.

[336] J. Yan et al. “Reviews on uncertainty analysis of wind power forecasting”. In: *Renewable and Sustainable Energy Reviews* 52 (2015), pp. 1322–1330. DOI: 10.1016/j.rser.2015.07.197.

[337] X. Yang et al. “Initial insights into the age and origin of the Kubuqi sand sea of northern China”. In: *Geomorphology* 259 (2016), pp. 30–39. DOI: 10.1016/j.geomorph.2016.02.004.

[338] Y. Yang et al. “Wind regime and sand transport in the corridor between the Badain Jaran and Tengger deserts, central Alxa Plateau, China”. In: *Aeolian Research* 12 (2014), pp. 143–156. DOI: 10.1016/j.aeolia.2013.12.006.

[339] J. A. Zakeri. “Investigation on railway track maintenance in sandy-dry areas”. In: *Structure and Infrastructure Engineering: Maintenance, Management, Life-Cycle Design and Performance* 8.2 (2012), pp. 135–140. DOI: 10.1080/15732470903384921.

[340] J. A. Zakeri and R. Abbasi. “Field investigation of variation of loading pattern of concrete sleeper due to ballast sandy contamination in sandy desert areas”. In: *Journal of Mechanical Science and Technology* 26.12 (2012), pp. 3885–3892. DOI: 10.1007/s12206-012-0886-5.

[341] J. A. Zakeri, M. Esmaeili, and M. Fathali. “Evaluation of humped slab track performance in desert railways”. In: *Proceedings of the Institution of Mechanical Engineers, Part F: Journal of Rail and Rapid Transit* 225.6 (2011), pp. 566–573. DOI: 10.1177/0954409711403677.

[342] J. A. Zakeri and M. Forghani. “Railway Route Design in Desert Areas”. In: *American Journal of Environmental Engineering* 2.2 (2012), pp. 13–18. DOI: 10.5923/j.ajee.20120202.03.

[343] J. A. Zakeri et al. “Effects of vibration in desert area caused by moving trains”. In: *Journal of Modern Transportation* 20.1 (2012), pp. 16–23. DOI: 10.1007/BF03325772.

[344] C. L. Zhang et al. “Engineering measures to control windblown sand in Shiquanhe Town, Tibet”. In: *Journal of Wind Engineering and Industrial Aerodynamics* 95 (2007), pp. 53–70. DOI: 10.1016/j.jweia.2006.05.006.

[345] D. Zhang et al. “Morphology and dynamics of star dunes from numerical modelling”. In: *Nature Geoscience* 5 (2012), pp. 463–467. DOI: 10.1038/ngeo1503.

[346] K. Zhang et al. “Damage by wind-blown sand and its control along Qinghai-Tibet Railway in China”. In: *Aeolian Research* 1.3-4 (2010), pp. 143–146. DOI: 10.1016/j.aeolia.2009.10.001.

[347] K. Zhang et al. "Particle Size Distribution Measurement Techniques and Their Relevance or Irrelevance to Sand Control Design". In: *Proceedings of the 2014 SPE International Symposium and Exhibition on Formation Damage Control, Lafayette, Louisiana, USA, February 26-28, 2014*. Society of Petroleum Engineers, 2014.

[348] N. Zhang, J. H. Kang, and S. J. Lee. "Wind tunnel observation on the effect of a porous wind fence on shelter of saltating sand particles". In: *Geomorphology* 120.3-4 (2010), pp. 224–232. DOI: 10.1016/j.geomorph.2010.03.032.

[349] L. Zhen-shan, Z. Xiao-hu, and H. Wen. "A stochastic model for initial movement of sand grains by wind". In: *Earth Surface Processes and Landforms* 33 (2008), pp. 1796–1803. DOI: 10.1002/esp.1638.

[350] X. Zheng. *Mechanics of Wind-blown Sand Movements*. Springer, 2009. DOI: 10.1007/978-3-540-88254-1.

[351] X. Zheng. *Mechanics Wind-Blown Sand Movements*. Springer-Verlag, 2009. DOI: 10.1007/978-3-540-88254-1.

[352] X. Zhou et al. "Wind tunnel test on responses of a lightweight roof structure under joint action of wind and snow loads". In: *Cold Regions Science and Technology* 132 (2016), pp. 19–32. DOI: 10.1016/j.coldregions.2016.09.011.

[353] A. D. Zimon. *Adhesion of Dust and Powder*. Springer, 1982. DOI: 10.1007/978-1-4615-8576-3.

[354] A. W. Zingg. "Wind tunnel studies of the movement of sedimentary material". In: *Proceedings of the 5th Hydraulic Conference Bulletin*. Vol. 34. Inst. of Hydraulics. Iowa City, 1953, pp. 111–135.

[355] E. Zio and N. Pedroni. *Literature review of methods for representing uncertainty*. Foundation for an Industrial Safety Culture, 2013.

List of publications

The thesis tackles a multidisciplinary engineering issue. As a result, the author's scientific production has been published in academic journals from different research fields in order to reflect a round trip from structural design to fundamental scientific fields.

Refereed journal papers:

- L. Raffaele, L. Bruno, F. Pellerey, L. Preziosi (2016). Windblown sand saltation: A statistical approach to fluid threshold shear velocity. *Aeolian Research*, 23, 79-91.
  doi: 10.1016/j.aeolia.2016.10.002.

- L. Raffaele, L. Bruno, D. Fransos, F. Pellerey (2017). Incoming windblown sand drift to civil infrastructures: A probabilistic evaluation. *Journal of Wind Engineering and Industrial Aerodynamics*, 166, 37-47.
  doi: 10.1016/j.jweia.2017.04.004.

- L. Raffaele, L. Bruno, G.F.S. Wiggs (2018). Uncertainty propagation in aeolian processes: From threshold shear velocity to sand transport rate. *Geomorphology*, 301, 28-38.
  doi: 10.1016/j.geomorph.2017.10.028.

- L. Bruno, M. Horvat, L. Raffaele (2018). Windblown sand along railway infrastructures: A review of challenges and mitigation measures. *Journal of Wind Engineering and Industrial Aerodynamics*, 177, 340-365.
  doi: 10.1016/j.jweia.2018.04.021.

- L. Bruno, N. Coste, D. Fransos, A. Lo Giudice, L. Preziosi, L. Raffaele (2018). Shield for Sand: an Innovative Barrier for Windblown Sand Mitigation. *Recent Patents on Engineering*, 12(3).
  doi: 10.2174/1872212112666180309151818. E-pub Ahead of Print.

- L. Raffaele and L. Bruno (2019). Windblown sand action on civil structures: Definition and probabilistic modelling. *Engineering Structures*, 178, 88-101.
  doi: 10.1016/j.engstruct.2018.10.017.

Conference proceedings & extended abstracts:

- L. Raffaele, L. Bruno, D. Fransos (2016). Windblown sand saltation: a probabilistic approach to sand transport rate, proceedings of the XIV Conference of the Italian Association for Wind Engineering, IN-VENTO 2016, September 25-28, Terni, Italy.
- L. Bruno, N. Coste, M. Horvat, L. Preziosi, L. Raffaele, G.F.S. Wiggs (2017). Interdisciplinary challenges in design of windblown sand barriers around desert railways, 6th International Workshop on Design in Civil and Environmental Engineering, DCEE 2017, November 9-11, University of Cagliari, Italy.
- L. Bruno, F. Pellerey, L. Preziosi, L. Raffaele (2017). An application of copulae in the analysis of sand transport phenomena, 10th International Conference of the ERCIM WG on Computational and Methodological Statistics, December 16-18, Senate House, University of London, UK.
- L. Raffaele, F. Pellerey, L. Preziosi, L. Bruno (2018). Aeolian windblown sand saltation: an application of copulae for the estimation of threshold shear velocity, XIV biennial congress of the Italian Society of Applied and Industrial Mathematics, SIMAI 2018, July 2-6, Sapienza Università di Roma, Italy.
- L. Raffaele, L. Bruno (2018). A semi-probabilistic framework for windblown sand action, XV Conference of the Italian Association for Wind Engineering, IN-VENTO 2018, September 9-12, Napoli, Italy.
- L. Raffaele, L. Bruno (2018). Railway megaprojects: a semi-probabilistic approach to windblown sand action, 40th IABSE Symposium, Tomorrow's Megastructures, September 19-21, Nantes, France.

Awards:

- First prize at the Tiziana Vitrano "My research in three minutes" award (17/11/2017): three minutes to effectively explain the research carried out at Politecnico di Torino by PhD students to a non-specialist audience. Prize awarded by panel of science reporters and experts in scientific dissemination on the basis of: (i) clarity and comprehensibility of the presentation for a non-specialist audience, (ii) suitability and accuracy of the language used, (iii) proper use of slides, (iv) respect of the maximum time of 3 minutes and proper use of the time. Two-stage evaluation: 38 candidates at 1st stage; 6 candidates at 2nd stage.

This Ph.D. thesis has been typeset by means of the TEX-system facilities. The typesetting engine was pdfLATEX. The document class was `toptesi`, by Claudio Beccari, with option `tipotesi=scudo`. This class is available in every up-to-date and complete TEX-system installation.